Catalyst Design for Low Temperature Oxidation of Methane to Methanol

Thesis submitted in accordance with the requirements of the University of Cardiff for the degree of:

Doctor of Philosophy

Christopher Paul Williams

2018

Cardiff
Catalysis Institute

Sefydliad Catalysis
Caerdydd

Declaration

This work has not been submitted in substance for any other degree or award at this or any other university or place of learning, nor is being submitted concurrently in candidature for any degree or other award.

Signed …… (candidate) Date……

STATEMENT 1

This thesis is being submitted in partial fulfillment of the requirements for the degree of ……(insert MCh, MD, MPhil, PhD etc, as appropriate)

Signed …… (candidate) Date……

STATEMENT 2

This thesis is the result of my own independent work/investigation, except where otherwise stated, and the thesis has not been edited by a third party beyond what is permitted by Cardiff University's Policy on the Use of Third Party Editors by Research Degree Students. Other sources are acknowledged by explicit references. The views expressed are my own.

Signed …… (candidate) Date……

STATEMENT 3

I hereby give consent for my thesis, if accepted, to be available online in the University's Open Access repository and for inter-library loan, and for the title and summary to be made available to outside organisations.

Signed …… (candidate) Date……

STATEMENT 4: PREVIOUSLY APPROVED BAR ON ACCESS

I hereby give consent for my thesis, if accepted, to be available online in the University's Open Access repository and for inter-library loans **after expiry of a bar on access previously approved by the Academic Standards & Quality Committee.**

Signed …… (candidate) Date……

Acknowledgements

For providing the opportunity to take on the challenge of a PhD at Cardiff Catalysis Institute, I thank Professor Graham Hutchings. The skills and experience gained will be invaluable for any future challenges in life. Thanks, is also extended to Dr. Randall Meyer and the team at ExxonMobil, to whom I am grateful to have worked with over the course of my PhD. Their encouragement, guidance and insights have been indispensable during my studies.

Furthermore, to Professor Stuart Taylor, Dr. David Willock, Dr. Nicholas Dummer and Dr. James Carter for their willingness to provide advice is very much appreciated, along with the encouragement and support offered during this work. To Dr. Robert Armstrong, I am grateful for the time and advice for all things methane. For the unfortunate job of reading and correcting this final piece of work, I thank Dr. James Hayward for the patience showed.

I would like to thank the many PhD students and PDRA's with whom I have had the pleasure of working, eating and laughing alongside during the course of my PhD. All of whom have made my studies that little bit easier. To Kit, I thank for being a friend and team mate as fellow PhD students during our studies within the methane team. Additionally, thanks is given to Steve Morris for the technical assistance in ensuring the running of autoclaves throughout the years.

To Dr. Richard Lewis, I express my deepest gratitude for being a friend during the difficulties, but importantly for the source of laughter needed to keep me sane during my studies.

To the Williams family, especially my Mother and Father, who have provided encouragement, support and patience during my education.

Finally, to Gwen for being the source of positivity and motivation needed during the completion of my studies.

Summary

Abundantly available through natural gas, methane is largely underutilised as a resource. Furthermore, providing a potential alternative to the production of valuable petrochemicals, direct valorisation of methane would prolong reserves of feedstock petrochemicals derived from dwindling crude oil.

Instead, due to lack of on-site valorisation processes, methane is largely flared during the production of crude oil. Even so, industrial application of used methane involves an indirect and energy intensive route transforming methane to synthesis gas (CO_2 and H_2). Further processing is then applied to effectively valorise to the desired liquid petrochemicals. Alternatively, a direct on-site route to methanol under mild conditions would limit the environmental impact of an energy intense indirect process. In addition, methanol provides a valuable non-crude oil source as an intermediate to a vast number of applications across several industries.

One avenue investigated, effectively utilised AuPd/TiO_2 catalyst for the oxidation of methane using H_2O_2 at low temperature (50 °C). Inspiring the first section of this thesis, the synthesis of AuPd/TiO_2 by impregnation provides poor control yielding a broad range of nanoparticle sizes with poor control of nanoparticle composition. Therefore, the first chapter investigates the influence of AuPd particle size, selecting sol immobilisation for controlled preparation of starting material with narrow size distribution. The application of heat treatment to promote particle size increases was investigated to confirm an influence for methane oxidation. During this work, further influences were observed during initial testing and were evaluated to improve understanding and increase catalyst productivity. These influences included variation in AuPd nanoparticle size, TiO_2 support phase and surface area changes. Producing variables which directly allowed controlled utilisation of H_2O_2 then provided avenues to produce a significantly improved catalyst, requiring lower metal loading (0.13 wt.%) with higher productivity and H_2O_2 efficiency.

The second section of this thesis investigates the application of perfluorinated solvent for the selective oxidation of methane. Although proposed to be environmentally benign, the application of pre-formed H_2O_2 requires its production via the anthraquinone process. Instead, the direct incorporation of molecular oxygen is considered the goal for catalytic oxidation processes. Offering higher gas solubilities for both methane and oxygen, a perfluorinated solvent was applied for investigations into use of molecular oxygen for methane oxidation. The development of biphasic system trialled the application of radical initiators but found activity independent of catalyst. Instead, the in-situ generation of H_2O_2 from H_2 and O_2 was investigated.

Table of Contents

Chapter 1: Introduction

1.1 Introduction to Natural Gas

Currently, global population is estimated at *ca.* 7.6 billion people and projected growth continuing to reach *ca.* 9.8 billion by 2050.[1] In addition to an increase in need for necessities such as food and water, an important consideration must be given to the increased demand for dwindling non-renewable resources such as fossil fuels. Responsible for 81% of US and 80% of UK primary energy production in 2016, the dependency on fossil fuels is an issue of concern.[2,3] Furthermore, crude oil remains a critical raw ingredient in the generation of commodity petrochemicals considered essential for everyday life. Crude oil is needed to produce petrochemicals used as transportation fuels and lubricants, solvents and pharmaceuticals. [4,5]

At present, current proven reserves of crude oil are estimated at 1.7 billion barrels (240.7 million tonnes), and importantly highlight the finite reserves of crude oil available.[2] Therefore, research and investment into renewable energy sources remains a key solution for the implementation of an alternative and sustainable future. Even so, the improvement in current oil technologies is still a logical approach to prolonging petroleum reserves, producing greener technologies with improved efficiencies.

Beyond crude oil, research has instead sought alternative modes to supplement the production of petrochemicals. Both affordable and readily available, natural gas has the potential to be an alternative feedstock for chemicals and high value fuels, also reducing the global dependence upon crude oil and prolonging current reserves.

Specifically, methane (CH_4), the principal component of natural gas provides a cleaner source of fossil fuel and an abundant platform resource. Comprising approximately 70-90% by volume, in addition to propane and butane, natural gas is a cheap and abundant non-renewable hydrocarbon with reserves of *ca.* 190 trillion cubic metres as published by BP Statistical Review of World Energy.[2,6] This represents only currently recoverable sources of CH_4. Further reserves may be located in remote locations, producing expensive costs associated with its exploitation. One such source includes methane found in crystalline form, or clathrates, at locations such as continental shelves.[7,8]
Furthermore, reserves of CH_4 can also be derived from the conversion of biomass to produce biogas using a broad range of micro-organisms. Considered an efficient

alternative technology, anaerobic digestion is also proposed as a solution to biofuel production and sustainable waste management. [9,10] With the increasing generation of waste material by agriculture, municipal or food, anaerobic digestion would transform waste into a valuable resource. Advantageously, the used digestate remains a high value fertiliser for crop cultivation, providing a substitution for conventional mineral fertilisers produced using energy intensive processes.[11] Although an attractive avenue, the use of biogas suffers major controversy due to the large amounts of biomass needed to produce sufficient quantities of chemical feedstocks. Importantly, the growth of biomass materials subverts agricultural lands required for production of food crops and increases food costs.[10]

In recent years, the extraction of natural gas from shale rock has provided particular improvements in the reserves of natural gas for countries such as the US, UK and China.[12] Despite the controversies associated with this intrusive method, the introduction of shale gas has reduced natural gas cost from $12.7 per million British thermal units (pmBTU) in 2008 to $3 pmBTU in 2017.[13,14]

Although in large reserve, with current technologies *ca.* 90% of the *ca*. 3.5 trillion cubic meters of CH_4 produced globally is combusted for the generation of heat or electrical energy.[15] For 2016, natural gas combustion produced 24% of global primary energy, supplying 36.7% and 31.5% of UK and US energy demand, respectively.[2,16]

Additionally a greenhouse gas, the influence of CH_4 upon global warming is 25 times stronger than CO_2.[17,18] Its transportation in large volumes from remote locations of crude oil reserves produces high costs associated with manufacturing and maintenance of pipelines, making it impractical.[19] Alternatively, the liquefaction of natural gas provides a more desirable route to its use. Significantly reducing from its original volume, liquefaction increases the energy density per volume of natural gas. Even so, liquefaction remains unsustainable. Possessing a boiling point of 90.6 K (-182.5 ˚C) at 1 atm, sustained cooling of natural gas to liquid form over prolonged periods is not viable.[20] Further still, the loss of high pressures or low temperatures consequently produces hazards with considerable implications, such as local fire or explosion.[21] Therefore, with no current methods of direct on-site valorisation, destruction via flaring remains the only option during the production of crude oil.

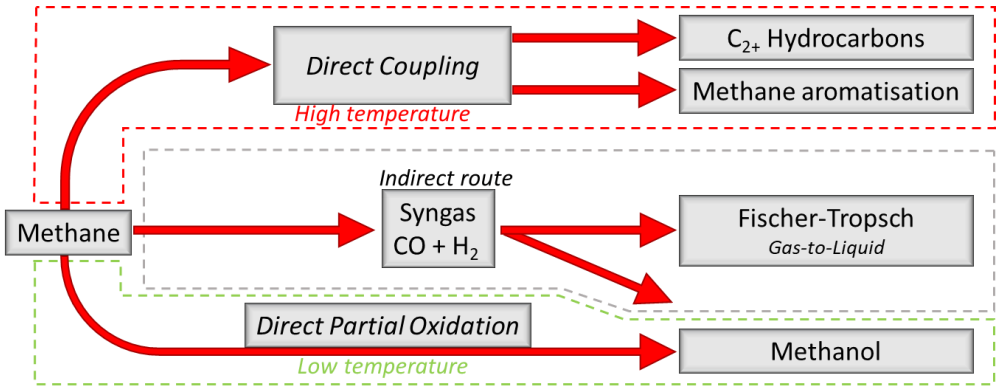

Figure 1.1: Potential routes for the valorisation of methane. Adapted from Olivos-Suarez *et al.*[22]

Despite having promising potential, natural gas remains under -utilised as a chemical feedstock. At present, only two large scale modes of CH_4 valorisation to liquid hydrocarbons exist; Methanol-to-gasoline or Fischer -Tropsch synthesis.[22] Both industrial methodologies, however, require steam reforming of CH_4 to produce syngas, (an intermediate composing of CO and H_2), before upgrading further to desired chemicals.[22] Although steam reforming is commonly used, alternative reforming methods such as dry- or auto thermal -reforming can be utilised to produce varying ratios of H_2 and CO_2.[23]

$$CH_4 + H_2O \rightarrow CO + 3H_2 \quad (equ. 3.1)$$

$$CO + H_2O \rightarrow CO_2 + H_2 \quad (equ. 3.2)$$

Operating at high temperatures (>1073 K), a nickel-alumina based catalyst is used to achieve the desired natural gas conversion, creating an energy intense process.[24] Consequently, higher conversion is achieved by feeding unreacted CH_4 into a secondary unit to be reformed with O_2 and steam at an elevated temperature. [25] Syngas additionally plays a crucial role in the production process of additional alternative feedstocks. These include the Haber-Bosch process for ammonia production and the production of higher chain aldehydes and alcohols via hydro-formulation or the “oxo-process”.[4,26]

Despite its importance, the production of synthetic gas remains an energy intensive process. Importantly, syngas technology remains restricted to large-scale basis for economic viability. Subsequently, high capital investment is required to implement and maintain these technologies and consequently means isolated or remote reserves of natural gas remaining inaccessible.

1.2 Direct routes of Methane to Petrochemicals

The direct conversion of CH_4 to derivatives remains the ultimate challenge for industry and academia. With increasing pressures on current reserves of crude petrochemicals and variations in prices, a direct on -site alternative for the valorisation of natural gas is greatly needed. Although a simple molecule, the chemistry of CH_4 is complicated by its intrinsic properties. Direct chemical reaction of nucleophilic or electrophilic species with CH_4 is made difficult by the symmetry of its tetrahedral structure, removing any dipolar moment or functionality. Subsequently, activation typically requires harsh reaction conditions to overcome the stable C-H bonds, possessing high dissociation energy (439.3 kJ mol^{-1}).[27,28] Once activated, the proceeding products demonstrate higher reactivity compared to the inert parent CH_4 molecule. Subsequently, control of selectivity remains a key issue when addressing the valorisation of CH_4 to higher valued chemicals.[29]

1.2.1 Methane to Olefins

1.2.1.1 Oxidative Coupling of methane

Ethylene, the simplest alkene is an important raw material for the production of commonly used plastics such as the synthesis of low- and high- density poly-ethylene. Ethylene (C_2H_4) is also an important feedstock petrochemical for solvent, cosmetic and paint production.[30] Its production is currently heavily reliant upon the refining of crude oil to provide its raw material, with naphtha steam cracking producing between 140-160 million tonnes of C_2H_4 per year, contributing for 73% of the total production capacity .[31–33] Requiring high temperatures for processing (>1073 K), this energy intense process also results in large emissions of CO_2. Alternatively, the direct conversion of CH_4 to C_2H_4 via oxidative coupling (OCM) provides a more beneficial technology utilising a cheaper resource with lower CO_2 emissions.[19]

Reporting the formation of C_2H_4 from CH_4, Keller and Bhasin first showed the oxidative coupling of CH_4 in 1982, and additional work followed by Hinsen and Baerns.[34,35] Employing a range of temperatures between 773-1273 K, oxidative coupling was shown to occur using a variety of α-alumina supported metal oxides under atmospheric pressures of O_2. Achieving similar conversion, Baerns and co-workers demonstrated 58% C_2 selectivity at 5% CH_4 conversion for PbO/Al_2O_3 catalysts.[35]

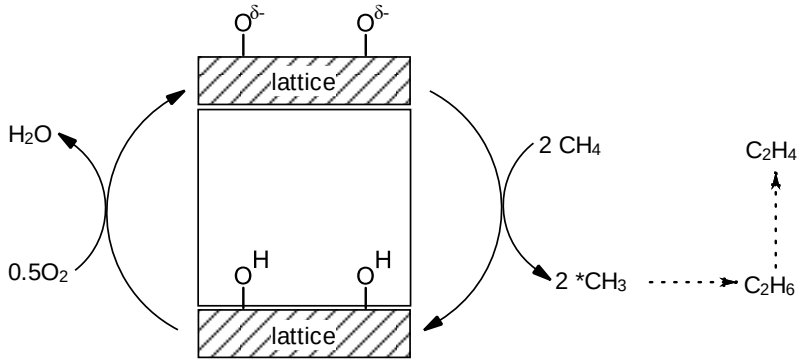

Figure 1.2: Generalised reaction pathway for the oxidative coupling reaction of CH_4 to C_2H_6 and C_2H_4, proceeding by heterogeneously catalysed (solid lines) and homogenous stages (dashed lines). Adapted from Hammond *et al.*[19]

Despite this interest, the works by Ito and Lunsford remain the standard for CH_4 conversion and selectivity.[36] Testing Li-doped MgO, oxidative coupling was achieved at 973 K with 50% selectivity to C_2 products whilst achieving *ca.* 38% CH_4 conversion at atmospheric pressure of O_2 (C_2 yield: 19%).[36]

Subsequent experiments by Lunsford and co-workers were able to discern a mechanistic description for the observed reaction. Using EPR spectroscopy, downstream trapping in solid argon identified the presence of gas phase methyl radicals.[37–39] Correlation between Li concentration in Li/MgO catalysts and both methyl and C_2 productivity lead to the conclusion that methyl radicals were generated by the Li/MgO, and that coupling of methyl radicals lead to the formation of ethane (C_2H_6). Although thought to be formed at Li^+O^- centres, with H -abstraction initiated by the active O^- species, no direct evidence has resolved this.[40] Despite this, the mechanism for oxidative coupling of CH_4 is considered a heterogeneous-homogenous mechanism. That is, C-H bond cleavage is achieved by surface oxygen species, generating methyl radicals which undergo coupling to produce ethane as a primary C_2 product in the gas phase (equations 3.3 and 3.4).δ

$$2CH_4 + O_2 \rightarrow C_2H_6 + 2H_2O \quad (equ. 3.3)$$

$$C_2H_6 + \frac{1}{2}O_2 \rightarrow C_2H_4 + H_2O \quad (equ. 3.4)$$

Recent development of a direct OCM demonstration plant by Siluria Technologies in 2015 highlights the importance of producing alternative technologies to current petrochemical routes.[41,42] Even so, to become industrially relevant, considerable improvements are required to increase C_2 yields. To produce economically viable quantities, C_2 yields of 30% with undiluted feedstock are required, achieving greater than 80% selectivity to C_2 products.[43]

Although a promising alternative, several challenges remain for OCM. Requiring high reaction temperature for C-H bond activation (>973 K) and typically employing high

pressures (30-60 bar), C_2 selectivity remains affected by several factors. Resulting in the formation of CO and CO_2, over-oxidation of CH_4 occurs from more reactive C_2 products. Additionally, loss of selectivity is catalysed by the unselective activation of C_2 products at the catalyst surface.[44] Consequently, attempts to increase CH_4 conversion produces the detrimental decrease in C_2 selectivity. Considering the kinetics associated with the predicted mechanism, an inherent limit was predicted by Labinger, suggesting a maximum barrier to C_2 yields at 30%.[45] Achieving, 18% C_2 yield, Jašo and co-workers reported 55% selectivity at 30% CH_4 conversion.[46] Here, the importance of reactor and experiment design were highlighted, utilising a fluidised bed reactor to improve yield over traditional methods. Furthermore, as predicted by Labinger and Ott[45,47], the limit of achievable yields in OCM systems remains higher at atmospheric pressures than typical industrial conditions. Subsequently, with catalyst performing close to current limits, the consideration of reaction engineering and mechanistic understanding is required to obtain new breakthroughs.[43]

1.2.1.2 Non-Oxidative Approaches

Non-Oxidative coupling to Ethane and Ethylene

Under oxygen free conditions, the conversion of CH_4 allows two potential avenues for the formation of higher hydrocarbons. The non-oxidative coupling of CH_4 to produce, primarily, C_2H_6 and C_2H_4 was first demonstrated by Belgued and co-workers in 1991.[48] Using Pt/SiO_2 catalysts at 523 K, the formation of C_2 products was followed by higher C_6 hydrocarbons with the introduction of H_2. Despite observing the formation of higher hydrocarbons, selectivity to C_2 species remained close to 63%.[48]

$$2CH_4 \rightarrow C_2H_6 + H_2 \quad (equ. 3.5)$$

$$2CH_4 \rightarrow C_2H_4 + 2H_2 \quad (equ. 3.6)$$

The mechanism of the two-step process was explained by Belgued, Amariglio and co-workers after further examination of Co, Pt and Ru catalysts.[49–51] This work was closely followed by van Santen *et al.* using group VIII metal catalysts, reporting a similar two-step process for temperatures between 500-800 K. [52]

Under isothermal conditions, conversion begins by cleavage of the C-H bond of chemisorbed CH_4, producing a H -deficient CH_x species with the accompanied desorption of H_2. The coupling of CH_x is facilitated by the increasing concentration of CH_x upon the catalysts surface, resulting in the formation of C-C bonds. Sequential introduction of H_2 then removed chemisorbed C_{2+} species and regenerated the catalyst surface. Introduction of H_2 at identical temperatures to methane activation was observed to increase higher alkanes yields (C_7-C_8). The use of a dual-temperature approach by van Santen and co-

workers utilised a lower hydrogenation temperature (373 K) after dissociative adsorption at 700 K.[52,53] This decrease in temperature yielded higher selectivity to C_4-C_5 length hydrocarbons.

Despite producing higher rates of C_2 formation in comparison to the oxidative methodology the direct conversion of CH_4 to C_2 remains thermodynamically unfavourable.[50] Consequently, the limitations to conversion results in low activity with high temperatures (>1073 K) required for practical yields.

Dehydroaromatisation to Aromatics

A more thermodynamically favourable route for conversion of CH_4 to aromatics was reported by Wang and co-workers in 1993.[54] Termed methane dehydroaromatisation (MDA), Wang and co-workers yielded aromatics (mainly benzene) and H_2 utilising Mo/H-ZSM-5 as a catalyst within a continuous flow reactor at 973 K. Detailed investigation by Ma *et al.*[55,56] revealed a bi-functionality to the catalysts, with aromatic formation dependent upon zeolite acidity and channel structure. Impregnation of Mo into H-ZSM-5 was found to modify the zeolite structure by exchanging with Brönsted acidic protons, forming framework Mo-O-Al species.[57] Subsequent reduction of the metal oxide by CH_4 during induction produces the required metal carbide species (referred as Mo_2C) capable of activating CH_4 to CH_x (Fig. 1.3).[58] The aromatisation of surface CH_x is then facilitated by Brönsted acid sites of the zeolite structure. Crucially, the Si/Al ratio produces an important influence on catalyst activity and Mo incorporation, in addition to giving rise to Brönsted acid sites.[59] At lower Si/Al ratios, facilitation of monomeric dihapto-$[Mo(=O)_2]^{2+}$ species is observed due to stabilisation by framework $[AlO_4]^-$.[60] At higher Si/Al ratios, variation in the optimal distances of Brönsted sites promotes the formation of monomeric monohapto-$[Mo(=O)_2(OH)]^+$ or dimeric $[Mo_2O_5]^{2+}$species. Subsequently, the variation from monomeric dihapto-$[Mo(=O)_2]^{2+}$, resulting from changes to Si/Al or Mo metal loadings, affects the catalytic activity. Similarly, the selectivity of zeolite support towards benzene formation was found to be dependent upon the zeolite cage dimensions. Cage sizes similar to the diameter of benzene demonstrated highest selectivity towards benzene formation.[61]

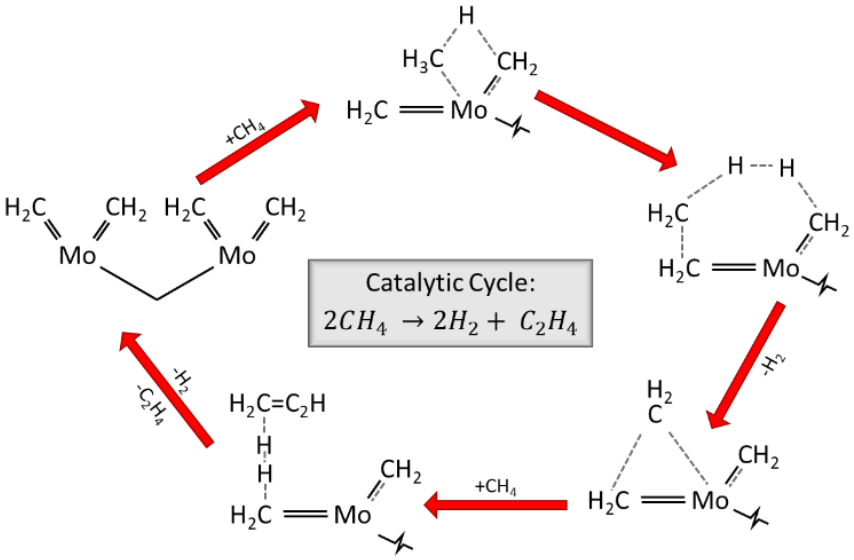

Figure 1.3: Proposed mechanism for activation of CH_4 to C_2H_4 by formation of $Mo_2(CH_2)_5$ active sites within Mo/H-ZSM-5. Images adapted from Karakay *et al.*[62,63]

Recent advances by Guo *et al.*[64] have provided promising improvements to previously reported experiments using single iron sites confined within a silica support ($Fe@SiO_2$). The non-oxidative conversion of CH_4 was demonstrated at 1363 K selectively to C_2H_4 and aromatics, with a maximum CH_4 conversion of 48% achieved. The isolation of active Fe-sites allowed generation of methyl radicals with no further C-C bond formation, oligomerisation or deactivation due to coke formation from nearby Fe sites. Instead, catalytically formed methyl radicals undergo a series of gas-phase reactions producing only C_2H_4, benzene and naphthalene. Impressively, CH_4 conversion at 48% produced an C_2H_4 yield of 23% at 1363 K, achieving a selectivity of *ca.* 48% for 0.5wt.% $Fe@SiO_2$. Additional products of benzene and naphthalene were produced at 28% and 24% selectivity.

Although promising technologies, several challenges remain for the non-oxidative conversion of CH_4 to more valuable chemicals. Commercialisation is primarily impeded by the current temperatures required for practical yields. Subsequently, improvements to catalyst performance is critical, with deactivation being a major issue. Thermodynamically more favourable, the deposition of carbon as coke inhibits catalyst activity, leading to catalyst deactivation. The generation of H_2 is another attractive aspect of MDA, with application of H_2 permeable membranes utilised to separate produced H_2 from the reaction stream.[65] However, the reduction of H_2 partial pressure facilitates unwanted deposition of carbon leading to catalyst deactivation despite promoting CH_4 conversion.[66] Consequently, novel approaches to enhance performance are not only required in catalysts design but in reactor and process design.[5]

1.2.2 Methane to Methanol

In contrast to routes converting CH_4 to higher hydrocarbons, the selective oxidation of $CH_4$to C_1 oxygenates is considerably more challenging. With uncertainty for current non-renewables and insufficient renewable alternatives, Nobel laureate George Olah is a proponent for methanol (CH_3OH) as potential basis for a future economy.[67,68] A potential solution for H_2 storage, the reduction of environmental CO_2 by H_2 is projected to produce 40-70 million tonnes of CH_3OH by 2050.[69] Subsequently, CH_3OH provides an important technological and economic challenge for both industry and academia.[70] With a large demand, CH_3OH is crucial as an industrial feedstock for transformation into valuable bulk chemicals (Fig. 1.4).[69]

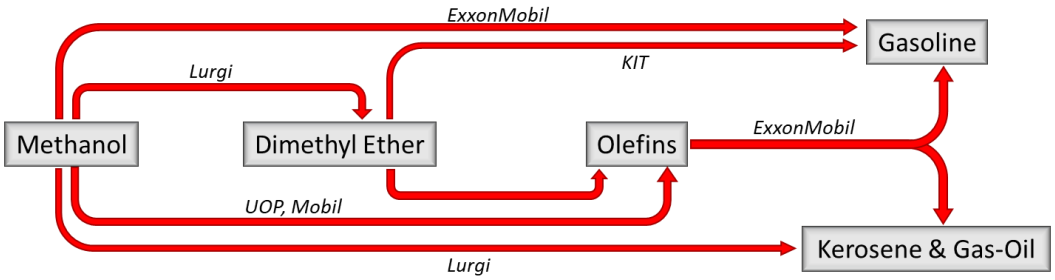

Figure 1.4: Overview of investigated liquid fuel products derived from methanol by various petrochemical companies. KIT: Karlsruhe Institute of Technology, UOP: Honeywell Universal Oil Products. Adapted from Laquaniello *et al.*[69]

Providing a valuable non-crude oil source for the production of olefin based petrochemicals, CH_3OH is transformed industrially by the methanol-to-olefin (MTO) or methanol-to-propylene (MTP) processes.[71,72] Alternatively bulk chemicals, such as acetic acid from CH_3OH are produced by BP based upon earlier Monsanto technologies.[73,74] Additionally, formaldehyde (CH_2O)[75], dimethyl ether[76] or methyl *tert*-butyl ether[67], important chemicals for production of plastics and pharmaceutical solvents, require CH_3OH as precursor. Furthermore, CH_3OH remains a clean and renewable energy-dense liquid fuel, capable of direct application as a fuel, or blended with gasoline for automobiles.[77] Methanol may also provide an intermediate source of green energy by application of direct methanol fuel cell technology.[77] Offering high power and energy generated at ambient conditions with low emissions whilst requiring only renewable CH_3OH.[77]

Initially demonstrated in the works of Bone and coworkers[78,79], interest in direct oxidation of CH_4 to oxygenates only returned upon implementation of industrial processes for

CH_3OH production from natural gas several decades later.[80,81] Even so, CH_3OH production is still carried out by industrial steam reforming of natural gas. This indirect route using syngas was responsible for producing 85 million tonnes of CH_3OH in 2016.[82] Utilising a $Cu/ZnO/Al_2O_3$ catalyst, industrial CH_3OH synthesis is maximised at temperatures ranging between 250-300 ˚C, pressures of 50-101 bar and CH_3OH selectivity of >99%.[83] Despite high selectivity, the energy and capital requirements for CH_3OH synthesis from natural gas is high. Subsequently, the direct conversion provides an attractive alternative to current complex processes, subsidising current production from limited crude oil sources. Furthermore, presenting the most attractive target, extensive research has invested in the development of a direct route to C_1 oxygenates.

1.2.2.1 Biological routes

Methane Mono-Oxygenates

In nature, the conversion of CH_4 is efficiently achieved at ambient conditions by methanotrophic bacteria utilising molecular oxygen (O_2).[84] Illustrated in Figure1.5, CH_4 is utilised as a primary source of carbon or energy by assimilation of formaldehyde or formation of CO_2.[84] Occupying the interface of aerobic and anaerobic boundaries in wet soils, lakes or near ocean vents methane is supplied by the anaerobic metabolism of methanogens [85]

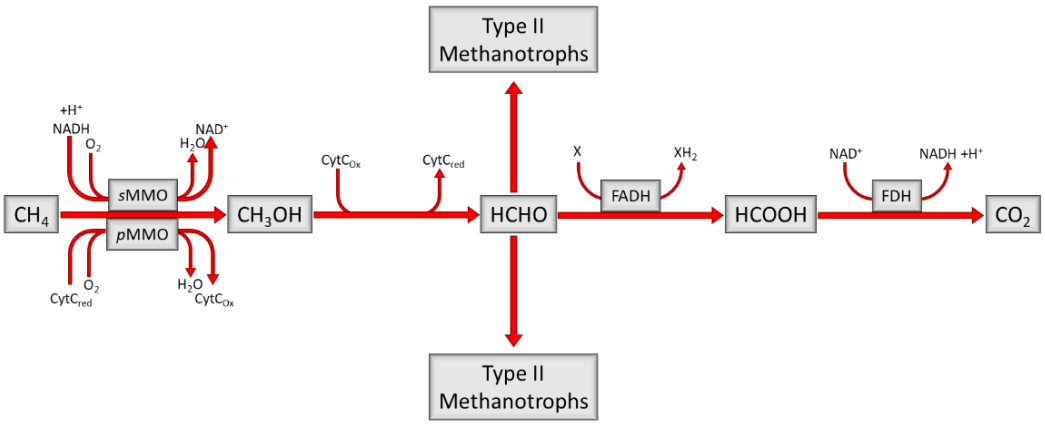

Figure. 1.5: Metabolic assimilation of CH_4 by methanotrophs utilising methane mono-oxygenase (MMO). Where NADH: nicotinamide adenine dinucleotide, CytC: cytochrome C, FADH: formaldehyde dehydrogenase, FDH: formate dehydrogenase. Adapted from Hanson *et al.*[85]

The initial activation of CH_4 is facilitated by the mono-oxygenase enzyme (MMO), selectively oxidising CH_4 to CH_3OH. Two distinct MMO forms have evolved to be capable of CH_4 oxidation, reflecting the extreme environments typically occupied by methanotrophs.[86] Expressing different amino acid sequences for their proteins, other

additional differences include the metal co-factors required for their chemistry and the location in which MMO is typically found.[87,88]

Typical of most methanotrophs, particulate MMO (*p*MMO) is a plasma membrane bound metalloenzyme.[84,89] Detailed description of the mechanism and structure of *p*MMO remain uncertain but recent progress proposes a complex active sites possessing di-nuclear copper and tri-copper clusters (Figure 1.6).[90,91] Further detailing of catalytic mechanism require the elucidation of metal cofactors involved.[92] Proving difficult to isolate, attempts to purify *p*MMO for characterisation is hampered by instabilities in detergents used.[88,93]

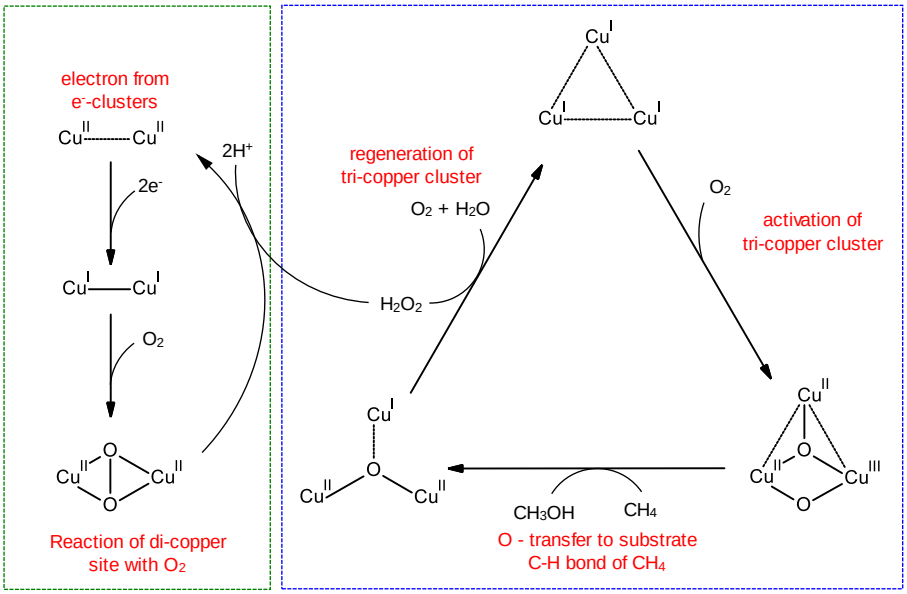

Figure 1.6: Proposed catalytic cycle involving O_2/H_2O_2 redox with di-copper and tri-copper clusters at *p*MMO active site. Adapted from Wang *et al.*[92]

Even so, the X-ray crystal structure of pMMO was reported by Lieberman and Rosenzweig, with 3 copper atoms identified within the crystal structure.[90] Initial assumptions, therefore, predicted a ferromagnetically coupled tri-copper cluster, with later works supporting this assumption with high turn-over frequency (TOF) demonstrated for the H_2O_2 assisted room temperature oxidation of cyclohexane.[94–97] Recent works, however, have demonstrated the presence of between 13-15 copper ions, which may be divided by their function.[98,99] Consistent with previous works, catalytic clusters comprising six copper ions were identified. The catalytic cluster contained a mononuclear copper centre, a di-nuclear copper site, and a tri-copper cluster responsible for substrate oxidation upon O_2 activation.[90,100–103]

Expressed more commonly in methanotrophs under Copper-limited conditions, the water soluble MMO (*s*MMO) is found within the cytoplasm of methanotrophic cells, consisting of a non-heme diiron cluster.[104] More successfully characterised, *s*MMO is a multicomponent enzyme comprised of three sub-units: hydroxylase, reductase and a regulatory protein.[92] The unique dinuclear $Fe^{(IV)}$ intermediate involved during CH_4 oxidation (Figure 1.7), identified by time resolved Raman spectroscopy, is located within the hydroxylase sub-unit of *s*MMO.[105] The homolytic dissociation of O_2 upon the diiron centre is catalysed by reduction via electron donation by nicotinamide adenine dinucleotide (NADH).[105]

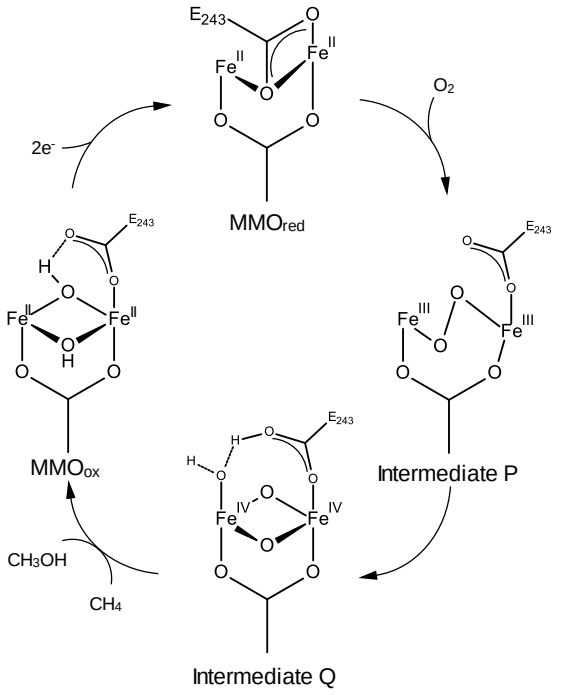

Fig. 1.7: Proposed active di-iron centre present in *s*MMO. Modified from *Ravi et al.*[29]

Although demonstrating high efficiency for the oxidation of methane to methanol, crucially, activity for CH_3OH production is low. Comparison of TOF's for *s*MMO and *p*MMO present in *Metholoccocus capsulatus* (Bath) for the oxidation of methane by O_2 are 0.19 s^{-1} and 1 s^{-1}, respectively.[106] Subsequently, the economic viability is hampered by the requirement of costly reductants (NADH) only to achieve low productivities.[107] In addition, the extraction and isolation of MMO enzymes from methanotrophs is still too costly an alternative compared to the application of methanotrophic bacteria themselves.[107]

Even so, mechanistic understanding from MMO studies provides opportunities for the design of novel catalysts. The seminal studies of Dalton *et al.* highlighted this importance, with *s*MMO shown to be non-specific and capable of oxidising a range of n-alkanes ranging

C_1-C_8.[108] Additionally, *s*MMO selectively epoxidizes alkenes, and hydroxylated cyclic alkanes and aromatics.[108] Importantly, the oxidation of methane by O_2 achieved a productivity of 5.05 $mol_{(methanol)}$ $kg_{(protein)}^{-1}$ h^{-1}, becoming an academic target for low temperature methane oxidation.[88,108]

pMMO and Cu-based biomimetics

The tricopper complex $[Cu^{(I)}Cu^{(I)}(\mu\text{-oxo})Cu^{(I)}(7\text{-}N\text{-Etppz})]^{1+}$ (where 7-N-Etppz = 3,3'-(1,4-diazepane-1,4-diyl)bis[1-(4-ethylpiperazine-1-yl)propan-2-ol] developed by Chan and co-workers, utilised a similar active Cu sites present in *p*MMO (Figure 1.8).[100]

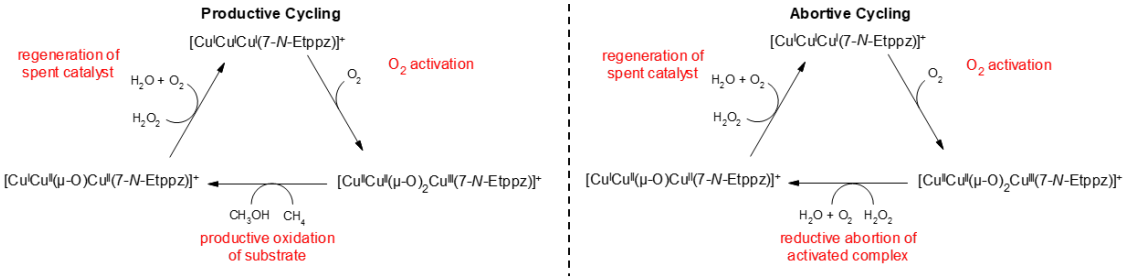

Figure 1.8: The productive and abortive cycling of the tri-copper complex, $Cu^ICu^ICu^I(7\text{-N-Etppz})^{1+}$, in the oxidation of CH_4 by O_2 and sacrificial H_2O_2. Adapted from Chan *et al.*[102]

Achieving a turn-over number(TON) of 0.92, the activation of $[Cu^{(I)}Cu^{(I)}(\mu\text{-oxo})Cu^{(I)}(7\text{-}N\text{-Etppz})]^{1+}$ by O_2 successfully oxidised CH_4 to CH_3OH at room temperature.[100] Introduction of H_2O_2, improved upon the single turnover by providing two electron reduction of the spent $[Cu^{(I)}Cu^{(II)}(\mu\text{-oxo})Cu^{(II)}(7\text{-}N\text{-Etppz})]^{1+}$ complex, and producing a catalytic process. Further work formulated a heterogenous analogue by immobilisation onto mesoporous SiO_2 support, producing dramatically higher TON (107) with increased CH_4 conversion (*ca.* 17%).[109]

In the homogenous form, a ratio of 30 equivalents of H_2O_2 was required to achieve TON of 6. This equivalent increased to 200 for the heterogenous form. The requirement of excess H_2O_2 to regenerate the active complex suffers competing H_2O_2 loss at steady state of H_2O_2 concentration at equivalents exceeding 10.[100,109] The onset of reductive abortion of the activated $[Cu^{(II)}Cu^{(II)}(\mu\text{-oxo})_2Cu^{(III)}(7\text{-}N\text{-Etppz})]^{1+}$ is detrimental to successful O-transfer to CH_4 to produce CH_3OH. Although producing an economical catalytic cycle when utilising H_2O_2 in place of O_2, however, the use of H_2O_2 is industrially unattractive. [100]

sMMO and Fe-based biomimetic

For *s*MMO, the active site of hydroxylase sub unit responsible for CH_4 oxidation features the di-$Fe^{(III)}$ centre contained by four glutamine and two histidine residues(Figure 1.7).[110] Possessing macrocyclic structures comparable with the porphyrin complexes found within sMMO enzymes, metal phthalocyanine (MPc) complexes are centred around a similar di-metal centred structure. Utilised in the selective oxidation of a broad range of hydrocarbons, investigations into structural and oxidant variations have provided opportunity to tune catalytic properties of the systems examined.[111]

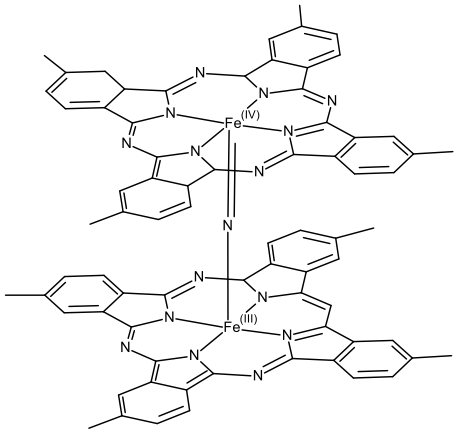

Figure 1.9: Structure of μ-Nitrido-bridged Fe-phthalocyanine ($(FePc)_2N$) reported by Sorokin *et al.*[111,112]

The detailed studies by Sorokin and co-workers is demonstrated for μ-nitrido diiron metallo-phthalocyanines $(FePc)_2N$, illustrated in (Fig 1.9).[111] The stable FePc showed significant activity for the low temperature activation of CH_4, utilising H_2O_2 at temperatures between 298 - 333 K.[113] Achieving a total TON of 437, the formation of a strongly oxidising $Fe^{(IV)}$-N-$Fe^{(V)}$=O was proposed to oxidise CH_4, evidenced by the enhanced activity upon 0.1M H_2SO_4 addition.[111,113,114] Importantly, the substitution to the μ-oxo (Fe-O-Fe) or carbide μ-carbido (Fe=C=Fe) complexes saw inactivity for the oxidation of CH_4.[115,116] Similarly, the formation of mononuclear tetra-*tert*-butyl-FePc, showed no activity for the oxidation of CH_4.[115,116] Exchanging *meta*-chloroperoxybenzoic acid (*m*CPBA) as oxidant produced a significant loss in activity, reducing calculated TON to 12.5 from 26.[115]

Industrially, MPcs present attractive catalysts. Currently utilised for the removal of alkyl and aromatic mercaptans, the "*sweetening*" of petroleum fractions via the Merox process is efficiently catalysed by sulfonated cobalt phthalocyanines.[115,117] Subsequently, research has provided means to reduce MPc costs with straightforward preparative methodologies

for large scale production.[115] Furthermore, immobilisation or encapsulation of MPC's onto solid supports provide industrially attractive, retrievable catalysts with increased reactivity.[115] Operating under similar conditions to Sorokin, the heterogenization of FePc catalyst via grafting to SiO_2 support was demonstrated by Hutchings and co-workers.[118] Although observing desirable CH_4 oxidation using H_2O_2, the μ-nitrido FePc was discovered to be unstable, suffering hydroxyl-radical degradation of the FePc complex and subsequent leaching of Fe ions.[118] Even so, the wet impregnation of Fe onto the active SiO_2 support (Fe/SiO_2) produced a material, demonstrating similar activity but with higher oxygenate selectivity (>80%) under identical reaction conditions.[118]

1.2.2.2 Homogenous Approaches

Electrophilic activation of Methane

The electrophilic activation of methane's C-H bonds was first described by Shilov *et al*. using a $Pt^{(II/IV)}$ based system.[119] The selective oxidation of methane to methanol and methyl chloride were achieved in acidic media at temperatures of 393 K.

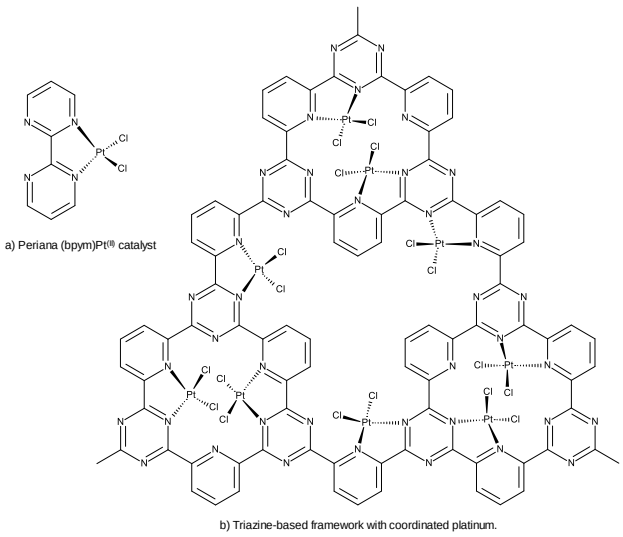

Figure 1.10: (a) (2,2' bipyrimidinyl) dichloroplatinum complex developed by Periana *et al.* [120] (b) covalent triazine-based polymer framework (CTF) with coordinated Pt developed by Palkovits as heterogenous analogue. Adapted from Palkovits *et al.*[121]

Inspired by this work, Periana *et al.* demonstrated the selective conversion of CH_4 to methyl bisulphate (CH_3OSO_2H) using ionic $Hg(SO_4)_2$ catalyst with concentrated sulfuric acid. [122] CH_4 conversion at 50% resulted in a yield of 43% to CH_3OSO_2H. Operating at 180 ˚C, selectivity to the CH_3OH-derivative was 80% with CO_2 being the only by-product.

Similarly, the application of a bipyrimidinyl (bpym) $Pt^{(II)}$ complex by Periana *et al.* enhanced selectivity to 81%, with CH_4 conversion increased to 90% (Figure 1.9(a)).[120] The achieved CH_3OSO_2H yield of 70% at 220 ˚C (1993) maintained as highest reported value until surpassed by Schüth and co-workers (2016). [123] Applying detailed studies for the dependency of Pt(II) complex activity on the SO_3 concentration, discovered the extremely active K_2PtCl_4. Showing 90% selectivity to CH_3OSO_2H in 20% H_2SO_4/SO_3, TOF of greater than 25,000 for K_2PtCl_4 complex was observed. Subsequent comparisons with industrial and large scale commercial processes, demonstrate simple Pt salts to be stable, selective and superior to Periana's catalyst.[123] Volumetric productivities of 0.48 kg L^{-1} h^{-1} were demonstrated for K_2PtCl_4, significantly increased from Periana's 0.115 kg L^{-1} h^{-1} for $(bpym)PtCl_2$.

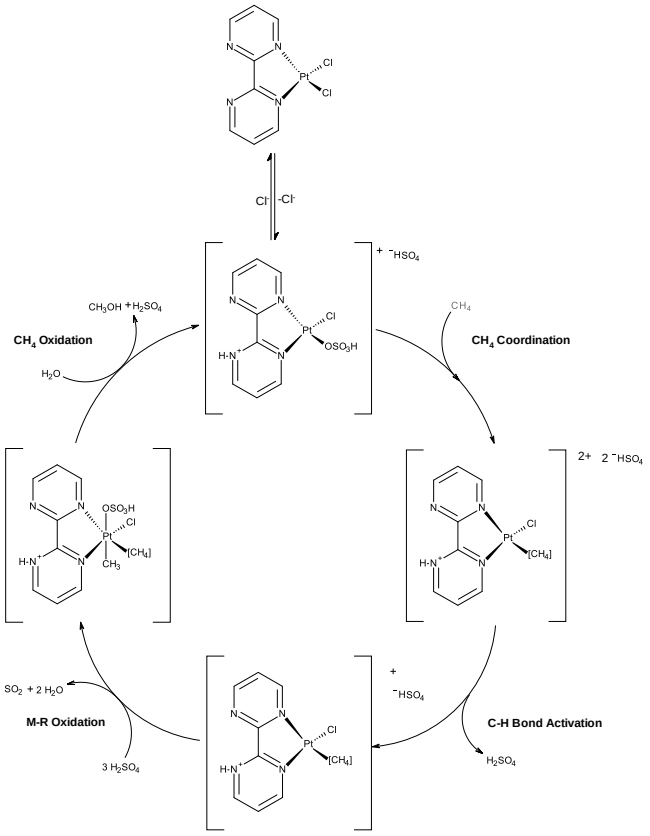

Figure 1.11: Mechanism for C-H bond activation mediated by Periana $(bpym)Pt^{(II)}$ complex using H_2SO_4 system proposed by Goddard and Musgraves.[124–126]

Represented in Figure 1.11, electrophilic attack of CH_4 is initiated by formation of metal-CH_3 intermediate. Successive oxidative addition and reductive elimination reactions produce the oxidised alkane species.[127] Variation of nucleophilic species during oxidative addition provides control of product moieties, allowing for the formation of several CH_3OH-derivatives such as methane sulfonic acid[128], methyl bisulfate[120] and methyl trifluoroacetate[129,130]. The requirement of strong concentrations of acid is crucial to the

high selectivity and activity observed. Acting as solvent and oxidising agent, H_2SO_4 regenerates the active Pt species, allowing a $Pt^{(0)}/Pt^{(II)}$ catalyst cycle to proceed rather than deactivation by formation of $Pt^{(0)}$. The requirement of a strong oxidant is critical to the regeneration of active metal species, as demonstrated by Periana *et al.* for the oxidation using $Au^{(I)}/Au^{(III)}$.[131] The application of H_2SO_4 was found to be insufficient, with metallic Au found not to dissolve and consequently no activity observed. Instead, addition of H_2SeO_4 was required to dissolve and produce the active cationic Au into an H_2SO_4/SO_3 solution. Corresponding oxidation of CH_4 achieved 8% CH_4 conversion with 77% selectivity towards CH_3OSO_2H for the 9 h reaction period. Furthermore, the stability offered by the formation of CH_3OH-derivatives, such as CH_3OSO_2H, prevent over oxidation of CH_3OH.[122] Despite producing attractive selectivities, unfortunately, the extraction of CH_3OH requires further processing via hydrolysis, with unknown efficiency.

Developing a polymer-based covalent triazine framework comprising a coordinated $Pt^{(II)}$ centre (Pt-CTF), Palkovits and co-workers successfully demonstrated the heterogenous equivalent to Periana's Pt catalyst for CH_4 oxidation (Fig.1.7(b)).[121] Achieving a TON of *ca.* 245, methanol selectivity of greater than 75% was reached under similar H_2SO_4/SO_3 conditions to Periana.[120,121] However, pre-activation under reaction conditions were required to improve initial TON from 26 to *ca.* 245 in successive cycles. Proving to be reusable, the initial advantage of heterogenous Pt-CTF is lost due to catalyst instability leading to Pt leaching. Furthermore, in comparison to Pt(bpym), methane conversion inferior for Pt-CTF at 220 ˚C, converting 18% and 7% respectively.[107]

Using a different approach for oxidative regeneration of active metal, Bao and co-workers[132] reported the application of an electron transfer chain cycle, allowing the oxidation of CH_4 by O_2. The complex mixture comprising three redox cycles, combines CH_4 functionalisation by $Pd^{(II)}/Pd^{(0)}$, catalyst regeneration by *p*-benzoquinone/ hydrobenzoquinone (termed the redox mediator) which is regenerated by a gaseous oxidants (N_2O/O_2).[132] Depicted below in Figure 1.12, the indirect incorporation of O_2 occurs via electron transfer from $Pd^{(II)}$ species. Transfer of oxidant therefore occurs by benzoquinone, an aerobic co-oxidant also used in many biological oxidising systems.[133]

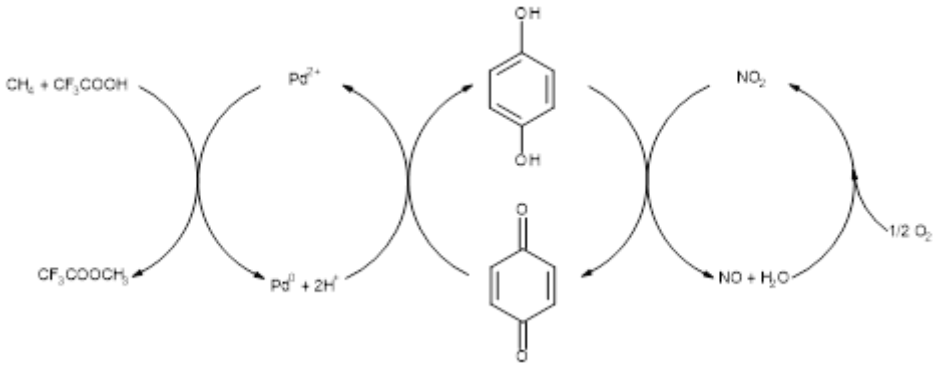

Fig. 1.12: Catalytic cycle for redox mediated oxidation of CH_4 for $Pd^{(II)}$ catalyst.[124,132]

Similar approaches have been reported by Bar-Nahum and coworkers[134] for the phospho-vanadium polyoxometalate ($H_5PV_2Mo_{10}O_{40}$) complex coupled with (bpym)$Pt^{(II)}$. The presence of polyoxometalate allowed regeneration of $Pt^{(II)}$ from $Pt^{(0)}$ with gaseous O_2 for the oxidation of CH_4 to CH_3OH.[134] $H_5PV_2Mo_{10}O_{40}$ polyoxometalate, in conjunction with $Pd(OAc)_2$ were later applied with benzoquinone by Yuan *et al*.[135] The catalytic redox system carried out in trifluoroacetic acid (CF_3COOH) converted CH_4 to CH_3OOCF_3, a CH_3OH-derivative, achieving the highest yields (9.1 μmol) at temperatures of 353-373 K.[135]

In these systems, the gradual irreversible loss of catalytic activity due to reduction of the active metal species requires strong oxidising agents. Regeneration of the active metal, allows further functionalisation of CH_4 and a TON >1..[107] Alternative approaches using redox mediators provide a desirable progression from environmentally undesirable oxidants, but possess substantially lower productivities to those achieved by Periana *et al.*[107] Additional attempts to utilised alternative oxidants, such as H_2O_2[136], H_2O_2/H_2SO_4[137], SO_2/O_2[138] or SO_3[139] similarly show low productivities. Finally, although producing commercially attractive yields and selectivities for CH_3OH-derivatives, the homogeneity of the active species produces complications when considering the recycling of metal species and CH_3OH extraction for industrial application.

1.2.2.3 Heterogenous Approaches

Zeolite application

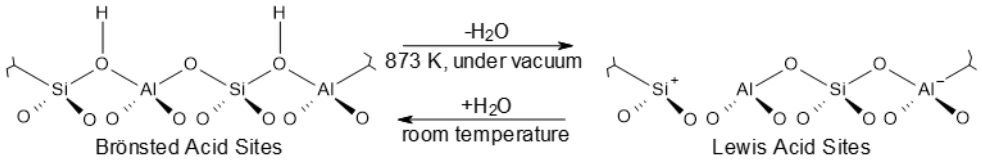

Figure 1.13: Structural representation of zeolite materials with Bronsted and Lewis acid sites.[140]

The microporous, crystalline structure of zeolites are comprised of an alumino -silicate framework.[141] The three dimensional network of SiO_4 and AlO_4^- units linked via bridging O atoms produce pores and cavities with dimensions ranging 3 - 14 angstroms.[141,142] Producing a uniform array of well-defined micropores, the resulting larger surface area environments act as reaction channels.[141,142] Furthermore, the presence of negative charge occurring from framework AlO_4^- results in interchangeable extra-framework cations (such as Na^+, H^+) to maintain neutrality (Figure 1.13).[143] The resulting ion-exchange of cations produces a diverse chemistry, allowing for tuneable activity and selectivity.[143]

Importantly, the ability to stabilise Cu-oxo and Fe-oxo species within the extra-framework of zeolites allows successful mimicking of MMOs.[29] For Fe-ZSM-5, the formation of bis(μ-oxo) diiron clusters at extra-framework sites resembles the diiron species found in *s*MMO.[22] Initial reports by Panov et al., demonstrated the generation of an activated oxygen species (α-O) from N_2O at diiron clusters comparable in reactivity to sMMO.[144,145] The resulting oxidation of $Fe^{(II)}$ to $Fe^{(III)}$ at diiron clusters was found to produce the active α-O species, with both Fe atoms capable of α-O generation as evidenced by Mössbauer spectroscopy.[146] Consequently, room temperature oxidation of CH_4 proceeds via the formation of mononuclear $Fe^{(IV)}$=O species.[147] At temperatures below 473 K, the formation of strongly bound CH_3OH species requires extraction via aqueous acetonitrile, producing a quasi-catalytic system.[148] At temperatures above 473 K, a conventional catalytic system was achieved with CH_3OH products desorbing into gas phase. Notable selectivity was not attained until introduction of H_2O vapour (30% feed), stabilising CH_3OH yields and increasing selectivity from 2.7% to 62% at 548 K.[148] Reported by Hutching *et al*., the influence of Brønsted and Lewis acid sites of Fe-ZSM-5 were investigated for oxidation of CH_4 using N_2O.[149] The presence of Brønsted acid sites were required for the formation of active Fe sites, at which active α-O species were generated allowing initial H-abstraction from CH_4. Further elucidate determined that Brønsted acid sites were more efficient for the formation of C_2H_4 and subsequent aromatics from dimethyl ether in a mechanism similar to the methane-to-olefin process.[149]

Alternatively, Tomkins *et al.*[150] utilising Cu-mordenite (MOR), successfully activated O_2 for CH_4 oxidation to CH_3OH in a quasi-catalytic system. Operating under isothermal conditions, pre-activation of Cu-MOR is achieved by prolonged O_2 (16 h) exposure at 473 K. This report contrasts with previous Cu-zeolite works, typically requiring pre-activation at elevated temperatures to generate active the bis(μ-oxo) di-copper species, prior to CH_4 oxidation at lower temperatures.[151,152] Instead, under isothermal temperatures and higher CH_4 pressures, the absence of bis(μ-oxo) di-copper discerned the formation of alternative Cu species, contrasting *p*MMO.[150] Introduction of CH_4 (*ca.* 35 bar), following pre-activation, obtained CH_3OH yields of *ca.* 55 μmol g^{-1}.

Using both Fe- and Cu-ZSM-5, Hammond *et al.* demonstrated the liquid phase oxidation of CH_4 using H_2O_2.[153] Building upon previous works for HZSM-5 by Ishihara *et al.*, pre-activated by high temperature calcination (823 K), H_2O_2 was utilised for CH_4 oxidation to formic acid (HCOOH) with *ca.* 68% selectivity at 373 K.[154] Identifying trace impurities of Fe, Hammond investigated ion-exchanged Fe-ZSM5 at 323 K, achieving oxygenate selectivity of 83 %, producing predominantly HCOOH (*ca.* 72%).[153] Similarly, Cu-ZSM-5 produced 88% oxygenate selectivity but drastically improved CH_3OH selectivity, increasing to 83% of total oxygenates. Producing higher selectivity, Fe-ZSM-5 demonstrated greater activity with 0.7% CH_4 conversion in comparison to 0.3% of initial 30.3 mmol CH_4. Formation of bimetallic CuFe-ZSM5, produced remarkably improved activity and selectivity. Further investigation revealed the presence of $Cu^{(II)}$ minimised hydroxyl-radical ($HO^{\cdot}$) formation, reducing the consecutive oxidation of CH_3OH to HCOOH (Figure 1.14).[155] Subsequently, methanol selectivity reached 93% whilst maintaining comparable CH_4 conversion to Fe-ZSM-5.[155]

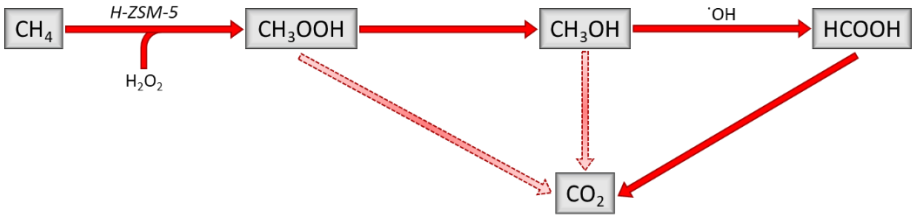

Fig. 1.14: Proposed reaction scheme for H-ZSM-5 (30) catalysed oxidation of CH_4 using H_2O_2.[153]

Similarly, Ayodele *et al*. investigated CH_4 conversion to CH_3OH over ferro-oxalate supported ZSM-5 (FeO_x/ZSM-5).[156] Identifying $Fe^{(II)}$ as the active phase generating highly reactive $HO^{\cdot}$ from H_2O_2 during a Fenton-like process which resulted in CH_4 activation. Methanol formation was reported to proceed via methoxy radical formation, as suggested by Hammond *et al.*[155]

Recently, Flytzani-Stephanopoulous et al.[157] reported the oxidation of CH_4 to CH_3OH and acetic acid (CH_3CO_2H) using mononuclear Rhodium (Rh) -species anchored upon ZSM-5.

Utilising O_2 and CO (5 bar) at 423 K, two independent pathways were discerned for the formation of acetic acid (CH_3CO_2H) or CH_3OH. Optimisation of conditions for CH_3CO_2H production by varying partial pressures of O_2 under constant CH_4 allowed yields of *ca.* 22,000 μmol $g_{(cat)}^{-1}$ to be reached in 3 h, with 60% selectivity. Alternatively, zeolite acidity was modified, having previously been demonstrated to promote CH_3CO_2H selectivity for Cu-ZSM-5.[158] Instead, application of Na-ZSM-5 was used to suppress CH_3O_2H formation, tuning selectivity towards CH_3OH. Resulting in CH_3OH yields of 430 μmol $g_{(cat)}^{-1}$ at *ca.* 55% selectivity, introduction of homogenous $Cu^{(II)}$ species enhanced yields to 550 μmol $g_{(cat)}^{-1}$ with ca. 70% CH_3OH selectivity.[157]

Noble metal application

Application of cheaper and cleaner oxidants are recurring themes for CH_4 oxidation and despite aims to utilise O_2, preformed H_2O_2 is often used. A strong oxidant, H_2O_2 represents a reactive oxygen species.[159] The synthesis of H_2O_2 is currently produced by the anthraquinone oxidation (AO) process, involving the sequential catalysed hydrogenation and oxidation of alkyl-anthraquinone precursor (Figure 1.15).[160] However, requiring extraction of H_2O_2 from a mixture of organic solvent, the AO remains a multistage process with significant energy and capital cost.[160] More importantly, the use of organic solvents produces an environmental impact which reduces its sustainability.[160] Providing an alternative to current environmentally unfriendly methods of H_2O_2 formation, the in-situ generation of environmentally benign oxidant is industrially attractive.[161]

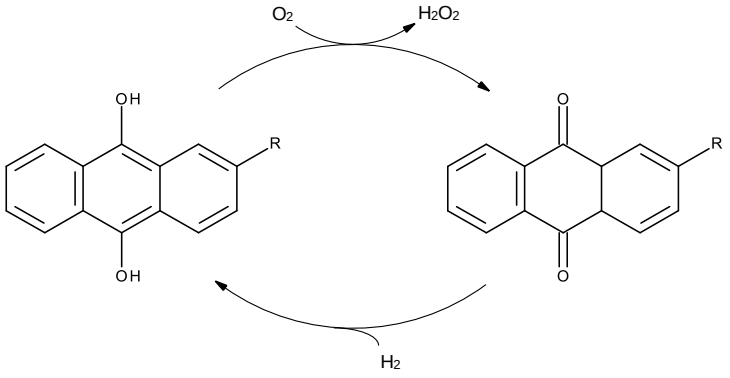

Figure 1.15: Simplified schematic for the anthraquinone oxidation process, demonstrating the sequential hydrogenation and oxidation of alkyl-anthraquinone for the indirect synthesis of H_2O_2.[160,162]

Addressing this, Lin and co-workers demonstrated the oxidation of alkanes by H_2O_2 generated in situ.[163] Using a Pd/C catalyst, initial investigations were carried out by

successful oxidation of C_2H_6 to predominantly CH_3CH_2OH at 30 ˚C.[163] Investigating temperatures ranging 100 ˚C to 30 ˚C revealed lower temperatures in addition to small quantities of acidic media were required to minimise Pd catalysed H_2O_2 decomposition. Illustrated in Figure 1.165, direct synthesis of H_2O_2 was produced from O_2 and H_2 over Pd catalyst, with H_2 sourced from the water gas shift reaction of CO and H_2O. Attempts to oxidise CH_4 succeeded and produced HCOOH, with a TON ranging from 80-160. Experiments carried out using H_2 and O_2 only rapidly produced H_2O_2, however, high rates of Pd- catalysed decomposition were observed. Similarly, the formation of unstable HCOOH from CH_4 was observed and resulted in over-oxidation to $CO_2$and H_2O.

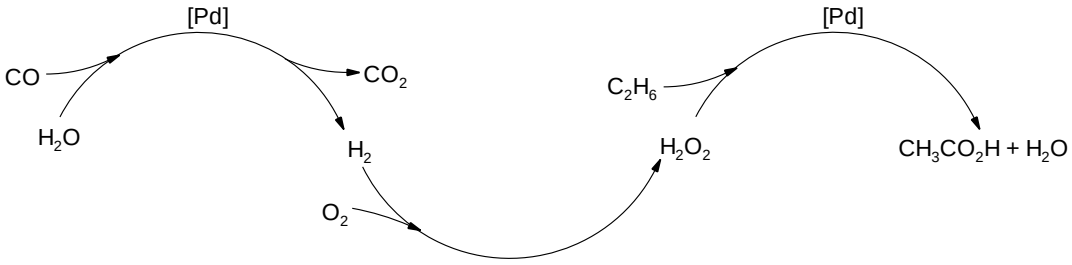

Figure 1.16: Proposed reaction scheme for C_2H_6 oxidation using in-situ generated H_2O_2 from CO and H_2O by Pd/Carbon. Recreated from Lin *et al.*[163]

Similarly, Ab Rahim and co-workers applying bimetallic 2.5wt.%Au-2.5wt.%Pd/TiO_2 (AuPd) catalysts demonstrated the efficient oxidation of CH_4 using preformed H_2O_2 to produce methyl hydroperoxide (CH_3OOH) and CH_3OH.[164,165] Observing high oxygenate selectivity (>80%) at 50 ˚C reaction temperature, large quantities of H_2O_2 were consumed, with 10% of the initial 5000 μmol H_2O_2 remaining.

Building upon the extensive work of Hutchings *et al.*[166,167], Ab Rahim demonstrated *in-situ* generation of H_2O_2 from gas phase H_2 and O_2 for CH_4 oxidation at 50 ˚C.[164,165] Improved CH_3OH selectivity was observed compared to experiments using preformed H_2O_2 (68% vs. 49%) whilst maintaining similar productivity. Importantly, the theoretical maximum quantity of H_2O_2 produced was calculated at *ca.* 250 μmol. Subsequently, *in-situ* generation produced a three-fold increase in H_2O_2 reactivity compared to similar quantities of preformed H_2O_2.[164] Despite this, low productivities for H_2O_2 synthesis from H_2 and O_2 resulted in a low oxidation rate of CH_4. Similarly, the use of preformed H_2O_2 yields low productivities, requiring excess H_2O_2 despite high selectivities to oxygenates.

The addition of Cu to produce a trimetallic AuPdCu/TiO_2 catalyst, enhanced CH_3OH selectivity to *ca.* 83% whilst operating under similar condition with preformed H_2O_2 for 2.5wt%Au-2.5wt%Pd-1.0wt.%Cu (AuPdCu).[168] The advantage of trimetallic catalyst,

however, did not continue for the *in-situ* generation of H_2O_2 from H_2 and O_2. Oxygenate productivity decreased from 0.11 $mol_{(oxygenates)}kg_{(cat)}^{-1}h^{-1}$ for bimetallic AuPd to 0.04 $mol_{(oxygenates)}kg_{(cat)}^{-1}h^{-1}$ for AuPdCu catalysts.[168]

Recent work by Agarwal *et al.*[169] investigating unsupported AuPd nanoparticles significantly improved upon the oxygenate productivity demonstrated by Ab Rahim. Utilising 1000 µmol H_2O_2, oxygenate productivity of 29.4 $mol_{(oxygenates)}kg_{(cat)}^{-1}h^{-1}$ was achieved, consuming 28% of initial H_2O_2 concentration with 6.6 µmol AuPd metal. Importantly, productivity was enhanced to 39.4 $mol_{(oxygenates)}kg_{(cat)}^{-1}h^{-1}$ further by reduction of H_2O_2 concentration to 50 µmol in conjunction with O_2 (5 bar) addition. Subsequent investigation using $^{18}O_2$ evidenced the incorporation of O_2 into *ca.* 70% of primary products.[169]

The incorporation of O_2 into primary CH_4 oxidation products represents important progress towards direct CH_3OH formation from O_2.[169] At present, ability to utilise O_2 as a direct, cheap and readily available oxidant is not possible. Instead, activation of O_2 by reduction with NADH or H_2 is required first.[19] Additionally, homogeneous catalysts performance is greatly superior to their heterogeneous counterparts in terms of CH_4 conversion and selectivity.[107] The challenge for a commercial low temperature process is the requirement of a highly active catalytic system, remaining stable whilst producing CH_3OH in high concentration. [19,29]

1.2.2.4 Gas phase Approaches

The non-catalytic activation of methane, utilising high temperature and high pressure approaches predominantly occurs via the gas-phase homolytic cleavage of C-H bonds. Typically operating at temperatures between 773-1073 K and pressures of 30-60 bar, product formation is dictated by radical reaction pathways.[170] Subsequently, the formation of CH_3OH achieving moderate selectivities can be controlled by considering reactor set up, residence time and product capture by quenching of unstable oxygenates.[170–172] Despite the difficulties associated with controlling this radical process, only low yields have been reported for CH_3OH and CH_2O formation.[173] Zhang and co-workers report yields of CH_3OH *ca.*8%, converting 13% of CH_4 with 60% selectivity.[174] Operating at high temperatures (723-773 K) and pressures (30-60 bar), several studies also reported similar CH_4 conversion (5-10%) with CH_3OH selectivities of 30-40%.[40,175–177]

Alternatively, Hargreaves *et al.* demonstrated an improvement to C_1 oxygenate selectivity by using low partial pressures of CH_4 over MgO catalysts.[178] Operating at high temperatures and pressures, MgO was demonstrated as an effective catalyst for the oxidative coupling of CH_4, generating C_{2+} species.[36] Careful control of reaction conditions

by reduction of partial pressure allowed Hargreaves control of competing coupling and oxidation reactions occurring in the gas-phase and upon the catalyst surface. Subsequently, reduction of CH_4 partial pressure reduced the concentration of methyl radicals produced, improving selectivity and yielded CH_2O as the major product. Furthermore, the ratio of O_2 and CH_4 played a crucial role. Importantly, the reduction in pressure afforded the ability to tune product yield and selectivity using solid catalysts.

Silica -supported MoO_x and VO_x have also been reported with yields of 3-4% for CH_2O synthesis whilst operating at temperatures between 623 to 773 K.[179] Initially reported by Dowden and Walker, the importance of the presence of oxide was described, with $Fe_2O_3(MoO_3)_3$ being most active for CH_3OH production.[180] Further work by Spencer and co-workers, examined the application of SiO_2 -supported MoO_3, forming primarily CH_2O, CO and CO_2. Selectivity to CH_2O was dependent upon CH_4 conversion, with low CH_4 conversion producing 71% CH_2O selectivity. High specific activity was determined to originate from isolated penta-coordinated $Mo^{(VI)}O_x$, demonstrating high selectivity towards CH_2O and CH_3OH.[181,182] Meanwhile, Taylor *et al.* investigating MoO_3 catalysed CH_4 partial oxidation using a range of metal oxide supports. [183] Experiments at 723 K, indicated Ga_2O_3/MoO_3 catalysts were able to form CH_3OH from O_2 with 22% selectivity, with cooperative interaction between Ga_2O_3 and MoO_3 attributed.[183]

Alternatively, Parmaliana and co -workers demonstrated the partial oxidation of CH_4 using SiO_2 -supported V_2O_5 catalyst.[184] Operating at 923 K, the application of a continuous flow recycle reactor allowed 10-18% yields of CH_2O to be obtained.[185] Addition of NO to reaction feed was also investigated by Barberos *et al.* using low surface area V_2O_5/SiO_2.[186] The introduction of low amounts of NO (0-2.92 %vol.) promoted the activation of CH_4 at moderate temperatures, with C_1 oxygenate selectivity reaching 40% at *ca.* 40% conversion.[186]

Recent work by Narimhan *et al.* reported the low temperature oxidation of CH_4 to CH_3OH using molecular oxygen over Cu -exchanged zeolites at low temperatures (483 -498 K).[187] Employing atmospheric pressures, zeolite topology was shown to affect reaction rates, with Cu-SSZ-13 possessing the highest activity (3.12 $\mu mol_{CH_3OH}\ g_{cat}^{-1}\ h^{-1}$). Similarly, Sushkevich *et al.* utilised an anaerobic approach to enhance CH_3OH selectivity.[188] Pre -activation of Cu -MOR was achieved in helium (He) at 673 K, followed by consecutive exposure of CH_4 (7 bar) at 473 K for 30 minutes. Water vapour in He was utilised as a cheap, abundant source of oxygen capable of regenerating the Cu active sites by facilitating the stabilised desorption of CH_3OH into gaseous phase. The desorption was achieved with steady increase of reaction temperature, returning to 673 K before repetition of reaction cycle, consistently achieving 0.204 moles CH_3OH per mole of Cu with *ca.* 97% selectivity.[188]

Despite considerable effort to develop highly active catalysts which demonstrate high selectivity to C_1 oxygenates, current yields are not sufficient for practical application. The

low CH_3OH yields reported correlate with poor O -insertion after initial H -abstraction by redox oxides such as MoO_3 and V_2O_5.[189] Attempts to improve this, however, lack mechanistic understanding, which remains difficult to describe.[22] Similarly, operating at the high reaction temperatures required for activation of stable C-H bonds is disadvantageous for oxygenate selectivity. Instead, high temperatures are conducive to continued oxidation, towards CO_x, in addition to facilitating the competing gas phase methyl radical pathways. This is made evident by the works of Otsuka *et al.*, demonstrating the complete conversion of CH_3OH feeds were observed at temperatures employed for CH_4 conversion over $Fe_2(MoO_4)_3$.[190] Reactions occurring in gas phase were concluded to be negligible overall, with significant reactivity occurring on the $Fe_2(MoO_4)_3$ catalyst surface by formation of dissociatively adsorbed oxygen.[190] Similar reactivity were shown for SiO_2 -supported V_2O_5 and MoO_3 catalyst under the same reaction conditions.[184,191]

Consequently, consecutive reactions result in loss of selectivity towards HCOOH and CO_x products. Subsequently, catalyst capable of activating CH_4 at low temperature and pressures is required.

1.3 Thesis Aims

The aims of the following investigations are described:

Chapter 3: Selective Oxidation of Methane to Methanol using Supported Au-Pd Catalysts Prepared by Stabiliser -free Sol-immobilisation

Previously reported by Ab Rahim et al.[164,165], the selective oxidation of CH_4 to CH_3OH was achieved using bimetallic AuPd/TiO_2 catalyst with H_2O_2 as the terminal oxidant. Possessing a broad range of AuPd nanoparticles (5-20 nm) and displaying high amounts of H_2O_2 decomposition, only moderate activity was achieved. In this section, AuPd nanoparticles produced by stabiliser free sol immobilisation are used to investigate the role of AuPd particle size upon the productivity for selective oxidation of methane using preformed H_2O_2. Further consideration is given to the efficient utilisation of H_2O_2 and demonstrates the influence of support as a vital parameter for efficient use of H_2O_2 for primary oxygenate production

Chapter 4: Methane Oxidation Using Hexafluorobenzene Solvent

Demonstrating higher gas solubility for CH_4, O_2 and H_2, the application of perfluorinated solvent was investigated for methane oxidation.[192,193] Representing a highly desired route for green oxidation chemistry, the use of O_2 was investigated as oxidant for the oxidation of methane to methanol.[19] This route considered the activation of C-H bonds via radical initiator induced H-abstraction, or by activation of O2 during in-situ generated H_2O_2.

1.4 References

1 *World Population Prospects: The 2017 Revision*, P. D. United Nations Department of Economic and Social Affairs, https://esa.un.org/unpd/wpp/Publications/Files/WPP2017_KeyFindings.pdf, (accessed 11 April 2018).

2 *BP Statistical Review of World Energy June 2017*, BP https://www.bp.com/content/dam/bp/en/corporate/pdf/energy-economics/statistical-review-2017/bp-statistical-review-of-world-energy-2017-full-report.pdf, (accessed 20 July 2017).

3 *UK Energy In Brief*, Energy & Industrial Strategy, Department for Business, https://assets.publishing.service.gov.uk/government/uploads/system/uploads/attachment_data/file/631146/UK_Energy_in_Brief_2017.pdf.

4 P. H. Pfromm, *J. Renew. Sustain. Energy*, 2017, **9**, 1–11.

5 P. Schwach, X. Pan and X. Bao, *Chem. Rev.*, 2017, **117**, 8497–8520.

6 R. Horn and R. Schlögl, *Catal. Letters*, 2015, **145**, 23–39.

7 R. A. Dawe and S. Thomas, *Energy Sources, Part A Recover. Util. Environ. Eff.*, 2007, **29**, 217–229.

8 Y. F. Makogon, S. A. Holditch and T. Y. Makogon, *J. Pet. Sci. Eng.*, 2007, **56**, 14–31.

9 S. Achinas, V. Achinas and G. J. W. Euverink, *Engineering*, 2017, **3**, 299–307.

10 P. Weiland, *Appl. Microbiol. Biotechnol.*, 2010, **85**, 849–860.

11 S. Achinas and G. J. W. Euverink, *Resour. Technol.*, 2016, **2**, 143–147.

12 Q. Wang, X. Chen, A. N. Jha and H. Rogers, *Renew. Sustain. Energy Rev.*, 2014, **30**, 1–28.

13 D. Costa, J. Jesus, D. Branco, A. Danko and A. Fiúza, *Environ. Sci. Pollut. Res.*, 2017, **24**, 14579–14594.

14 *Henry Hub Natural Gas Spot Price*, U.S. Energy Information Administration, https://www.eia.gov/dnav/ng/hist/rngwhhdM.htm, (accessed 22 July 2017).

15 E. McFarland, *Science*, 2012, **338**, 340-342.

16 *U.S. Energy Production and Consumption* U.S Energy Information Administration, , https://www.eia.gov/energyexplained/?page=us_energy_home, (accessed 18 April 2018).

17 R. W. Howarth, R. Santoro and A. Ingraffea, *Clim. Change*, 2011, **106**, 679–690.

18 T. S. Rhee, A. J. Kettle and M. O. Andreae, *J. Geophys. Res. Atmos.*, 2009, **114**, 1–20.

19 C. Hammond, S. Conrad and I. Hermans, *ChemSusChem*, 2012, **5**, 1668–1686.

20 N. Tchouar, F. Ould-Kaddour and D. Levesque, *J. Chem. Phys.*, 2004, **121**, 7326–7331.

21 R. K. Eckhoff, *Mar. Pollut. Bull.*, 1994, **29**, 304–306.

22 A. I. Olivos-Suarez, À. Szécsényi, E. J. M. Hensen, J. Ruiz-Martinez, E. A. Pidko and J. Gascon, *ACS Catal.*, 2016, **6**, 2965–2981.

23 J. R. Rostrup-Nielsen, J. Sehested and J. K. Nørskov, *Advances in Catalysis*, Academic Press, 2002, **47**, 65–139.

24 A. Caballero and P. J. Pérez, *Chem. Soc. Rev.*, 2013, **42**, 8809–8820.

25 M. J. Gradassi and N. Wayne Green, *Fuel Process. Technol.*, 1995, **42**, 65–83.

26 R. Franke, D. Selent and A. Börner, *Chem. Rev.*, 2012, **112**, 5675–5732.

27 S. J. Blanksby and G. B. Ellison, *Acc. Chem. Res.*, 2003, **36**, 255–263.

28 R. Price, T. T. Eralp-Erden, E. Crumlin, S. Rani, S. Garcia, R. Smith, L. Deacon, C. Euaruksakul and G. Held, *Top. Catal.*, 2016, **59**, 516–525.

29 M. Ravi, M. Ranocchiari and J. A. van Bokhoven, *Angew. Chemie Int. Ed.*, 2017, **56**, 16464–16483.

30 K. Kubo, H. Iida, S. Namba and A. Igarashi, *J. Japan Pet. Inst.*, 2018, **61**, 10–19.

31 D. Lippe, *Oil Gas J.*, 2013, **111**, 72.

32 V. Spallina, I. C. Velarde, J. A. M. Jimenez, H. R. Godini, F. Gallucci and M. Van Sint Annaland, *Energy Convers. Manag.*, 2017, **154**, 244–261.

33 M. Bender, *ChemBioEng Rev.*, 2014, **1**, 136–147.

34 G. E. Keller and M. M. Bhasin, *J. Catal.*, 1982, **73**, 9–19.

35 W. Hinsen and M. Baerns, *Chem. Ztg*, 1983, **107**, 223–226.

36 T. Ito and J. H. Lunsford, *Nature*, 1985, **314**, 721.

37 J. H. Lunsford, *Angew. Chemie Int. Ed. English*, 1995, 34, 970–980.

38 D. J. Driscoll and J. H. Lunsford, *J. Phys. Chem.*, 1985, **89**, 4415–4418.

39 D. J. Driscoll, W. Martir, J. X. Wang and J. H. Lunsford, *J. Am. Chem. Soc.*, 1985, **107**, 58–63.

40 A. Holmen, *Catal. Today*, 2009, **142**, 2–8.

41 A. Tullo, *Chem. Eng. News Arch.*, 2014, **92**, 10.

42 A. TULLO, *Chem. Eng. News Arch.*, 2015, **92**, 23.

43 Y. S. Su, J. Y. Ying and W. H. Green, *J. Catal.*, 2003, **218**, 321–333.

44 R. L. P. Gonçalves, F. C. Muniz, F. B. Passos and M. Schmal, *Catal. Letters*, 2010, **135**, 26–32.

45 J. A. Labinger, *Catal. Letters*, 1988, **1**, 371–376.

46 S. Jašo, H. Arellano-Garcia and G. Wozny, *Chem. Eng. J.*, 2011, **171**, 255–271.

47 J. A. Labinger and K. C. Ott, *J. Phys. Chem.*, 1987, **91**, 2682–2684.

48 M. Belgued, P. Pareja, A. Amariglio and H. Amariglio, *Nature*, 1991, **352**, 789.

49 M. Belgued, A. Amariglio, L. Lefort, P. Paréja and H. Amariglio, *J. Catal.*, 1996, **161**, 282–291.

50 H. Amariglio, J. Saint-Just and A. Amariglio, *Fuel Process. Technol.*, 1995, **42**, 291–323.

51 M. Belgued, H. Amariglio, P. Pareja, A. Amariglio and J. Saint-Just, *Catal. Today*, 1992, **13**, 437–445.

52 T. Koerts and R. A. van Santen, *J. Chem. Soc. Chem. Commun.*, 1991, **0**, 1281–1283.

53 T. Koerts, M. J. A. G. Deelen and R. A. van Santen, *J. Catal.*, 1992, **138**, 101–114.

54 L. Wang, L. Tao, M. Xie, G. Xu, J. Huang and Y. Xu, *Catal. Letters*, 1993, **21**, 35–41.

55 D. Ma, Y. Shu, X. Bao and Y. Xu, *J. Catal.*, 2000, **189**, 314–325.

56 D. Ma, W. Zhang, Y. Shu, X. Liu, Y. Xu and X. Bao, *Catal. Letters*, 2000, **66**, 155–160.

57 D. Ma, X. W. Han, D. H. Zhou, Z. M. Yan, R. Q. Fu, Y. Xu, X. H. Bao, H. B. Hu and S. C. F. Au-Yeung, *Chem. Eur. J.*, 2002, **8**, 4557–4561.

58 H. Zheng, D. Ma, X. Bao, J. Z. Hu, J. H. Kwak, Y. Wang and C. H. F. Peden, *J. Am. Chem. Soc.*, 2008, **130**, 3722–3723.

59 J.-P. Tessonnier, B. Louis, S. Rigolet, M. J. Ledoux and C. Pham-Huu, *Appl. Catal. A Gen.*, 2008, **336**, 79–88.

60 M. J. Rice, A. K. Chakraborty and A. T. Bell, *J. Catal.*, 1999, **186**, 222–227.

61 C. L. Zhang, S. A. Li, Y. Yuan, W. X. Zhang, T. H. Wu and L. W. Lin, *Catal. Letters*, 1998, **56**, 207–213.

62 C. Karakaya, H. Zhu and R. J. Kee, *Chem. Eng. Sci.*, 2015, **123**, 474–486.

63 C. Karakaya and R. J. Kee, *Prog. Energy Combust. Sci.*, 2016, **55**, 60–97.

64 X. Guo, G. Fang, G. Li, H. Ma, H. Fan, L. Yu, C. Ma, X. Wu, D. Deng, M. Wei, D. Tan, R. Si, S. Zhang, J. Li, L. Sun, Z. Tang, X. Pan and X. Bao, *Science*, 2014, **344**, 616–619.

65 S. Mann, W. Yiqing, O. S. Cheun, W. E. D. and L. Dongxia, *Angew. Chemie Int. Ed.*, **55**, 16149–16152.

66 Z. Liu, L. Li and E. Iglesia, *Catal. Letters*, 2002, **82**, 175–180.

67 G. A. Olah, *Angew. Chemie - Int. Ed.*, 2005, **44**, 2636–2639.

68 G. A. Olah, A. Goeppert and G. K. S. Prakash, *Beyond Oil and Gas: The Methanol Economy: Second Edition*, 2009.

69 G. Iaquaniello, G. Centi, A. Salladini and E. Palo, in *Methanol*, Elsevier, 2018, 595–612.

70 P. Tang, Q. Zhu, Z. Wu and D. Ma, *Energy Environ. Sci.*, 2014, **7**, 2580–2591.

71 P. Tian, Y. Wei, M. Ye and Z. Liu, *ACS Catal.*, 2015, **5**, 1922–1938.

72 M. Khanmohammadi, S. Amani, A. B. Garmarudi and A. Niaei, *Chinese J. Catal.*, 2016, **37**, 325–339.

73 Q. Smejkal, D. Linke and M. Baerns, *Chem. Eng. Process. Process Intensif.*, 2005, **44**, 421–428.

74 P. M. Maitlis, A. Haynes, G. J. Sunley and M. J. Howard, *J. Chem. Soc. Dalt. Trans.*, 1996, 2187–2196.

75 R. O. dos Santos, L. de Sousa Santos and D. M. Prata, *J. Clean. Prod.*, 2018, **186**, 821–830.

76 A. Hankin and N. Shah, *Sustain. Energy Fuels*, 2017, **1**, 1541–1556.

77 F. Achmad, S. K. Kamarudin, W. R. W. Daud and E. H. Majlan, *Appl. Energy*, 2011, **88**, 1681–1689.

78 W. A. Bone and R. V. Wheeler, *J. Chem. Soc. Trans.*, 1903, 83, 1074–1087.

79 W. A. Bone and R. V Wheeler, *J. Chem. Soc. Trans.*, 1902, **81**, 535–549.

80 W. A. Bone and R. A. Allum, *Proc. R. Soc. London. Ser. A*, 1932, **134**, 578–591.

81 V. Arutyunov, in *Methanol*, Elsevier, 2018, 129–172.

82 D. Sheldon, *Johnson Matthey Technol. Rev.*, 2017, **61**, 172–182.

83 P. Khirsariya and R. K. Mewada, *Procedia Eng.*, 2013, **51**, 409–415.

84 Y. A. Trotsenko and J. C. Murrell, *Adv. Appl. Microbiol.*, 2008, **63**, 183–229.

85 R. S. Hanson and T. E. Hanson, *Microbiol.Rev.*, 1996, **60**, 439–471.

86 M. O. Ross and A. C. Rosenzweig, *J. Biol. Inorg. Chem.*, 2017, **22**, 307—319.

87 T. J. Smith and H. Dalton, *Stud. Surf. Sci. Catal.*, 2004, **151**, 177–192.

88 M. Merkx, D. A. Kopp, M. H. Sazinsky, J. L. Blazyk, J. Muanödller and S. J. Lippard, *Angew. Chemie - Int. Ed.*, 2001, 40, 2782–2807.

89 C. E. Tinberg and S. J. Lippard, *Acc. Chem. Res.*, 2011, **44**, 280–288.

90 R. L. Lieberman and A. C. Rosenzweig, *Nature*, 2005, **434**, 177–182.

91 R. Balasubramanian, S. M. Smith, S. Rawat, L. A. Yatsunyk, T. L. Stemmler and A. C. Rosenzweig, *Nature*, 2010, **465**, 115–119.

92 V. C.-C. Wang, S. Maji, P. P.-Y. Chen, H. K. Lee, S. S.-F. Yu and S. I. Chan, *Chem. Rev.*, 2017, **117**, 8574–8621.

93 S. Sirajuddin and A. C. Rosenzweig, *Biochemistry*, 2015, **54**, 2283–2294.

94 A. S. Hakemian and A. C. Rosenzweig, *Annu. Rev. Biochem.*, 2007, **76**, 223–241.

95 P. P.-Y. Chen, R. B.-G. Yang, J. C.-M. Lee and S. I. Chan, *Proc. Natl. Acad. Sci. U. S. A.*, 2007, **104**, 14570–14575.

96 P. Nagababu, S. Maji, M. P. Kumar, P. P. Y. Chen, S. S. F. Yu and S. I. Chan, *Adv. Synth. Catal.*, 2012, **354**, 3275–3282.

97 S. I. Chan, C. Y.-C. Chien, C. S.-C. Yu, P. Nagababu, S. Maji and P. P.-Y. Chen, *J. Catal.*, 2012, **293**, 186–194.

98 H.-H. T. Nguyen, K. H. Nakagawa, B. Hedman, S. J. Elliott, M. E. Lidstrom, K. O. Hodgson and S. I. Chan, *J. Am. Chem. Soc.*, 1996, **118**, 12766–12776.

99 S. I. Chan, K. H.-C. Chen, S. S.-F. Yu, C.-L. Chen and S. S.-J. Kuo, *Biochemistry*, 2004, **43**, 4421–4430.

100 S. I. Chan, Y. J. Lu, P. Nagababu, S. Maji, M. C. Hung, M. M. Lee, I. J. Hsu, P. D. Minh, J. C. H. Lai, K. Y. Ng, S. Ramalingam, S. S. F. Yu and M. K. Chan, *Angew. Chemie - Int. Ed.*, 2013, **52**, 3731–3735.

101 K. H. C. Chen, C. L. Chen, C. F. Tseng, S. S. F. Yu, S. C. Ke, J. F. Lee, H. T. Nguyen, S. J. Elliott, J. O. Alben and S. I. Chan, *J. Chinese Chem. Soc.*, 2004, **51**, 1081–1098.

102 S. I. Chan, V. C. C. Wang, J. C. H. Lai, S. S. F. Yu, P. P. Y. Chen, K. H. C. Chen, C. L. Chen and M. K. Chan, *Angew. Chemie - Int. Ed.*, 2007, **46**, 1992–1994.

103 P. P. Y. Chen, P. Nagababu, S. S. F. Yu and S. I. Chan, *ChemCatChem*, 2014, 6, 429–437.

104 A. L. Feig and S. J. Lippard, *Chem. Rev.*, 1994, **94**, 759–805.

105 R. Banerjee, Y. Proshlyakov, J. D. Lipscomb and D. A. Proshlyakov, *Nature*, 2015,

518, 431–434.

106 J. D. Semrau, A. A. Dispirito and S. Yoon, *FEMS Microbiol. Rev.*, 2010, 34, 496–531.

107 E. V. Kondratenko, T. Peppel, D. Seeburg, V. Kondratenko, N. Kalevaru, A. Martin and S. Wohlrab, *Catal. Sci. Technol.*, 2017, **7**, 366–381.

108 J. Colby, D. I. Stirling and H. Dalton, *Biochem. J.*, 1977, **165**, 395–402.

109 C.-C. Liu, ab Chung-Yuan Mou, S. S-F Yu and S. I. Chan, *Energy Environ. Sci. Energy Environ. Sci*, 2016, **9**, 1361–1374.

110 E. Y. Tshuva and S. J. Lippard, *Chem. Rev.*, 2004, 104, 987–1012.

111 A. B. Sorokin and E. V. Kudrik, in *Catalysis Today*, 2011, vol. 159, pp. 37–46.

112 A. B. Sorokin, E. V Kudrik and D. Bouchu, *Chem. Commun.*, 2008, 2562–2564.

113 A. B. Sorokin, E. V Kudrik and D. Bouchu, *Chem. Commun.*, 2008, 2562–2564.

114 M. C. Alvarez-Galvan, N. Mota, M. Ojeda, S. Rojas, R. M. Navarro and J. L. G. Fierro, in *Catalysis Today*, 2011, **171**, 15–23.

115 A. B. Sorokin, *Chem. Rev.*, 2013, **113**, 8152–8191.

116 E. V. Kudrik, P. Afanasiev, L. X. Alvarez, P. Dubourdeaux, M. Clémancey, J. M. Latour, G. Blondin, D. Bouchu, F. Albrieux, S. E. Nefedov and A. B. Sorokin, *Nat. Chem.*, 2012, **4**, 1024–1029.

117 B. Basu, S. Sat Apathy and A. K. Bhatnagar, *Catal. Rev.*, 1993, **35**, 571–609.

118 M. M. Forde, B. C. Grazia, R. Armstrong, R. L. Jenkins, M. H. A. Rahim, A. F. Carley, N. Dimitratos, J. A. Lopez-Sanchez, S. H. Taylor, N. B. McKeown and G. J. Hutchings, *J. Catal.*, 2012, **290**, 177–185.

119 A. E. N. F. Goldshle, A. A. Shteinman and V. V. E. Shilov, *Russ. J. Phys. Chem. USSR*, 1972, **46**, 785–786.

120 R. A. Periana, D. J. Taube, S. Gamble, H. Taube, T. Satoh and H. Fujii, *Science*, 1998, **280**, 560–564.

121 R. Palkovits, M. Antonietti, P. Kuhn, A. Thomas and F. Schüth, *Angew. Chemie - Int. Ed.*, 2009, **48**, 6909–6912.

122 R. A. Periana, D. J. Taube, E. R. Evitt, D. G. Löffler, P. R. Wentrcek, G. Voss, T. Masuda and D. G. Löffler, *Science*, 1993, **259**, 340–343.

123 T. Zimmermann, M. Soorholtz, M. Bilke and F. Schüth, *J. Am. Chem. Soc.*, 2016, **138**, 12395–12400.

124 N. J. Gunsalus, A. Koppaka, S. H. Park, S. M. Bischof, B. G. Hashiguchi and R. A.

Periana, *Chem. Rev.*, 2017, **117**, 8521–8573.

125 X. Xu, J. Kua, R. A. Periana and W. A. Goddard, *Organometallics*, 2003, **22**, 2057–2068.

126 A. Paul and C. B. Musgrave, *Organometallics*, 2007, **26**, 793–809.

127 B. G. Hashiguchi, S. M. Bischof, M. M. Konnick and R. A. Periana, *Acc. Chem. Res.*, 2012, **45**, 885–898.

128 S. Mukhopadhyay and A. T. Bell, *J. Mol. Catal. A Chem.*, 2004, **211**, 59–65.

129 D. Piao, K. Inoue, H. Shibasaki, Y. Taniguchi, T. Kitamura and Y. Fujiwara, *J. Organomet. Chem.*, 1999, **574**, 116–120.

130 G. R. Williams, S. T. Kolaczkowski and P. Plucinski, *Catal. Today*, 2003, **81**, 631–640.

131 C. J. C. J. Jones, D. Taube, V. R. Ziatdinov, R. A. Periana, R. J. Nielsen, J. Oxgaard and W. A. Goddard, *Angew. Chemie - Int. Ed.*, 2004, **43**, 4626–4629.

132 Z. An, X. Pan, X. Liu, X. Han and X. Bao, *J. Am. Chem. Soc.*, 2006, **128**, 16028–16029.

133 I. Abraham, R. Joshi, P. Pardasani and R. T. Pardasani, *J. Braz. Chem. Soc.*, 2011, **22**, 385–421.

134 I. Bar-Nahum, A. M. Khenkin and R. Neumann, *J. Am. Chem. Soc.*, 2004, **126**, 10236–10237.

135 J. Yuan, L. Wang and Y. Wang, *Ind. Eng. Chem. Res.*, 2011, **50**, 6513–6516.

136 G. B. Shul'pin, G. Suss-Fink and L. S. Shul'pina, *Chem. Commun.*, 2000, 1131–1132.

137 E. D. Park, Y.-S. Hwang, C. W. Lee and J. S. Lee, *Appl. Catal. A Gen.*, 2003, **247**, 269–281.

138 S. Mukhopadhyay and A. T. Bell, *Chem. Commun.*, 2003, 1590–1591.

139 S. Mukhopadhyay and A. T. Bell, *Angew. Chemie - Int. Ed.*, 2003, **42**, 1019–1021.

140 J. N. Kondo, R. Nishitani, E. Yoda, T. Yokoi, T. Tatsumi and K. Domen, *Phys. Chem. Chem. Phys.*, 2010, **12**, 11576–11586.

141 M. Moshoeshoe, M. S. Nadiye-Tabbiruka and V. Obuseng, *Am. J. Mater. Sci.*, 2017, **7**, 196–221.

142 A. Corma, *Journal of Catalysis*, 2003, **216**, pp. 298–312.

143 R. P. Townsend and E. N. Coker, *Stud. Surf. Sci. Catal.*, 2001, **137**, 467–524.

144 G. I. Pannov, V. I. Sobolev and A. S. Kharitonov, *J. Mol. Catal.*, 1990, **61**, 85–97.

145 G. I. Panov, V. I. Sobolev, K. A. Dubkov, V. N. Parmon, N. S. Ovanesyan, A. E. Shilov and A. A. Shteinman, *React. Kinet. Catal. Lett.*, 1997, **61**, 251–258.

146 K. A. A. Dubkov, N. S. S. Ovanesyan, A. A. A. Shteinman, E. V. V. Starokon and G. I. I. Panov, *J. Catal.*, 2002, **207**, 341–352.

147 B. E. R. Snyder, P. Vanelderen, M. L. Bols, S. D. Hallaert, L. H. Böttger, L. Ungur, K. Pierloot, R. A. Schoonheydt, B. F. Sels and E. I. Solomon, *Nature*, 2016, **536**, 317–321.

148 M. V. Parfenov, E. V. Starokon, L. V. Pirutko and G. I. Panov, *J. Catal.*, 2014, **318**, 14–21.

149 Y. K. Chow, N. F. Dummer, J. H. Carter, C. Williams, G. Shaw, D. J. Willock, S. H. Taylor, S. Yacob, R. J. Meyer, M. M. Bhasin and G. J. Hutchings, *Catal. Sci. Technol.*, 2018, **8**, 154–163.

150 P. Tomkins, A. Mansouri, S. E. Bozbag, F. Krumeich, M. B. Park, E. M. C. Alayon, M. Ranocchiari and J. A. Vanbokhoven, *Angew. Chemie - Int. Ed.*, 2016, **55**, 5467–5471.

151 E. M. C. Alayon, M. Nachtegaal, A. Bodi, M. Ranocchiari and J. A. Van Bokhoven, *Phys. Chem. Chem. Phys.*, 2015, **17**, 7681–7693.

152 P. J. Smeets, M. H. Groothaert and R. A. Schoonheydt, *Catalysis Today*, 2005, **110**, 303–309.

153 C. Hammond, M. M. Forde, M. H. Ab Rahim, A. Thetford, Q. He, R. L. Jenkins, N. Dimitratos, J. A. Lopez-Sanchez, N. F. Dummer, D. M. Murphy, A. F. Carley, S. H. Taylor, D. J. Willock, E. E. Stangland, J. Kang, H. Hagen, C. J. Kiely and G. J. Hutchings, *Angew. Chemie - Int. Ed.*, 2012, **51**, 5129–5133.

154 A. K. M. L. Rahman, M. Kumashiro and T. Ishihara, *Catal. Commun.*, 2011, **12**, 1198–1200.

155 C. Hammond, R. L. Jenkins, N. Dimitratos, J. A. Lopez-Sanchez, M. H. Ab Rahim, M. M. Forde, A. Thetford, D. M. Murphy, H. Hagen, E. E. Stangland, J. M. Moulijn, S. H. Taylor, D. J. Willock and G. J. Hutchings, *Chem. - A Eur. J.*, 2012, **18**, 15735–15745.

156 O. B. Ayodele, *Energy Convers. Manag.*, 2016, **126**, 537–547.

157 J. Shan, M. Li, L. F. Allard, S. Lee and M. Flytzani-Stephanopoulos, *Nature*, 2017, **551**, 605–608.

158 K. Narsimhan, V. K. Michaelis, G. Mathies, W. R. Gunther, R. G. Griffin and Y. Román-Leshkov, *J. Am. Chem. Soc.*, 2015, **137**, 1825–1832.

159 J. Tang, H. Y. Yin and J. L. Zhang, in *Inorganic and Organometallic Transition Metal Complexes with Biological Molecules and Living Cells*, 2017, 1–53.

160 J. M. Campos-Martin, G. Blanco-Brieva and J. L. G. Fierro, *Angew. Chemie - Int. Ed.*, 2006, 45, 6962–6984.

161 J. K. Edwards, B. E. Solsona, P. Landon, A. F. Carley, A. Herzing, C. J. Kiely and G. J. Hutchings, *J. Catal.*, 2005, **236**, 69–79.

162 T. Nishimi, T. Kamachi, K. Kato, T. Kato and K. Yoshizawa, *European J. Org. Chem.*, 2011, 4113–4120.

163 M. Lin and A. Sen, *J. Am. Chem. Soc.*, 1992, **114**, 7307–7308.

164 M. H. Ab Rahim, M. M. Forde, R. L. Jenkins, C. Hammond, Q. He, N. Dimitratos, J. A. Lopez-Sanchez, A. F. Carley, S. H. Taylor, D. J. Willock, D. M. Murphy, C. J. Kiely and G. J. Hutchings, *Angew. Chemie - Int. Ed.*, 2013, **52**, 1280–1284.

165 M. H. Ab Rahim, M. M. Forde, C. Hammond, R. L. Jenkins, N. Dimitratos, J. A. Lopez-Sanchez, A. F. Carley, S. H. Taylor, D. J. Willock, G. J. Hutchings, M. Hasbi, A. Rahim, M. M. Forde, C. Hammond, R. L. Jenkins, N. Dimitratos, J. A. Lopez-Sanchez, A. F. Carley, S. H. Taylor, D. J. Willock and G. J. Hutchings, *Top. Catal.*, 2013, **56**, 1843–1857.

166 J. K. Edwards and G. J. Hutchings, *Angew. Chemie - Int. Ed.*, 2008, **47**, 9192–9198.

167 J. K. Edwards, S. J. Freakley, R. J. Lewis, J. C. Pritchard and G. J. Hutchings, *Catal. Today*, 2015, **248**, 3–9.

168 M. H. Ab Rahim, R. D. Armstrong, C. Hammond, N. Dimitratos, S. J. Freakley, M. M. Forde, D. J. Morgan, G. Lalev, R. L. Jenkins, J. A. Lopez-Sanchez, S. H. Taylor, G. J. Hutchings, M. Hasbi, A. Rahim, R. D. Armstrong, C. Hammond, N. Dimitratos, S. J. Freakley, M. M. Forde, D. J. Morgan, G. Lalev, R. L. Jenkins, J. A. Lopez-Sanchez, S. H. Taylor and G. J. Hutchings, *Catal. Sci. Technol.*, 2016, **6**, 3410–3418.

169 N. Agarwal, S. J. Freakley, R. U. McVicker, S. M. Althahban, N. Dimitratos, Q. He, D. J. Morgan, R. L. Jenkins, D. J. Willock, S. H. Taylor, C. J. Kiely and G. J. Hutchings, *Science*, 2017, **358**, 223–227.

170 K. Otsuka and Y. Wang, *Appl. Catal. A Gen.*, 2001, **222**, 145–161.

171 R. Burch, G. D. Squire and S. C. Tsang, *J. Chem. Soc. Faraday Trans. 1*, 1989, **85**, 3561–3568.

172 G. S. Walker, J. A. Lapszewicz and G. A. Foulds, *Catal. Today*, 1994, **21**, 519–526.

173 W. Feng, F. C. Knopf and K. M. Dooley, *Energy & Fuels*, 1994, **8**, 815–822.

174 Q. Zhang, D. He, J. Li, B. Xu, Y. Liang and Q. Zhu, *Appl. Catal. A Gen.*, 2002, **224**, 201–207.

175 G. A. Foulds, B. F. Gray, S. A. Miller and G. S. Walker, *Ind. Eng. Chem. Res.*, 1993, **32**, 780–787.

176 J. W. Chun and R. G. Anthony, *Ind. Eng. Chem. Res.*, 1993, **32**, 788–795.

177 D. W. Rytz and A. Baiker, *Ind. Eng. Chem. Res.*, 1991, **30**, 2287–2292.

178 J. S. J. Hargreaves, G. J. Hutchings and R. W. Joyner, *Nature*, 1990, **348**, 428–429.

179 A. V de Vekki and S. T. Marakaev, *Russ. J. Appl. Chem.*, 2009, **82**, 521–536.

180 Q. Zhang, D. He and Q. Zhu, *J. Nat. Gas Chem.*, 2003, **12**, 81–89.

181 N. Ohler and A. T. Bell, *J. Phys. Chem. B*, 2006, **110**, 2700–2709.

182 M. A. Banares, L. Dauphin, V. Calvoperez, T. P. Fehlner and E. E. Wolf, *J. Catal.*, 1995, **152**, 396–409.

183 S. H. Taylor, J. S. J. Hargreaves, G. J. Hutchings, R. W. Joyner and C. W. Lembacher, *Catal. Today*, 1998, **42**, 217–224.

184 A. Parmaliana, F. Frusteri, A. Mezzapica, M. S. Scurrell and N. Giordano, *J. Chem. Soc. Chem. Commun.*, 1993, 751–753.

185 F. Frusteri, F. Arena, G. Martra, S. Coluccia, A. Mezzapica and A. Parmaliana, *Catal. Today*, 2001, **64**, 97–102.

186 J. A. Barbero, M. C. Alvarez, M. A. Banares, M. A. Pena and J. L. G. Fierro, *Chem. Commun.*, 2002, 1184–1185.

187 K. Narsimhan, K. Iyoki, K. Dinh and Y. Román-Leshkov, *ACS Cent. Sci.*, 2016, **2**, 424–429.

188 V. L. Sushkevich, D. Palagin, M. Ranocchiari and J. A. Van Bokhoven, *Science* , 2017, **356**, 523–527.

189 K. Tabata, Y. Teng, T. Takemoto and E. Suzuki, *Catal. Rev. - Sci. Eng.*, 2002, **44**, 1–58.

190 K. Otsuka, Y. Wang, I. Yamanaka and A. Morikawa, *J. Chem. Soc. Faraday Trans.*, 1993, **89**, 4225–4230.

191 N. D. Spencer, *J. Catal.*, 1988, **109**, 187–197.

192 E. P. Wesseler, R. Iltis and L. C. Clark, *J. Fluor. Chem.*, 1977, **9**, 137–146.

193 C. M. Sharts, H. R. Reese, K. A. Ginsberg, F. K. Multer, M. D. Nielson, A. G. Greenburg, G. W. Peskin and D. M. Long, *J. Fluor. Chem.*, 1978, **11**, 637–641.

Chapter 2: Experimental Procedures

2.1 Introduction

The following chapter will cover the preparative, experimental and characterisation procedures used to complete the work described.

2.2 Materials

The materials used during this project are listed and categorised:

Materials used in the preparation of catalysts;

- Chloroauric acid, $HAuCl_4.xH_2O$ (99.999%, Sigma Aldrich)
- Palladium Chloride, $PdCl_2$ (Sigma Aldrich)
- Sodium borohydride, $NaBH_4$ (Sigma Aldrich)
- Trisodium citrate, $Na_3C_6H_5O_7$ (Sigma Aldrich)
- L-Ascorbic acid, $C_6H_8O_6$ (99%, Sigma Aldrich)
- Tannic Acid, $C_{76}H_{52}O_{46}$ (>99.995%, Sigma Aldrich)
- Potassium Carbonate, K_2CO_3 (>99.995%, Sigma Aldrich)
- Titanium dioxide, TiO_2 (P25, Degussa)
- Hydrochloric acid, HCl (37% , Fischer Scientific)
- Sulfuric acid, H_2SO_4 (90% , Fischer Scientific)
- Zeolite, NH_4-ZSM5-5 (SiO_2/Al_2O_3: 30, Zeolyst)
- Polyvinyl alcohol, $(C_2H_4O)_x$ (M_W= 10,000 Da, Sigma Aldrich)
- Carbon (Darco G60, Sigma Aldrich)

Materials used in the catalyst testing of catalysts

- Methane, CH_4 (99.999%, Air Products)
- Nitrogen, N_2 (99.999%, BOC gases)
- Oxygen, O_2 (99.999%, BOC gases
- Hydrogen peroxide, H_2O_2 (50 wt. % in H_2O, Sigma Aldrich)
- Deuterium oxide, D_2O (99.9 atom%, Sigma Aldrich)
- Hexafluorobenzene, C_6F_6 (99.9%, Fluorochem)
- 2,2'-Azobis(2-methylpropriontrile), $C_8H_{12}N_4$ (98%. Sigma Aldrich)
- Benzoyl peroxide, $C_{14}H_{10}O_4$ (97%, Alfa Aesar)
- 1,1'-Azobis(cyclohexanecarbonitrile), $C_{14}H_{20}N_4$ (98%, Sigma Aldrich)
- Methanol, CH_3OH (HPLC grade, Fisher Scientific)
- Cerium Sulfate, $Ce(SO_4)_2$ (99%, Sigma Aldrich)
- Toluene, C_7H_8 (>99.9%, Sigma Aldrich)
- Benzyl alcohol, C_7H_8O (99.8%, Sigma Aldrich)
- Benzaldehyde, C_7H_6O (>99.9%, Sigma Aldrich)
- Benzyl benzoate, $C_{12}H_{13}O_2$ (>99.0%, Sigma Aldrich)
- Benzoic acid, $C_7H_6O_2$ (>99.5%, Sigma Aldrich)
- 1,3,5, trimethyl benzene, C_9H_{12} (98%, Sigma Aldrich)
- Ferroin Indicator, $[C_{36}H_{24}FeN_6]SO_4$ (0.025M, Sigma Aldrich)

2.3 Definitions

The definitions of common terms used in this work are/is described below:

Selective oxygenates include: Methyl hydroperoxide (MeOOH), Methanol (MeOH), Formaldehyde (H_2CO) and Formic acid (HCOOH),
Unselective oxygenates include: Carbon dioxide (CO_2)

Selective Oxygenate Selectivity (%)

$$\frac{Moles\ (MeOOH + MeOH + HCOOH) formed}{Moles\ (MeOH + MeOOH + HCOOH + CO_2) formed} x100$$

Catalyst Productivity

$$\frac{Moles_{(oxygenated\ products)}}{kg_{catalyst}\ x\ \ time(h)}$$

Turnover Frequency

$$Moles_{(oxygenated\ products)}\ x\ Moles^{-1}_{(metals\ in\ catalyst)}\ x\ h^{-1}$$

$$\frac{Moles_{(oxygenated\ products)}}{Moles_{(metal\ in\ catalyst)}\ x\ time(h)}$$

Turnover Number

$$\frac{Moles_{(oxygenated\ products)}}{Moles_{(metals\ in\ catalyst)}}$$

Gain Factor

$$\frac{Moles_{(oxygenated\ products)}}{Moles_{H_2O_2\ consumed}}$$

Magic Cluster Theory

The magic cluster calculations determined for Au nanoparticles (NP).

Shell number [n]	Number of atoms in shell [$n_{(atom)}$][a]	Total number of Au atoms in NP [$n_{(total)}$][b]	Calculated Au Nanoparticle diameter [nm]
	1	1	0.27
1	12	13	0.81
2	42	55	1.35
3	92	147	1.89
4	162	309	2.43
5	252	561	2.97
6	362	923	3.51
7	492	1415	4.05
8	642	2057	4.59
9	812	2869	5.13
10	1002	3871	5.67

[a] $n_{(atom)} = 10n^2+2$. [b] $n(total) = (10n^3+15n^2+11n+3)/3$.

Intrinsic activity for the Decomposition of H_2O_2

$$\frac{Moles_{(H_2O_2\ decomposed)}}{Moles_{(total\ metal\ nanoparticle\ surface\ atoms)}\ x\ time(h)}$$

where $Moles_{(Metal\ nanoparticle\ surface\ atoms)}$ is calculated as for 10 mg of catalyst.

Intrinsic Activity for the Oxidation of Methane

$$\frac{Moles_{(total\ oxygenate\ products)}}{Moles_{(total\ metal\ nanoparticle\ surface\ atoms)}\ x\ time(h)}$$

where $Moles_{(Metal\ nanoparticle\ surface\ atoms)}$ is calculated as for 10 mg of catalyst.

2.4 Catalyst preparation

2.4.1 Preparation of Metal Precursor Solutions

The preparation of $PdCl_2$ solution is as follows:

Solid $PdCl_2$ (0.9998 g, 99.9%) was added to a 100 mL volumetric flask and deionised H_2O (95 mL) added. To assist with Pd dissolution, several drops of concentrated HCl (*ca.* 37%) was added and the resulting solution stirred vigorously until complete dissolution of solid precursor (typically 48 hrs at room temperature). Once dissolved, an additional aliquot of H_2O was added to produce a final volume of 100 mL and Pd concentration of 6mg mL^{-1}.

For the preparation of acidified $PdCl_2$ solution, 0.58M HCl concentration was selected and the above preparation followed with the addition of HCl (*ca.* 37%, 4.84 mL).[1]

The preparation of $HAuCl_4.xH_2O$ solution is as follows:

Solid $HAuCl_4.xH_2O$ (4.90 g, 99.9%) was added to a 500 mL amber volumetric flask and deionised water added. The solution was stirred vigorously until complete dissolution of the solid precursor to produce a Au Concentration of 12.25 mg mL^{-1}.

2.4.2 Preparation of supported nanoparticles by Wet impregnation

The preparation of 0.5 wt. % Au-0.5 wt. % Pd/ TiO_2 is carried out as follows:
A solution of $PdCl_2$ (0.4167 mL, 6mg mL^{-1}) was added to a 35mL glass vial containing a solution of $HAuCl_4.xH_2O$ (0.2041 mL, 12.25 mg mL^{-1}). Additional H_2O (0.5 mL) was also added to the solution and the resulting mixture heated to 60°C under moderate stirring. The required quantity of support, TiO_2 (0.495 g, Degussa P25) was then added and stirred until a homogeneous slurry was formed. Heating was raised to 90 °C and stirring continued until the water evaporated to form paste. The paste was then dried at 110 °C in an oven for 16 h.

The preparation of AuPd was similarly described by Edwards *et al.*[2]

2.4.3 Preparation of supported nanoparticles by Sol Immobilisation (Stabiliser free)

The preparation of 0.5 wt.% Au-0.5 wt.% Pd/ TiO_2 is carried as follows:
Aqueous solutions of $HAuCl_4.xH_2O$ (1.667 mL, 12.25mg mL^{-1}) and $PdCl_2$ (0.816 mL, 6 mg mL^{-1}) were added to 800 mL deionised water under vigorous stirring at room temperature. The resulting solution was stirred for 2 min before the addition of freshly prepared $NaBH_4$ (7.23 mL, 0.1M) such that the molar ratio of $NaBH_4$ to metal was 5:1[3]. Upon the addition of $NaBH_4$, the mixture turned dark brown-black and was then vigorously stirred for 30 min. The required quantity of support material was then added (P25 Degussa TiO_2, 1.98 g) allowing a minute for the solution to form a homogeneous mixture, the solution was acidified to pH 1 by the drop-wise addition of sulfuric acid (>95%). The mixture was then stirred for 1 h during which the reduced nanoparticles were adsorbed to the support. The suspension was then filtered under vacuum and washed thoroughly with distilled water. The filtered catalyst was then dried in an oven for 16 h at 110°C.

For catalyst prepared at elevated temperature (70 °C), the initial solution of de-ionised water (800 mL) was heated under stirring using a PTFE thermocouple to regulate heating. At the set temperature, the above procedure was carried out.

A similar method was followed for the preparation of 0.065 wt.% Au-0.065 wt.% Pd/ rutile TiO_2 alternatively using aqueous solutions of $HAuCl_4.xH_2O$ (0.1061 mL, 12.25mg mL^{-1}) and $PdCl_2$ (0.2167 mL, 6 mg mL^{-1}), with TiO_2 (P25 Degussa, 1.997 g) support.

This stabiliser free method was similarly described by Abis and co-workers.[4]

2.4.4 Preparation of Au (20nm) Colloids by Sol Immobilisation

The preparation of *ca.*20 nm Au nanoparticles is described. This method was a modification of the Citrate reduction method described by Wong and co-workers.[5]

Using a 500 mL beaker, 200 mL of deionised water was heated to 90 °C under stirring using a PTFE thermocouple to regulate heating rate. At the set temperature, $HAuCl_4$, solution (804 µL, 62.2 mM) was added under vigorous stirring. A solution of trisodium citrate solution (12 mL, 0.0345 M) was then added and the solution further heated for 30 minutes. During this period, the clear-pale coloured solution darkens to a deep wine colour. Following this, the solution was removed from heating and cooled to 25 °C under moderate stirring. At 25 ˚C, the solution volume was returned to 200 mL by addition of H_2O. Following H_2O, the required quantity of support (P25 Degussa TiO_2, 0.985 g) under vigorous stirring and allowed to form a homogeneous mixture. The solution was then acidified to pH 1 by the drop-wise addition of sulfuric acid (>95%). The mixture was then stirred for 1 h during which the reduced nanoparticles were adsorbed to the support. The suspension was then filtered under vacuum and washed thoroughly with distilled water. The filtered catalyst was then dried in an oven for 16 h at 110°C.

2.4.5 Deposition of Pd in Pd-on-Au Colloids by Sol Immobilisation

Table 2.1: Examples of Pd-on-Au catalyst preparation amounts.

Pd-on-Au Weight Loading	Pd layer	Volume Pd Solution mL	Mass of Support g
5.0	1	0.0818	1.034
10.3	2	0.1685	1.086
15.9	3	0.2602	1.141
21.8	4	0.3570	1.199
28.0	5	0.4592	1.260

The preparation of bimetallic Pd-on-Au nanoparticles are described for the 5 wt.% Pd-on-Au/TiO_2.

Using a 1L beaker, the previously prepared colloidal Au solution was diluted by addition to 450 mL H_2O under vigorous stirring. A freshly prepared solution of ascorbic acid (0.8806 g, 50 mL, 0.1 M) was then added to create a total volume of 700 mL. An aqueous solution of acidified $PdCl_2$ (0.58M HCl, 0.0818 mL, 6 mg mL^{-1}) was then added and the solution

stirred for 30 minutes. Following this period, the required amount of support material was added (P25 Degussa TiO_2, 1.034 g) to create a final metal loading of 1 wt.%. The suspension was then acidified to pH 1 by drop-wise addition of H_2SO_4 and vigorously stirred for 1 h before the suspension was then filtered under vacuum and washed thoroughly with distilled water. The filtered catalyst was then dried in an oven for 16 h at 110°C.

2.4.6 Heat treatment procedures

The dried sample was collected and ground using a mortar and pestle to a produce a uniform and fine powder. The powdered sample (~300mg) was then added to a porcelain combustion boat and loaded into a furnace. The sample was calcined in static air and the temperature raised from 25 °C to 400 °C at 20 °C min^{-1}. The temperature was maintained at 400°C for 3 h, and on completion was allowed to return to 25°C before removal of the catalyst.[2] Alternatively, the samples were heat treated under a reducing atmosphere of 5%H_2/Ar (35ml min^{-1}) at 400 °C for 4 hours with a heating rate of 10 °C min^{-1}.[1]

Investigations requiring higher heat treatment followed a similar procedure however, modifying the set temperature.

2.5 Catalyst Testing

2.5.1 Oxidation of methane using preformed H_2O_2

The oxidation of methane was carried out using a 50 mL Parr stainless steel autoclave reactor. The autoclave was fitted with a removable Teflon liner (35 mL volume). Reactor heating and stirring was controlled by a pre-set programme run using purpose-fitted software associated with the reactor.

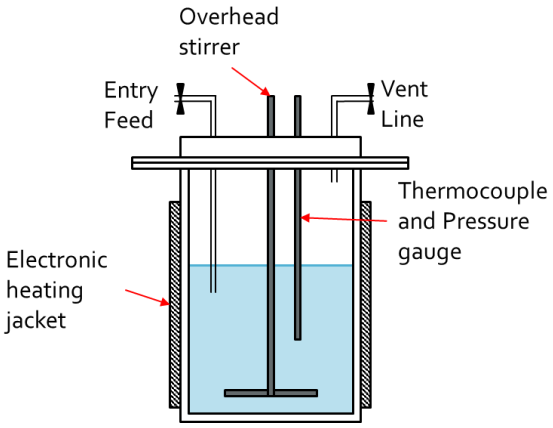

Figure 2.1: Schematic of Parr stainless steel autoclave reactor

Catalytic testing was carried out using a 10 mL reaction mixture comprising an aqueous solution of H_2O_2 (10 mL, 0.5 M, 5000 µmol) and the solid catalyst (10 mg). Prior to use, the reactor was purged with methane to remove residual air from the reactor before being pressurised with methane to 30.5 bar. The autoclave was then heated to the desired reaction temperature (50 °C) using the pre-set programme. At reaction temperature (t= 0 min), the solution was vigorously stirred at 1500 RPM and both heating and stirring were maintained for the required length (typically 30 min, 2.5 °C min^{-1}). Following the reaction, the stirring was stopped and the temperature was reduced to 10 °C using an ice bath to minimise the loss of volatile products. Gaseous samples were removed by extraction into a gas bag for analysis via gas chromatography. The Varian GC was fitted with a methaniser and analysed by flame ionisation detector. The reaction mixture was filtered to remove catalyst particulates and analysed by ^{1}H NMR using a Bruker 500 MHz Ultra-shield NMR spectrometer. All ^{1}H NMR samples were analysed against a calibrated co-axially sealed

insert containing tetramethylsilane (TMS) in deuterated chloroform (99.9 % D). The remaining H_2O_2 was determined by titration of aliquots (0.1 mL) with acidified $Ce(SO_4)_2$ of known concentration using one drop of ferroin indicator (0.025 M).

2.5.2 Decomposition of H_2O_2

$$H_2O_2 + 2Ce(SO_4)_2 \rightarrow Ce_2(SO_4)_3 + H_2SO_4 + O_2 \qquad (equ. 2.1)$$

$$[Fe(o-phen)_3]^{2+} \rightarrow [Fe(o-phen)_3]^{3+} \qquad (equ. 2.2)$$

The decomposition of H_2O_2 was carried out in a 35 mL glass vial. A typical reaction was carried out using 10 mL reaction mixture comprising an aqueous solution of H_2O_2 (10 mL, 0.5 M, 5000 µmol) and a measured amount of solid catalyst (10 mg). At intervals, H_2O_2 concentration was determined by titration of 0.1 mL sample of reaction solution against an acidified $Ce(SO_4)_2$ solution of known concentration (equ. 2.1) using one drop of ferroin indicator (0.025 M, equ. 2.2). The reactions were carried out at room temperature, with stirring maintained at 1000 RPM.

2.5.3 Toluene Oxidation using hexafluorobenzene (HFB)

The oxidation of toluene was carried out using a 50 mL Parr stainless steel autoclave reactor. The autoclave was fitted with a removable glass vessel (35 mL volume). Reactor heating and stirring are controlled by a pre-set programme run using purpose fitted software associated with the reactor.

A typical reaction is carried out using 10 mL reaction mixture comprising hexafluorobenzene (5 mL) and toluene (5mL). A measured quantity of solid catalyst (200mg). Once added into the glass vessel, the reactor is sealed, and the reactor purged with nitrogen to remove residual air from the reactor (40 bar), followed by additional purges using oxygen (10 bar). Finally, the reactor is pressurised with oxygen (10 bar). The autoclave is then heated to the desired reaction temperature (typically 160 °C, 10 °C min^{-}

[1]) using the pre-set programme. At reaction temperature, the solution is vigorously stirred at 1500 rpm and both heating and stirring are maintained for the required length (typically 48 h). Afterwards, stirring is stopped and the reaction temperature reduced to below 10°C using an ice bath to minimise the loss of volatile products. Gaseous samples were removed by extraction into a gas bag for analysis via gas chromatography. Quantification of liquid products were carried out using a Varian GC equipped with methaniser FID and TCD. Products were quantified using an external calibration method utilising 1, 3, 5-trimethyl benzene as the standard.

2.5.4 Oxidation of methane using a hexafluorobenzene-water biphasic system

The oxidation of methane was carried out using a 50mL Parr stainless steel autoclave reactor. The autoclave was fitted with a removable glass vessel (35 mL volume). Reactor heating and stirring are controlled by a pre-set programme run using purpose fitted software associated with the reactor.

A typical reaction is carried out using 15mL reaction mixture comprising an organic solution containing hexafluorobenzene (10mL), a measured quantity of radical initiator (benzoyl peroxide, 250μmol), water (10mL) and a measured quantity of solid catalyst (10mg). Once added into the glass vessel, the reactor is sealed, and the reactor purged with methane to remove residual air from the reactor (40 bar) before being pressurised with methane (30 bar), and oxygen (3.05 bar). The autoclave is then heated to the desired reaction temperature (typically 80 °C, 2.5 °C min^{-1}) using the pre-set programme. At reaction temperature, the solution is vigorously stirred at 1500rpm and both heating and stirring are maintained for the required length (typically 3 hours). Afterwards, stirring is stopped and the reaction temperature reduced to below 10°C using an ice bath to minimise the loss of volatile products. Gaseous samples were removed by extraction into a gas bag for analysis via gas chromatography. The Varian GC was fitted with a methaniser and analysed by flame ionisation detector. The reaction mixture is filtered, then analysed by ^{1}H NMR (oxygenate products) and the remaining benzoyl peroxide determined by HPLC analysis.

All ^{1}H NMR samples are analysed against a calibrated insert containing tetramethylsilane (TMS) in deuterated chloroform (99.9%D).

2.5.6 Methane Oxidation by *In Situ* generated H_2O_2 from H_2 and O_2 using hexafluorobenzene-water biphasic system

The oxidation of methane was carried out using a 50mL Parr stainless steel autoclave reactor. The autoclave was fitted with a removable glass vessel (35 mL volume). Reactor heating and stirring are controlled by a pre-set programme run using purpose fitted software associated with the reactor.

A typical reaction was carried out using 15mL reaction mixture comprised of hexafluorobenzene (10mL, 16.1 g, density: 1.61 g mL^{-1}), H_2O (5 mL) and a measured quantity of solid catalyst (28 mg). Once added, the reactor was sealed, and purged with nitrogen (40 bar). A gaseous mixture comprising of hydrogen (0.5 bar, 0.86%), nitrogen (12.9 bar, 21.55%), methane (45.5 bar, 75.86%) and oxygen (1.1 bar, 1.72%) was prepared. Preparation of gaseous mixtures was facilitated by gas burettes connected to each reactor, using a total pressure of 60 bar. The reactor was then purged three times using the prepared mixture and then pressurised to 30.5 bar.

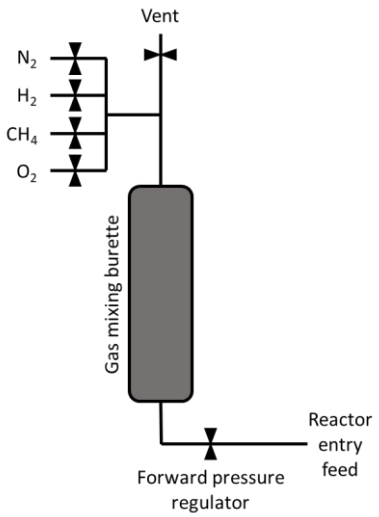

Figure 2.2: Schematic of burette for gas mixing.

The autoclave is then heated to the desired reaction temperature (typically 50°C) using the pre-set programme. At reaction temperature, the solution is vigorously stirred at 1500rpm and both heating and stirring are maintained for the required length (typically 30 mins, 2.5 °C min^{-1}). Afterwards, stirring is stopped and the reaction temperature reduced to below 10°C using an ice bath to minimise the loss of volatile products. Gaseous samples were removed by extraction into a gas bag for analysis via gas chromatography. The Varian GC was fitted with a methaniser and analysed by flame ionisation detector. The reaction mixture was filtered to remove catalyst particulates and analysed by ^{1}H NMR using a Bruker 500 MHz Ultra-shield NMR spectrometer. All ^{1}H NMR samples were analysed against a calibrated co-axially sealed insert containing tetramethylsilane (TMS) in deuterated chloroform (99.9 % D). The remaining H_2O_2 was determined by titration of aliquots (0.1 mL) with acidified $Ce(SO_4)_2$ of known concentration using one drop of ferroin indicator (0.025 M).

2.6 Product analysis

2.6.1 ^{1}H NMR Spectroscopy.

Nuclear magnetic resonance spectroscopy is an important analytical tool which exploits the magnetic properties of certain nuclei. Molecules possess a magnetic moment arising from an uneven number of protons and/or neutrons in the nucleus (e.g. ^{1}H, ^{13}C , ^{15}N). The application of an external magnetic field to these nuclei results in the splitting of the degenerate energy levels due to the alignment of the magnetic moments parallel to (low energy state) or antiparallel to (high energy state) the external field (β_O).[6] The application of electromagnetic frequency, typically radiofrequency, allows the identification of these nuclei by resonating between the two energy states.

The corresponding frequency is the principle of NMR, since, the chemical environment surrounding the nuclei will distinguish it from other nuclei. Consequently, this information can be used to identify molecules in a sample. Furthermore, the intensity of a signal produced via ^{1}H NMR is proportional to the number of protons responsible for the signal

observed. This allows the quantitative analysis of products such as methanol by their corresponding protons.

^{1}H-NMR analysis of the post reaction liquid was achieved using a Bruker 500 MHz Ultra-shield NMR spectrometer. A solvent suppression program was performed during sample analysis to minimise solvent (H_2O) signal intensity. The analyte signals are reported in parts per million relative to the Me_4Si standard (s, δ=0ppm). The oxygenate species typically identified are presented in Table 2.2. An example of a H-ZSM-5 catalysed oxidation of methane using H_2O_2 is provided in Figure 2.1.

Table 2.2: ^{1}H NMR signal assignments for typically observed analytes.[7,8]

Chemical Compound	Chemical Shift / Multiplicity
Tetramethylsilane, Me_4Si	δ 0 ppm, s
Methane, CH_4	δ 0.1 ppm, s
H_2O in $CDCl_3$	δ 1.55 ppm, s
Acetone, $CH_3C(O)CH_3$	δ 2.05 ppm, s
Acetic Acid, CH_3COOH	δ 2.2 ppm, s
Methanol, CH_3OH	δ 3.38 ppm, s
Methyl hydroperoxide, CH_3OOH	δ 3.85 ppm, s
Water, H_2O	δ 4.8 ppm, s
Formaldehyde, CH_2O	δ 5.2 ppm, s
$CHCl_3$ in $CDCl_3$	δ 7.24 ppm, s
Formic Acid, HCOOH	δ 8.4 ppm, s

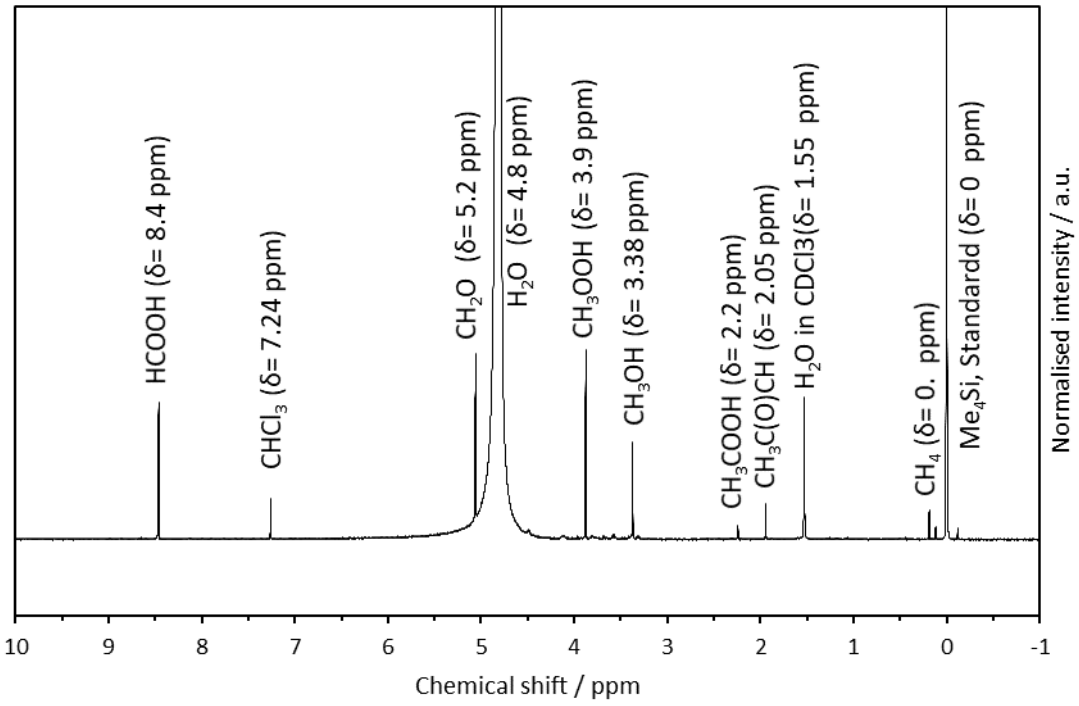

Figure 2.3: ^{1}H NMR spectrum of the post reaction solution of methane oxidation catalysed by commercial H-ZSM-5.

Typical NMR analysis was carried out by adding 0.7mL of filtered solution and 0.1mL D_2O (required for locking) to an NMR tube. An internal standard, consisting of 1%TMS in $CDCl_3$ sealed within a capillary tube, was added to the NMR tube. An example of post reaction ^{1}H NMR analysis is provided in Figure 2.3. The internal standard was calibrated against solutions containing known quantities methanol and formic acid (Figure 2.4).

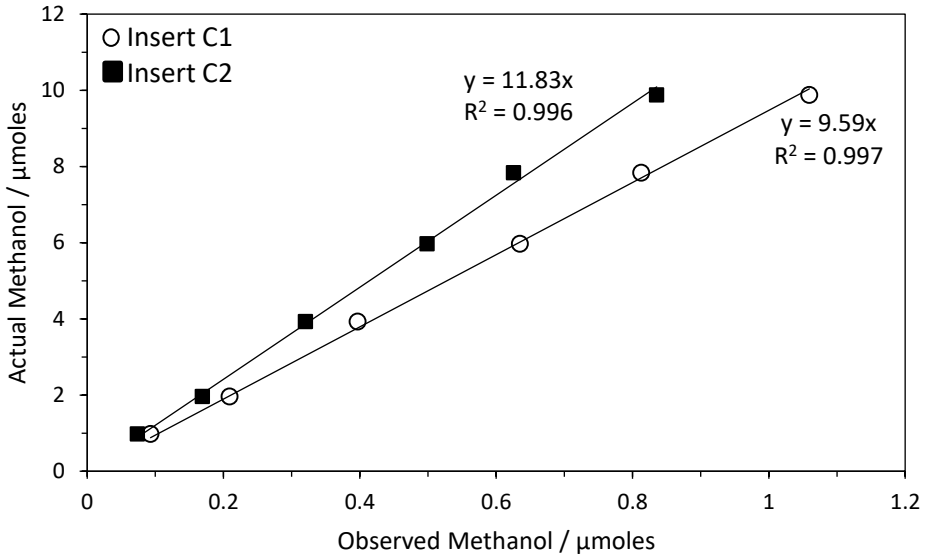

Figure 2.4: An example of calibration factors obtained for methanol standards against the Me_4Si inserts C1 and C2.

2.6.2 Gas Chromatography

Gas chromatography is a separation technique used to analyse complex samples of volatile organic compounds. These volatile samples should remain thermally stable under the temperatures employed for analysis. A sample is introduced by injection into a heated injection port, where liquid samples can be vaporised. The vaporised sample is then carried through the column by an inert carrier gas (typically Helium), also referred to as the mobile phase. The column, acting as the stationary phase, consists of a microlayer of viscous liquid immobilised onto the inert capillary wall.

The interaction of analyte within the mobile phase and the stationary phase creates an exchange-equilibrium (such as dipole-dipole) resulting in the retention of analyte within the column for different lengths of time.[9] Subsequently, constituents of a sample may be separated into individual components and elute with varying retention times. The careful design of heating within the thermo-stated oven, or flow rate allows control of separation and retention to be optimally tuned.

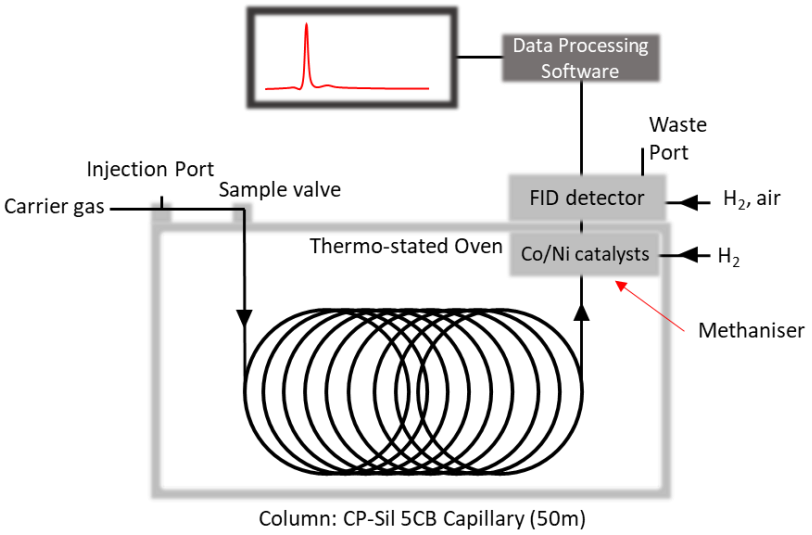

Figure 2.5: Schematic of Varian 450-GC used for analysis of volatile gaseous samples.

The detector used was a flame ionisation detector (FID), where analytes are detected by combustion of the eluting solutes. The analyte passing through the FID flame is subsequently oxidised to yield ions of the parent species, which are detected when passing through two oppositely charged plates. The conductivity of the FID flame is increased during combustion and the resulting ions are collected at the negative electrode. The resulting current is proportional to the concentration of ions detected allowing the quantitative analysis of species. Qualitative identification of the species identity can be achieved by comparison of the products retention time with a commercially available standard.[10]

High oxidation state carbons (such as CO_2 or CO) show minimal or zero detectability by FID analysis. The addition of a methaniser unit, consisting a Ni-Co catalyst, positioned after the separation of analyte by the column resolves this issue. The methaniser, in the presence of H_2, reduces the effluent to lower oxidation state hydrocarbons (such as CH_4) which show increased detectability.

$$CO_2 + 2H_2 \leftrightarrow CH_4 + O_2 \qquad (equ. 2.3)$$

Gas phase products for methane oxidation and liquid phase products for the oxidation of toluene were analysed by GC chromatography using a Varian 450-GC. The Varian 450-GC was fitted with FID and TCD detector. The Varian-GC was equipped with a CP-SiL5CB

column (50nm, 0.33mm Internal diameter) and a methaniser. CO_2 was quantified against a calibration curve produced using commercial standards (Figure 2.6). Liquid phase products for toluene oxidation were dissolved using 5 mL methanol to dissolve solid products, typically obtained after long reaction periods. Products were quantified against an external calibration standard using 1, 3, 5 -trimethyl benzene.

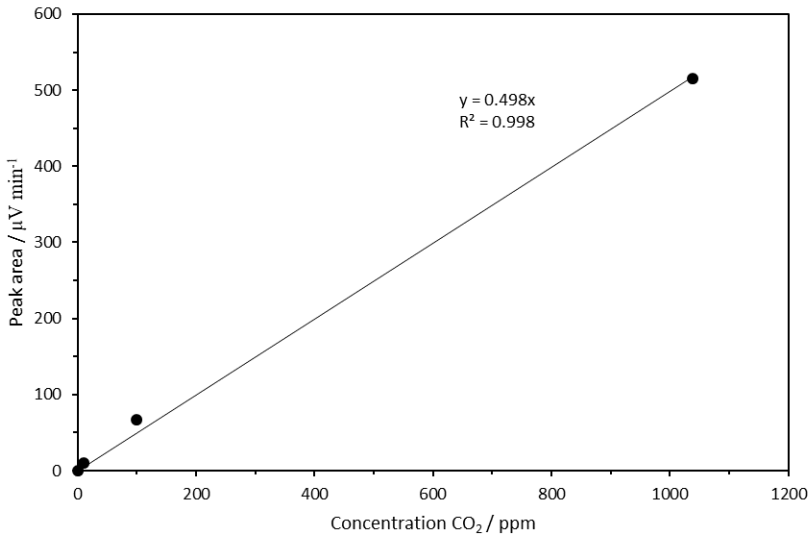

Figure 2.6: Calibration obtained for CO_2 standards (10-1000 ppm) using Varian 450-GC.

2.6.3 High Performance Liquid Chromatography(HPLC)

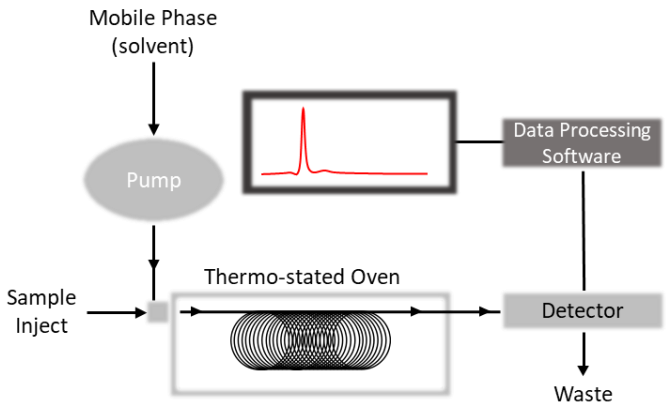

Figure 2.7: Schematic of Agilent 1260 Infinity series HPLC used for analysis of liquid phase samples.

High performance liquid chromatography is a separation technique similar to gas chromatography.For HPLC, the solvent is supplied under higher pressures (ca. 50-400 atm) via a pump, regulating a specified flow rate of the mobile phase. Application of high pressure allows for more densely packed columns (stationary phase) to be used, resulting in enhanced separation and greater resolution of analytes within a sample. Analysis was performed on an Agilent 1260 Infinity series HPLC comprising a quaternary pump, automated sample injector, column oven, diode array detector (DAD) and refractive index detector (RID). Detection via DAD is suitable for compounds capable of UV absorbance.

The HPLC was fitted with a MetaCarb 67h column and phosphoric acid (0.1% H_3PO_4) used as the mobile phase. The following conditions were employed for the analysis: flow rate (mobile phase) = 0.8 ml / min, column temperature = 50 °C, Injection volume = 1 µl. Quantification of benzoyl peroxide was carried out using a calibration curve, produced from known standards.

2.6.4 Titration of H_2O_2

$$H_2O_2 + 2Ce(SO_4)_2 \rightarrow Ce_2(SO_4)_3 + H_2SO_4 + O_2 \qquad (equ.\,2.1)$$

$$[Fe(o-phen)_3]^{2+} \rightarrow [Fe(o-phen)_3]^{3+} \qquad (equ.\,2.2)$$

Post reaction H_2O_2 was quantified by titrating aliquots of filtered reaction mixture against a standardised acidified solution of $Ce(SO_4)_2$. Ferroin (0.025 M) was used as an indicator for reaction described in equation 2.1.

The preparation of $Ce(SO_4)_2$ solution (*ca.* $8x10^{-3}$ M) is as follows:

Solid $Ce(SO_4)_2$ (6g) was added to a solution of concentrated sulfuric acid (32%, 80mL) whilst stirring. The mixture was then added to a 2L volumetric flask and the remaining volume filled with de-ionised water. The resulting solution was stirred until the solid $Ce(SO_4)_2$ was fully dissolved. The $Ce(SO_4)_2$ concentration determined by titration against a known mass of $(NH_4)_2Fe(SO_4)_2.6H_2O$ dissolved completely in 2% H_2SO_4 (v/v).

2.7 Catalyst Characterisation

2.7.1 Brunauer-Emmett-Teller (BET) Isotherm Theory

BET analysis is a method used to determine surface area and pore volume by the adsorption of a gas onto a materials surface. More specifically, BET is a multilayer adsorption theory of an inert gaseous adsorbate onto a surface, typically nitrogen.[11]

BET surface area analysis was performed at -196 °C on a Quantachrome Quadrasorb SI instrument after each sample was evacuated. Surface areas were calculated using Brunauer–Emmet–Teller (BET) theory over the range P/P0 = 0.05-0.2. Gaseous adsorbates are removed from dry solid sample by gentle heating (120 °C) under a vacuum for 1 hour. The sample is then cooled to 77K (196.15 °C), by liquid nitrogen. The gaseous adsorbate (typically N_2) is introduced and the relationship between quantity of adsorbed gas and adsorbate pressure, termed adsorption isotherm, is used to determine the sample surface area.[12]

$$\frac{P}{v(P_0 - P)} = \frac{1}{v_m . C} + \frac{C - 1}{v_m . C}\frac{P}{P_0} \qquad (equ. 2.4)$$

BET adsorption isotherm where; P: equilibrium pressure of adsorbate, P_0: saturation pressure of adsorbate, v: volume of adsorbed gas, v_m: volume required to form monolayer coverage, C: BET constant

Subsequently, a plot of $\frac{P}{v(P_0-P)}$ against P/P_0 produces a linear relationship with intercept $\frac{1}{v_m C}$. The volume of gas, given as v_m, is the volume required to form a complete uni-molecular layer of adsorbate. When multiplied by the cross-sectional surface area of the adsorbate gas allows the calculation of surface area(equ. 2.5 and 2.6).

$$S_{total} = \frac{v_m . N . s}{V} \qquad (equ. 2.5)$$

$$S_{BET} = \frac{S_{total}}{M_c} \qquad (equ. 2.6)$$

S_{total}: total surface area, S_{BET}: specific surface area, N: Avogadro's constant (6.022×10^{23}), S: adsorption cross section of adsorbate gas, V: molar volume, M_c: Mass of solid sample

2.7.3 Microwave Plasma Atomic Emission Spectroscopy (MP-AES)

Atomic emission spectroscopy (AES) is a chemical analysis technique utilising the intensity of emitted light from a plasma, flame, arc or spark.[13] Microwave plasma -AES utilises microwave radiation to produce a nitrogen-based plasma (5000 K) within a quartz torch. Atomised samples, via a nebuliser, are passed through the plasma resulting in the promotion of electrons to the excited state. The relaxation of an excited electron to its ground state results in an emission of light characteristic of the parent atom. Subsequently, this signature wavelength produced during emission is used to determine the species identity and the intensity utilised for quantification.[13]

MP-AES analysis was carried out using an Agilent MP-AES 4100 spectrometer. The digested samples were analysed for Au and Pd using multiple wavelength calibrations. Sample preparation was as follows:

Standard Acid Digestion

Solid catalyst sample (50mg) was acid digested for 72 h using freshly prepared *aqua regia* (7mL, 1mL HCl (70%): 6mL HNO_3 (35%)) in a 50 mL volumetric flask. Following digestion, the samples were diluted by addition of deionised H_2O to a total volume of 50 mL. Prior to analysis, the sample solution was filtered using PTFE syringe filters (0.45 µm).

Microwave Assisted Acid Digestion

Solid catalyst sample (50mg) was acid digested for 72 h using freshly prepared *aqua regia* (7mL, 1mL HCl (70%): 6mL HNO_3 (35%)) in a 50 mL volumetric flask.

2.7.4 Transmission Electron Microscopy (TEM)

Electron Microscopy utilises the wavelength of electrons to image samples. Wavelengths of electrons are sufficiently small (<1Å) that the resolution obtained allows the imaging of nanoparticles. This resolution is markedly improved over conventional optical microscopy due to the shorter wavelength used. [14]

Consequently, electron microscopy can be used to determine particle size, orientation and morphology. In addition, consideration of the resulting interaction of an incident electron with the sample can also be used to discern compositional and structural information, such as via emitted X-rays. Figure 2.7.[14] illustrates the interaction of the incident electron beam with sample, leading to the formation of several detectable signals. Therefore, the electron microscopy used is dependent upon the signal being analysed.[15]

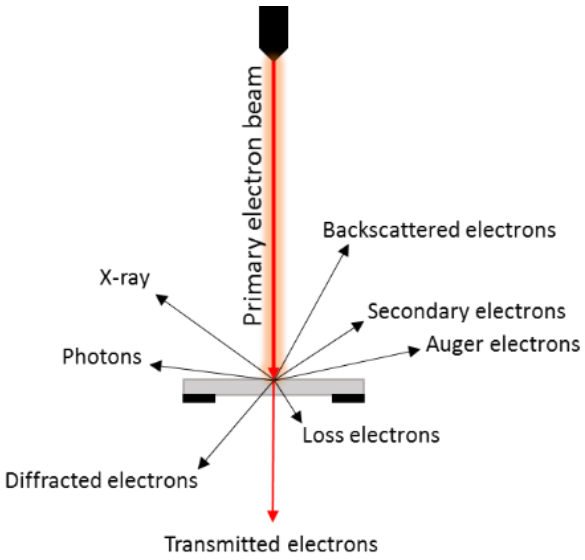

Figure 2.7: Interaction of incident electron beam with sample during transmission electron microscopy.

Transmission electron microscopy (TEM), most commonly used for the characterisation of supported metal particles utilises transmitted electrons to produce a two-dimensional projection of the sample. The projection is magnified by an objective lens to produce a

bright field image. The use of diffracted electron to collect images are referred to as dark field images.[14,15]

Alternatively, scanning electron microscopy (SEM) is performed by rastering a narrow electron beam over a sample surface. The resulting secondary and backscattered electron are detected and the intensity as a function of incident beam position used to map images of a sample surface.[15] Changes in contrast result from the variation of the sample surface orientation, with surfaces facing the detector appearing brighter. Secondary electrons, consist of low energy electrons which originate from the surface and describe the surface region. High energy backscattered electrons originate from deeper within the sample and carry more detailed information on the sample, such as sample composition. As such more efficient scatterers, such as heavy elements, appear brighter than their lighter counterparts.

Transmission electron microscopy (TEM) and scanning transmission electron microscopy (STEM) were performed on a JEOL JEM-2100 operating at 200 kV. Energy dispersive X-ray analysis (EDX) was done using an Oxford Instruments X-Maxn 80 detector and the data analysed using the Aztec software. samples were prepared by dispersion in ethanol by sonication and deposited on 300 mesh copper grids coated with holey carbon film.

2.7.5 Energy Dispersive X-ray Analysis (EDX)

Energy dispersive X-ray analysis is quantitative analytical tool utilising the X-ray emission of a sample during analysis by an incident beam (Figure 2.7). During analysis, the excitation of inner electron by the incident beam creates an electron hole after ejection. Relaxation of a higher energy valence electron to this lower energy orbital is followed by the emission of energy corresponding to the difference. The resulting energy of the X-ray emission are measured by an EDX spectrophotometer and are characteristic of the emitting element. As such, EDX provides information upon the sample composition.[15]

Energy dispersive X-ray analysis (EDX) was performed on a Tescan Maia3 field emission gun scanning electron microscope (FEG-SEM) fitted with an Oxford Instruments XMAXN

80 Images were acquired using the secondary electron and backscattered electron detectors. Samples were dispersed as a powder onto adhesive carbon Leit discs mounted onto aluminium stubs.

2.7.6 X-ray Powder diffraction (pXRD)

X-ray diffraction is atechnique primarily used to obtain information on the bulk crystallographic phase of a sample. However, in X-ray powder diffraction the pattern is achieved by using a powder sample rather than an individual crystal. Subsequently, the incident beam is moved around the sample to produce the diffraction pattern of the variously orientated crystals.[11]

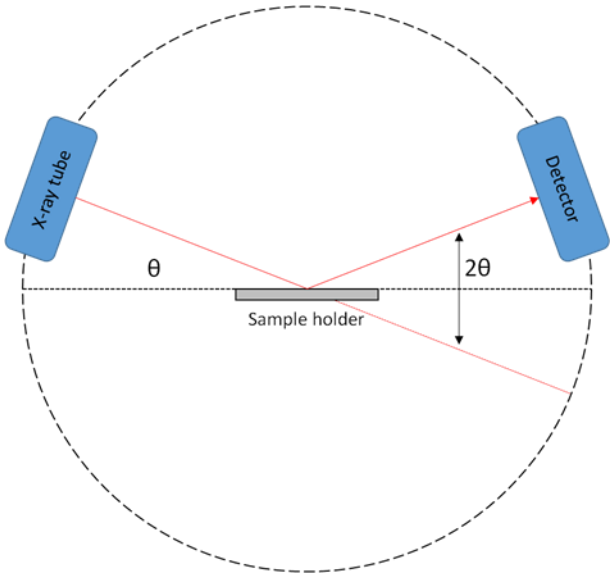

Figure 2.8: Schematic representation of an X-ray diffraction system.

X-ray electromagnetic radiation is a high energy radiation (wavelengths of order 10^{-10}m) with sufficient energy to penetrate and probe solid structures. The X-ray radiation is generated by directing high energy electrons from a heated filament towards a metal target (contained) within a cathode ray tube/xray tube. The resulting x-ray photons produced are a continuous range of wavelengths called Bremsstrahlung.

For x-ray diffraction studies to be achieved, two requirements must be met: (i) the wavelength of the incident radiation must be of the same order of magnitude as the periodic spacing's in the lattice and (ii) that the incident radiation is monochromatic. The implementation of a copper metal target to produce the bremsstrahlung continuum is filtered by a nickel filter resulting in the monochromatic Cu Kα at λ=1.51 Å.[11]

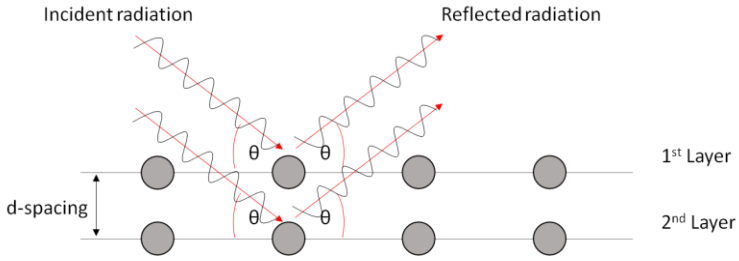

Figure 2.9: Schematic representation of X-ray diffraction.

Irradiation of a crystalline sample with monochromatic x-ray radiation produces scattering of the incident radiation. A diffraction pattern is produced when the radiation reflected interacts constructively, resulting in a single wavelength.[11] During this constructive interaction of diffracted radiation the path length difference is an integer value of the wavelength, as described by Bragg's equation (equ. 2.6).

$$n\lambda = 2d\ sin\theta \qquad (equ. 2.6)$$

n: integer value, λ: wavelength of incident radiation, d; d spacing of crystal lattice, θ: angle of incident radiation.

During pXRD, the angle of incident radiation is monitored as the detector is rotated around the sample in a plane containing the incident ray. Additionally, rotation of sample during analysis increases the contribution of the various orientations towards the constructive interference.

Finally, comparison of the diffraction pattern on a large data-bank allows the identification of crystalline phases present. Figure provides an illustrative pXRD for TiO_2 (P25).

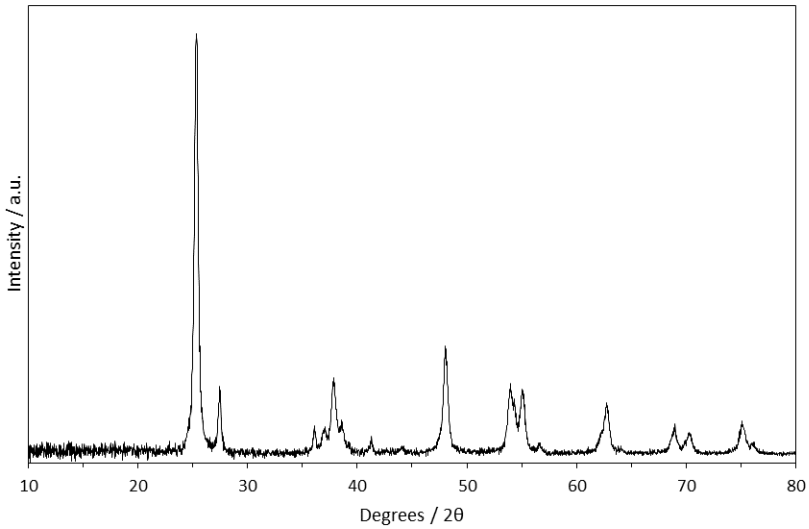

Figure 2.10: Powder X-ray diffraction pattern of commercially available TiO_2 (P25) obtained from Degussa.

Powder X-ray Diffraction (XRD) patterns were collected using a PANalytical X'PertPRO X-ray diffractometer, with Cu K_α radiation source (λ=0.154 nm) with Ni filter at ambient conditions. Samples were recorded between 15-20° at 40 kV and 40 mA with step sizes of 0.0167°.

2.7.7 X-ray Photoelectron Spectroscopy (XPS)

This surface sensitive (1-10nm) spectroscopic method is based upon the photoelectric effect. XPS provides characterisation of the elemental composition of a samples surface along with the oxidation states of the elements present. Analysis is achieved by irradiating the sample with monochromatic radiation sufficient in energy (X-ray) to expel electrons (Valence or core) from the atom of an element.[11] The emission of a photoelectron is discrete and characteristic to the parent element via its binding energy. Subsequently, the specific binding energy (E_b) of the photoelectron may be determined by measuring the kinetic energy of the emitted electron (equ. 2.7).[10]

$$E_k = h\nu - E_b - \phi \qquad (equ. 2.7)$$

Where; E_k: kinetic energy, h: Planck's constant (6.626 x10^{-34} m^2 kg s^{-1}), v: frequency of incident radiation, E_b: binding energy of electron, ϕ: XPS constant describing spectrometer's work function.

X-ray photoelectron spectroscopy (XPS) was performed using a Kratos Axis Ultra DLD spectrometer, using monochromatic Al $K\alpha$ X-ray source operating at 120 W. Data was collected with pass energies of 160 eV for survey spectra, and 40 eV for higher resolution scans. The system was operated in the Hybrid mode, using a combination of magnetic immersion and electrostatic lenses and acquired over an area approximately 300 × 700 μm^2. A magnetically confined charge compensation system was used to minimize charging of the sample surface, and all spectra were taken with a 90 ° take of angle. A base pressure of ~ 1×10^{-9} Torr was maintained during collection of the spectra.

2.8 References

1 M. Sankar, Q. He, M. Morad, J. Pritchard, S. J. Freakley, J. K. Edwards, S. H. Taylor, D. J. Morgan, A. F. Carley, D. W. Knight, C. J. Kiely and G. J. Hutchings, *ACS Nano*, 2012, **6**, 6600–6613.

2 J. K. Edwards, B. E. Solsona, P. Landon, A. F. Carley, A. Herzing, C. J. Kiely and G. J. Hutchings, *J. Catal.*, 2005, **236**, 69–79.

3 L. Kesavan, R. Tiruvalam, M. H. A. Rahim, M. I. bin Saiman, D. I. Enache, R. L. Jenkins, N. Dimitratos, J. A. Lopez-Sanchez, S. H. Taylor, D. W. Knight, C. J. Kiely and G. J. Hutchings, *Science* , 2011, **331**, 195–199.

4 L. Abis, S. J. Freakley, G. Dodekatos, D. J. Morgan, M. Sankar, N. Dimitratos, Q. He, C. J. Kiely and G. J. Hutchings, *ChemCatChem*, 2017, **15**, 2914–2918.

5 M. O. Nutt, J. B. Hughes and M. S. Wong, *Environ. Sci. Technol.*, 2005, **39**, 1346–1353.

6 P. J. Hore, *Nuclear magnetic resonance*, Oxford University Press, Oxford ; New York, 1995.

7 R. McVicker, N. Agarwal, S. J. Freakley, Q. He, S. Althahban, S. H. Taylor, C. J. Kiely and G. J. Hutchings, *Catal. Today*, 2018,, https://doi.org/10.1016/j.cattod.2018.12.017.

8 C. Williams* and S. H. T. and G. J. H. , James Carter, Ying Kit Chow, Nicholas F. Dummer, David J. Morgan, Sara Yacob, David J. Willock, Randall J. Meyer, .

9 D. A. Skoog, D. M. West, F. J. Holler and S. R. Crouch, *Analytical Chemistry: An Introduction*, Saunders College Pub., 7th Edn., 2000.

10 D. Kealey, *Instant Notes: Analytical Chemistry*, BIOS Scientific Publishers Ltd, 1st Edn., 2002.

11 P. Atkins and J. De Paula, *Atkins' physical chemistry*, Oxford University Press, 2009.

12 G. Leofanti, M. Padovan, G. Tozzola and B. Venturelli, *Catal. Today*, 1998, **41**, 207–219.

13 D. A. Skoog, F. J. Holler and S. R. Crouch, *Principles of Instrumental Analysis*, 2007.

14 P. J. Goodhew, J. Humphreys and R. Beanland, *Electron Microscopy and Analysis*, 2001, 30.

15 J. W. Niemantsverdriet, *Spectroscopy in Catalysis: An Introduction: Third Edition*, WILEY-VCH Verlag, 3rd Edn., 2007.

Chapter 3: Selective oxidation of methane to methanol using supported Au-Pd catalysts prepared by stabiliser-free sol-immobilisation

3.1 Introduction

The activation of C-H bonds has been a subject extensively studied in recent decades, with huge scientific interest in their application for methane (CH_4) upgrading. Initiated by Fenton[1], recent developments were made after the application of chloroplatinic acid salts some time later by Shilov *et al.*[2,3]

Similarly, the catalytic application of gold as a selective oxidation catalyst has increased drastically after the seminal studies by Haruta *et al.*[4] in 1987. Here, the importance of preparative method was highlighted for generating highly active catalysts. The formation of predominantly nanoparticle gold (<5 nm) produced significant activity for CO oxidation, operating at very low temperatures (0 °C). Since this discovery, gold (Au) has found application in a wide array of important reactions; the epoxidation of alkenes[5,6], the oxidation of alcohols[7,8] and olefins[9] and the direct synthesis of hydrogen peroxide (H_2O_2).[10]

Despite the high activity demonstrated by monometallic Au catalysts, several methods to improve their activity have been used. One method often used is the addition of a secondary metal, such as palladium (Pd). In the case of AuPd, the addition of a second metal sees important improvements in catalyst activity. During the direct synthesis of hydrogen peroxide (H_2O_2), the productivity and selectivity is enhanced for both TiO_2 and carbon supported AuPd compared with the monometallic counterparts.[11] For TiO_2-supported AuPd, the two fold increase in productivity to 64 $moles_{H2O2}$ kg_{cat}^{-1} h^{-1} also sees a three-fold improvement in H_2O_2 selectivity (70%). The oxidation of benzyl alcohol reported by Corma and co-workers[8] for Au-only catalyst demonstrated highly effective under solvent-free conditions. Additionally, utilising O_2 as the oxidant, the activity observed was produced after careful preparation of the gold- nanoparticles supported on ceria (CeO_2). Alternatively, the preparation of AuPd alloyed particles by impregnation

produced a catalyst with an improved activity by a factor *ca.* 27, with high selectivity towards benzaldehyde (>95%).[12]

The oxidation of toluene was previously reported by Kesavan *et al.*[13] Here, C-H bonds present in the methyl group of toluene were selectively oxidised to benzyl benzoate in the absence of solvent over TiO_2- and carbon- supported AuPd catalysts using O_2. Demonstrating high selectivity towards benzyl benzoate in both cases (*ca.* 80%), carbon – supported AuPd showed higher conversion of toluene at 120 °C (10.6%) compared to TiO_2 (4.0%). Increasing reaction temperature to 160 °C raised toluene conversion. Achieving 50% and 24% conversion for carbon- and TiO_2- supported AuPd respectively, benzyl benzoate selectivity was simultaneously increased to >94%. The disparity observed in catalytic activity between TiO_2 and carbon supports resulted from the differences in AuPd morphologies due to support-metal interactions.

The direct oxidation of CH_4 using O_2, however, has proven a significant challenge for bimetallic AuPd catalysts. The use of H_2O_2 has found an important alternative to industrial oxidants such as sodium hypochlorite (NaClO), permanganate ($[MnO_4]^-$) or chromates ($[CrO_2]^-$).[14] Considered attractive as a green oxidant because of the production of H_2O only as a by-product of its use. Its application for green oxidation was notably made by Tarassamo and co-workers[15] when combined with a titanium silicate (TS-1) catalyst. Importantly, TS-1 demonstrated the direct ammoxidation of cyclohexanone to its oxime, a route for caprolactam synthesis and a method of producing an important industrial feedstock for Nylon 6 production.

Alternatively, the use of hydroperoxy- species for CH_4 oxidation has been reported by several groups.[16–18] Ab Rahim and co-workers[19,20] have reported the investigation of TiO_2-supported AuPd catalysts using H_2O_2. The aqueous application of H_2O_2 produces an attractive environmentally benign alternative to traditional routes, employing harsh reaction conditions such as acidic media.[2,3,21,22] The AuPd catalysts, prepared by wet impregnation, showed moderate activity for the one step oxidation of CH_4 to methanol (CH_3OH) under mild reaction temperatures (50 °C). Prepared by impregnation of the chloride precursors onto the support, this method produces a broad range of AuPd particle sizes with poor control of speciation. The catalysts produced comprised of alloyed AuPd nanoparticles ranging from 5-20 nm in size with larger Au rich nanoparticles (100-200 nm) also observed.[14,19] Evidence of poor metal dispersion was reflected in the identification of sub-nm AuPd particles and Pd clusters. Even so, Table 3.1 illustrates the moderate activity observed for selective oxidation of CH_4 to CH_3OH by the AuPd/TiO_2 catalysts presented by Ab Rahim and co-workers[19].

Table 3.1: Catalytic activity of bimetallic AuPd catalysts prepared by incipient wetness. Data previously published by Ab Rahim.[19,20]

Catalyst	Products [μmol]				Oxy. Sel. [%]	TOF [h^{-1}]	H_2O_2 Rem. [%]
	CH_3OH	HCOOH	CH_3OOH	CO_2			
0.5wt.%Au-0.5wt.%Pd/TiO_2	0.30	0	1.82	0.36	85.4	6.85	57.9
2.5wt.%Au-2.5wt.%Pd/TiO_2	1.89	0	1.57	0.37	90.3	0.77	7.7
2.5wt.%Au-2.5wt.%Pd/C	0.63	0	0	1.55	28.9	0.44	1.7

Standard reaction conditions: time: 30 minutes, temperature: 50 °C, P_{CH_4}: 30.5 bar, stirring rate: 1500 rpm, volume: 10 mL of H_2O.[H_2O_2]: 0.5 M, all 1 wt. % catalyst: 7.24×10^{-7} moles metal equal to 10 mg of solid catalyst, all 5 wt. % catalyst: 1.0×10^{-5} moles of metal equal to 28 mg solid catalyst, Oxy. Sel.: Oxygenate selectivity, Rem.: Remaining, TOF: Turn-over frequency.

Initial investigations using 1 wt.% AuPd/TiO_2 demonstrated high selectivity towards methyl hydroperoxide (73%, CH_3OOH), an intermediate in the formation of CH_3OH (Table 3.1, entry 1). Low selectivity to CH_3OH (12%), argued to be due to low metal loading, was increased to 49% when total metal loading was raised to 5 wt.% AuPd/TiO_2, with similar oxygenate selectivity achieved. Yet, the increase in metal loading yielded a significant increase in the decomposition of H_2O_2, with *ca.* 8% remaining post reaction (Entry 2). Subsequently, this augmentation in H_2O_2 decomposition resulted in a decrease in overall productivity, proving deleterious for the oxidation of CH_4. Despite this, the systematic studies by Ab Rahim *et al.*[20] showed TiO_2-supported AuPd (5 wt.%) to produce the highest CH_3OH and oxygenate selectivity of supports investigated, including carbon.

Recently, significant improvements in productivity and selectivity were achieved by Agarwal *et al.*[23] using unsupported AuPd nanoparticles. Preparation of colloidal AuPd using poly-(vinyl pyrrolidine) produced catalysts which exhibited high oxygenate productivity (29.4 mol kg_{cat}^{-1} h^{-1}) and TOF (5.09 h^{-1}) with preformed H_2O_2. The introduction of gaseous O_2 increased catalyst activity further with TOF of 8.58 h^{-1} (productivity: 53.6 mol kg_{cat}^{-1} h^{-1}), achieving up to 70% $^{18}O_2$ incorporation into CH_3OH produced during labelled experiments. Critically, the significant reduction in the rate of H_2O_2 decomposition was achieved by eliminating the metal-support interaction. The resulting excellent productivity was therefore attributed to the controlled H_2O_2 breakdown, affording lower H_2O_2 concentrations to be used during testing.

Contrasting this work, considerable activity was reported by Hammond and co-workers[24] utilising Fe-ZSM5 under identically mild, aqueous conditions with H_2O_2 as terminal oxidant. Inspired by methane mono-oxygenase, the enzyme commonly found in methanotrophs is capable of one step oxidation of methane to methanol under mild conditions.[25] The Fe- and Cu- promoted Fe-ZSM-5 catalysts demonstrated significant activity, reporting high turnover frequencies (TOFs) of >2200 h^{-1} for CH_4 oxidation with CH_3OH selectivity above 80%.[18]

However, although exhibiting lower overall activity for oxygenate formation, CH_3OH selectivity and TOF to the ZSM-5 catalysts, AuPd catalysts remain an attractive approach. Capable of the direct synthesis of H_2O_2 from H_2 and O_2 using AuPd, the application of Fe or Cu doped zeolite materials instead produce efficient Fenton-type catalysts with poor activity H_2O_2 synthesis.[26–29] Industrially, therefore, the potential in-situ generation H_2O_2 removes the cost and environmental impact associated with the indirect synthesis of H_2O_2 via the anthraquinone oxidation process.[30]

The generation of H_2O_2 from H_2 and O_2 *in situ* by AuPd/TiO_2catalysts was applied by Ab Rahim[19] *et al.* to oxidise CH_4 to CH_3OH. Industrially, *in situ* generation of H_2O_2 provides a more desirable approach to the required preformed H_2O_2 when using MFI-zeolite catalysts such as ZSM-5. Comparison against reactions utilising preformed H_2O_2, the *in-situ* approach by 5wt.% AuPd/TiO_2 catalysts showed lower productivity (0.50 mol kg_{cat}^{-1} h^{-1}). However, CH_3OH selectivity was improved (68% vs 49%) and H_2O_2 reactivity yielded a 3-fold improvement compared with similar quantities of preformed H_2O_2.

In this chapter, the role of particle size is investigated for AuPd/TiO_2 materials adopting sol immobilisation as the preferred methodology for catalyst preparation. In contrast to the wet impregnation technique used by Ab Rahim, sol immobilisation (S_i) provides a method to control particle size, distribution, composition and morphology.[31,32] Control of these variables has allowed catalyst activity or product selectivity to be more easily tuned for several reactions, including hydrogenation of furfural[33] or benzyl alcohol oxidation[34].The formation of AuPd catalysts with a narrow size distribution, by S_i, then allows further manipulation of particle size to evaluate their influence for the selective oxidation of methane. Notably, the relationship between efficient H_2O_2 utilisation and methanol productivity is considered through manipulation of particle size.

3.2 The Role of AuPd Particle Size

The effect of supported AuPd particle size was evaluated for the selective oxidation of methane to methanol by preparation of a series of 1 wt.% AuPd/TiO_2 (P25). The series was produced using sol immobilisation (S_i), a method which uses polymer stabilisers to produce nanoparticles with a narrow distribution of particle sizes.[35,36] It was shown by Abis and co-workers[36] that using a stabiliser-free sol-immobilisation (SF-S_i) methodology produced nanoparticles with no significant variation in particle morphology, but the absence of polymer additive did result in a marginal increase in mean particle size when compared against conventionally used polymer additives.

Additionally, the absence of polymer additives then allowed further manipulation of particle size via post synthesis heat treatment. Heat treatments at 400, 600 and 800 °C

were used to induce sintering and thereby increase the particle size. Typical testing conditions for CH_4 oxidation reactions were carried out at 50 °C in an aqueous solution of H_2O_2 (0.5M, 10mL) using an autoclave reactor. The mass of catalyst used remained fixed at 10 mg, and the reactor pressurised to 30.5 bar CH_4. During testing, stirring speed was maintained at 1500 rpm from the initiation of heating to the end of reaction period (30 mins). Unless specified, these conditions were used for all reactions.

Liquid phase products such as methyl hydroperoxide (CH_3OOH), methanol (CH_3OH) or formic acid (HCOOH) were analysed via ^1H NMR and quantified against an internal standard consisting 1% trimethylsilane in $CDCl_3$. Remaining H_2O_2 was determined by titration against standardised acidified solution of $Ce(SO_4)_2$, using a Ferroin indicator (0.025M). Gaseous products, such as CO_2, were analysed by gas chromatography fitted with FID detector. Products were quantified using a CO_2 calibration curve.

Preliminary Testing

Prior to catalyst testing, control reactions were carried out in the absence of catalyst or using TiO_2 (P25) support only (Table 3.2). Illustrating background contributions, the absence of catalysts shows activity resulting from the Parr Autoclave under standard reaction conditions.

Table 3.2: Determination of background reaction contributions during testing for methane oxidation without catalyst.[a]

Entry	Catalyst	Products [μmol]				Total Productivity[a]	H_2O_2 Remaining[b]
		CH_3OH	HCOOH	CH_3OOH	CO_2	[mol $kg_{(cat)}^{-1}$ h^{-1}]	[%]
1	Blank	0	0	0	0.24	0	97.6
2[c]	Blank	0	0	0	0.27	0	95.7
3	TiO_2	0	0	0	0.14	0.028	94

[a] Total productivity calculated as $moles_{total\ products}/weight_{catalyst}\ /time$). [b] Calculated as $(\mu moles_{final}/\mu moles_{initial})x100$. [c] CH_4 substituted for N_2, $P(N_2)$: 30.5 bar.

Initial inspection of background reactivity shows no formation of selective oxygenates, however, detection of CO_2 is observed (0.24 μmol). Importantly, the low decomposition of H_2O_2, determined post reaction via titration, suggests that the detected CO_2 is adventitious in origin. The substitution of CH_4 for N_2 was evaluated to confirm the adventitious source of CO_2, with entry 2 showing a similar quantity of CO_2 detected. Likewise, the observed H_2O_2 decomposition (*ca.* 4.3%) originates from thermal decomposition during the initial heating stages. Similarly, introduction of bare TiO_2 P25 support also sees no further contribution beyond the background decomposition of H_2O_2 (*ca.* 6%) or detected CO_2 (0.14 μmoles).

3.2.1 The Effect of Catalyst Heat Treatment on Methane Oxidation

Testing and comparison of as-prepared catalyst

Table 3.3: Comparison of the catalytic activity of 1 wt.% AuPd/TiO_2 prepared by sol immobilisation.

Entry	Stabi-lising agent	Init. H_2O_2	Products [µmoles]				Oxy. Sel.[a] [%]	Tot. Prod.[b] [mol kg_{cat}^{-1} h^{-1}]	H_2O_2 rem.[c] [%]
			CH_3OH	HCOOH	CH_3OOH	CO_2			
1[d]	SF	5000	0	0	0	0.3	0	0.05	<1%
2[19][e]	PVA	5000	0.6	0	0	0.4	59.4	0.10	<1%
3[23][f]	PVP	1000	0.4	0	0	1.2	26	0.32	23

[a] Oxy.Sel.: Oxygenate selectivity. Calculated as $(\mu moles_{oxygenates}/\mu moles_{total\ products})x100$. [b] Total productivity calculated as $moles_{total\ products}/weight_{catalyst}\ /time$.[c] Calculated as $(\mu moles_{final}/\mu moles_{initial})x100$. [d] This work, 1wt.% AuPd/TiO_2 prepared by stabiliser-free sol immobilisation. [e] Reported by Ab Rahim *et al.*[19], 1wt.%AuPd/TiO_2 prepared by sol-immobilisation using poly-(vinyl alcohol). [f] reported by Agarwal *et al.*[23], 1wt.%AuPd/TiO_2 prepared by sol-immobilisation using poly-vinyl pyrrolidone.

Screening of the 1 wt.% AuPd/TiO_2 (P25, SF-S_i) for CH_4 oxidation began by comparing the parent dried only catalyst with previously published data by Ab Rahim.[19] Showing almost complete decomposition of H_2O_2, the dried-only 1 wt.% AuPd/TiO_2 catalyst produced no selective oxygenates. In contrast, Hasbi et al[19] (Table 3.3, entry 2) using poly-(vinyl alcohol) (PVA) stabilised AuPd catalyst showed the formation of CH_3OH, but, with poor oxygenate productivity (0.10 mol kg_{cat}^{-1} h^{-1}). Despite this poor activity, CH_4 oxidation to CH_3OH was achieved with 60% selectivity. This result was similarly reported by Agarwal *et al.*[23], but, a lower productivity and CH_3OH selectivity was observed (0.03 mol kg_{cat}^{-1} h^{-1}, 26%). In both examples near complete consumption of H_2O_2 was reported. The high decomposition of H_2O_2 exhibited were proposed to originate from small AuPd nanoparticle size produced by the sol immobilisation method.[37,38]

To evidence this, the mean particle size of AuPd nanoparticles produced using stabiliser free sol-immobilisation (SF-S_i) method was determined by transmission electron microscopy (TEM) analysis. Representative images are illustrated in Figure 3.1, and mean particle size determined from approximately 250 nanoparticles. Inspection of the dried only catalyst (Figure 3.1a) shows a particle size distribution ranging 2-10 nm, sharing a similar profile with previously published stabiliser free AuPd/TiO_2 catalyst.[36]

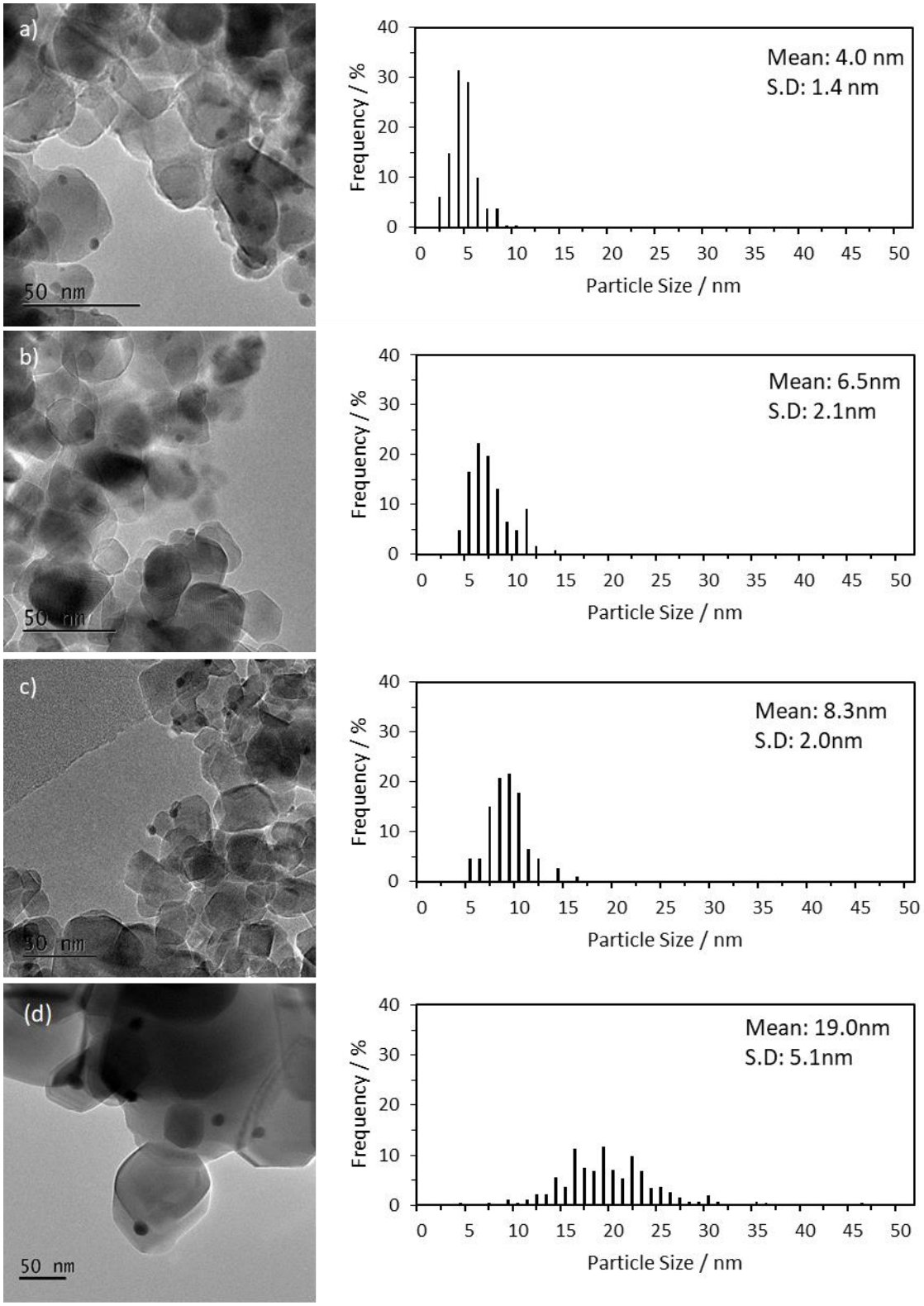

Figure 3.1: Transmission electron microscopy of 1 wt. % AuPd/ TiO_2 (S_i) prepared at room temperature; (a) Dried, (b) calcined at 400 ˚C, (c) 600 ˚C and (d) 800 ˚C.

Testing of heat-treated catalyst

Producing nanoparticles of small size (*ca.* 4.0 nm ±1.4), the preparation of stabiliser free 1wt.% AuPd/TiO_2 resulted in poor activity for the oxidation of CH_4 to CH_3OH. Additionally, the post reaction analysis by gas chromatography shows the detection of CO_2 in comparable quantities to preliminary testing of supports only. In contrast, the preparation of a broad range of nanoparticle sizes (*ca.* 5-20nm) by impregnation, as reported by Ab Rahim[19], demonstrated considerably better activity. Therefore, to investigate the relationship between AuPd particle size and selective oxygenate formation, heat treatment of 400 °C, 600 °C and 800 °C were used to promote nanoparticle growth. The resulting effect of post synthesis heat treatment to 1wt.% AuPd/TiO_2 (S_i) for CH_4 oxidation is presented in Figure 3.2.

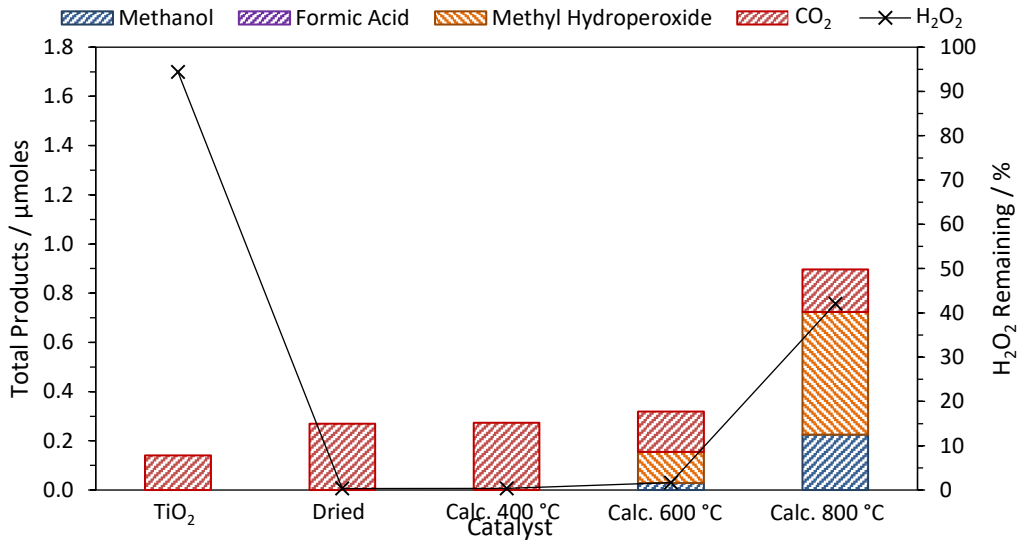

Figure 3.2: Comparison of the effect of post synthesis heat treatment on 1 wt. % AuPd/TiO_2 prepared at room temperature on the catalytic activity for methane oxidation.

Standard reaction conditions: time: 30 minutes, temperature: 50 °C, P_{CH_4}: 30.5 bar, stirring rate: 1500 rpm, all catalysts (1 wt. % total): 7.24×10^{-7} mol of metals equal to 10 mg of solid catalysts, volume: 10 mL of H_2O.[H_2O_2]: 0.5 M

Heat treatment at 400 °C yielded a marginal increase in mean particle size in comparison to the dried only, increasing from 4.0 nm to 6.5 nm (Figures 3.1(a) and 3.1(b)). Despite this growth in particle size, the activity observed mirrors the dried only catalyst with almost complete decomposition of H_2O_2 and no selective oxygenate formation. This high activity towards H_2O_2 decomposition by the dried-only and catalysts heat treated at 400 °C is typical of materials possessing small particle sizes.[39] Consequently, the high activity towards H_2O_2 decomposition results in the low productivity for CH_4 oxidation observed (0.054 mol kg_{cat}^{-1} h^{-1}).

Raising the heat treatment temperature to 600 °C, 1%AuPd/RT-600 °C produces an increase in catalytic activity that coincides with an increase in mean particle size to *ca.* 10 nm. Although an improvement in activity is observed, productivity remains low (0.063 mol kg_{cat}^{-1} h^{-1}) with overall oxygenate selectivity of 46.6%. Notwithstanding, the improvement in catalyst activity towards selective oxygenates continues to proceed with almost complete decomposition of H_2O_2 during the reaction period, with 1.7% remaining.

At 800 °C, a notable improvement is observed in selective oxygenate formation, with an improvement in the H_2O_2 remaining post reaction (*ca.* 42%). Significant growth is measured in mean particle size, increasing to *ca.* 19 nm (Figure 3.1(d)), and catalyst selective oxygenate productivity improves to 0.172 mol kg_{cat}^{-1} h^{-1} from 0.063 mol kg_{cat}^{-1} h^{-1}. After 30 minutes, total products equal 0.90 micromoles (μmol) with 80% selectivity towards CH_3OH (25.5%) and CH_3OOH (55.6%).

Importantly, an initial relationship is seen between quantities of selective oxygenates produced and temperature of catalyst heat treatment. Specifically, catalysts possessing the largest mean particle size, facilitated by increased treatment temperature, also observed the highest oxygenate formation. Furthermore, these catalysts showed higher amounts of H_2O_2 remaining post reaction, a relationship which is proposed to originate from increases in AuPd particle size. Despite this, however, additional parameters such as metal oxidation state and support influence may be altered during heat treatments to produce the enhanced activity.[40]

3.2.2 The Effect of Catalyst Preparation Temperature

Previously, Rogers *et al.*[41] reported a temperature influence upon poly- (vinyl alcohol) stabilised Au nanoparticles prepared by sol immobilisation. The 1 wt.% Au/TiO_2 prepared at room temperature (RT) were observed to possess a mean particle size of 2.3 nm. Increasing the preparation temperature during synthesis and deposition of colloidal Au nanoparticles, from RT to 70 °C, resulted in mean particle size increasing to 3.3 nm.

The effect of small changes in particle size were investigated for CH_4 oxidation by preparation of 1 wt.% AuPd/TiO_2 (P25) at 70 °C. Identical heat treatments of 400, 600 and 800 °C were applied to produce a series for comparison with the previously prepared room temperature series. To differentiate between catalyst series and treatments, the following nomenclature is adopted; Metal loading% AuPd/ Phase of TiO_2-preparation temperature-heat treatment. Subsequently, a 1 wt.% AuPd/TiO_2 (P25) catalyst prepared at room temperature followed by heat treatment at 800 °C is given the following nomenclature; 1%AuPd/P25-RT-800 °C.

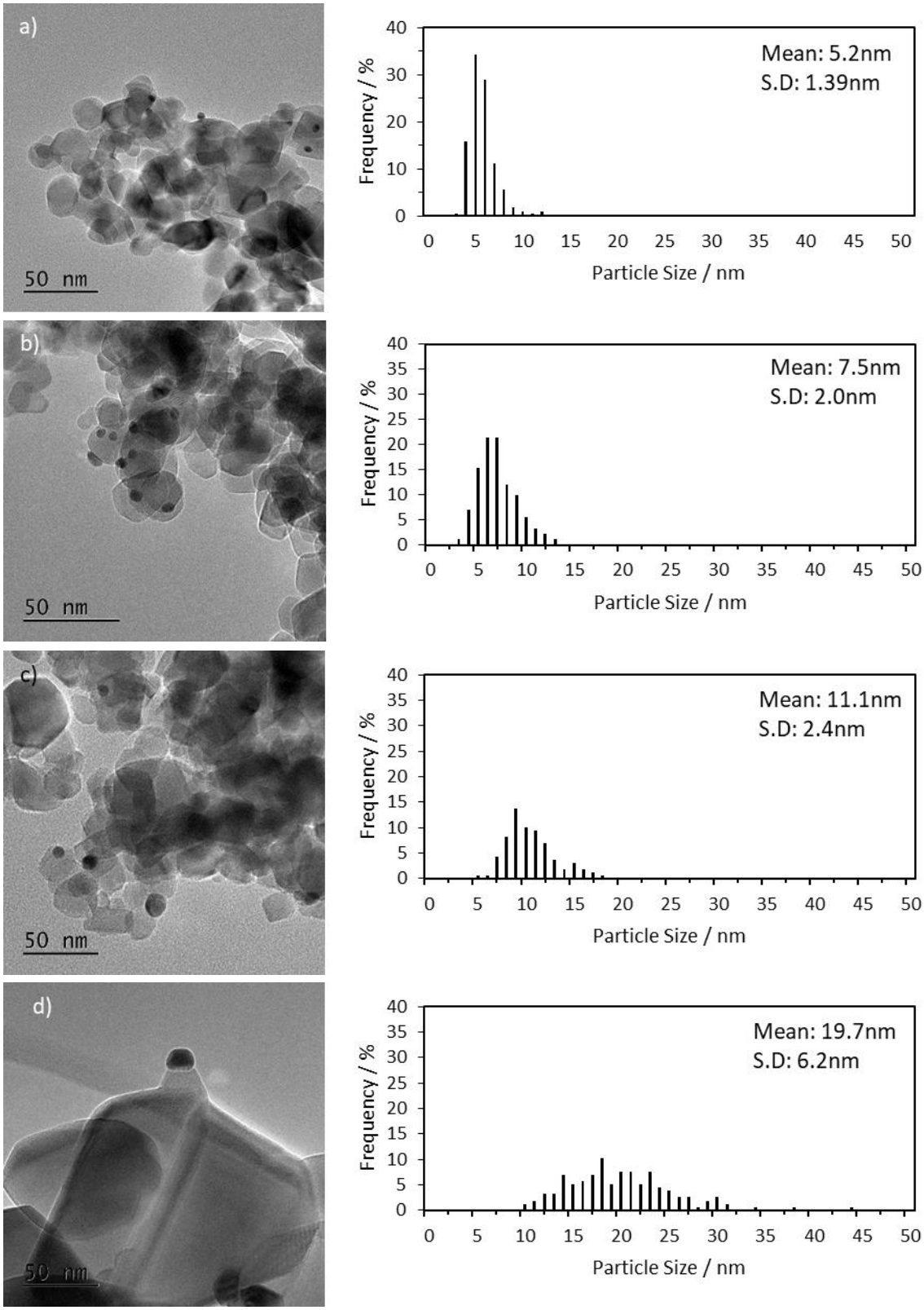

Figure 3.3: Transmission electron microscopy of 1 wt. % AuPd/ TiO_2 (S_i) prepared at 70 ˚C; (a) Dried, (b) calcined at 400 ˚C, (c) 600 ˚C and (d) 800 ˚C.

TEM analysis was carried out to determine the effect of increasing preparation temperature on particle size. Representative images and mean particle sizes determined from approximately 250 nanoparticles are presented in Figure 3.3.

The mean particle size possessed by the parent dried only catalyst was determined to be 5.2 nm. Therefore, raising the preparation temperature yields an increase of 1.2 nm in mean particles size from previously determined 1%AuPd/P25-RT-Dried (Figure 3.1(a), 4.0 nm). This difference is consistent with previous work by Rogers *et al.*[41] Even so, the marginal increase in particle size yields no activity for selective oxygenate formation and productivity remains low at 0.018 mol kg_{cat}^{-1} h^{-1}. Catalyst activity for the decomposition of H2O2 remains high with almost complete decomposition observed.

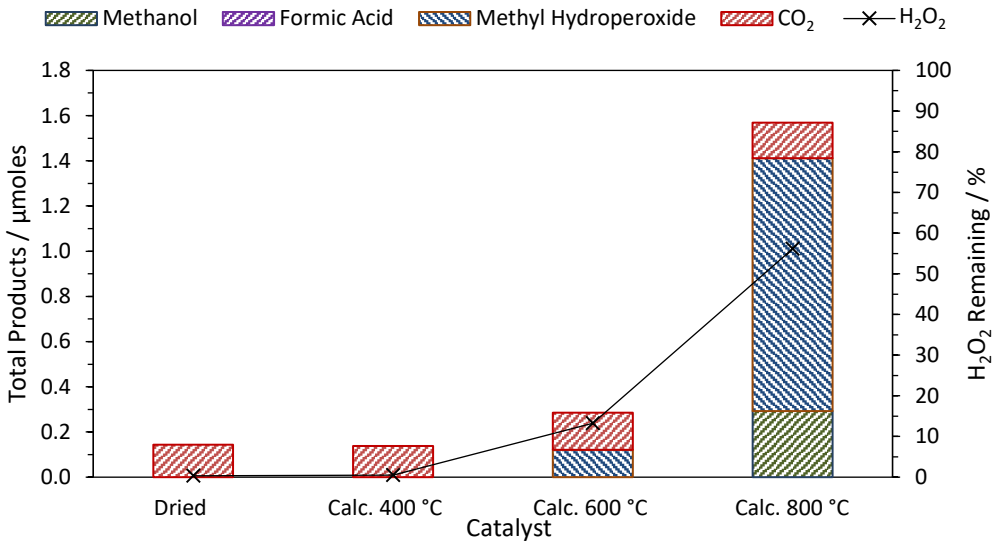

Figure 3.4: Comparison of the effect of post synthesis heat treatment on 1wt. % AuPd/TiO_2 (P25) prepared at 70 ˚C on the catalytic activity for methane oxidation.

Standard reaction conditions: time: 30 minutes, temperature: 50 °C, P_{CH_4}: 30.5 bar, stirring rate: 1500 rpm, all catalysts (1 wt. % total): 7.24 x10^{-7} mol of metals equal to 10 mg of solid catalysts, volume: 10 mL of H_2O.[H_2O_2]: 0.5 M

The onset of selective oxygenate formation is observed after heat treatment at 600 °C, achieving a productivity of 0.057 mol kg_{cat}^{-1} h^{-1} when mean particle size increases to *ca.* 11 nm. The activity demonstrated by 1%AuPd/P25-70-600 °C is comparable with the RT counterpart, despite possessing larger particle size (RT: 8.3 nm vs. 70 ˚C: 11.1 nm). Although no difference in activity is observed, disparity in mean particle size between RT and 70 °C materials does yield a small improvement in H_2O_2 decomposition. For 1%AuPd/P25-RT-600 °C near-complete decomposition of H_2O_2 is observed increasing from 1.7% remaining to 13.3% for 1%AuPd/P25-70-600 °C (Figure 3.2 and Figure 3.4).

Treatment at 800 °C yields the greatest improvement in both 1%AuPd/P25-RT and -70 °C series. Increasing productivity for CH_4 oxidation to 0.317 mol kg_{cat}^{-1} h^{-1}, oxygenate

selectivity to CH_3OH (18.5%) and CH_3OOH (71.3%) is greatly improved. Analogously to the RT counterparts, 1%AuPd/P25-70-800 °C particle size growth is considerable, increasing mean particle size to *ca.* 19.7 nm (Figure 3.3(d)). Although possessing similar profiles for mean particle size and distribution, (Figure 3.2(d) and Figure 3.4(d)), total oxygenate formation for 1%AuPd/P25-70-800 °C is considerably higher at 1.57 μmol (Figure 3.3). Consequently, 1%AuPd/P25-70-800 °C demonstrates an approximate two-fold improvement in productivity, seemingly originating from the two-fold increase in CH_3OOH formation (RT: 0.53 μmol, 70 ˚C: 1.12 μmol). This large variation in activity, despite similar AuPd particle profiles, could suggest an additional influence of preparation temperature on AuPd nanoparticle structure. Reported by Rogers *et al.*[41], a similar variation in catalyst activity for glycerol oxidation was observed. Examining the influence of solvent used during Au nanoparticle preparation, Rogers reported a decrease in TOF from 915 h^{-1} to 202 h^{-1}, despite producing Au nanoparticles of similar average size. For Rogers *et al.* the preparation temperature and solvent system was determined to influence the density of highly active Au clusters, but, provides an insight into the structure-activity relationship. Further work was proposed by Rogers *et al.* to elucidate the relationship further.

For 1%AuPd/P25-70-800 °C, H_2O_2 decomposition is reduced with 56% remaining post reaction, a reduction in consumed H_2O_2 from 42% with 1%AuPd/P25-RT-800 °C. This variation, however, may originate from the presence of sub-10 nm nanoparticles identified in 1%AuPd/P25-RT-800 °C catalyst, in contrast to 1%AuPd/P25-70-800 °C. This is similarly observed in catalysts heat treated at 600 °C. Possessing a higher population of sub-10 nm nanoparticles (*ca*. 85%, vs *ca.* 28%), 1%AuPd/P25-RT-600 °C observes an increased amount of initial H_2O_2 decomposition post reaction (1.7% remaining) compared to 70-600 C (13.3%). Potentially more active, the sub -10 nm particles consequently deleteriously catalyse the decomposition of H_2O_2, lowering activity for the formation of selectivity oxygenates.

Although present, consideration of the standard deviation of identified nanoparticle sizes also suggest that particle size disparity for RT and 70 °C catalysts may be greater than represented in Figure 3.4. In contrast, the identification of sub-10nm nanoparticles represent a small fraction (*ca.* 1.8% total) of the supported nanoparticles present.

Analysis by X-ray Diffraction

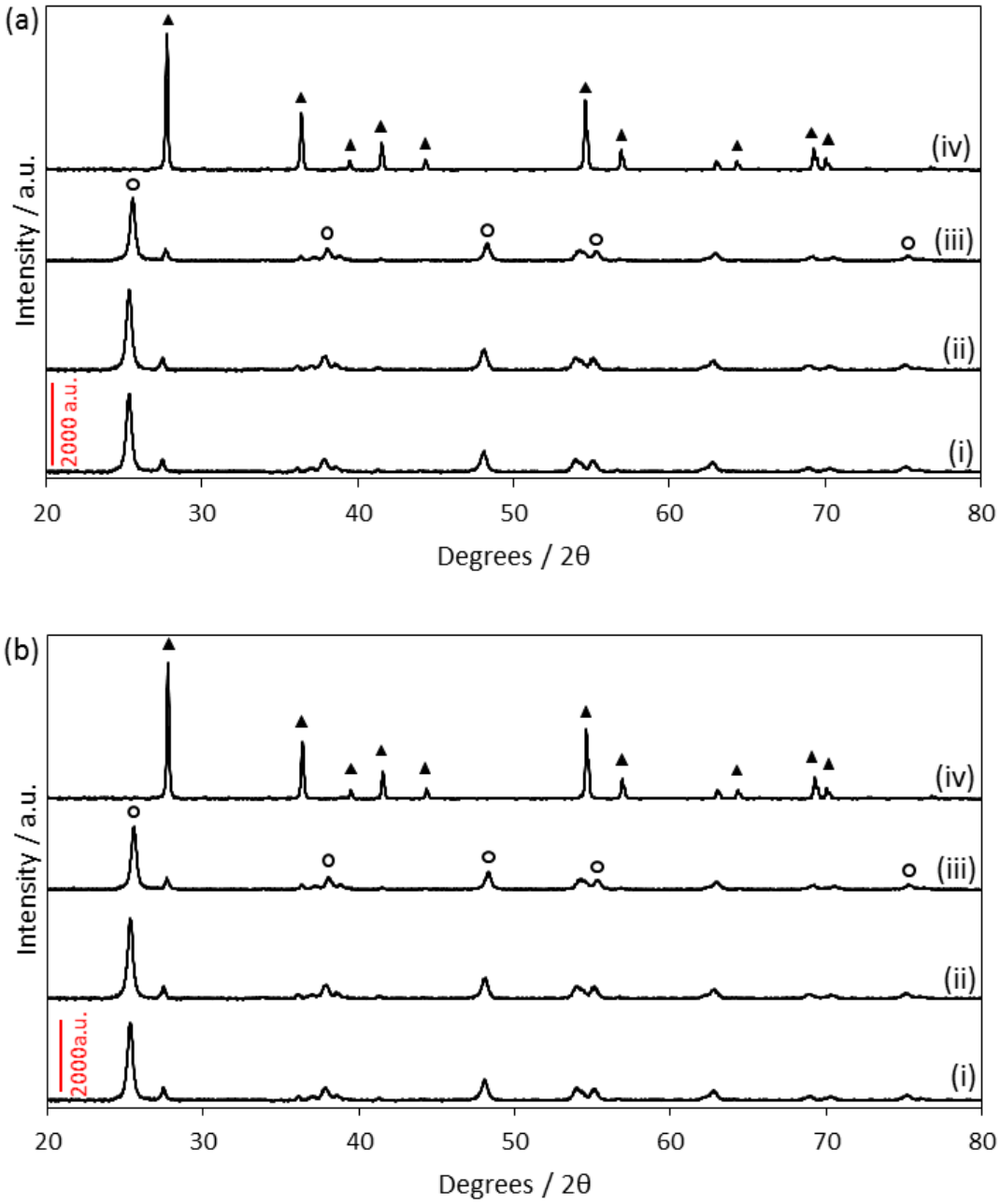

Figure 3.5: Powder X-ray diffraction of 1 wt. % AuPd/ TiO_2 S_i catalysts prepared at (a) room temperature and (b) elevated temperature (70 °C). (i) Dried only, (ii) heat treated at 400 °C, (iii) 600 °C, and (iv) 800 °C. ▲ = Rutile; ◯ = Anatase.

To elucidate any further changes in catalyst structure induced by heat treatment at 400, 600 and 800 °C, catalyst sampled were analysed by powder X-ray diffraction (XRD). Using a Cu Kα radiation source (λ= 0.154 nm) samples were recorded between 15 and 80 ° utilising 0.0167° steps sizes under ambient temperature and pressure.

Comprising a physical mixture of anatase (80%) and rutile (20%) phase TiO_2, the preparation of parent dried only catalyst produces no influence upon the phase composition of P25 TiO_2 (Figure 3.5). Furthermore, remaining comprised of predominantly anatase (80%), P25 TiO_2 support remains thermally stable at 400 and 600 °C. Importantly, however, heat treatment at 800 C facilitates the phase transition of P25 TiO_2 to rutile phase, coinciding with significant improvements observed in catalytic activity (Figure 3.5 (a-iv) and (b-iv)). As such, the improvement produce through heat treatment may result from the combination of particle size and catalyst support.

Even so, a relationship linking average nanoparticle size and selective oxygenate formation is clearly observed and shown in Figure 3.6. Here, mean particle size increase correlates with an increase in the formation of selective oxygenates. Extrapolation suggests meaningful selective oxygenate productivity is not observed in particles below *ca.* 8 nm, although further evidence suggest an influence of support phase and activity for H_2O_2 decomposition.

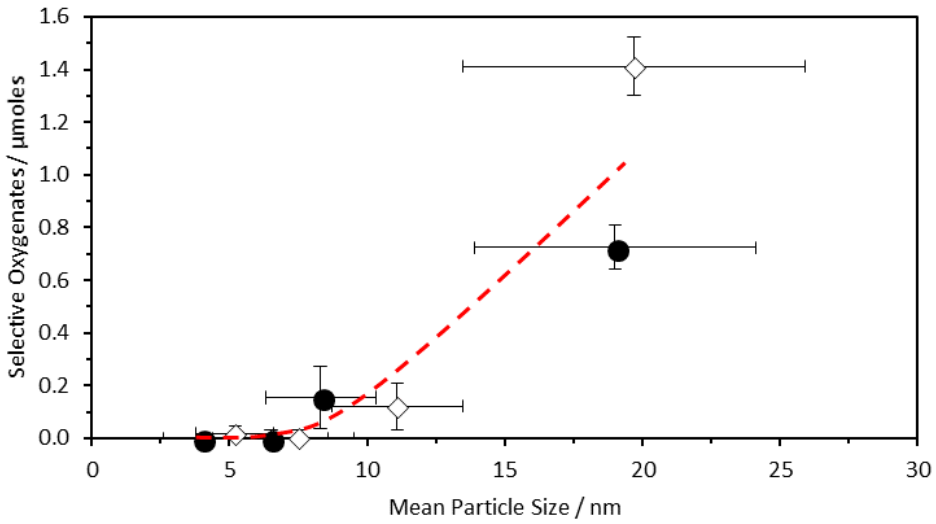

Figure 3.6: Structure-activity relationship of 1 wt.% AuPd/TiO_2 (P25) showing larger mean nanoparticle size resulting in higher selective oxygenate productivity during oxidation of methane at 50 °C, using preformed H_2O_2. ● = RT and ◊ = 70 °C.

3.2.3 The Effect on H_2O_2 decomposition

To further elucidate the effect of heat treatment upon the properties for H_2O_2 decomposition, the relative rates of H_2O_2 decomposition were determined. Using a series of room temperature reactions, the catalyst series were tested whilst stirred using dilute solutions of H_2O_2 (0.5M, 10 mL) under atmospheric conditions. At regular intervals, H_2O_2 decomposition was determined through analysis of the aqueous reaction solution as a function of time and presented in appendix Figure A7.1. The decomposition rates, expressed as μmoles min^{-1}, for 1%AuPd/P25- RT and 70 °C catalyst series are collated in Table 3.3. As shown in Figure A7.1(a) and (b), the dried only catalysts demonstrate the highest rates of H_2O_2 decomposition with less than 10% H_2O_2 remaining after room temperature testing for 30 minutes. The rate of H_2O_2 decomposition of 1%AuPd/P25-RT-dried was found to be 557 μmol min^{-1} and 278 μmol min^{-1} for the 1%AuPd/P25-70 °C-dried (Table 3.3, Entries 1 and 5). The high rates of H_2O_2 decomposition are characteristic of the high activity of smaller AuPd nanoparticles.[19]

Table 3.3: Relative rates of H_2O_2 decomposition and elemental surface composition data determined for 1wt.% AuPd/TiO_2 (P25). Entries 1-4: prepared at room temperature, Entries 5-8: prepared at 70 ˚C

Entry	Catalyst	Sel. Oxy. [μmoles]	Oxy. Sel. [%]	Mean Particle Size[a] [nm]	H_2O_2 Decomp. Rate[b] [μmoles min^{-1}]	Surface Elemental Composition [c]		
						AuPd /Ti	Pd Species[d] [%]	
							Pd^{2+}	Pd^0
1	RT, dried	0	0.0	4.0 ±1.4	557	0.009	0	100
2	RT, 400 ˚C	0	0.0	6.5 ±2.1	198	0.006	100	0
3	RT, 600 ˚C	0.15	46.6	8.3 ±2.0	105	0.004	100	0
4	RT, 800 ˚C	0.72	80.8	19.0 ±5.1	99	0.022	100	0
5	70 ˚C, dried	0	0.0	5.2 ±1.4	278	0.005	0	100
6	70 ˚C, 400 ˚C	0	0.0	7.5 ±2.0	251	0.004	100	0
7	70 ˚C, 600 ˚C	0.12	42.5	11.1 ±2.4	145	0.004	100	0
8	70 ˚C, 800 ˚C	1.41	90.0	19.7 ±6.2	31	0.011	100	0

[a] Determined by transmission electron spectroscopy. [b] H_2O_2 decomposition reaction conditions: time: 30mins, temperature: 24 °C, atmospheric pressure, stirring rate: 1000rpm, all catalysts (1 wt. % total): $7.24x10^{-7}$ mol of metals equal to 10 mg of solid catalysts, volume: 10 mL of H_2O.[H_2O_2]: 0.5 M. [c] Determined by x-ray photoelectron spectroscopy and calibrated to Carbon 1s region (284.4 eV). [d] Calculated as (Pd species/total Pd species)x100. Sel. Oxy.: Selective oxygenates, Oxy. Sel.: Oxygenate selectivity, Decomp.: Decomposition

In addition to particle size, the oxidation state of Pd present has been demonstrated to determine the rate of H_2O_2 decomposition, with metallic Pd^0 resulting in an increased rate of H_2O_2 decomposition.[42] Therefore, XPS analysis was used to investigate any effect of Pd oxidation state and potential relationships to the rate of H_2O_2 decomposition and consequently selective oxygenate formation. The corresponding XPS spectra for Au (4f)

and Pd (3d) region are illustrated in Figures 3.8 and 3.9, with surface elemental analysis displayed in Table 3.3.

The presence of reduced, metallic Pd-only in the dried catalyst is evidently a consequence of the preparative method, utilising the reducing agent $NaBH_4$ (Entry 1 and 5, Table 3.3). The presence of Pd^0-only, in combination with small AuPd nanoparticle size leads to the high rate of H_2O_2 decomposition exhibited by 1%AuPd/P25-RT- and 1%AuPd/P25-70-dried only catalysts. Additionally, the application of heat treatment expectedly results in the oxidation of metallic Pd^0 to Pd^{2+}(Figure 3.7 and 3.8)(Entries 2-4 and 6-8, Table 3.3). This effect is consistent with that observed by Edwards and coworkers[43], who saw near complete oxidation of metallic Pd^0 to Pd^{2+}. In addition, the observed increase in nanoparticle is also suggested by changes in the ratio of AuPd and Ti ratio determined by XPS (Table 3.4). For RT-series, initial AuPd-to-Ti ratio is determined to be 0.009 and decreases at heat treatments of 400 °C (0.006) and 600 °C (0.004). A surface sensitive technique, the reduction in observed AuPd surface area due to increasing particle size would be observed by a decreasing ratio in relation to Ti during XPS analysis. Contrastingly, the phase transition of high surface area anatase TiO_2 to low surface area rutile TiO2, would result in the large increase in ratio of AuPd-to-Ti (Table 3.3, entries 4 & 8).

Table 3.4: Surface elemental composition of 1 wt. % AuPd/ TiO_2 (P25) catalysts and calculated intrinsic activity for the oxidation of methane. Entries 1-4: prepared at room temperature, Entries 5-8: prepared at 70 ˚C.

Entry	Catalyst	Surface Elemental Composition[a] Binding Energy [eV]			SEM-EDX Metal Loading		MPAES Metal Loading		Intrinsic Activity[b] [h^{-1}]
		Pd^{2+}	Pd^0	Au (4f)	Total [wt.%]	Au [wt.%]	Total [wt.%]	Au [wt.%]	
1	RT, dried	-	334.7	82.9	0.92	0.4	0.97	0.49	$5.46x10^2$
2	RT, 400 °C	336.3	-	83.1					$2.55x10^3$
3	RT, 600 °C	336.5	-	83.1					$5.66x10^3$
4	RT, 800 °C	336.6	-	83.3					$1.91x10^5$
5	70 ˚C, dried	-	334.3	82.8	0.85	0.4	0.89	0.44	$7.15x10^2$
6	70 ˚C, 400 °C	336.4	-	83.1					$2.18x10^3$
7	70 ˚C, 600 °C	337	-	83.8					$1.27x10^4$
8	70 ˚C, 800 °C	337	-	83.3					$3.94x10^5$

[a] Determined by x-ray photoelectron spectroscopy and calibrated to Carbon 1s region (284.4 eV). [b] Intrinsic Activity: calculated as $moles_{(Oxygenated\ Products)}/moles_{(total\ nanoparticle\ surface\ atoms)}$/time (h)

Importantly, further inspection of the Pd(3d) spectra reveals a shift in binding energy for the $Pd^{(II)}$ band, with binding energy increasing from 336.3 eV (400 °C) to 336.6 eV (800 °C) (Table 3.4, entries 2-4). A similar increase in binding energy is observed for 70 °C counterparts, increasing from 336.4 eV to 337 eV (Table 3.4, entries 6-7). This effect may

result from (i) an increasing AuPd nanoparticle size or (ii) strong metal-support interactions. Similarly observed by Guadix-Montero *et al.*, a shift to higher energy was proposed to originate from an increase in nanoparticle size.[44] Alternatively, the influence of heat treatment may be to strengthen support-metal interactions.

Initially believed to stabilise the active metal nanoparticles dispersed on the support, additional physiochemical interactions resulting in changes in catalytic performances have been observed.[45] Subsequently the interactions of metals and supports have been of fundamental interest for the design of heterogenous catalysts.[46] Strong metal-support interactions therefore have been studied to enhance understanding and develop improved catalytic systems.[46] Typically, the SMSI phenomenon is observed in reducible oxide supports (e.g. TiO_2,CeO_2, V_2O_5) after high temperature reducing treatments. [47–49] However, work by Tang et al.[50] has shown the first example of oxidative- SMSI (OMSI) between platinum group metals and hydroxyapatite, additionally extending to ZnO.

The influences of SMSI upon catalytic performance originate from three major effects (electronic, geometric and bifunctional). The induction of electronic effect is the result of electron transfer between interfaces of the metal and support material, resulting in a redistribution of local charge. The extent of which may induce strong or weak influences, influencing different interactions between metal and support or within respective systems such as the metal nanoparticles only. Therefore, the shift to higher binding energy observed in Pd (3d) bands are attributed to a strong electronic interaction between support and metal.

Secondly, the partial or complete encapsulation of AuPd nanoparticle by the TiO2 support is described as the geometric effect.[46] Encapsulation by TiO_x is driven by the high surface energy of the metal nanoparticle and the low surface energy of the oxide support. Despite this, inspection via TEM showed no signs of nanoparticle encapsulation, although this maybe a limitation of instrument resolution.

To confirm the metal loadings of Au and Pd, elemental analysis of parent dried only catalyst was carried out by MP-AES after acid digestion using aqua regia (Table 3.4). For RT prepared 1%AuPd catalyst, a metal loading of 0.97 wt.% AuPd was determined, achieving the nominal ratio for Au:Pd of 1. The weight loading of 0.97 wt.% is close to nominal loading of 1 wt.%. This contrast with 1 wt.% AuPd prepared at 70 °C, which shows 0.89% total loading of Au and Pd metal. Attributed to inefficient digestion of TiO_2 support when using aqua regia, additional SEM-EDX analysis was used to compliment analysis of metal loadings. Shown in Table 3.4, SEM-EDX analysis of both RT and 70 °C catalysts are consistent with determined MP-AES data. Using the confirmed metal loadings, the corrected TOF values demonstrate a clear enhancement of catalyst activity by preparation at elevated temperatures (70 °C). Prepared at 70 °C, 1%AuPd/P25-800 °C oxygenate formation occurs at TOF of 4.87 h^{-1}, an almost two-fold increase from RT counterpart.

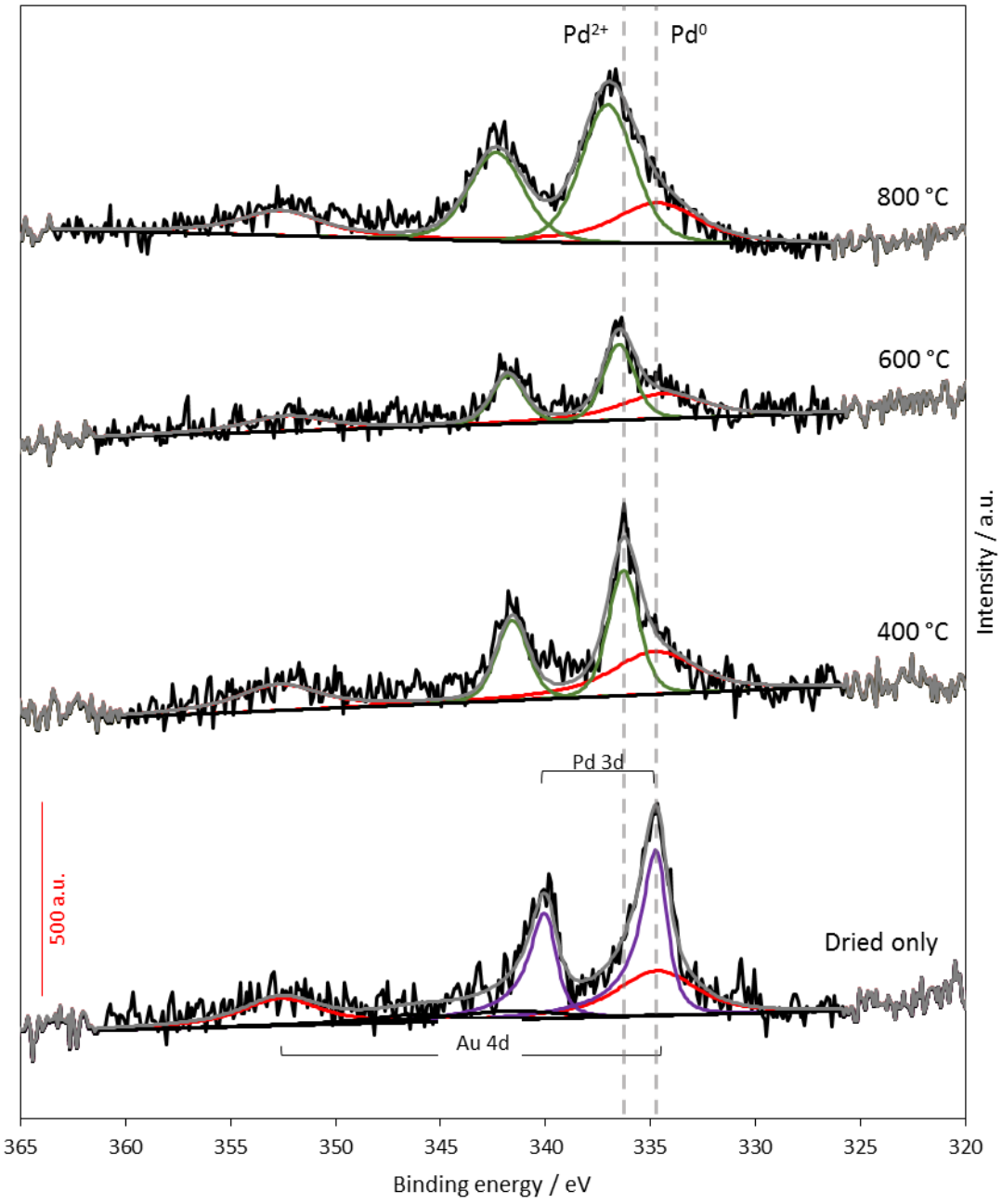

Figure 3.7: X-ray photoelectron spectra of Pd 3d region for 1 wt. % AuPd/ TiO_2 (P25) prepared by SF-S_i at room temperature. Pd^0 = purple line; Pd^{2+} = green line; Au 4d = red line. The dashed lines indicate the peaks due to Pd^0 and Pd^{2+}. All peaks calibrated against Carbon 1s (284.8 eV).

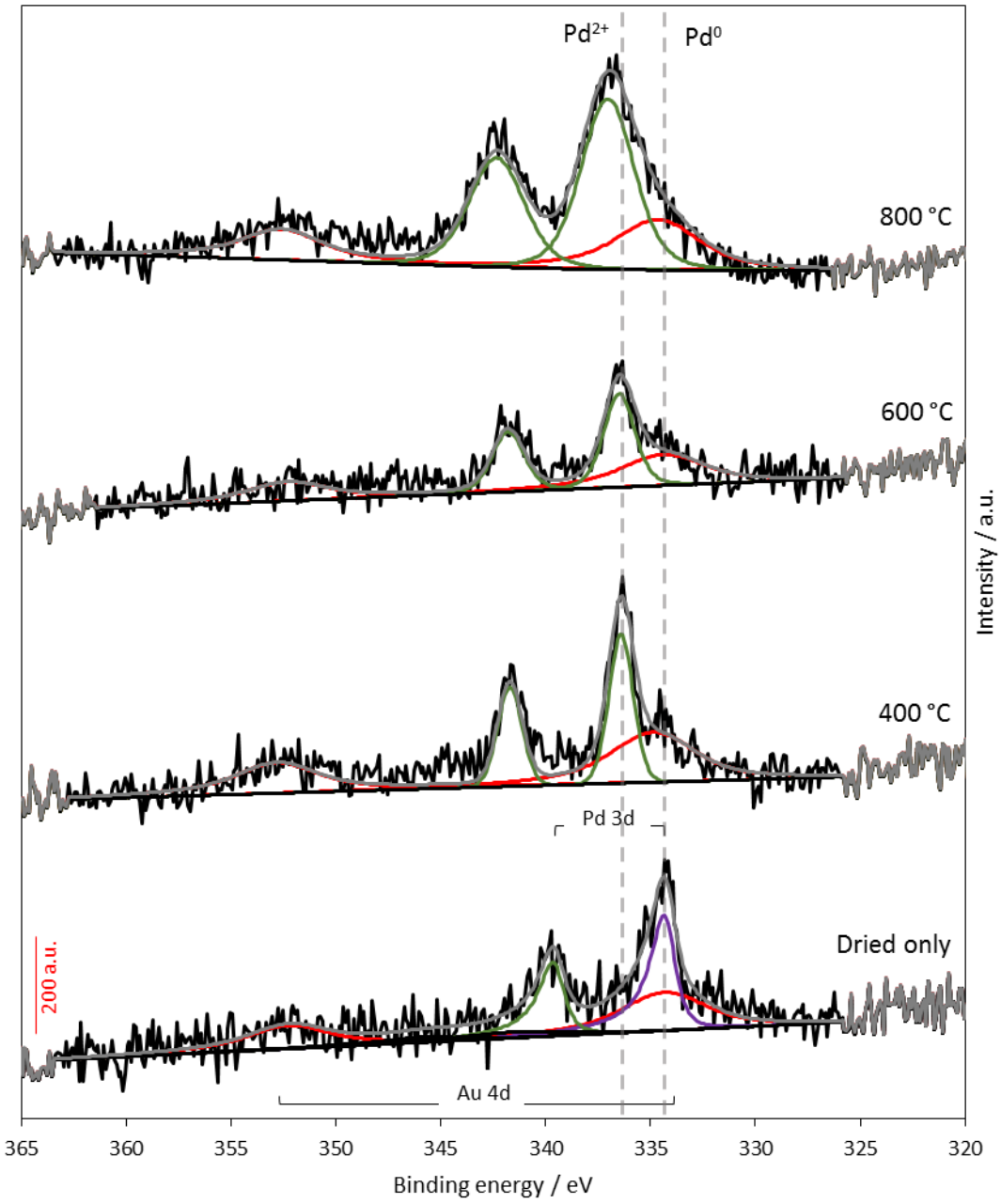

Figure 3.8: X-ray photoelectron spectra of Pd 3d region of 1 wt. % AuPd/ TiO_2 prepared by SF-S_i at elevated temperature (70 °C). Pd^0 = purple line; Pd^{2+} = green line; Au 4d = red line. The dashed lines indicate the peaks due to Pd^0 and Pd^{2+}. All peaks calibrated against Carbon 1s (284.8 eV).

Table 3.5: Effect of reduction on 1wt.% AuPd/TiO_2 (P25) prepared by S_i at 70 ˚C.

Reduction Temp. [°C]	Products [µmol]				Oxyg. Sel.[a] [%]	Product.[b] [mol $kg_{(cat)}^{-1}h^{-1}$]	H_2O_2 Rem.[c] [%]
	CH_3OH	HCOOH	CH_3OOH	CO_2			
400	0	0	0	0.41	0	0.077	1.3
800	0.13	0	0.13	0.38	40.6	0.127	2.9

[a] Oxygenate selectivity calculated as (moles oxygenates/total moles of products) x 100. [b] Total productivity calculated as (moles(products) /weight(catalyst))/time). [c] Calculated as (moles(initial)/moles(final)) x100. Temp.: Temperature, Oxyg. Sel.: Oxygenate selectivity, Product.: Productivity, H_2O_2 Rem.: H_2O_2 remaining.

To further elucidate the effect of oxidised Pd^{2+} against metallic Pd^0, 1%AuPd/P25-70-dried was heat treated under reducing atmosphere (5% H_2/Ar) prior to testing for CH_4 oxidation. Reported by Sankar *et al.*, prepared AuPd/TiO_2 catalysts possessing Pd^{2+} were reduced to Pd^0 by treatment under flowing H_2/Ar at temperatures of 400 °C.[51] Presented in Table 3.5, the effect of reduction is clearly detrimental towards activity for CH_4 oxidation. Analogously, reduction of 1%AuPd/P25-70-dried at 400 °C seemingly produces no selective oxygenates, with almost complete decomposition of preformed H_2O_2 (1.3% H_2O_2 remaining). In contrast to 1%AuPd/P25-70-800 °C, reduction at 800 °C yields no major improvement to catalyst activity for CH_4 oxidation. Producing minimal activity for the formation of selective oxygenates with 40% selectivity, the reduced catalyst again exhibits almost complete decomposition of H_2O_2, comparable with the dried only catalyst. In both entries, however, detected CO_2 is found to be higher than previously reported during catalysed and background experiments. This may indicate the formation of selective oxygenates which are rapidly oxidised further under high rates of H_2O_2 decomposition catalysed by reduced Pd^0 species.

The careful consideration of relationships between H_2O_2 decomposition rate and selective oxygenate formation sees an important link to producing effective catalysts for CH_4 oxidation. These relationships are illustrated in Figure 3.9. Clearly, the reduction in the rate of H_2O_2 decomposition leads to the favourable production of selective oxygenates (Figure 3.10(a)). Possessing the lowest rate of H_2O_2 decomposition (30 µmoles min^{-1}), 1%AuPd/P25-70-800 °C exhibits the highest productivity (0.312 mol kg_{cat}^{-1} h^{-1}) of oxygenates (Figure 3.9(a)). Additionally, the reduction in H_2O_2 decomposition rate produces a similar enhancement in oxygenate selectivity, improving to achieve a final selectivity of 90%.

Illustrated in Figure 3.9(b), the intrinsic activity of AuPd nanoparticles was determined using the magic cluster theory for the approximation of metal atoms in nanoparticle surface. More representative values were produced by utilising determined MP-AES values for metal loadings. Therefore, the intrinsic activity approximates the activity of catalysts using the total surface area of metal nanoparticles as potential active sites for the decomposition of H_2O_2.

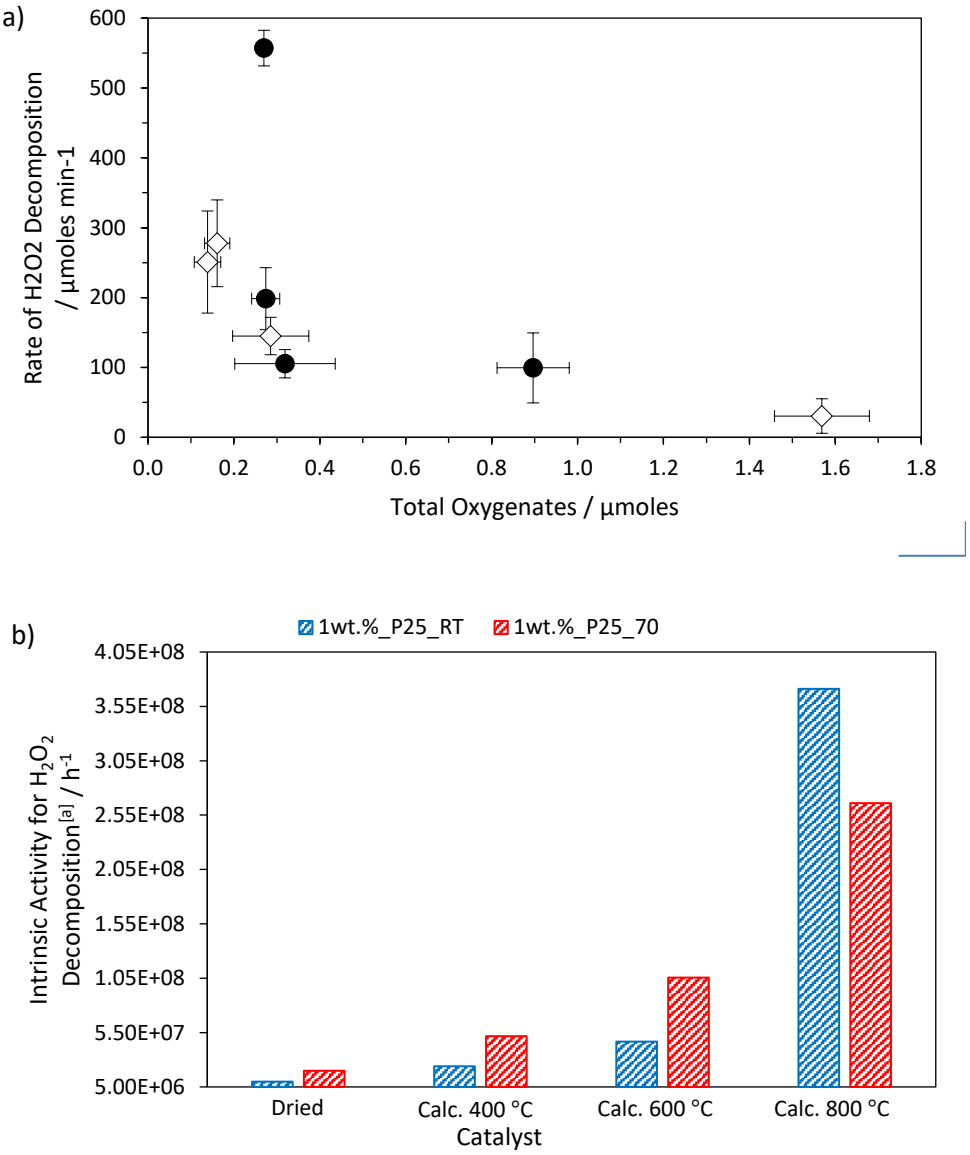

Figure 3.9: (a) Structure-activity relationship of 1 wt.% AuPd/TiO_2 (P25) prepared by SF-S_i for methane oxidation illustrating the overall decrease in H_2O_2 decomposition rates are consistent with the production of larger quantities of selective oxygenates. (b) The intrinsic activity of AuPd for the decomposition of H_2O_2, showing that larger mean particles size possess higher activity for H_2O_2 decomposition. ● = RT and ◊ = 70 ˚C.

Standard reaction conditions: time: 30 minutes, temperature: 24 °C, stirring rate: 1000 rpm, all catalysts (1 wt. % total): 7.24×10^{-7} mol of metals equal to 10 mg of solid catalysts, volume: 10 mL of H_2O.[H_2O_2]: 0.5 M [a] calculated as $Moles_{(H2O2\ decomposed)}/Moles_{(metal\ surface\ atoms)}/time\ (h)$

Initial inspection of H_2O_2 decomposition suggests that the rate of H2O2 decomposition is influenced by nanoparticle size, with increasing particle size resulting in the suppression of detrimental H_2O_2 decomposition (Figure A7.1). Possessing the largest mean particle size (19.7 nm ±6.2), 1%AuPd/P25-70-800 °C shows the lowest rate of H_2O_2 decomposition. In

contrast, the intrinsic activity for H_2O_2 decomposition of catalyst is shown to increase, with catalyst heat treated at 800 °C showing the highest activity for the decomposition of H_2O_2 (Figure 3.9(b)). Consequently, the effect of heat treatment may be to increase intrinsic selectivity of the AuPd nanoparticles.

3.3 The Effect of Support Phase

Previously, the greatest increase in oxygenate productivity was notably made when heat treatment of 1wt.% AuPd catalyst was carried out at 800 °C. The resulting increase in particle size observed was attributed as the source of improved activity, reducing overall disadvantageous H_2O_2 decomposition and resulting in the selective oxidation of CH_4. Additional characterisation by XRD reveals the phase transition of predominantly anatase phase (80%) P25 TiO_2 to rutile TiO_2. This transition is evidenced by characteristic reflections in its XRD pattern, shown in Figure 3.5, and is consistent with previous studies.[52–54] Furthermore, additional nitrogen adsorption measurements revealed a decrease of TiO_2 surface area during the transition of P25 (45 $m^2 g^{-1}$) to rutile TiO_2 (6 $m^2 g^{-1}$). The resulting decrease in surface area during particle growth phase, may also explain the broad distribution of AuPd nanoparticle sizes observed.

The role of TiO_2 support phase has been extensively studied for several applications including the photocatalytic activity of TiO_2.[55,56] Possessing higher surface area, anatase-TiO_2 is considered superior to rutile-TiO_2 due to a larger number of photoactive sites per unit surface area. Consequently, the higher density of surface sites results in the generation of a higher density of adsorbed reactive species leading to the superior activity.[53] Notably for heterogenous catalysis, the significantly low surface area is typically undesirable for application of rutile -TiO_2 as support material. Even so, several studies have reported an improvement in performance for rutile- versus anatase- TiO_2 supported catalysts. The Pd-M/TiO_2 (M=Sb, Bi or Cu) catalysed gas phase acetoxylation of toluene to benzyl acetate is achieved typically with yields of *ca.* 80%.[57] Although high conversion and benzyl acetate selectivity (>95%) are achieved, the required time for catalyst conditioning and deactivation of catalysts are continuing issues for anatase-TiO_2 supported Pd-M. Alternatively, the application of rutile-TiO_2 for Pd-Sb improves benzyl acetate selectivity to almost 100%, and importantly sees no catalyst deactiviation.[58] The change of TiO_2 phase resulted in the formation of regular, well facetted Pd-Sb of *ca.* 80 nm contrasting the irregular Pd-Sb shape and size observed with anatase-TiO_2. Resultantly, deposition of carbon during acetoxylation was not observed for Pd-Sb/rutile TiO_2 and therefore did not suffer from deactivation.

Similarly, the influence of rutile TiO_2 benefits the direct oxidation of H_2 to H_2O_2 using O_2 by AuPd/TiO_2 catalyst, as reported by Ishihara *et al.*[59] For H_2O_2 synthesis the conversion

of H_2 and H_2O_2 selectivity was clearly influenced by TiO_2 crystal phase. At low H_2 pressure (0.1 MPa), brookite TiO_2 was most effective for H_2O_2 synthesis, demonstrating high H_2 conversion (40%) and H_2O_2 selectivity (67%).[60] Meanwhile, rutile TiO_2 exhibited high conversion of H_2 (60%) but poor selectivity (43%) was achieved at similar pressures. The poor selectivity towards H_2O_2 for rutile TiO_2 was, however, resolved by increasing H_2 pressure, with rutile TiO_2 exhibiting higher selectivity and conversion than brookite or anatase at pressures above1 MPa.

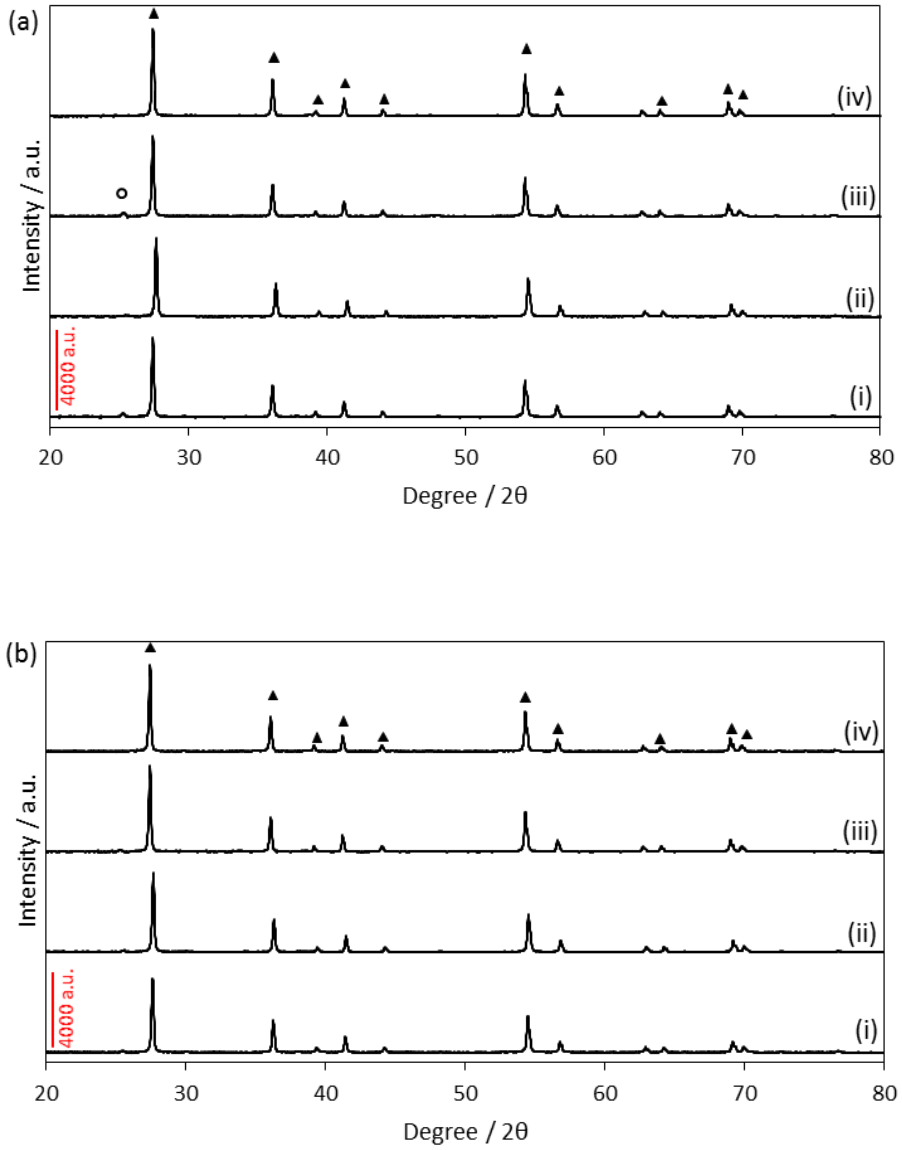

Figure 3.10: Powder X-ray diffraction of 1 wt. % AuPd/ rutile TiO_2 S_i catalysts prepared at (a) room temperature and (b) elevated temperature (70 °C). (i) Dried only, (ii) heat treated at 400 °C, (iii) 600 °C, and (iv) 800 °C. ▲ = Rutile; ○ = Anatase.

To understand the role of support phase for CH_4 oxidation, a series of analogous 1 wt. % AuPd/TiO_2 were prepared by pre-calcination of TiO_2 (P25) support at 800 °C before deposition of 1wt.% AuPd. Similar to earlier investigations, a series of RT and 70 °C catalysts were produced for consistency and tested for CH_4 oxidation using preformed H_2O_2. Subsequent XRD patterns of rutile supported catalysts are presented above in Figure 3.10. Importantly, no further phase changes are observed in TiO_2 support upon increasing treatment temperature. Additionally, no further reduction to rutile TiO_2 surface area were detected by N_2 adsorption experiments with surface area remaining at *ca.* 6 $m^2 g^{-1}$.

3.3.1 The Effect of TiO_2 Phase on Methane Oxidation Activity

Initial investigation into the effect of rutile supported AuPd began by considering the effect of support only. Illustrated in Figure 3.11(a), the bare rutile support shows no catalytic activity towards selective oxygenates. Similarly, the presence of CO_2 (0.33 μmoles) is marked as adventitious due to low decomposition of H_2O_2 (*ca.*3%), as with P25 TiO_2.

Catalytic testing of 1%AuPd/rutile-RT- and 1%AuPd/rutile-70- dried catalyst show consistency with previously tested dried-only catalysts. Showing high activity for the decomposition of H_2O_2, the activity again was considered to originate from Pd metallic oxidation state and the formation of small AuPd nanoparticle size. In sharp contrast, however, an interesting phenomenon was discovered during TEM analysis. As shown in Figures 3.12(a) and 3.13(a), the stabiliser-free deposition of AuPd onto the low surface area rutile TiO_2 leads to the agglomeration of AuPd, which remain after drying (110 °C, 16 hrs). This effect may originate from surface defects upon the rutile support.[61] Heat treatment of the parent dried only catalysts then yields the formation of distinct, hemispherical AuPd nanoparticles. Similarly, the increase of treatment temperature results in the similar promotional effect for particle size observed with previous P25 supported catalysts. Treatment at 800 °C, the highest temperature applied, yields mean particle sizes of 19.6 nm and 22.6 nm for the RT and 70 °C catalysts, respectively. Further inspection of decorating nanoparticles sees no indication of complete or partial encapsulation by TiO2, removing geometric influences of SMSI for changes in catalysts activity.

For rutile supported AuPd, the onset of catalytic activity and the selective formation of oxygenates begins at 400 °C, contrasting the P25 counterpart. Achieving 47% oxygenate selectivity, almost complete decomposition of H_2O_2 decomposition is still observed for 1%AuPd/rutile-RT-dried catalyst. Similarly, improvement to the 0.26 μmoles selective oxygenate formation is achieved when catalysts are prepared at elevated temperature

(70 °C), achieving 0.92 µmoles with 86.2% oxygenate selectivity. Treatment at higher temperature continues to marginally improve both selective oxygenate formation and selectivity for 1%AuPd/rutile-RT series with a maximum achieved at 800 °C. The 1%AuPd/rutile-RT-800 ˚C possesses a lower productivity than 1%AuPd/rutile-RT-600 °C 0.163 mol kg_{cat}^{-1} h^{-1} and 0.176 mol kg_{cat}^{-1} h^{-1} respectively. However, this difference may originate from the decreased quantity of CO_2 detected, consequently increasing oxygenate selectivity artificially. Alternatively, the variation in CO_2, may result from improvement in the intrinsic selectivity of the catalysts with increasing heat treatment temperature. Interestingly, 1%AuPd/rutile-RT- 600 °C displays selectivity to CH_3OOH (40.4%), but treatment at 800 °C results in selectivity towards CH_3OH (53.6%).

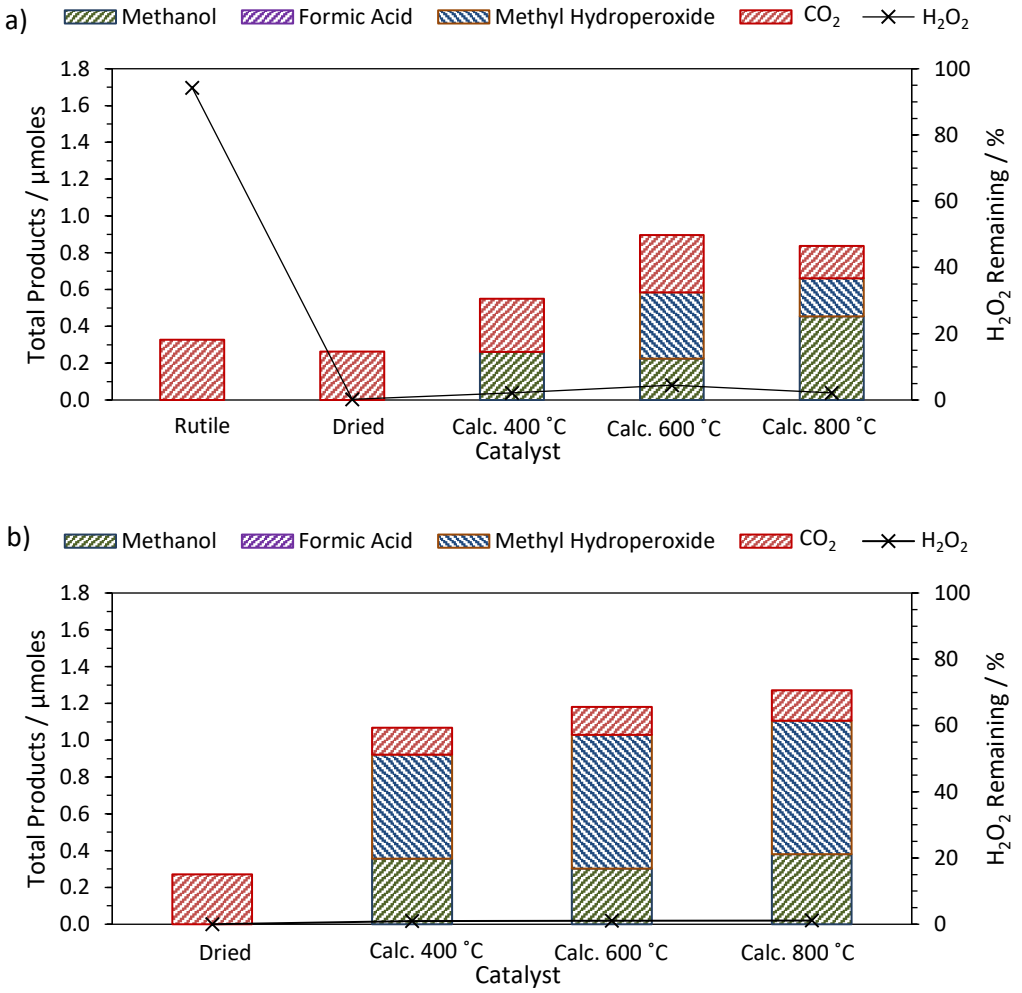

Figure 3.11: Comparison of the effect of post synthesis heat treatment on 1wt. % AuPd/ rutile TiO_2 rutile prepared by S_i at a) room temperature and b) elevated temperature (70 °C) on the catalytic activity for methane oxidation.

Standard reaction conditions: time: 30 minutes, temperature: 50 °C, P_{CH_4}: 30.5 bar, stirring rate: 1500 rpm, all catalysts (1 wt. % total): 7.24×10^{-7} mol of metals equal to 10 mg of solid catalysts, volume: 10 mL of H_2O.[H_2O_2]: 0.5 M

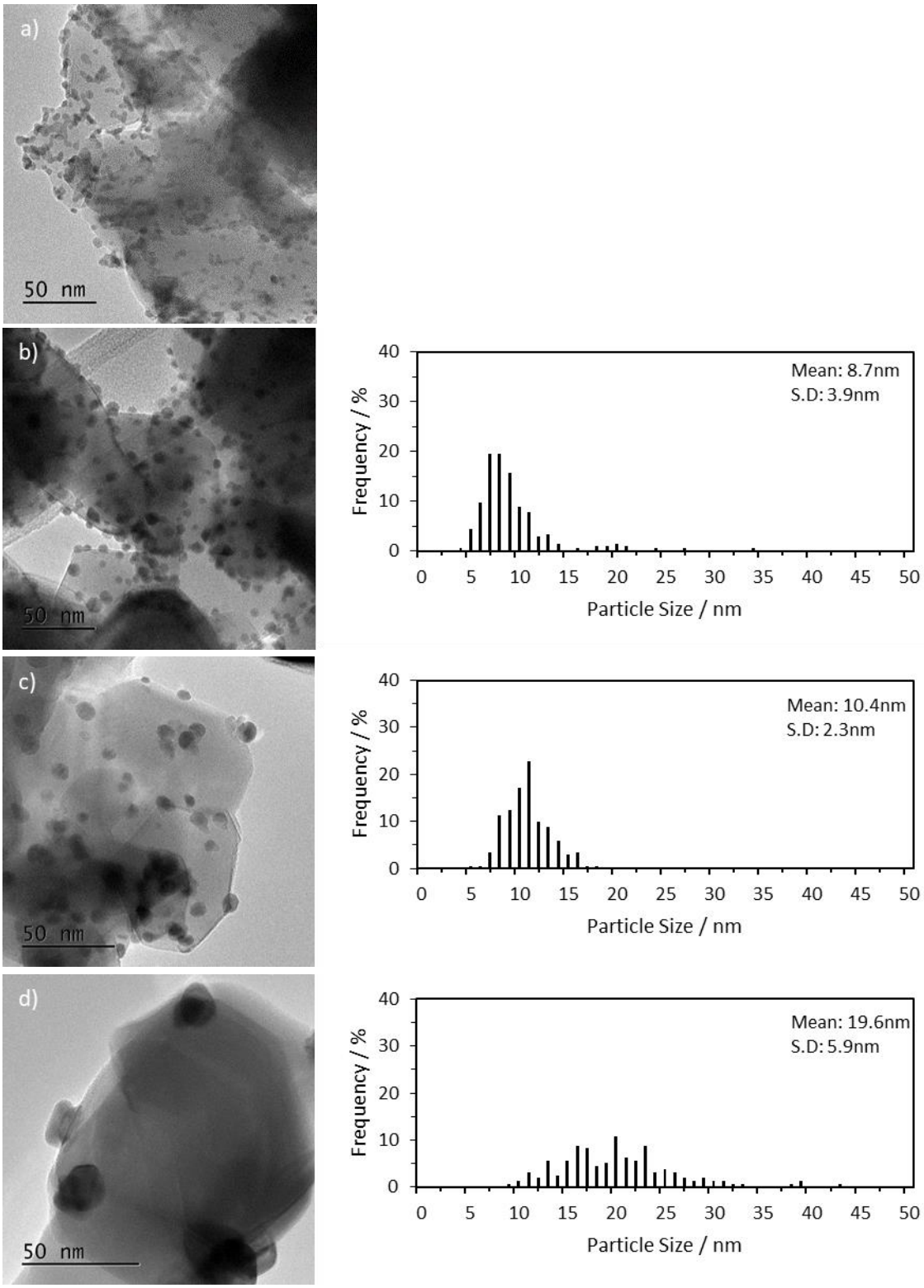

Figure 3.12: Transmission electron microscopy of 1 wt. % AuPd/ rutile TiO_2 (S_i) prepared at room temperature: (a) Dried, (b) calcined at 400 °C, (c) 600 °C and (d) 800 °C.

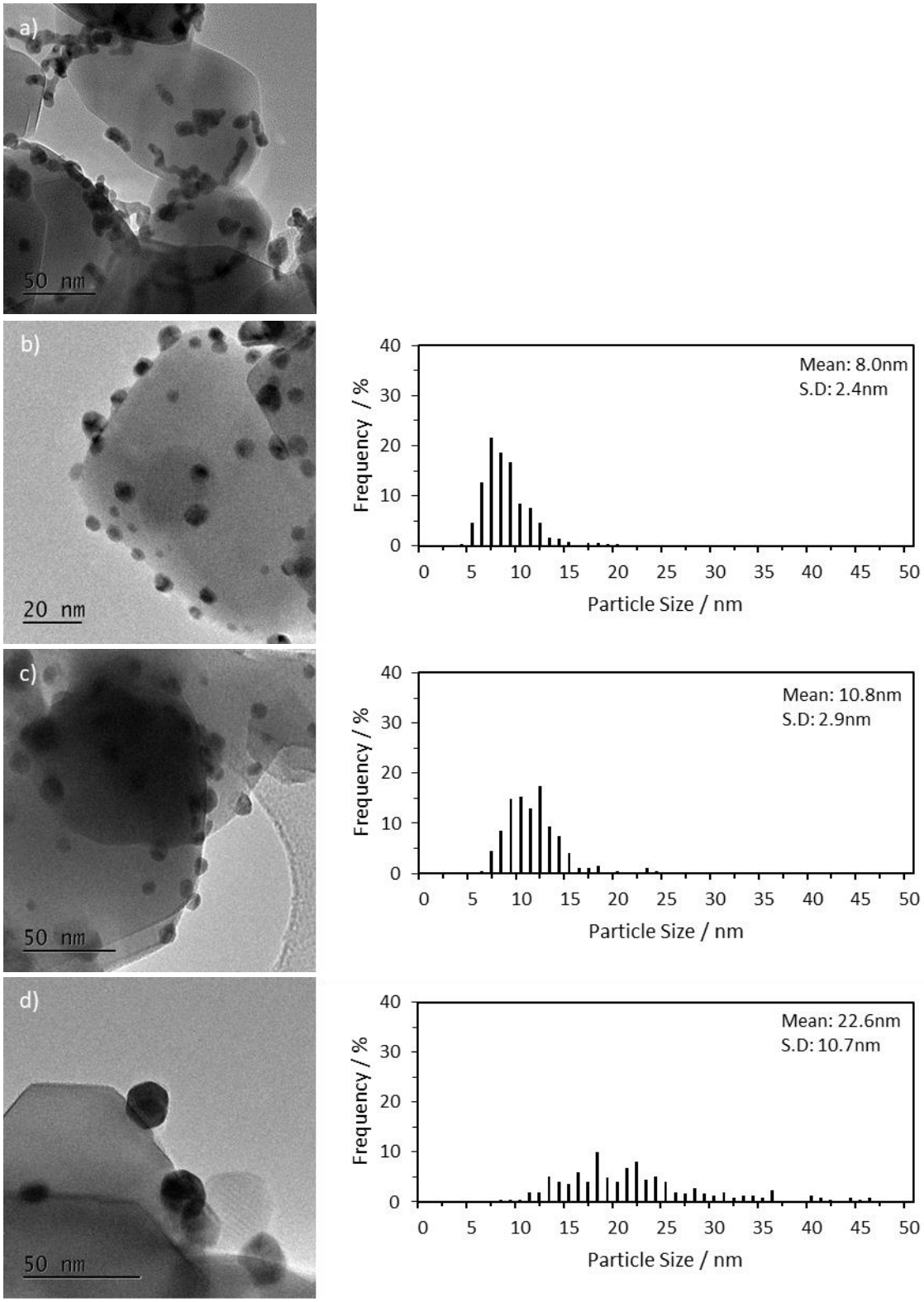

Figure 3.13: Transmission electron microscopy of 1 wt. % AuPd/ rutile TiO_2 (S_i) prepared at 70 ˚C: (a) Dried, (b) calcined at 400 °C, (c) 600 °C and (d) 800 °C.

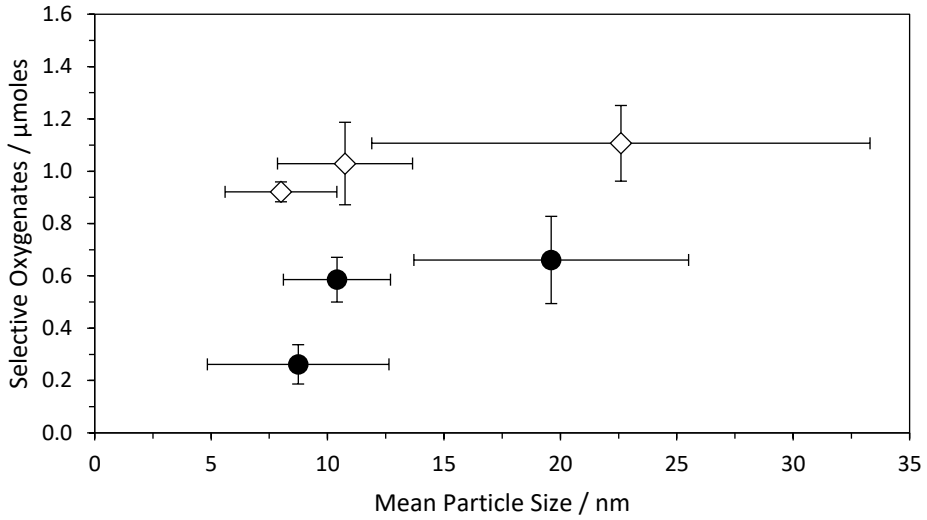

Figure 3.14: Structure-activity relationship of 1 wt.% AuPd/rutile TiO_2 for methane oxidation, illustrating the absence of relationship of mean particle size and selective formation of oxygenates. ● = RT and ◊ = 70 ˚C.

The preparation of 1 wt.% AuPd/rutile TiO_2 at 70 °C produces a clear enhancement in catalyst activity over to the RT series (Figure 3.12). The onset of selective oxygenate formation begins with heat treatment at 400 °C, achieving a near 2-fold improvement in oxygenate selectivity (86.2%) compared to 1%AuPd/rutile-RT-400 °C (47.9%). However, further increases to treatment temperature resulted in only marginal enhancement in the production of primary oxygenates beyond 400 ˚°C. Catalyst productivity remains *ca.* 0.210 mol kg_{cat}^{-1} h^{-1} and oxygenate selectivity does not improve above *ca.* 86%. In addition, increases in mean particle size are observed with increasing treatment temperature. After treatment at 400 °C, comparable particle sizes are produced for rutile supported AuPd to P25 TiO_2, albeit marginally larger. Heat treatment at 800 °C sees a similar enhancement to particle size, growing to 19.6 nm and 22.6 nm for RT and 70 ˚C series, respectively. In contrast to P25 series, the correlation between mean particle size and selective oxygenate formation is not present (Figure 3.14). For RT series, an initial improvement is observed after heat treatment at 600 °C, producing mean particle sizes of *ca.* 11 nm which yield *ca.* 0.6 µmoles of selective oxygenates during methane oxidation. An improvement of ca. 0.3 µmoles at 400 °C heat treatment (*ca.* 8.1 nm) The increase of treatment temperature to 800 °C, whilst producing particles of *ca.* 19.0 nm, only produces a marginal increase in oxygenates. This increase is within experimental error of yields achieved by 600 °C heat treatment, contrasting the significant improvements observed in P25 series (Figure 3.14). A similar effect is observed for catalysts prepared at 70 °C, with activity being moderately higher for oxygenate formation compared to RT series.

Importantly, investigations upon the effect of rutile support have shown the strong influence of rutile support on the catalyst activity of 1wt.%AuPd. This is evidenced by the

onset of selective oxygenate activity at reduced treatment temperature of 400 °C, despite possessing particle of <10 nm conflicting with previous observations for TiO2 P25 supported catalysts. Furthermore, although producing incremental increases in particle size, systematic temperature increases does not extend to significant improvements in oxygenate formation or H_2O_2 decomposition rates. Similarly, the previous improvements to remaining H_2O_2 are not observed post reaction. Instead, selective oxygenate formation is observed with near- complete decomposition of H_2O_2 for all 1%AuPd/rutile catalysts. The resulting changes are therefore proposed to be changes in support effects due to heat treatment.

3.3.2 The Effect on H_2O_2 Decomposition

Although exhibiting high catalytic activity towards the selective oxidation of CH_4, the rate of H_2O_2 decomposition remains high, irrespective of treatment temperature. The absence of relationship with increasing particle size therefore suggests an effect of support upon the activity observed. Inconsistent with previous P25 materials, the higher rate of H_2O_2 decomposition for AuPd/rutile TiO_2 is consistent with work reported by Marin et al.[52] for direct synthesis of H_2O_2. Prepared by supercritical antisolvent precipitation, rutile -TiO_2 was produced by heat treatment of anatase TiO_2. Subsequent testing for direct H_2O_2 synthesis found anatase-TiO_2 to be superior to rutile, with rutile TiO_2 demonstrating higher activity for H_2O_2 degradation.[52]

Previously for P25 TiO_2, the rate of H_2O_2 decomposition was found to decrease after heat treatment (Figure 3.6 and Table 3.3). Continued reduction in consumed H_2O_2 was observed with increasing treatment temperature. Furthermore, this relationship has been linked to the selective production of oxygenates, allowing catalyst activity to be tuned by control of H_2O_2 decomposition rate. For consistency, the difference in activity for CH_4 oxidation was investigated by consideration of the effect of H_2O_2 decomposition rate for rutile supported AuPd.

Using an aqueous solution of H_2O_2 (0.5M, 10 mL), determination of H2O2 decomposition was carried out under ambient temperature (24 °C) and pressure (1 atm, air). The mass of catalysts used during testing was fixed at 10 mg and added to the stirred aqueous solution (1000 rpm). Stirring rate was maintained throughout testing. At regular intervals, H_2O_2 decomposition was determined through analysis of the aqueous reaction solution as a function of time. Time-on-line analysis is illustrated in appendix Figure A7.2and rate of decomposition presented in Table 3.6.

Characteristic of prepared parent catalyst, both RT and 70 ˚C rutile -series exhibit high rates of H_2O_2 decomposition. Forming extended agglomerates of AuPd, the origin of high

activity for H_2O_2 decomposition originates from the reduced oxidation state produced during catalysts preparation, in contrast to previous P25 supported catalyst. This again highlights the crucial influence of Pd oxidation state upon catalyst activity for H_2O_2 decomposition and CH_4 oxidation. Even so, H_2O_2 concentration is reduced to <10% after *ca.* 15 minutes for 1%AuPd/rutile-70-dried, and *ca.* 10 minutes for RT catalyst. Producing an onset in activity for selective oxidation of CH_4, heat treatment at 400 ˚C notably reduces H_2O_2 decomposition rates of both RT and 70 ˚C series. This is consistent with previous P25 catalyst series, however, unlike previous catalysts further increasing treatment temperature to 600 °C and 800 °C does not yield any continuing improvements.

Table 3.6: Relative rates of H_2O_2 decomposition and elemental surface composition data determined for1 wt.%AuPd/ rutile TiO_2/rutile. Entries 1-4: prepared at room temperature, entries 5-8: prepared at 70 ˚C

Entry	Catalyst	Sel. Oxy. [μmol]	Oxy. Sel. [%]	Mean Particle Size[a] [nm]	H_2O_2 Decomp. Rate[b] [μmol min^{-1}]	Surface Elemental Composition[c]		
						AuPd /Ti	Pd Species[d][%]	
							Pd^{2+}	Pd^0
1	RT, dried	0	0	n/a	830	0.065	0	100
2	RT, 400 ˚C	0.26	47.9	8.7 ±3.9	251	0.059	52.0	48.0
3	RT, 600 ˚C	0.59	65.4	10.4 ±2.3	147	0.038	58.4	41.6
4	RT, 800 ˚C	0.66	83.4	19.6 ±5.9	317	0.027	52.7	47.3
5	70 ˚C, dried	0	0	n/a	529	0.040	0	100
6	70 ˚C, 400 ˚C	0.92	86.2	8.0 ±2.4	236	0.037	37.1	62.9
7	70 ˚C, 600 ˚C	1.03	87.1	10.8 ±7.9	243	0.029	39.6	60.4
8	70 ˚C, 800 ˚C	1.11	86.5	22.6 ±10.7	157	0.019	40.5	59.5

[a] Determined by transmission electron spectroscopy. [c] Determined by x-ray photoelectron spectroscopy and calibrated to Carbon 1s region (284.4 eV). [d] Calculated as (Pd species/total Pd species)x100. Sel. Oxy.: Selective oxygenates, Oxy. Sel.: Oxygenate selectivity, Decomp.: Decomposition.

Decreasing to 251 μmoles min^{-1} with treatment at 400 ˚C, treatment of 1%AuPd/rutile-RT at 600 ˚C reduces the decomposition rate to 147 μmoles min^{-1}. This decrease is not observed when the parent catalyst is treated at 800 ˚C, instead exhibiting a higher rate of 317 μmoles min^{-1} for 1%AuPd/rutile-RT-800 ˚C. Heat treatment of the parent 1%AuPd/rutile-70-dried catalyst at 400 ˚C and 600 ˚C sees similar activities of 236 μmoles min^{-1} and 248 μmoles min^{-1}, respectively. However, treatment at 800 ˚C does see improvement to 157 μmoles min^{-1}.

Although exhibiting inconsistent activities for the decomposition of H_2O_2, a relationship between H_2O_2 decomposition rate and oxygenate formation is still present for rutile supported AuPd (Figure 3.17(a)). Even so, the intrinsic activity of AuPd nanoparticles continues to increase, similarly to P25 supported catalysts. For catalysts heat treated at 400 °C and 600 °C, similar activities are observed for the decomposition of H_2O_2 but not

for the oxidation of CH_4. Calcination at 800 °C sees a marked difference for both RT and 70 °C rutile supported catalysts when compared with P25 counterparts, seeing a 4 -fold and 2 -fold increase, respectively (Figure 3.17(b)). The reduction of decomposition rate to below 300 µmoles min^{-1} results in the onset of selective oxygenates observed after treatment at 400 ˚C.

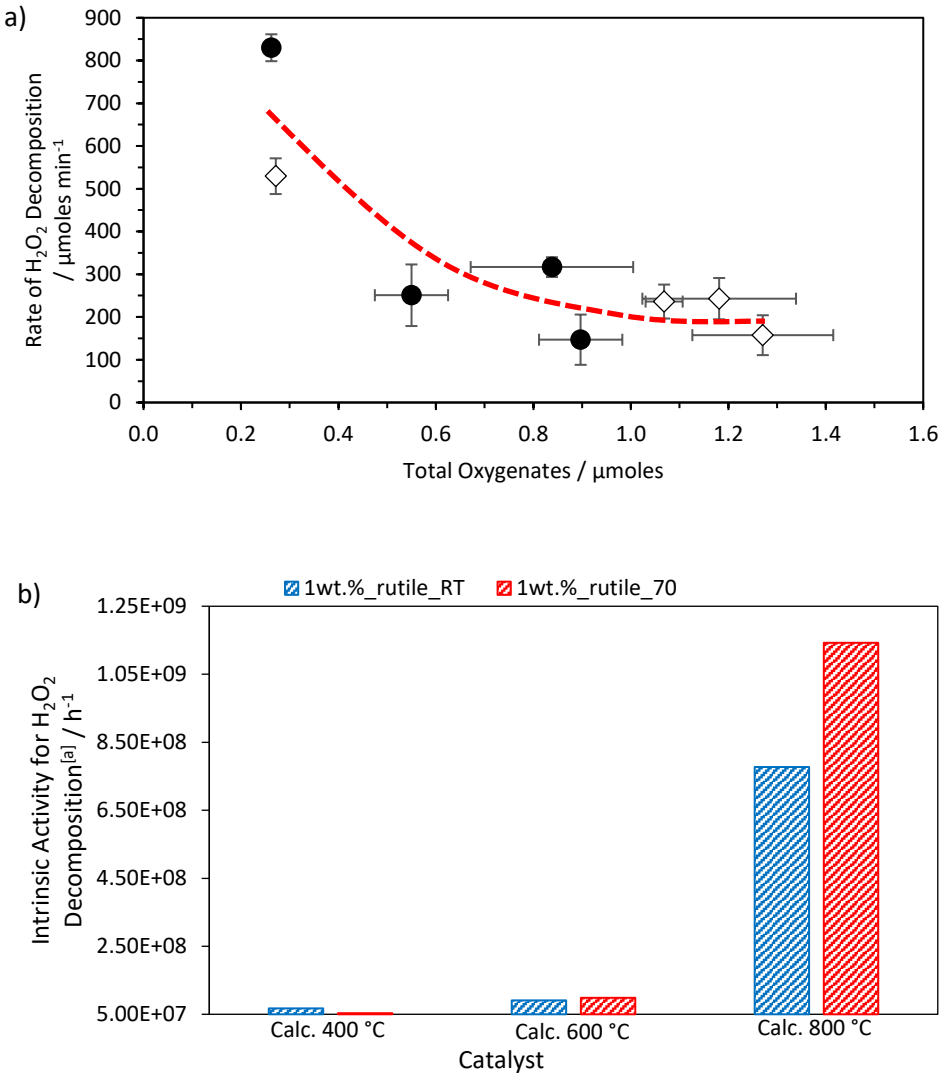

Figure 3.17: Structure-activity relationship for 1 wt.% AuPd/TiO_2 (rutile) catalyst series for methane oxidation: (a) correlating H_2O_2 decomposition rate with total oxygenates produced after 0.5 h b) The intrinsic activity of AuPd for the decomposition of H_2O_2, showing that larger mean particles size possess higher activity for H_2O_2 decomposition. ● = RT and ◊ = 70 °C.

Standard reaction conditions: time: 30 minutes, temperature: 24 °C, stirring rate: 1000 rpm, all catalysts (1 wt. % total): 7.24x10^{-7} mol of metals equal to 10 mg of solid catalysts, volume: 10 mL of H_2O.[H_2O_2]: 0.5 M [a] calculated as $Moles_{(H2O2\ decomposed)}/Moles_{(metal\ surface\ atoms)}/time\ (h)$

Varying from the P25 TiO_2 analogues, however, the relationship between H_2O_2 decomposition activity and mean particles size is not as apparent. Inspection of catalyst series prepared at 70 ˚C shows marginal decrease in deleterious activity with increasing nanoparticle size, although within experimental error. This contrasts with RT rutile catalyst series which sees no clear correlation. Possessing AuPd nanoparticles with mean size *ca.* 10.4 nm, 1%AuPd/rutile-RT-600 ˚C decomposes H_2O_2 with a rate of 147 μmoles min^{-1}. Meanwhile, treatment at 800 ˚C produces significantly larger nanoparticles sizes at *ca.* 19.6 nm but exhibit a higher H_2O_2 decomposition rate of 316 μmoles min^{-1}. This is

This effect may originate from the relative composition of Pd species present in 600 ˚C and 800 ˚C treated catalysts. Surface elemental composition, shown in Table 3.7 (Entries 2-4), suggests that deleterious Pd^0 is less prevalent in 1%AuPd/rutile-RT-600 ˚C (*ca.* 41%, Entry 3) compared with 1%AuPd/rutile-RT-800 ˚C (48%, Entry 4). This *ca.* 6% increase in surface Pd^0 species, is in addition to the increase in nanoparticle size. Therefore, an increase in deleterious Pd^0 results in the increase in decomposition rate. Contrasting catalyst produced using P25 TiO_2, the increase in AuPd nanoparticle size is observed in AuPd:Ti ratio determined by XPS analysis (Table 3.6). For 1wt.%_rutile_RT, the increase in particle size results in a decrease in AuPd ratio from 0.065 for parent catalysts to 0.027 in 800 c heat treated catalysts.

Table 3.7: Surface elemental composition of 1 wt. % AuPd/rutile TiO_2 catalysts and calculated intrinsic activity for the oxidation of methane. Entries 1-4: prepared at room temperature, Entries 5-8: prepared at 70 °C.

Entry	Catalyst	Surface Elemental Composition[a] Binding Energy [eV]			SEM-EDX Metal loading		MP-AES Metal Loading		Intrinsic Activity[b] [h^{-1}]
		Pd^{2+}	Pd^0	Au (3d)	Total [wt.%]	Au [wt.%]	Total [wt.%]	Au [wt.%]	
1	RT, dried	-	334.6	334.5	1.03	0.52	1	0.49	n/a
2	RT, 400 ˚C	336.4	334.4	334.3					$1.13x10^4$
3	RT, 600 ˚C	336.5	334.4	334.3					$3.03x10^4$
4	RT, 800˚C	336.5	334.4	334.3					$1.86x10^5$
5	70 ˚C, dried	-	334.6	334.5	0.74	0.41	0.94	0.48	n/a
6	70 ˚C, 400 ˚C	336.4	334.4	334.6					$1.98x10^4$
7	70 ˚C, 600 ˚C	336.4	334.3	334.6					$5.05x10^4$
8	70 ˚C, 800 ˚C	336.4	334.3	334.5					$4.84x10^5$

[a] Determined by x-ray photoelectron spectroscopy and calibrated to Carbon 1s region (284.4 eV). [b] Intrinsic Activity: calculated as $moles_{(Oxygenated\ Products)}/moles_{(total\ nanoparticle\ surface\ atoms)}$/time (h)

Previously, evidence for the formation of SMSI in P25 TiO_2 supported AuPd catalysts were detected by XPS, observed as a shift to higher binding energy for Pd^{II} species. The resulting electronic effect, producing an increase in binding energy, was suggested to produce the

increase in AuPd catalyst selectivity for oxygenate formation and H_2O_2 decomposition. Further contributions were thought to come from increasing nanoparticle size. In contrast to P25 analogues, the preparation and heat treatment of rutile supported catalysts sees no increase in binding energy for Pd^{II} species, as illustrated in Pd(3d) bands shown in Figure 3.18 and Figure 3.19. Consequently, the absence of SMSI electronic contribution for rutile supported catalysts may explain the observed similarity in Pd^{II}-to-Pd^{0} ratio and determined H_2O_2 decomposition rates.

For consistency with previous P25 catalysts, elemental analysis of parent catalysts by MP-AES was employed to determine actual AuPd metal loading by digestion using aqua regia. Variation in metal loading between RT and 70 ˚C series, may therefore be explained by differences in the amounts of reactive metals present. For RT preparation, the determination by MP-AES confirms expected metal loading to be 1 wt.% AuPd with the correct ratio for Au:Pd of *ca.* 1. Corroborated by EDX analysis, marginally increased amounts of Au is detected (0.52 wt.%).

Similar for P25 supported homologues, catalyst prepared at 70 ˚C displayed marginally lower amount of AuPd. Determined by MP-AES, 0.94wt.% AuPd was detected during elemental analysis. Subsequent analysis by SEM-EDX however, observed lower amounts yet, only determining 0.74 wt.% AuPd. This decrease is consistent with previous P25 catalyst and may suggest poor or unfavourable interaction of metal-support during catalyst preparation at elevated temperatures.

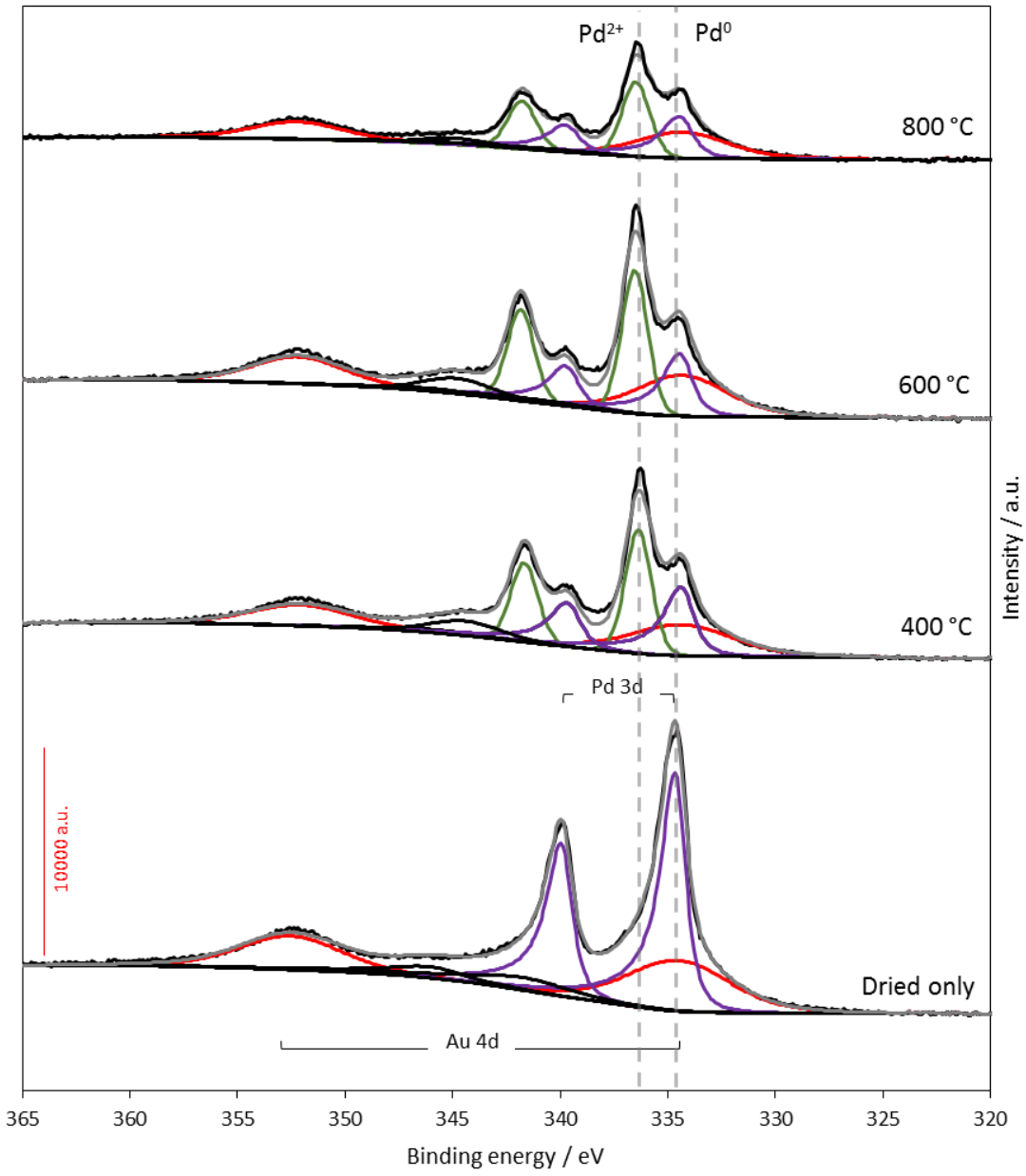

Figure 3.18: X-ray photoelectron spectra of Pd 3d region for 1 wt. % AuPd/rutile TiO_2 prepared by SI at room temperature. Pd^0 = purple line; Pd^{2+} = green line; Au 4d = red line. The dashed lines indicate the peaks due to Pd^0 and Pd^{2+}.

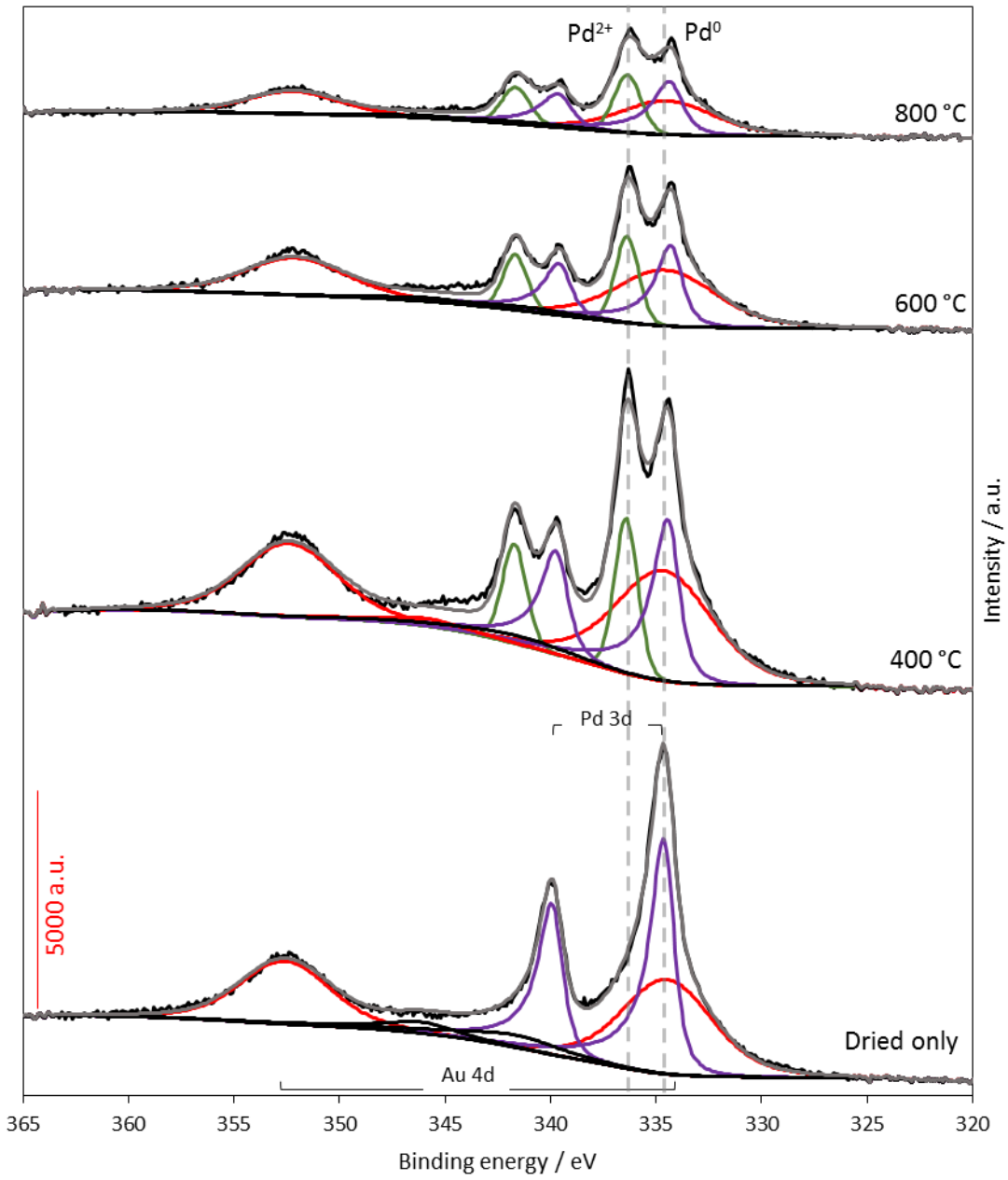

Figure 3.19: X-ray photoelectron spectra of Pd 3d region of 1 wt. % AuPd/rutile TiO_2 prepared by SI at elevated temperature (70 °C). Pd^0 = purple line; Pd^{2+} = green line; Au 4d = red line. The dashed lines indicate the peaks due to Pd^0 and Pd^{2+}.

3.4 The Effect of Surface Area: Metal Loading Ratio

Previously, initial investigations began by considering the role of particle size on 1 wt.% AuPd/ TiO_2 (P25) catalysts. Possessing a surface area of 45 m^2 g^{-1}, considerable activity for CH_4 oxidation was only achieved after heat treatment at 800 ˚C. In addition to exhibiting a productivity of 0.312 mol kg_{cat}^{-1} h^{-1}, the transition of anatase TiO_2 to rutile TiO_2 was also observed during pXRD analysis. Consequently, to discern the effect of support from observed increases in mean particle size, the effect of TiO_2 phase was investigated by preparation of 1 wt.%AuPd/rutile TiO_2.

Utilising bare TiO_2 (P25), heat treatments were applied to facilitate phase transition to rutile TiO_2 prior to metal deposition. Although successful, the deposition of 1 wt.% AuPd upon a reduced surface area (*ca.* 6 m^2 g^{-1}) subsequently modified the ratio between surface area and metal loading. For P25 supported AuPd, a ratio of 0.022 wt.% AuPd m^{-2} was formed which increased to 0.167 wt.% m^{-2} when rutile TiO_2 supported was used. Although producing an increase in metal loading per area, the heat treatment of rutile supported AuPd produced catalyst which displayed marked differences in catalyst activity to P25 supported TiO_2. Displaying comparable productivities across all employed temperature treatments within a catalyst, the productivities achieved were only matched by treatment of P25 catalysts at 800˚ C. Even so, deleterious activity towards H_2O_2 decomposition was consistently observed, in contrast to P25 catalyst which observed beneficial improvements to remaining H_2O_2 after each successive treatment. The significance of metal loading per area for rutile supported catalysts was, therefore, investigated by preparation of lower metal loading catalyst, to discern further influences of rutile TiO_2 support. The preparation of a nominal 0.13 wt.% AuPd/ rutile TiO_2 allows the comparable 0.22 wt.% AuPd m^{-2} to be investigated, consistent with 1 wt.% AuPd/ TiO_2 (P25).

3.4.1 The Effect of Catalyst on Methane Oxidation Activity

Although prepared with reduced metal loading (0.13 wt.% AuPd/rutile TiO_2), Figure 3.20(a) shows that the agglomeration of AuPd nanoparticles is still observed. The repetition of this phenomenon may be suggestive of an influence from rutile TiO_2 support, not observed in P25 TiO_2. Analogous to 1wt.% AuPd/rutile TiO_2, the formation of selective oxygenates is not observed with use of dried only parent catalyst. Only small quantities of CO_2 were detected (0.22 µmol) and *ca.* 9% H_2O_2 remaining post reaction (Figure 3.21).

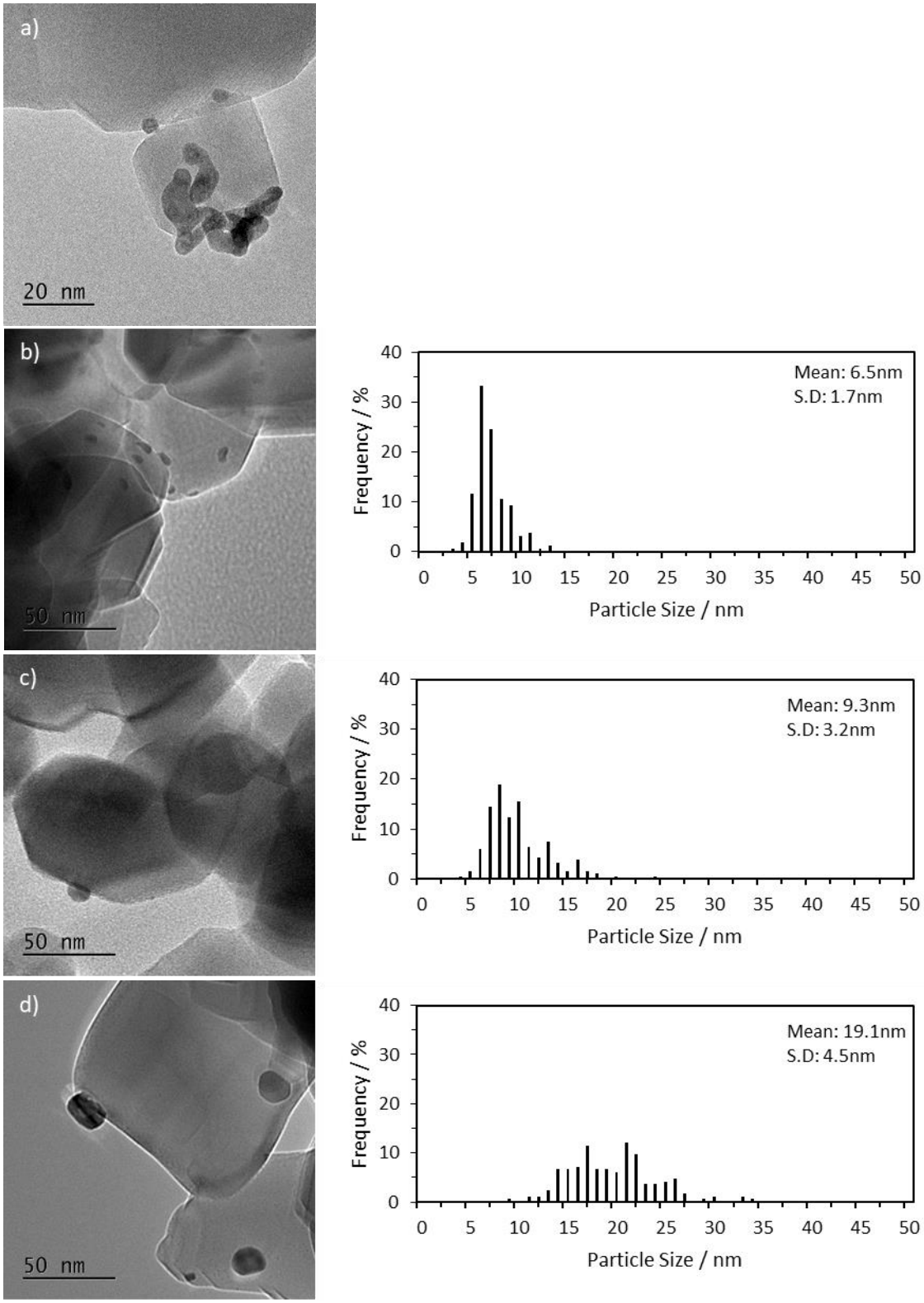

Figure 3.20: Transmission electron microscopy of 0.13 wt. % AuPd/ rutile TiO_2 (SI) prepared at room temperature; (a) Dried, (b) calcined at 400 °C, (c) 600 °C and (d) 800 °C.

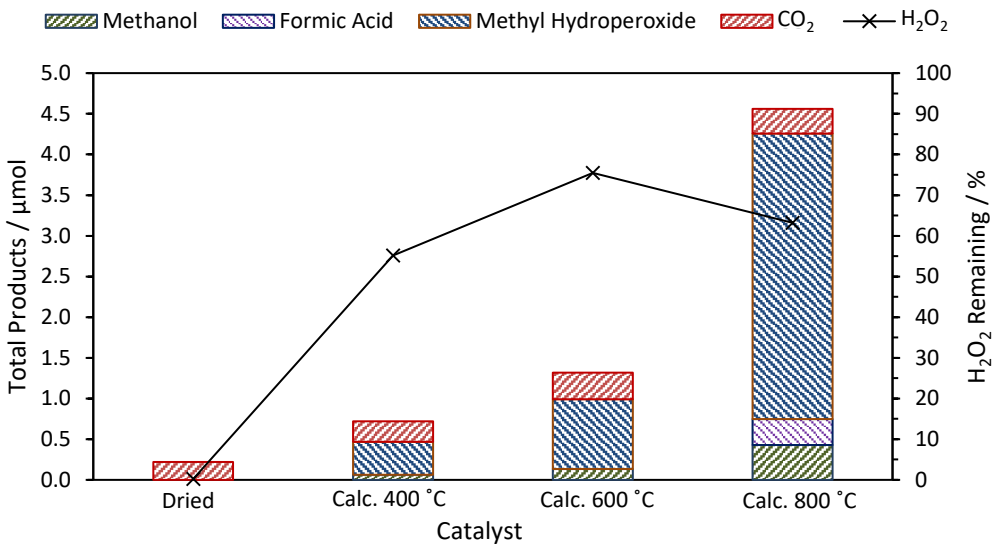

Figure 3.21: Comparison of the effect of post synthesis heat treatment on 0.13 wt. % AuPd/rutile TiO_2 prepared by SF-S_i at room temperature on the catalytic activity for methane oxidation.

Standard reaction conditions: time: 30 minutes, temperature: 50 °C, P_{CH_4}: 30.5 bar, stirring rate: 1500 rpm, all catalysts (0.13 wt. % total): 9.41 x10^{-8} mol of metals equal to 10 mg of solid catalysts, volume: 10 mL of H_2O.[H_2O_2]: 0.5 M

The onset of selective oxygenate formation is observed after 400 ˚C heat treatment, similarly to previous rutile -supported catalysts, additionally observing the formation of hemispherical nanoparticles (Figure 3.20(b)). Possessing mean particle size of 6.5 nm, CH_4 oxidation leads to predominantly CH_3OOH (0.4 µmoles), achieving oxygenate selectivity *ca.* 65% with low levels of CO_2 observed (0.25 µmol). Although possessing reduced metal loading, selective oxygenate formation improves upon previously tested 1%AuPd/rutile-RT-400 ˚C, producing 0.47 µmol selective oxygenates compared to 0.26 µmoles for 1%AuPd catalyst. Moreover, a significant amount H_2O_2 remains post reaction (*ca.* 55%), indicating reduced activity for the decomposition of H_2O_2.

Increasing the temperature of heat treatment to 600 ˚C, shows continued enhancement to catalyst activity towards selective CH_4 oxidation. Furthermore, activity continues to be an improvement on 1%AuPd/rutile-RT-400 ˚C and comparable with 1%AuPd/rutile-70-600 ˚C. Achieving 75 % oxygenate selectivity, *ca.* 1 µmole of selective oxygenates are produced by 0.13%AuPd/rutile-RT-600 ˚C, with selectivity CH_3OOH (86.7%). The improvement to productivity compared to 0.13%AuPd/rutile-RT-400 ˚C (0.25 µmol kg_{cat}^{-1} h^{-1} vs 0.14 µmol kg_{cat}^{-1} h^{-1}) follows an increase in mean particle size (*ca.* 9.3 nm) (Figure 3.20(c)). Similarly, a greater quantity of remaining H_2O_2 was detected post reaction (75.5%), in contrast to previous 1%AuPd/rutile catalyst which showed almost complete consumption (<25% remaining).

Notably, the most significant improvement in catalyst activity is observed at 800 ˚C heat treatment. Surpassing all tested SF-S_i catalyst, 0.13%AuPd/rutile-RT-800 ˚C possesses a productivity of 0.90 µmoles kg_{cat}^{-1} h^{-1}, producing 3.16 µmoles of selective oxygenates after 30 minutes. With 93 % oxygenate selectivity, product selectivity remains with CH_3OOH formation at 77 %. Interestingly, formation of formic acid (HCOOH) is observed (0.32 µmoles), produced by the successive over-oxidation of CH_3OH.[62] Post reaction analysis of remaining H_2O_2 (63%) shows an increase in consumed H_2O_2, despite continued increase in mean particle size to *ca.* 19 nm (Figure 3.20(d)). The higher consumption of H_2O_2, however, may result from the significant increase in oxygenates produced. This is evidenced by corresponding gain factors for 0.13%AuPd/rutile-RT-800 ˚C and -600 ˚C catalyst, calculated at 2.3x10^{-3} and 8x10^{-4} $\mu moles_{oxygenates} \mu moles^{-1}_{H_2O_2\ consumed}$ respectively.

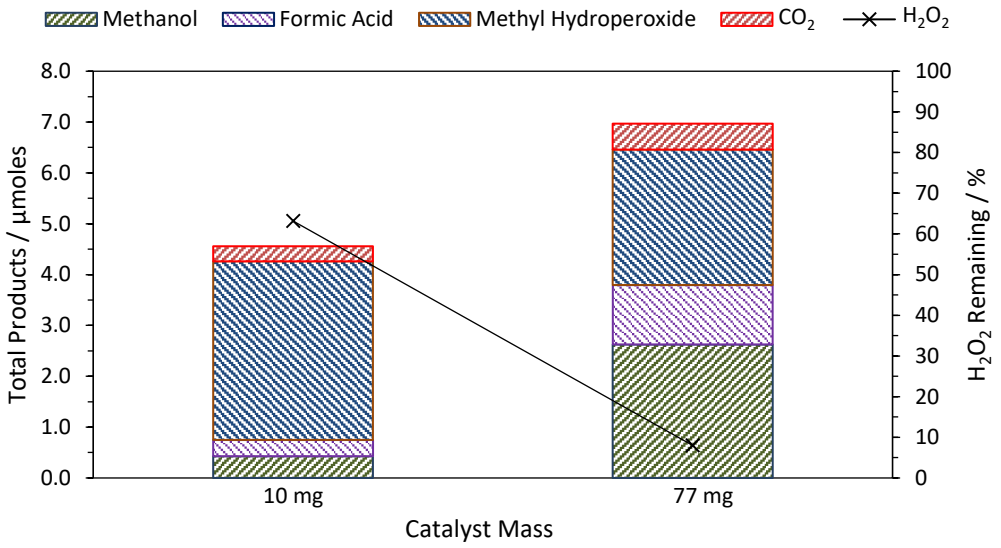

Figure 3.22: Comparison of the effect of catalyst mass for 0.13 wt. % AuPd/rutile TiO_2 prepared by SF-S_i at room temperature on the catalytic activity for methane oxidation.

Standard reaction conditions: time: 30 minutes, temperature: 50 °C, P_{CH_4}: 30.5 bar, stirring rate: 1500 rpm, all catalysts (0.13 wt. % total): 9.41 x10^{-8} mol of metals equal to 10 mg of solid catalysts or 7.24 x10^{-7} mol of metals equal to 77 mg of solid catalysts, volume: 10 mL of H_2O.[H_2O_2]: 0.5 M

The reduction of AuPd metal loading upon rutile support produces a significant improvement in catalyst productivity compared with previous 1 wt.% AuPd/ TiO_2 for 800 ˚C heat treated catalyst. Importantly, the unfavourable loss of H_2O_2 due to decomposition is reversed by reduction of metal loading to 0.13 wt.% AuPd. Subsequently, the decrease in deleterious activity can be concluded to result from the reduction of metal species. This effect is illustrated in Figure 3.22, whereby increase of 0.13 wt.% AuPd/rutile-RT-800 ˚C catalyst mass to produce comparable moles of metal to 1wt.% AuPd/rutile TiO_2 leads to a

drastic increase in H_2O_2 consumed. Even so, the catalyst activity is expectedly increased, but the *ca.* 7.5 -fold increase to catalyst loading, and increase in reactive metal species, only improves catalyst activity by a factor of 1.5. Producing *ca.* 7 µmoles of total oxygenates with comparable 92% oxygenate selectivity, selectivity to CH_3OH is increased from <10% to 37%. This shift of selectivity was similarly observed by Ab Rahim *et al.*[19], resulting in selectivity towards CH_3OOH (*ca.* 73%) for 1 wt. AuPd/TiO_2 but transitioning to CH_3OH (*ca.* 49%) when using 5wt.% AuPd/TiO_2.

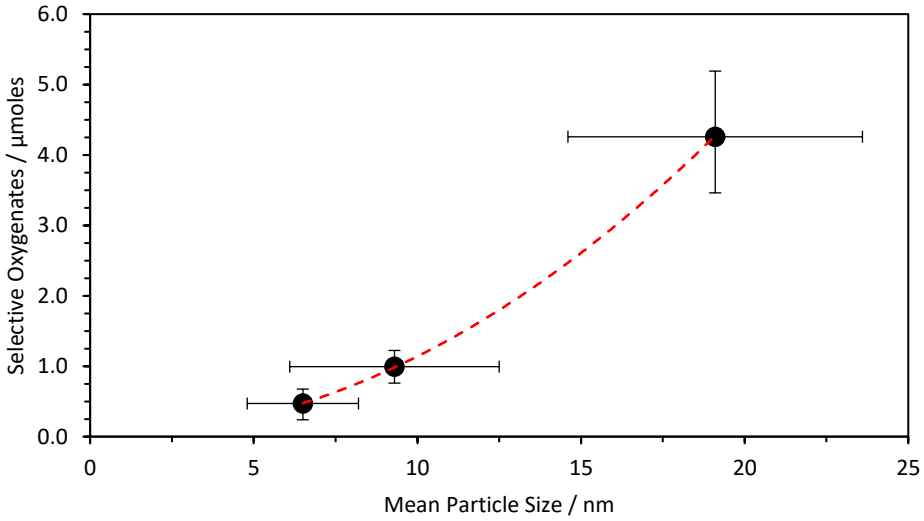

Figure 3.23: Structure-activity relationship of 0.13 wt.% AuPd/rutile TiO_2 for methane oxidation, illustrating the relationship between mean particle size and selective oxygenate formation. ● = RT

The relationship between selective oxygenate formation and increasing mean particle size is again observed for 0.13 wt.% AuPd/rutile TiO_2, illustrated in Figure 3.23. Comparably with P25 -supported catalysts, a strong correlation is observed. Although reduced metal loading is employed, interestingly, mean particle size are consistent with previous 1wt.% AuPd catalysts. Initial formation of agglomerated AuPd is consistent with previous rutile support, strongly suggesting an influence of rutile surface upon forming nanoparticles. However, heat treatment at 400 ˚C, facilitates formation of hemispherical AuPd nanoparticles with mean nanoparticle of 6.5 nm. Similarly, heat treatment at 600 ˚C and 800 ˚C increases nanoparticles to *ca.* 9.3 nm and *ca.* 19.1 nm. The resulting particle size distribution of produced nanoparticles are approximate to those displayed in previous catalysts. With lower quantities of reactive metal species, the increased activity must originate from the influence of rutile TiO_2 support.

3.4.2 The Effect on H_2O_2 decomposition

Predictably for 0.13 wt.% AuPd/rutile TiO_2, the reduction in the quantity of reactive metals shows significant decrease in the disadvantageous activity for H_2O_2 decomposition. This observation supports previously reported works by Han *et al.*[63] and Landon *et al.*[64], demonstrating the proportional rise in H_2O_2 hydrogenation produced when increasing catalyst mass. Represented in appendix Figure A7.3, the high activity characteristic of the parent dried only catalyst is observed. Possessing only Pd^0 (Table 3.6, Entry 1), H_2O_2 is decomposed at higher rates to subsequent heat-treated catalysts. However, *ca.* 45% H_2O_2 remains after 30 minutes, in contrast to previous 1wt.% parent catalysts with typically <10% remaining, evidence of the reduced number of available active species. Expectedly, heat treatment of parent catalyst saw significant reduction to unfavourable H_2O_2 decomposition, as evidenced during testing for CH_4 oxidation which saw improvements to selective oxygenate formation (Figure 3.21). In previous RT prepared rutile supported AuPd catalyst (Table 3.7, Entries 2-4), the presence of *ca.* 48% Pd^0 was identified as the source of high activity towards H_2O_2 decomposition. Stabilised by the rutile support, increasing heat treatment did not minimise the presence of deleterious Pd species, with 47% Pd^0 present after calcination of RT catalysts at 800 ˚C.

Table 3.8: Relative rates of H_2O_2 decomposition and elemental surface composition data determined for0.13% AuPd/rutile. Entries 1-4: prepared at room temperature.

Entry	Catalyst	Total Oxy. [µmol]	Oxy. Sel. [%]	Mean Particle Size[a] [nm]	H_2O_2 Decomp. Rate[b] [µmol min^{-1}]	Surface Elemental Composition[c] AuPd /Ti	Pd Species[d] [%] Pd^{2+}	Pd Species[d] [%] Pd^0
1	RT, dried	0	0	n/a	242	0.015	0	100
2	RT, 400 ˚C	0.47	64.8	6.5 ±1.7	11	0.009	70.6	29.4
3	RT, 600 ˚C	0.99	75.0	9.3 ±3.2	26	0.010	73.9	26.1
4	RT, 800 ˚C	4.56	93.2	19.1 ±4.5	21	0.008	74.6	25.4

[a] Determined by transmission electron spectroscopy. [b] H_2O_2 decomposition reaction conditions: time: 30mins, temperature: 24 °C, atmospheric pressure, stirring rate: 1000rpm, all catalysts (0.13 wt. % total): $9.41x10^{-8}$ mol of metals equal to 10 mg of solid catalysts, volume: 10 mL of H_2O.[H_2O_2]: 0.5 M. [c] Determined by x-ray photoelectron spectroscopy and calibrated to Carbon 1s region (284.4 eV). [d] Calculated as (Pd species/total Pd species)x100. Total Oxy.: Total oxygenates, Oxy. Sel.: Oxygenate selectivity, Decomp.: Decomposition.

A similar stabilisation of Pd^0 is observed for 0.13 wt.% AuPd/rutile TiO_2, although, detected Pd species is comprised of *ca.* 30% Pd^0 (Table 3.8, Entry 1). Therefore, decreased activity for unwanted decomposition of H_2O_2 is ascribed to the reduction in not only total metal species, but also deleterious Pd^0. The resulting combination produces catalyst materials which display *ca.* 95% of initial H_2O_2 concentrations remaining post reaction. Furthermore, the reduced loading of metal limits the detection of increasing metal nanoparticle size by XPS analysis. This is evident with similar AuPd:Ti ratios (*ca.* 0.010) for heat treated catalysts. The detected activity for H_2O_2 decomposition is consistent

between heat treated catalysts, showing decomposition with *ca.* 11 - 25 µmoles min^{-1} (Table 3.8, Entries 2-4).

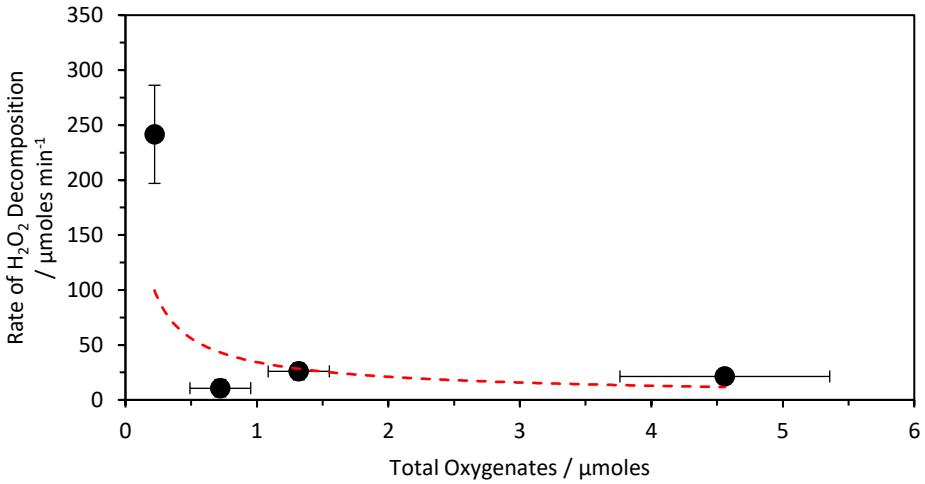

Figure 3.25: Structure-activity relationship for 0.13 wt.% AuPd/TiO_2 (rutile) catalyst series for methane oxidation correlating H_2O_2 decomposition rate with total oxygenates produced after 0.5 h, ● = RT

Displaying minor variations in catalytic activity towards H_2O_2 decomposition, the effect of heat treatment upon H_2O_2 decomposition rates share no correlation with mean particle size (Figure A7.6). This effect is observed despite increasing intrinsic activity of AuPd nanoparticles for the decomposition of H_2O_2 (Figure A7.7). This observation is consistent with previous rutile supported catalysts. For total oxygenate formation, the reduction in H_2O_2 decomposition suggests correlation with increased oxygenate formation (Figure 3.25). However, possessing similar decomposition rates for all heat treatmented 0.13wt.% catalysts suggests that further influences from support results in the increased activity for selective oxygenates observed. Consistent with previous rutile supported AuPd catlysts, the influence from SMSI electronic contributions are not observed during XPS analysis of Pd(3d) region (Figure 3.26).

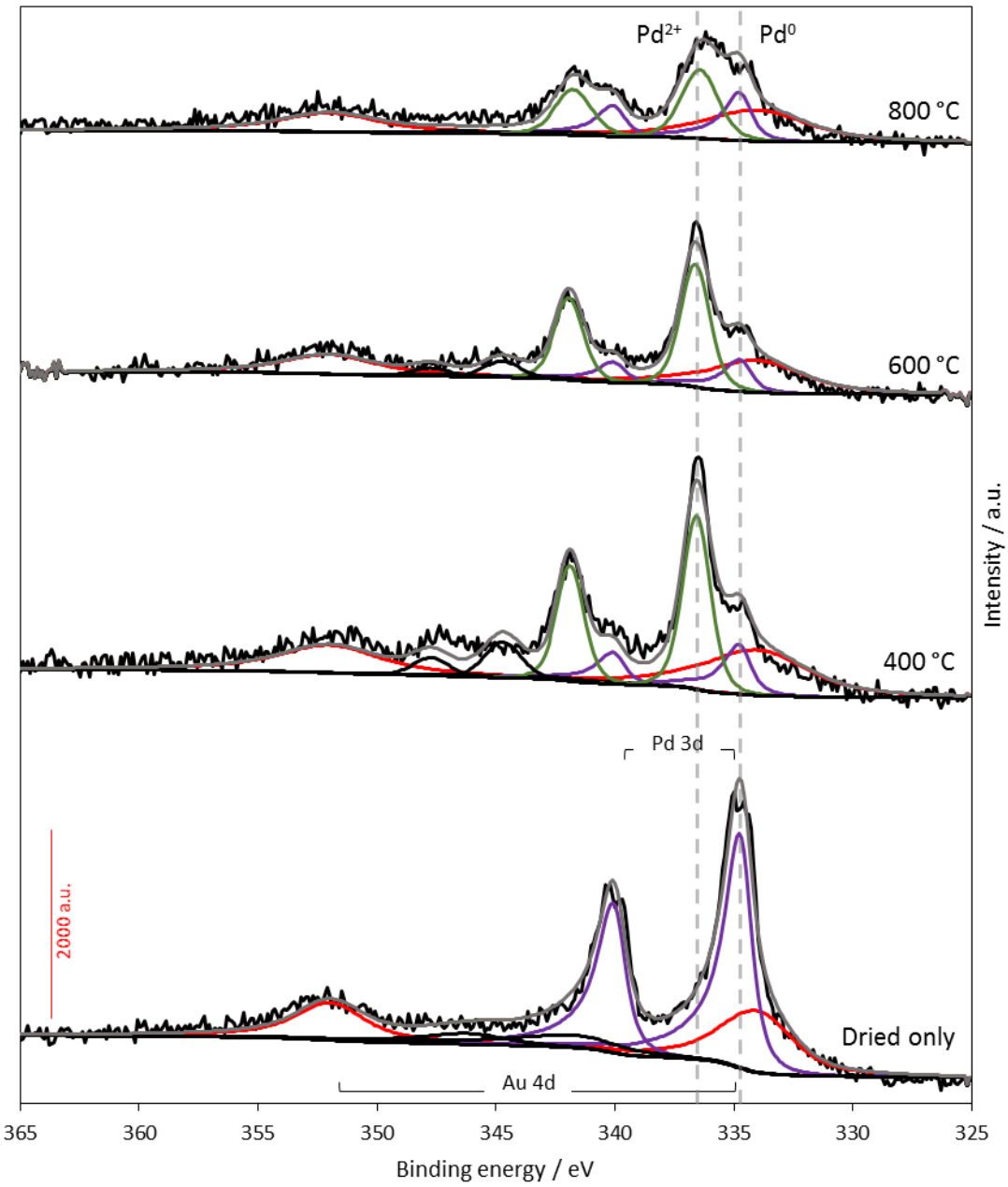

Figure 3.26: X-ray photoelectron spectra of Pd (3d) region for 0.13 wt. % AuPd/ rutile TiO_2 prepared SI at room temperature. Pd^0 = Purple; Pd^{2+} = green line; Au 4d = red line. Peak contribution due to Pd^0 and Pd^{2+} are highlighted via dashed lines.

Table 3.9: Relative rates of H_2O_2 decomposition and elemental surface composition data determined for 0.13% AuPd/rutile and calculated intrinsic activity for the oxidation of methane. Entries 1-4: room temperature.

Entry	Catalyst	Surface Elemental Composition[a] Binding Energy [eV]			MP-AES Metal Loading		Corr. TOF[b] [h^{-1}]
		Pd^{2+}	Pd^0	Au (4f)	Total [wt.%]	Au [wt.%]	
1	RT, dried		334.8	83.2	0.11	0.1	n/a
2	RT, 400 ˚C	336.6	334.8	83.4			$7.83x10^4$
3	RT, 600 ˚C	336.6	334.7	83.3			$3.92x10^5$
4	RT, 800 ˚C	336.4	334.7	83.2			$1.13x10^7$

[a] Determined by x-ray photoelectron spectroscopy and calibrated to Carbon 1s region (284.4 eV). [b] Intrinsic Activity: calculated as $moles_{(Oxygenated\ Products)}/moles_{(total\ nanoparticle\ surface\ atoms)}$/time (h)

Elemental analysis carried out by MPAES detected total loading of 0.11wt.% AuPd, predominantly comprised of Au (0.1 wt.%) (Table 3.9). Subsequently, determined Au: Pd ratio was calculated to be 10, however, these very low loadings may reside at the limit of reliable detection and quantification, as noted for similarities in AuPd:Ti ratios. Similarly, confirmation by SEM-EDX was not possible due to the low loadings used. Even so, producing slightly lower weight loading of Pd results in further decreased activity for decomposition of H_2O_2, with increased Au:Pd ratio potentially producing the enhanced activity for selective oxygenate formation.

3.5 Conclusions

The selective oxidation of CH_4 to CH_3OH, using preformed H_2O_2, under mild reaction condition was studied using bimetallic 1wt.% AuPd/TiO_2 (P25). Utilising a stabiliser-free sol immobilisation methodology, the influence of particle size was evaluated by modification of nanoparticle size via post synthesis heat treatment of the parent dried only catalyst.

Subsequent testing of heat treated P25 supported catalysts observed an increase in selective oxygenate formation. The decrease in deleterious activity for the decomposition of H_2O_2, proposedly due to increasing size, was suggested to increase catalysts selectivity for utilisation of H_2O_2 leading to selective oxygenate formation.

However, despite increasing nanoparticle size, the greatest improvements in the formation of selective oxygenates occurred after the phase transition of predominantly anatase P25 TiO_2 to rutile TiO_2. Further characterisation revealed an electronic influence with transition to rutile TiO_2, observed as increasing binding energy for Pd^{II} species in the Pd(3d) bands. The electronic influences were proposed to be due to strong metal-support interactions induced by heat treatments Attempts to deconvolute the influence of support from particle size effects were trialled by preparation of rutile supported AuPd catalysts.

Demonstrating marked differences in catalysts activity, rutile supported materials displayed improved activity for selective CH_4 oxidation. The efficient use of H_2O_2 during testing was not observed, with near complete decomposition of H_2O_2. The deleterious behaviour continued despite increasing nanoparticle size, contrasting previous P25 catalysts. Analysis for SMSI electronic contributions via XPS analysis did not reveal any change in binding energy for Pd^{II} species with heat treatment. The distinct differences observed between P25 and rutile supported are evidenced by the absence of electronic SMSI contribution and no correlation to particle size.

To address the high decomposition rates displayed by rutile supported $TiO_2$the proportional reduction of metal loading was carried out. The resulting reduction of active metal loading produced significant improvements to catalyst activity for CH_4 oxidation and improvements in H_2O_2 selectivity.

Overall, the following work has shown evidence that the influence of support plays a critical role in the activity displayed by AuPd particles. Initially investigating the influence of nanoparticle size, the absence of correlation in markedly active rutile supported AuPd catalysts suggests that support interaction via SMSI is the determining factor. Adventitiously, this influence can be utilised to produce catalysts with significant activity for CH_4 oxidation, whilst demonstrating efficient use of preformed H_2O_2 with reduced

metal loading. However, these results are hoped to help inform of future catalytic design considerations for the selective oxidation of CH_4.

3.6 References

1 H. J. H. Fenton, *J. Chem. Soc., Trans.*, 1894, **65**, 899–910.

2 A. E. N. F. Goldshle, A. A. Shteinman and V. V. E. Shilov, *Russ. J. Phys. Chem. USSR*, 1972, **46**, 785–786.

3 A. E. Shilov and G. B. Shul'pin, *Chem. Rev.*, 1997, **97**, 2879–2932.

4 M. Haruta, T. Kobayashi, H. Sano and N. Yamada, *Chem. Lett.*, 1987, **16**, 405–408.

5 T. Hayashi, K. Tanaka and M. Haruta, *J. Catal.*, 1998, **178**, 566–575.

6 M. D. Hughes, Y.-J. Xu, P. Jenkins, P. McMorn, P. Landon, D. I. Enache, A. F. Carley, G. A. Attard, G. J. Hutchings, F. King, E. H. Stitt, P. Johnston, K. Griffin and C. J. Kiely, *Nature*, 2005, **437**, 1132.

7 L. Prati and M. Rossi, *J. Catal.*, 1998, **176**, 552–560.

8 A. Abad, P. Concepción, A. Corma and H. García, *Angew. Chemie Int. Ed.*, 2005, **44**, 4066–4069.

9 S. Carrettin, P. McMorn, P. Johnston, K. Griffin and G. J. Hutchings, *Chem. Commun.*, 2002, 696–697.

10 P. Landon, P. J. Collier, A. J. Papworth, C. J. Kiely, G. J. Hutchings, J. Kiely and J. Graham, *Chem. Commun.*, 2002, 2058–2059.

11 J. K. Edwards and G. J. Hutchings, *Angew. Chemie Int. Ed.*, 2008, **47**, 9192–9198.

12 D. I. Enache, J. K. Edwards, P. Landon, B. Solsona-Espriu, A. F. Carley, A. A. Herzing, M. Watanabe, C. J. Kiely, D. W. Knight and G. J. Hutchings, *Science*, 2006, **311**, 362 -365.

13 Q. He, P. J. Miedziak, L. Kesavan, N. Dimitratos, M. Sankar, J. A. Lopez-Sanchez, M. M. Forde, J. K. Edwards, D. W. Knight, S. H. Taylor, C. J. Kiely and G. J. Hutchings, *Faraday Discuss.*, 2013, **162**, 365–378.

14 J. K. Edwards, B. E. Solsona, P. Landon, A. F. Carley, A. Herzing, C. J. Kiely and G. J. Hutchings, *J. Catal.*, 2005, **236**, 69–79.

15 M. Taramasso, G. Perego, B. Notari, *Preparation of porous crystalline synthetic material comprised of silicon and titanium oxides*, **1983**, *US4410501A*.

16 G. B. Shul'pin and Y. N. Kozlov, *Org. Biomol. Chem.*, 2003, **1**, 2303–2306.

17 N. Mizuno, Y. Seki, Y. Nishiyama, I. Kiyoto and M. Misono, *J. Catal.*, 1999, **184**, 550–552.

18 C. Hammond, M. M. Forde, M. H. Ab Rahim, A. Thetford, Q. He, R. L. Jenkins, N. Dimitratos, J. A. Lopez-Sanchez, N. F. Dummer, D. M. Murphy, A. F. Carley, S. H.

Taylor, D. J. Willock, E. E. Stangland, J. Kang, H. Hagen, C. J. Kiely and G. J. Hutchings, *Angew. Chemie - Int. Ed.*, 2012, **51**, 5129–5133.

19 M. H. Ab Rahim, M. M. Forde, R. L. Jenkins, C. Hammond, Q. He, N. Dimitratos, J. A. Lopez-Sanchez, A. F. Carley, S. H. Taylor, D. J. Willock, D. M. Murphy, C. J. Kiely and G. J. Hutchings, *Angew. Chemie - Int. Ed.*, 2013, **52**, 1280–1284.

20 M. H. Ab Rahim, M. M. Forde, C. Hammond, R. L. Jenkins, N. Dimitratos, J. A. Lopez-Sanchez, A. F. Carley, S. H. Taylor, D. J. Willock, G. J. Hutchings, M. Hasbi, A. Rahim, M. M. Forde, C. Hammond, R. L. Jenkins, N. Dimitratos, J. A. Lopez-Sanchez, A. F. Carley, S. H. Taylor, D. J. Willock and G. J. Hutchings, *Top. Catal.*, 2013, **56**, 1843–1857.

21 R. A. Periana, D. J. Taube, S. Gamble, H. Taube, T. Satoh and H. Fujii, *Science*, 1998, **280**, 560–564.

22 R. A. Periana, D. J. Taube, E. R. Evitt, D. G. Löffler, P. R. Wentrcek, G. Voss, T. Masuda and D. G. L6ffler, *Science*, 1993, **259**, 340–343.

23 N. Agarwal, S. J. Freakley, R. U. McVicker, S. M. Althahban, N. Dimitratos, Q. He, D. J. Morgan, R. L. Jenkins, D. J. Willock, S. H. Taylor, C. J. Kiely and G. J. Hutchings, *Science*, 2017, **358**, 223–227.

24 C. Hammond, N. Dimitratos, J. A. Lopez-Sanchez, R. L. Jenkins, G. Whiting, S. A. Kondrat, M. H. Ab Rahim, M. M. Forde, A. Thetford, H. Hagen, E. E. Stangland, J. M. Moulijn, S. H. Taylor, D. J. Willock and G. J. Hutchings, *ACS Catal.*, 2013, **3**, 1835–1844.

25 V. C.-C. Wang, S. Maji, P. P.-Y. Chen, H. K. Lee, S. S.-F. Yu and S. I. Chan, *Chem. Rev.*, 2017, **117**, 8574–8621.

26 H. Kušić, N. Koprivanac and I. Selanec, *Chemosphere*, 2006, **65**, 65–73.

27 K. Valkaj, O. Wittine, K. Margeta, T. Granato, A. Katović and S. Zrnčević, *Polish J. Chem. Technol.*, 2011, **13**, 28–36.

28 G. Li, J. Edwards, A. F. Carley and G. J. Hutchings, *Catal. Today*, 2007, **122**, 361–364.

29 G. Li, J. Edwards, A. F. Carley and G. J. Hutchings, *Catal. Today*, 2006, **114**, 369–371.

30 S. Ranganathan and V. Sieber, *Catalysts*, 2018, **8**, 379.

31 A. Villa, D. Wang, G. M. Veith, F. Vindigni and L. Prati, *Catal. Sci. Technol.*, 2013, **3**, 3036–3041.

32 M. Signoretto, F. Menegazzo, A. Di Michele and E. Fioriniello, *Catalysts*, 2016, **6**, 87.

33 S. M. Rogers, C. R. A. Catlow, C. E. Chan-Thaw, A. Chutia, N. Jian, R. E. Palmer, M.

Perdjon, A. Thetford, N. Dimitratos, A. Villa and P. P. Wells, *ACS Catal.*, 2017, **7**, 2266–2274.

34 S. Campisi, D. Ferri, A. Villa, W. Wang, D. Wang, O. Kröcher and L. Prati, *J. Phys. Chem. C*, 2016, **120**, 14027–14033.

35 L. Prati and A. Villa, *Acc. Chem. Res.*, 2014, **47**, 855–863.

36 L. Abis, S. J. Freakley, G. Dodekatos, D. J. Morgan, M. Sankar, N. Dimitratos, Q. He, C. J. Kiely and G. J. Hutchings, *ChemCatChem*, 2017, **15**, 2914–2918.

37 G. J. Hutchings and C. J. Kiely, *Acc. Chem. Res.*, 2013, **46**, 1759–1772.

38 V. R. Choudhary, A. G. Gaikwad and S. D. Sansare, *Catal. Letters*, 2002, **83**, 235–239.

39 J. Pritchard, L. Kesavan, M. Piccinini, Q. He, R. Tiruvalam, N. Dimitratos, J. A. Lopez-Sanchez, A. F. Carley, J. K. Edwards, C. J. Kiely and G. J. Hutchings, *Langmuir*, 2010, **26**, 16568–16577.

40 J. K. Edwards, S. J. Freakley, A. F. Carley, C. J. Kiely and G. J. Hutchings, *Acc. Chem. Res.*, 2013, **47**, 845–854.

41 S. M. Rogers, C. R. A. Catlow, C. E. Chan-Thaw, D. Gianolio, E. K. Gibson, A. L. Gould, N. Jian, A. J. Logsdail, R. E. Palmer, L. Prati, N. Dimitratos, A. Villa and P. P. Wells, *ACS Catal.*, 2015, **5**, 4377–4384.

42 V. R. Choudhary, S. D. Sansare and A. G. Gaikwad, *Catal. Letters*, 2002, **84**, 81–87.

43 J. K. Edwards, A. Thomas, A. F. Carley, A. a. Herzing, C. J. Kiely and G. J. Hutchings, *Green Chem.*, 2008, **10**, 388–394.

44 S. Guadix-Montero, H. Alshammari, R. Dalebout, E. Nowicka, D. J. Morgan, G. Shaw, Q. He and M. Sankar, *Appl. Catal. A Gen.*, 2017, **546**, 58–66.

45 P. Munnik, P. E. De Jongh and K. P. De Jong, *Chem. Rev.*, 2015.

46 C. J. Pan, M. C. Tsai, W. N. Su, J. Rick, N. G. Akalework, A. K. Agegnehu, S. Y. Cheng and B. J. Hwang, *J. Taiwan Inst. Chem. Eng.*, 2017, **74**, 154–186.

47 S. J. Tauster, S. C. Fung and R. L. Garten, *J. Am. Chem. Soc.*, 1978, **100**, 170–175.

48 S. J. Tauster, S. C. Fung, R. T. K. Baker and J. A. Horsley, *Science*, 1981, **211**, 1121–1125.

49 S. J. Tauster, *J. Sci. Ind. Res.*, 1985, **44**, 580–587.

50 H. Tang, Y. Su, Y. Guo, L. Zhang, T. Li, K. Zang, F. Liu, L. Li, J. Luo, B. Qiao and J. Wang, *Chem. Sci.*, 2018, **9**, 6679–6684.

51 M. Sankar, Q. He, M. Morad, J. Pritchard, S. J. Freakley, J. K. Edwards, S. H. Taylor, D. J. Morgan, A. F. Carley, D. W. Knight, C. J. Kiely and G. J. Hutchings, *ACS Nano*,

2012, **6**, 6600–6613.

52 R. P. Marin, S. Ishikawa, H. Bahruji, G. Shaw, S. A. Kondrat, P. J. Miedziak, D. J. Morgan, S. H. Taylor, J. K. Bartley, J. K. Edwards, M. Bowker, W. Ueda and G. J. Hutchings, *Appl. Catal. A Gen.*, 2015, **504**, 62–73.

53 D. A. H. Hanaor and C. C. Sorrell, *J. Mater. Sci.*, 2011, **46**, 855–874.

54 J. J. Dodson and H. E. Hagelin-Weaver, *J. Mol. Catal. A Chem.*, 2015, **410**, 271–279.

55 H. Bahruji, M. Bowker, P. R. Davies, D. J. Morgan, C. A. Morton, T. A. Egerton, J. Kennedy and W. Jones, *Top. Catal.*, 2015, **58**, 70–76.

56 X.-M. Wang and Y.-Y. Xia, *Electrochim. Acta*, 2010, **55**, 851–856.

57 A. Benhmid, K. V Narayana, A. Martin, B. Lucke and M.-M. Pohl, *Chem. Commun.*, 2004, 2416–2417.

58 S. Gatla, N. Madaan, J. Radnik, V. N. Kalevaru, M.-M. Pohl, B. Lücke, A. Martin, U. Bentrup and A. Brückner, *J. Catal.*, 2013, **297**, 256–263.

59 T. Ishihara, Y. Hata, Y. Nomura, K. Kaneko and H. Matsumoto, *Chem. Lett.*, 2007, **36**, 878–879.

60 T. Ishihara, K. Shigeta, Y. Ooishi, M. Matsuka, H. Hagiwara and S. Ida, *Catal. Sci. Technol.*, 2013, **3**, 2971–2975.

61 M. J. J. Jak, C. Konstapel, A. Van Kreuningen, J. Chrost, J. Verhoeven and J. W. M. Frenken, *Surf. Sci.*, 2001, **474**, 28–36.

62 C. Hammond, R. L. Jenkins, N. Dimitratos, J. A. Lopez-Sanchez, M. H. Ab Rahim, M. M. Forde, A. Thetford, D. M. Murphy, H. Hagen, E. E. Stangland, J. M. Moulijn, S. H. Taylor, D. J. Willock and G. J. Hutchings, *Chem. - A Eur. J.*, 2012, **18**, 15735–15745.

63 Y.-F. Han and J. H. Lunsford, *J. Catal.*, 2005, **230**, 313–316.

64 P. Landon, P. J. Collier, A. F. Carley, D. Chadwick, A. J. Papworth, A. Burrows, C. J. Kiely and G. J. Hutchings, *Phys. Chem. Chem. Phys.*, 2003, **5**, 1917–1923.

Chapter 4: Hexafluorobenzene as alternative solvent media

4.1 Introduction

Used during the preparation of catalyst and liquid phase testing of catalyst processes, the consideration of solvent properties is an important variable that strongly influences the performance of a catalyst.[1] For catalysis, one ideal influence of a solvent is to improve the activation of starting reagents as a method to promote enhanced productivity.[1] Driven by increasing atmospheric CO_2 produced during anthropogenic sources, interest in the transformation of CO_2 to useful products such as formic acid is considered a potential method of addressing rising levels of CO_2. However, conventional processes indirectly hydrogenate HCO_3^- or CO_3^{2-} formed during dissolution into water, deactivating direct hydrogenation when aqueous media is utilised. Alternatively, the direct hydrogenation of CO_2 was reported by Moret *et al.*[2], using dimethyl sulphoxide (DMSO) as preferred reaction media. The substitution of solvent increased formic acid yield, producing 1.9 M formic acid (HCOOH) compared to the indirect approach with aqueous media (0.2 M).[2]

Alternatively, the unfavourable dissolution or low solubility of a reaction product within one solvent phase may facilitate the formation of a separate phase. Similarly, the introduction of a second solvent phase possessing favourable solubility for products only produces a method of simple catalyst recycling and quick product extraction, improving product selectivity.[3,4] Reported by Scott and co-workers, the catalytic hydrogenation of CO_2 to produce formate-amine adducts was carried out using a biphasic system.[5] The highly active and easily accessible *cis*-[Ru(bis-diphenylphosphinomethane)$_2$Cl$_2$] catalyst was immobilised in a hydrophobic organic solvent, achieving a TOF *ca.* 35000 h^{-1}. The aqueous phase was then used as the product phase, for simple extraction. Interestingly, *Wang et al.*[6] reported the application of thermoregulated phase transfer catalyst for a two-liquid phase system. At elevated temperatures, increased solvent solubility occurs facilitates coalescence to a single reaction phase during the catalytic process. The regulation of temperature then allowed catalyst retrieval and separation from products into one phase via thermally dependent solubility, showing preference for two-phases at decreased temperature.[6]

Comprising strong C-F bonds, the physical properties of perfluorinated solvents (PFS) make them unique for application as an inert reaction media for a wide variety of

industrial and academic applications; such as drug delivery[7], lubricant technology[8] and fuel cell and battery technology[9,10].

Characteristic of PFS, exceptionally high gas solubilities are exhibited due to low polarizability of C-F bonds, producing weak van der Waals interactions.[11–13] Importantly, the high solubility of gases such as O_2, H_2 and CH_4 make them particularly attractive for a wide variety of synthetic processes. The resulting poor solubility in water and most organic solvents have also made PFS particularly applicable for oxidation reactions using biphasic systems.[12]

Notably reported by Grubbs, Ru -catalysts provide efficient and selective catalysts for the metathesis of olefins.[14] Even so, using commercially available Ru pre-catalysts, the total synthesis of natural or biologically active compounds produces unsatisfactory conversions.[14] However, the use of aromatic PFS allowed substantially higher yields to be obtained for ring closing and cross -metathesis reactions. This benefit was similarly reported by Blechert *et al.* using hexafluorobenzene (HFB) to produce tetra-substituted olefins via ring-closing metathesis.[15] Notably, the promoting effect of HFB allowed lower Ru-catalyst loadings, producing high yields at very short reaction times.[15]

Reported by Neimann and co-worker[16], the introduction of perfluoro-propan-2-ol (PFP-2-ol) allowed electrophilic activation of H_2O_2 for the epoxidation of several alkenes, in addition to the Baeyer-Villiger oxidation of ketones. Notably, the application of PFP-2-ol removed the requirement of previously required transition metal catalysts, activating H_2O_2 to yield similar activity. Solubilised manganese catalysts were demonstrated by Vincent *et al.* in perfluoroheptane (PFH) as suitable oxidation catalysts for cyclohexene to its corresponding alcohol and aldehyde using a biphasic system.[17] Using *tert*-butyl hydroperoxide (*t*-BuOOH) in an oxygen atmosphere, cyclohexene 650 % conversion relative to *t*-BuOOH achieved, with 1:3 ratio of cyclohexanol to cyclohexanone. [17]

Reported by Lin and co-workers, the Rh- catalysed direct functionalisation of CH_4 to methanol or acetic acid using CO and O_2 at mild reaction conditions was found to be dependent upon solvent choice.[18] Demonstrating an ability to tune product selectivity, the application of 6:1 mixture of perfluoro-butyric acid and water preferentially yielded methanol (CH_3OH) and methanol derivative products ($C_3F_7CO_2CH_3$) over acetic acid (HOAc).[18] Furthermore, the substitution to Rh functionalisation of ethane demonstrated C-C bond cleavage to produce methanol, in addition to oxidation products such as ethanol, acetic acid..

Alternatively, Ohkubo *et al.* utilising a biphasic solvent system of perfluorohexane (PFH) and water successfully demonstrated the light driven oxidation of methane (CH_4) to methanol (CH_3OH) by sodium chlorite (Figure 4.1).[19] The photochemical cleavage of Cl-O bond in $ClO_2^{\cdot}$ produced highly active $Cl^{\cdot}$ radicals, in addition to singlet oxygen, which successfully abstracted H from CH_4 to produce methyl radicals, converting 99% of CH_4 (1

atm). Importantly, beyond promoting higher gas solubility of CH_4, the application of fluorous solvent also prevented deactivation of reactive radical species ($Cl^{\cdot}$ + $CH_3^{\cdot}$) by unselective H -abstraction with solvents (i.e. H_2O).[19]

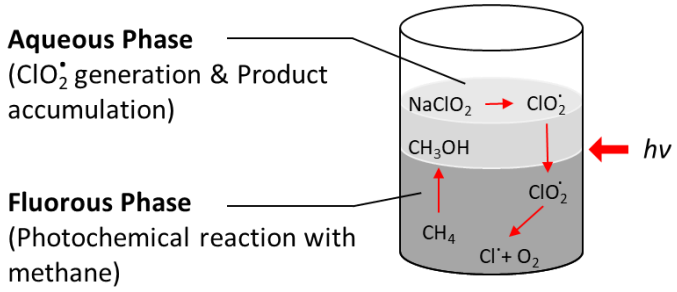

Figure 4.1: Two-phase system for the photo-oxidation of CH_4 by $ClO_2^{\cdot}$ dissolved as $NaClO_2$ in aqueous system, with CH_4 soluble in fluorous phase. Adapted from Ohkuba *et al.*[19]

In this chapter, the application of perfluorinated solvent for the selective oxidation of CH_4 to CH_3OH was investigated. Specifically, hexafluorobenzene was first compared against previously studied systems using preformed H_2O_2 [20–22] for CH_4 oxidation or O_2 for the direct oxidation of toluene[23]. Hexafluorobenzene was further used to investigate the incorporation of molecular oxygen (O_2) as oxidant in the oxidation of CH_4 to CH_3OH. This route considered the use of radical initiators (such as 2, 2'-azobisisobutyronitrile or benzoyl peroxide) before applying the *in situ* generated H_2O_2 from O_2 and H_2.

4.2 Solvent Purification

Investigations into the applicability of hexafluorobenzene (HFB) as a suitable solvent for CH_4 oxidation began by pre-reaction analysis of the solvent via ^1H NMR. Utilising deuterium oxide (D_2O), the sample of HFB was washed and the extractant analysed by ^1H NMR. The resulting spectra is illustrated in Figure 4.2. Characteristic of aromatics, such as benzene, the absence of signals within the region 6.5 – 8.5 ppm suggests no protonated analogues of HFB present. Despite this, the presence of signals is observed within the region of expected CH_4 oxidation products, such as CH_3OH (δ= 3.38 ppm, *s*) or methyl hydroperoxide (CH_3OOH, δ= 3.85 ppm, *s*). Evidenced in Figure 4.2 insert, the presence of a signal at *ca.* 3.4 ppm, may result in difficulties in the identification or quantification of produced CH_3OH. Furthermore, potentially more reactive than CH_4, the presence of impurities may result in unwanted side reactions, removing from the primary aim of this work.

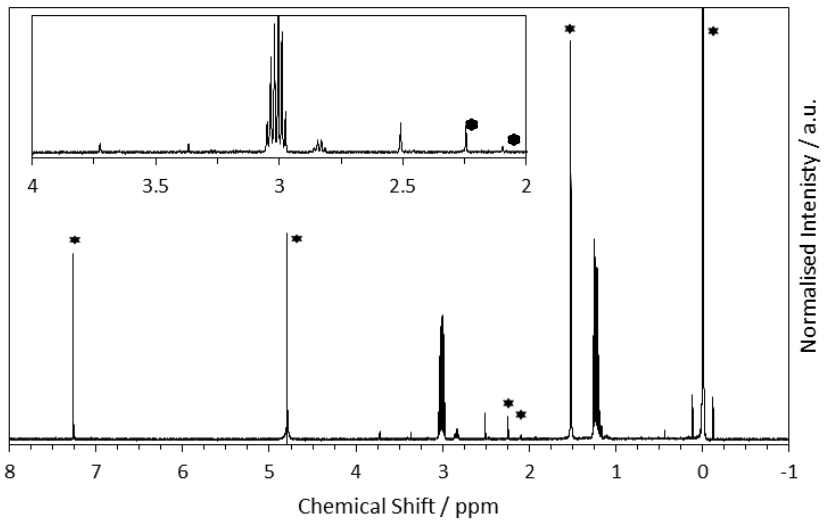

Figure 4.2: ^{1}H NMR spectrum of D_2O extract used to wash hexafluorobenzene. Insert: Magnification of 4.0 – 2.0 ppm region showing presence of impurities originating from HFB source. (*: signals present in internal standard)

The removal of small quantities of impurities from HFB was deemed necessary and the addition of several different retrievable solids were trialled as adsorbants. Investigations considered the application of readily available metal oxide or zeolite solid (1.0 g) for washing small quantities of HFB (50 mL). Prior to use, the metal oxide solids were heat treated by calcination at 400 °C, to remove adsorbed water.[24] After treatment, HFB was washed for 16 hours in a sealed flask.

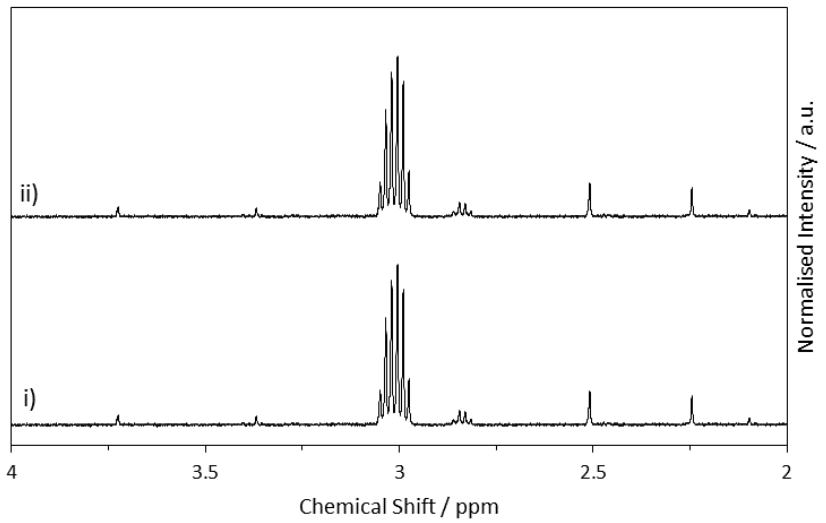

Figure 4.3: Magnified spectrum of ^{1}H NMR of D_2O extract of hexafluorobenzene phase for region 2.0 – 4.0 ppm. (i) before washing and (ii) after washing with TiO_2 (P25) solid for 16 h.

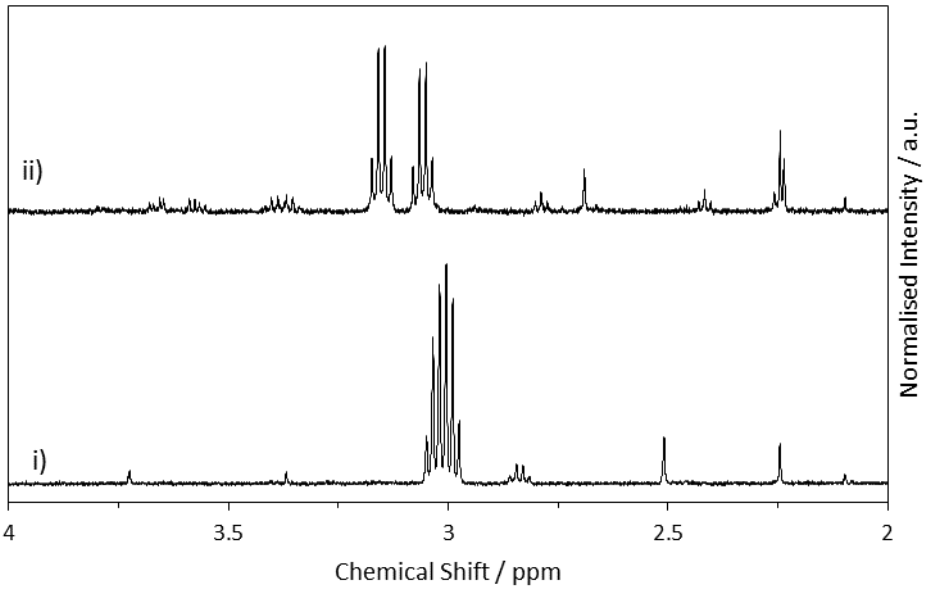

Figure 4.4: Magnified spectrum of ^{1}H NMR of D_2O extract of hexafluorobenzene phase for region 2.0 – 4.0 ppm. (i) before washing and (ii) after washing with activated charcoal (Darco G60) solid for 16 h.

[a]Standard reaction conditions: time: 16 h, ambient temperature and pressure, stirring rate: 1200 rpm, volume: 50 mL of HFB. mass: 1.0 g of solid support. Support material heat treated prior to use (400 ˚C, 3h, 20 ˚C min^{-1}, flowing air).[b] Analysed by ^{1}H NMR spectroscopy post extraction into D_2O with a 1% TMS in $CDCl_3$ internal standard.

The application of TiO_2 (P25) had no influence on the removal of impurities, evidenced by Figure 4.3. Similarly, peak intensity for all signals remained consistent with pre-washing analysis, with signal at 3.36 ppm equating to 0.1 μmoles of CH_3OH in both samples. Similarly, the application of SiO_2 and γ-Al_2O_3 did not appear to influence the NMR observable impurities.

The application of activated carbon resulted in further contamination of HFB source. Although removing species identified in the initial source, the application of carbon support imparted further undesirable impurities within the region of 2.0 – 4.0 ppm, illustrated in Fig 4.4. Likewise, the addition of graphite produced similar contamination of HFB but did produce a removal of impurities presented in the source HFB.

The addition of ZSM-5 (30) appeared to reduce to level of impurities observed in the NMR spectra. Application of its commercially available ammonia form (NH_4-ZSM-5), did not improve upon the HFB source. However, protonation of ZSM-5 by heat treatment at 550 °C, produced significant improvements. Presented in Figure 4.5, the addition of H-ZSM-5 results in the removal of all previously observed signals.

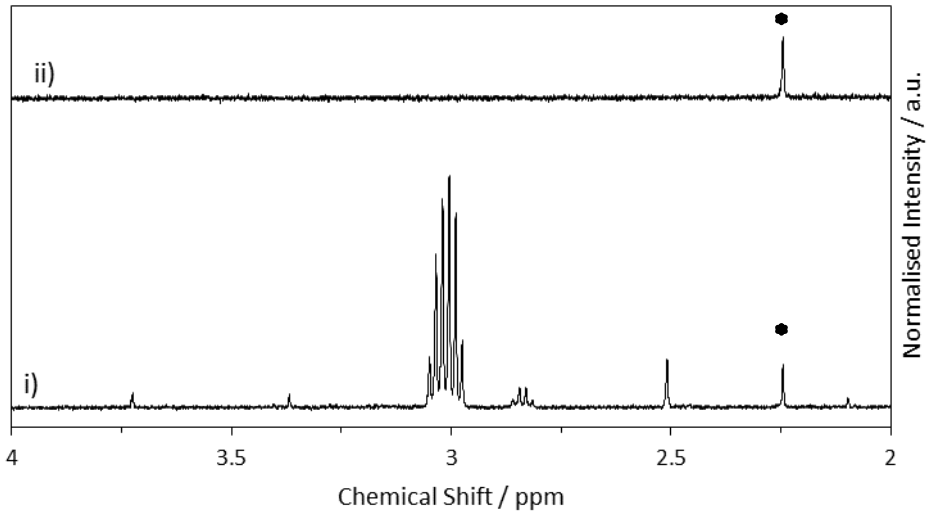

Figure 4.5: ^{1}H NMR of D_2O extract of hexafluorobenzene phase (i) before washing and (ii) after washing with H-ZSM-5 solid for 16 h. (✷: signals present in internal standard)

[a]Standard reaction conditions: time: 16 h, ambient temperature and pressure, stirring rate: 1200 rpm, volume: 50 mL of HFB. mass: 1.0 g of solid support. Support material heat treated prior to use (550 ˚C, 3h, 10 ˚C min^{-1}, flowing air).[b] Analysed by ^{1}H NMR spectroscopy post extraction into D_2O with a 1% TMS in $CDCl_3$ internal standard.

4.3 Investigations using preformed H_2O_2

The initial investigations of the effect of HFB began by comparison with previously reported systems. The application of H_2O_2 as a terminal oxidant was previously reported by Ab Rahim and co-workers for CH_4 oxidation.[20,21] The environmentally benign system demonstrated selective oxidation to CH_3OH, with an oxygenate selectivity *ca.* 90% at 50 °C. Similarly, 5 wt.% $AuPd/TiO_2$ was prepared by impregnation of a metal chloride precursor solution and applied under identical reaction conditions after calcination at 400 °C.

Previous reactions for the oxidation of CH_4 was carried out at 50 °C in an aqueous solution of H_2O_2 (0.5M, 10mL) using an autoclave reactor. For investigation of the effect of HFB, H_2O was substituted for an equal amount of HFB (0.5 M H_2O_2, 10 mL). The mass of catalyst was fixed at 27 mg, and the reactor pressurised to 30.5 bar CH_4. During testing, stirring speed was maintained at 1500 rpm from the initiation of heating to the end of reaction period (30 mins).

Liquid phase products such as methyl hydroperoxide (CH_3OOH), methanol (CH_3OH) or formic acid (HCOOH) could be identified with ^{1}H NMR and quantified against an internal standard consisting 1% trimethylsilane in $CDCl_3$. For reactions carried out in HFB, products

were extracted by addition of deuterium oxide (5 mL), prior to analysis by ^{1}H NMR. Remaining H_2O_2 was determined by titration against standardised acidified solution of $Ce(SO_4)_2$, using a Ferroin indicator (0.025M). Gaseous products, such as CO_2, were analysed by gas chromatography fitted with a methaniser and FID detector. Products were quantified using a CO_2 calibration curve.

Table 4.1: Comparison of the catalytic activity for 2.5 wt.%Au-2.5 wt.%Pd/TiO_2 for methane oxidation using preformed H_2O_2 carried out in H_2O or in hexafluorobenzene.

Entry	Cat.	Solv.	Products [µmoles]				Oxy. Sel.[a] [%]	H_2O_2 remain.[b] [%]
			CH_3OH	HCOOH	CH_3OOH	CO_2		
1	Y	H_2O[21]	1.89	0	1.57	0.37	90.3	<8
2	Y	H_2O	1.1	0.0	1.2	0.5	83.9	<6.5
3	N	HFB/H_2O	0	0	0	1.22	0	-
4	N	HFB/H_2O[c]	0	0	0	0.29	0	-
5	N	HFB/H_2O[d]	0	0	0	1.34	0	58.2
6	Y	HFB/H_2O[e]	0.91	0	0.75	1.45	53.4	<10
7	Y	HFB	0.3	0	0.1	1.30	22.5	<1.1

[a] Oxygenate selectivity calculated as $(moles_{oxygenates}/moles_{total\ products})x100$. [b] Calculated as $(moles_{final}/moles_{initial})x100$. [c] HFB degassed by N_2 bubbling, volume: 50 mL, 3 hours. [d] 10 mL HFB:H_2O (1:1 vol/vol). [H_2O_2:0.5 M]. [e] 10 mL HFB:H_2O (1:1 vol/vol). [H_2O_2:0.5 M].Cat.: Catalyst, Solv.: Solvent, Oxy. Sel.: Oxygenate selectivity, H_2O_2 Remain.: H_2O_2 remaining, Y: Yes (5 wt.% AuPd/ TiO_2), N: None.

The oxidation of CH_4 using 5 wt.% AuPd/TiO_2, was first carried out using an aqueous solution of H_2O_2 for comparison against previous work. Shown in Table 4.1 (Entry 2), marginally lower amounts of oxygenates were detected to entry 1. Even so, similar oxygenate selectivity is achieved (*ca.* 84%), resulting from marginal increase in detected CO_2. For reactions carried out using HFB, initial work determined the background contributions by experimenting with CH_4 and HFB/H_2O only under standard reaction conditions (Table 4.1, Entry 3). In the absence of oxidant or an oxygen source, no CH_4 oxygenates are detected however, significant quantities of CO_2 (1.22 µmoles) was detected. Possessing an appreciably larger gas solubility for CH_4 than H_2O (*ca.* 130 times), the high quantities are reasoned to originate from dissolved gaseous CO_2.[25] To evidence this, degassing of HFB was employed using N_2 prior to testing. Demonstrated in Table 4.1 (Entry 4), the bubbling of N_2 through HFB solution for 3 hours, results in the decrease of CO_2 detected post reaction. Further examination of background contributions considered the effect of H_2O_2 addition (Table 4.1, Entry 5). The absence of catalyst results in no CH_4 oxygenate formation, despite the presence of oxidant (H_2O_2) which sees decomposition of *ca.* 40% of initial concentration. Similar CO_2 levels were detected to examples with neither H_2O_2 nor catalyst, supporting earlier assumptions as to CO_2 origins. Furthermore, it is suggestive that the reactions carried out with HFB facilitate the rapid decomposition of H_2O_2, due to poor solubility, suggesting the incompatibility of H_2O_2 as terminal oxidant.

Even so, the addition of 5wt.% AuPd/TiO_2 catalyst sees the formation of primary oxygenates (1.66 μmoles), with *ca.* 53% oxygenate (Entry 6). Comparable quantities of CO_2 to previous tests are detected (1.3 μmoles). The observation of high rates of H_2O_2 decomposition, proposed to originate from poor solubility in HFB, is considered unfavourable for selective oxygenate formation.[26] Shown in Table 4.1 (Entry 7), the use of H_2O_2 in HFB only, shows reduced activity for CH_4 oxidation. Oxygenate selectivity is decreased to 22.5%, producing *ca.* 0.30 μmoles CH_3OH. Again, poor stability of H_2O_2 in organic solvent yielded high amounts of H_2O_2 decomposition, a factor considered crucial to selective oxygenate formation in previous investigations. with less than 1% detected post reaction. Demonstrating considerably higher activity to supported noble metal catalysts, Hammond *et al.*[27] reported markedly enhanced yields of selective oxygenates using commercial H-ZSM-5. Importantly, H-ZSM-5 catalysts exhibit high oxygenate formation with low H_2O_2 decomposition. Therefore, a similar comparison for HFB was investigated using H-ZSM-5. Prior to reaction, commercial ZSM-5 was activated by calcination at 550 °C under flowing air (10 °C min^{-1}, 3 hours). Activated H-ZSM-5 was then applied to CH_4 oxidation using similar reaction conditions to previously tested 5 wt.% AuPd/TiO_2. The results of experimentation of presented in table 4.2.

Table 4.2: Comparison of the catalytic activity of H-ZSM-5 for methane oxidation using preformed H_2O_2 carried out in H_2O or in hexafluorobenzene.

Entry	Catalyst	Solv.	Products [μmoles]				Oxy. Sel.[a] [%]	H_2O_2 remain.[b] [%]
			CH_3OH	HCOOH	CH_3OOH	CO_2		
1	H-ZSM-5	H_2O	9.6	30.9	10.4	3.12	94.2	83.7
2	H-ZSM-5	HFB/H_2O	5.1	3.8	2.0	3.09	77.9	<1

[a] Oxygenate selectivity calculated as $(moles_{oxygenates}/moles_{total\ products})x100$. [b] Remaining H_2O_2 assayed by Ce^{4+}(aq.) titration. Calculated as $(moles_{final}/moles_{initial})x100$. Solv.: Solvent, Oxy. Sel.: Oxygenate selectivity, H_2O_2 Remain.: H_2O_2 remaining

Initial testing under aqueous conditions produced *ca.* 54 μmoles of total oxygenates with *ca.* 94% oxygenate selectivity. Notably, only *ca.* 16% of the initial H_2O_2 is consumed during the reaction period. This activity is lower than reported by Hammond *et al.*[28] who reported *ca.* 81 μmoles of products at 96 % oxygenate selectivity. In contrast, the application of H-ZSM-5 to HFB sees a considerable decrease to oxygenate formation. As with previous experiments, oxidation of CH_4 proceeds with high H_2O_2 decomposition, however, results in poor selective oxygenate formation (10.9 μmoles)(Table 4.2, Entry 2). Even so, oxygenate selectivity remains with CH_3OH for HFB solvent (*ca.* 36.5% vs *ca.* 17.7%).

Despite possessing a higher gas solubility for CH_4 than H_2O, the use of HFB results in near-complete decomposition of H_2O_2. Possessing no solubility in HFB, the large decomposition is facilitated by poor stabilisation by the solvent, as observed with H_2O.

4.4 Application of Molecular Oxygen

Providing a cheap and abundant source of oxidant, the application of molecular oxygen (O_2) is an ideal oxidant to address the priorities of green chemistry.[29] Typically requiring the application of redox-active metals[30,31] or peroxides[32] for C-H bond activation, environmental concerns have sought to apply O_2 as an environmentally benign alternative. In contrast to commonly used oxidants for C-H bond activation, such as benzoquinone, the use of O_2 produces no toxic by-products associated with its use.[29] Despite this, the difficulty in applying O_2 stems from the high dissociation energy (497 kJ mol^{-1}) and kinetically hindered formation of highly reactive oxygen radicals by the triplet ground state of O_2.[33]

Even so, the biological oxidation of alkanes, such as CH_4, via O_2 activation is commonly observed in nature. The four-electron reduction of adsorbed O_2, in soluble methane mono-oxygenase (*s*MMO), is achieved by electron transfer from the reduced Fe^{II}-O-Fe^{II} centre.[34] Carried out under ambient conditions, the completion of the catalytic cycle requires assistance from additional components of the enzyme. The regeneration of active centre uses the redox cycle of NADH and FAD acting as proton and electron transfer agent, facilitating the oxygen transfer through a reduced metal centre.[33]

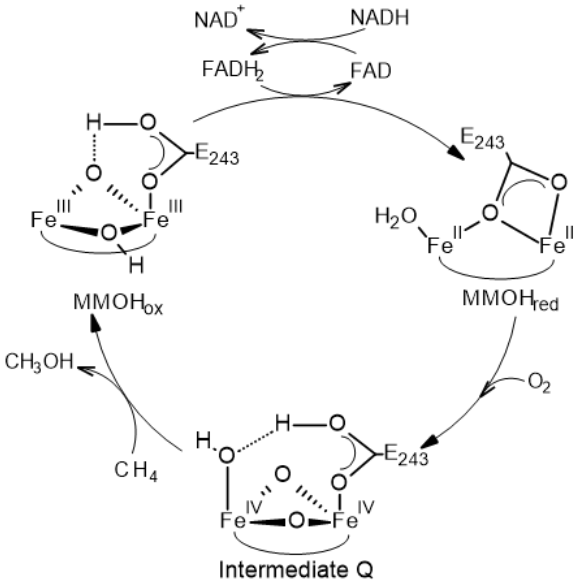

Figure 4.6: Simplified catalytic cycle for the activation of O_2 for hydroxylation of CH_4 in *s*MMO.[35]

Many approaches have been attempted to incorporate O_2, as described by Munz et al.[36] Inspired by the oxygen rebound mechanism displayed by sMMO and cytochrome P450, both O_2 and C-H activation occur at a transition metal centre. The oxidation of transition

metal (TM) centre, such as Fe (Fe=O), produces a species capable of C-H activation by H-abstraction. The rebound of hydroxyl removal by the generated alkyl radical species produces the desired alcohol and regenerates the active TM centre.[36]

Due to its effectiveness in biology, the application of bio-mimetic Fe-oxo species has been widely reported for a broad range of oxidative transformations, including CH_4.[37,38] High valent oxo-iron species of metallo-porphyrins have allowed vital insights into the mechanisms of enzymatic reactions carried out by heme and non-heme proteins.[39,40] Similarly, the application of phthalocyanines containing analogous μ-oxo or μ-nitrido bridged Fe have been studied with great detail.[41,42] However, these systems often utilise activated oxygen sources, like H_2O_2, with little examples of direct O_2 available or catalytic turn-overs achieved for CH_4 oxidation.[36]

In contrast, the use of trifluoroacetic acid solvents has allowed several reports of CH_4 oxidation by O_2 using an array of catalysts such as manganese (Mn)[43] and cobalt (Co)[44]. Even so, over-oxidation to CO_2 is commonly observed, resulting in poor selectivities to the trifluoroacetate derivative, with Mn demonstrating a moderate yield of 36%.[43,45] In the case of Co salts, Strassner *et al.*[45] reported 50% yields of methyl trifluoroacetate, with the nitrate salt ($Co(NO_3)_2$) producing the most active catalyst. Catalyst deactivation by formation of a precipitated cobalt fluoride salts was overcome by addition of trifluoroacetic anhydride (HOTFA). However, catalyst deactivation continued after complete consumption of added HOTFA.[45]

Alternatively, the role of the catalyst may be divided by addition of a secondary co-catalyst, allowing activation of C-H and O_2 to take place at separately.[36]

Interestingly, the application of a series of redox coupled reactions allows O_2 activation and insertion into activated C-H bonds with regeneration of active catalyst. Reported by Bao and co-workers, initial selective C-H activation of CH_4 is achieved using $Pd(OAc)_2$ in a non-superacid medium of trifluoroacetic acid and methyl trifluoroacetate. [46,47] The resulting reduced Pd^0 is then regenerated by the oxidant cycle of benzoquinone (Bq) to hydrobenzoquinone (H_2Bq), allowing continued catalytic activity. During initial investigations, direct O_2 use was employed as a method for Bq regeneration by oxidation of H_2Bq. However, insufficient rates were observed which resulted in catalyst deactivation by formation of Pd^0.[47] This issue was overcome by use of NO_2 to NO cycle, with O_2 utilised as terminal oxidant, with oxygen transfer via Bq.

Similarly, polyoxometalates (such as $H_5PMo_{10}V_2O_{40}$) have been employed as alternatives to previous Bq redox couples using HOTFA solvent.[48] The initial works by Yuan *et al.*[49] utilised $H_5PMo_{10}V_2O_{40}$ in conjunction with Bq, demonstrating moderate activity for the formation of MeOTFA with $Pd(OAc)_2$ using O_2. Later application of K_2PdCl_4 salts were attempted using O_2 directly.[50] Unsuccessfully, only trace observations of MeOTFA were detected, primarily producing acetic acid (CH_3COOH) after 8h. Instead, proceeding works

applied $PdCl_2$(bpy), with substitution of the catalyst complex resulting in 310 μmoles of CH_3OH detected when carried out at 100 ˚C for 8h.[51]

For Au catalysts, little examples of direct O_2 oxidation of CH_4 to CH_3OH can be found within the literature. The application of Au, however for direct oxidation using molecular O_2 has been described for an array of other alkanes. The epoxidation of propane to propylene oxide was reported by Oyama *et al*.[52] using a two catalysts system in a two-step approach at 170 ˚C. Initial dehydrogenation was conducted by Au/TiO_2, with epoxidation then carried out by Au/TS-1 in a system using H_2 and O_2.

The oxidation of cyclohexane using O_2 has been reported for an array of supported Au catalysts.[53–56] Fang and co-workers[55] demonstrated the highly active oxidation of cyclohexane (C_6H_{12}) to cyclohexanol ($C_6H_{11}OH$) and cyclohexanone ($C_6H_{10}O$) under mild reaction conditions. Carried out at 150 ˚C, the solvent free oxidation of C_6H_{12} achieved a maximum conversion of *ca.* 13% producing $C_6H_{11}OH$ and $C_6H_{10}O$ with *ca.* 53% and 32% selectivity, respectively.[55] Reported by Liu *et al*., oxidation of C_6H_{12} for Au/hydroxyapatite (HAP) also showed dependence for Au-cluster size, with TOF increasing with Au particle size.[57] This affect was similarly observed by Fang and co-workers, with Liu observing highest TOF (18,500 h^{-1}) for Au cluster of 39 atoms.[55,57]

Despite attempts at O_2 activation for CH_4 oxidation, the elevated temperature required to facilitate activation of O_2 produce highly reactive radical species. Subsequently, poor control of radicals leads to poor selectivity during CH_4 oxidation resulting in over-oxidation and the formation of CO_2.[58,59]

Goddard *et al*. demonstrated the oxy-functionalisation of CH_4 using auric oxide (Au_2O_3) as a homogenous catalyst.[60] Initially using sulfuric acid, as in previous Periana reports for Hg[30] and Pt[31] complexes, the formation of metallic Au was evidently observed with catalyst deactivation. Instead, a stronger oxidant was employed using H_2SeO_4 to re-oxidise Au^0 to Au^{III}, enabling continued catalytic activity. For this system, the solution of H_2SeO_4/H_2SO_4 acts as stoichiometric oxidants for the conversion of CH_4 (11%) to methyl bisulfate (81%).

Hutchings and co-workers[61], however, demonstrated the incorporation of O_2 into CH_4 oxygenates by combination of H_2O_2. Utilising unsupported AuPd nanoparticles, stabilised using polyvinyl pyrrolidone, CH_4 oxidation was initially demonstrated for preformed H_2O_2. The addition of O_2 observed increase in selective oxygenate formation, with further $^{18}O_2$ experiments demonstrating greater than 70% incorporation of $^{18}O_2$ into primary oxygenates.

Preliminary Investigations

Considered a model for activated CH_4, the solvent free oxidation of toluene was reported by Kesavan *et al.*[23] utilising O_2 as the oxidant. Using supported AuPd nanoparticles upon carbon and TiO_2 supports, high activity for the oxidation of primary C-H bonds of methyl group was achieved (Figure 4.7). Carbon supported AuPd converted 94% of toluene over 24 hours, with selectivity towards benzyl benzoate (95%) at 160 °C.

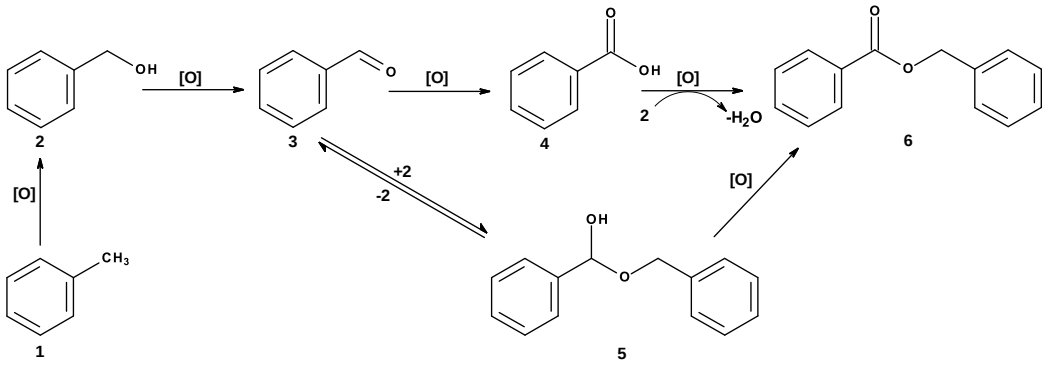

Figure 4.7: Oxidation pathway of toluene (1) to benzyl benzoate (6) via benzyl alcohol (2), benzaldehyde (3), benzoic acid (4) and hemiacetal (5). Adapted from Kesevan *et al.*[23]

However, this was achieved using an excessive amount of catalyst (1.6 g). During instances of more realistic quantities of catalyst (0.2g), conversion expectedly decreased to a toluene conversion of *ca.* 51%, with *ca.* 95% benzyl benzoate selectivity. However, an extended reaction time of 48 hours was required to achieve this moderate conversion.

Previously discussed, the application of heteropolyacid redox-mediated reaction was reported by Yuan *et al*. for functionalization of CH_4 to a CH_3OH derivative, methyl trifluoroacetate (MeOTFA). Additionally, attempts to improve O_2 solubility were investigated by use of perfluoro-octane (C_8F_{18}), with additional benefits to the transport properties of HOTFA.[49,51] The resulting improvements to MeOTFA yield was proposed to originate from increased O_2 solubility, allowing enhancement for the re-oxidation of $H_5PMO_{10}V_2O_{40}$/Bq.[49,51] Consequently, a near -linear dependence was observed with volume ratio of C_8F_{18} to HOTFA, with MeOTFA yield increasing *ca.* 46 μmoles to *ca.*350 μmoles when volume of C_8F_{18} increased from 0 to 10 mL.

Background contributions

Possessing a higher O_2 gas solubility than toluene (*ca.* 2.7 times greater)[25,62,63] the use of perfluorinated solvent (HFB) was applied to increase O_2 solubility for the oxidation of toluene.

Utilising reaction conditions used by Kesavan *et al.*[23], toluene oxidation was carried out at 160 °C in a 1:1 mixture of substrate to solvent (10 mL total volume) using an autoclave reactor. The mass of 1 wt.% $AuPd/TiO_2$ (P25) catalysts was fixed at 200 mg, and the reactor pressurised with 10 bar O_2. Stirring speed was maintained at 1500 rpm from the initiation of heating to the end of reaction period.

Liquid phase products were analysed by gas chromatography, and quantified against 1, 3, 5 -trimethyl benzene, an external standard. Prior to analysis 5 mL CH_3OH was added to dissolve solid products, typically obtained after long reaction periods.

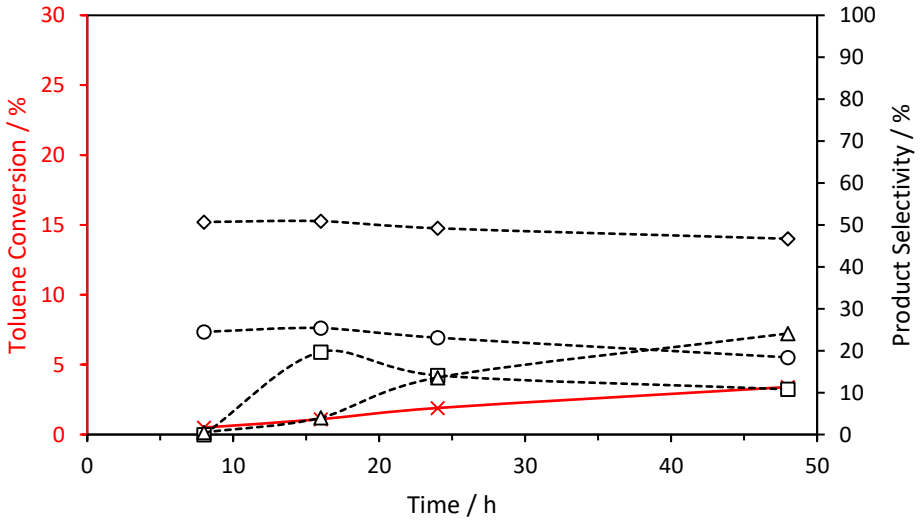

Figure 4.8: Time-on-line analysis for toluene oxidation using hexafluorobenzene solvent in the absence of catalyst at 160 °C. X: toluene conversion, □: Benzyl alcohol, ◇: Benzaldehyde, △: Benzoic acid, ○: Benzyl benzoate.

Standard reaction conditions: time: 48 hours, temperature: 160 °C, $P(O_2)$: 10 bar, stirring rate: 1500 rpm, Catalyst: none, total volume: 10 mL of H_2O (5 mL).HFB (5 mL)

The time-on-line (TOL) analysis of uncatalyzed reactions are illustrated by Figure 4.8. Illustrating the background contribution prior to the addition of catalyst, consideration of the auto-oxidation of toluene by O_2 was determined at 160 °C. Initial toluene conversion of *ca.* 0.5% was observed after 8 hours, increasing to a maximum of *ca.* 3.4 % after 48 h,

signifying a small portion of activity overall. Selectivity of the auto-oxidised reaction was found towards benzaldehyde (*ca.* 50%), agreeing with activity observed by Kesavan *et al.* after 7 hours.[23] Even so, prolonged experiments resulted in a decrease in selectivity for benzyl alcohol, benzaldehyde and benzyl benzoate with benzoic acid selectivity increasing from *ca.* 0.5 % to *ca.* 24 %.

4.4.1 Toluene Oxidation Using Hexafluorobenzene

For the catalysed oxidation of toluene, 1 wt.% AuPd/TiO_2 was prepared by sol immobilisation using poly- (vinyl alcohol) as the stabilising agent. In contrast to sol immobilisation, the impregnation method was found to result in particles with a broad distribution of sizes, however, the low activity observed was proposed to originate from the large variation in nanoparticle composition. [23] Therefore, producing materials with narrow size distribution (*ca.* 5 nm)[64] and affording greater control of nanoparticle composition, sol immobilisation was used as preferred method.

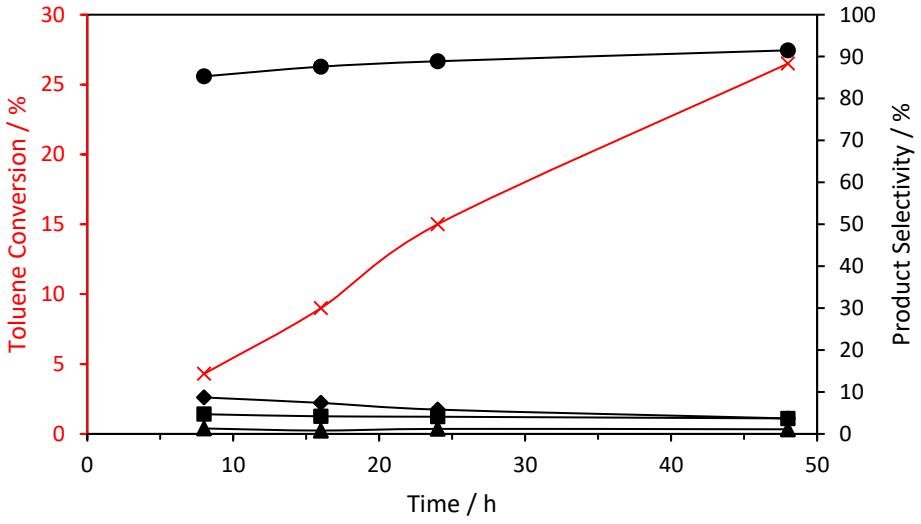

Figure 4.9: Time-on-line analysis for toluene oxidation using 1 wt.% AuPd/TiO_2 (S_i) carried out using hexafluorobenzene solvent at 160 °C. X: toluene conversion, ■: Benzyl alcohol, ◆: Benzaldehyde, ▲: Benzoic acid, ●: Benzyl benzoate.

Standard reaction conditions: time: 48 hours, temperature: 160 °C, P(O_2): 10 bar, stirring rate: 1500 rpm, all catalysts (1 wt. % total): 1.45×10^{-5} mol of metals equal to 200 mg of solid catalysts, total volume: 10 mL of H_2O (5 mL).HFB (5 mL)

Shown in Figure 4.9, the time-on-line analysis for toluene oxidation was investigated over 48 hours. The conversion of toluene after 8 hours was determined to be *ca.* 4.3%, with

product selectivity towards benzyl benzoate (*ca.* 85%) being observed. This contrasts with earlier auto-oxidation reactions which demonstrated selectivity to benzaldehyde (*ca.* 50%, Figure 4.9) and benzyl benzoate selectivity of *ca.* 25%. Even so, these results observed are consistent with previous works by Kesavan et al., who observed *ca.* 89 % selectivity to benzyl benzoate after 7 h.[23] Extending reaction time to 16, 24 and 48 h sees marginal increase in benzoate selectivity, increasing from *ca.* 85% to *ca.* 92%. The conversion of toluene increases from 4.3% to *ca.* 27% after 48 h.

To further investigate the influence of increased O_2 solubility upon toluene conversion, the variation of substrate and solvent was varied whilst maintaining constant volume (10 mL total). Therefore, toluene oxidation was carried out at 160 °C using an autoclave reactor, with reactions carried out for 48 h. The mass of 1 wt.% AuPd/TiO_2 (P25) catalysts was fixed at 200 mg, and the reactor pressurised with 10 bar O_2. Stirring speed was maintained at 1500 rpm from the initiation of heating to the end of reaction period.

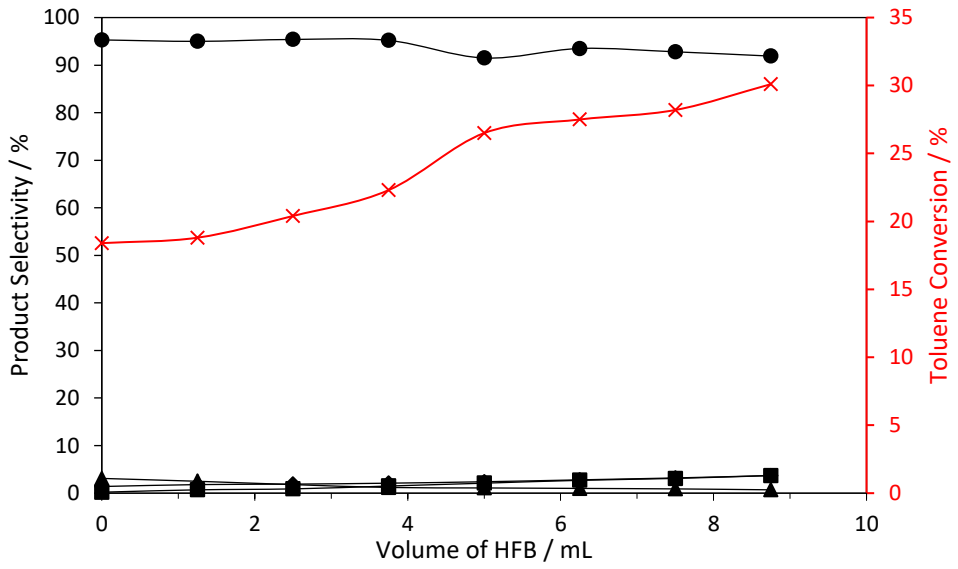

Figure 4.10: The effect of HFB volume on the conversion of toluene by 1 wt.% AuPd/TiO_2 (S_i) at 160 °C after 48 hours. X: toluene conversion, ■: Benzyl alcohol, ◆: Benzaldehyde, ▲: Benzoic acid, ●: Benzyl benzoate.

Standard reaction conditions: time: 48 hours, temperature: 160 °C, P(O_2): 10 bar, stirring rate: 1500 rpm, all catalysts (1 wt. % total): 1.45x10^{-5} mol of metals equal to 200 mg of solid catalysts, total volume: 10 mL of H_2O.HFB. Ratio varied.

Under solvent-free conditions, the conversion of toluene over 1 wt.% AuPd/TiO_2 was determined to be 18.4%. This activity is lower than previous reported by Kesavan et al., observing *ca.* 24% conversion of toluene after 48 hours.[23] Shown in Figure 4.10, the addition of HFB sees an improvement to toluene oxidation. The introduction of HFB (1.25

mL) produces only a marginal increase to observed conversion (18.8%), however, only represents a small portion of total reaction volume. Further addition of HFB produces only a marginal increase in toluene conversion, increasing from 18.4% to 26.5% when HFB is raised from 1.25 mL to 5 mL. Notable improvements to the toluene conversion is seen at volumes above 5 mL, with 6.25 mL HFB enhancing conversion to *ca.* 36% and maximum conversion of 58.4% achieved with 8.75 mL HFB. Product selectivity is dominated by benzyl benzoate formation; decreasing marginally to *ca.* 92% at *ca.* 58.4 % conversion (8.75mL, Figure 4.10).

4.5 Screening of Radical Initiators

A great amount of effort has been dedicated to understanding the mechanisms of alkane activation.[65] Even so, the reaction mechanism may be complicated by factors such as formation of reaction complexes between a hydrocarbon and an activating species. Of particular interest for selective functionalisation is that the reported rates of H-abstraction show only a small correlation to well defined C-H bond dissociation energies.[65] However, for the transformation of CH_4, the activation of C-H bond by H abstraction is a crucial step.[19] As such, radical species are often utilised to promote H-abstraction as a method of alkane activation.

The homolytic cleavage of radical initiators can be used to generate significantly more reactive radical intermediate species, capable of activating other molecules. The key for polymer synthesis, radical polymerisation is involved in producing *ca.* 50 % of all synthetic polymers.[66] In previous investigations, considerable activity was achieved by Kesavan *et al.* using bimetallic AuPd catayst for toluene oxidation at 160 ˚C. Converting *ca.* 50.8 % of toluene, carbon supported AuPd demonstrated a two- fold enhancement in catalytic activity compared with TiO_2 supported (*ca.* 24 %). Further works by Hutchings *et al.*, succeeded in reducing reaction temperatures and reported toluene oxidation at milder temperatures of 80 °C.[67] Utilising AuPd/TiO_2 and *tert*- butyl hydroperoxide (tBuOOH) as the oxidant, the toluene conversions after 48 hours were comparable, converting *ca.* 24-25%. Contrastingly, selectivity to benzoic acid was observed (92%) for tBuOOH initiated oxidation compared to benzyl benzoate (96%) during initiator-free work. Importantly, mechanistic information revealed the involvement of surface- bound oxygen-centred radicals.

The application of radical initiators was therefore investigated as potential method to promote the activation of C-H bonds for the oxidation of CH_4 using O_2.

4.4.1 Azo based radical initiators

Azo (-N=N-) compounds are thermally sensitive molecules demonstrating a first order rate of decomposition, independent of solvent effects.[68] Primarily stable under temperatures of 40 °C, the dissociation of azo compounds above 40 °C are driven towards the liberation of stable N_2 and the generation of substituted alkyl radical.[68]

Of interest industrially, 2,2'-azobisiisobutyronitrile (AIBN) is used extensively as initiator for the polymerisation of plastics such as polyethylene, or poly ethylene terephthalate.[69,70] In contrast, AIBN may be used as a method of recycling plastics, by conversion to its raw materials, as reported by Siddiqui.[71]

Further catalytic applications of AIBN include the direct cyanation of aryl C-H, reported by Xu *et al.*, employing AIBN as the free radical CN source.[72] The free radical CN source provided a more efficient pathway, reporting yields of up to 92% when using $Cu(OAc)_2$. Ramplin and co-workers[73] utilised azobisisobutyronitrile (AIBN) for the oxidation of heptane at 100 °C. Ramplin and coworkers found that during the use of small quantities of AIBN produced activity for only a short period. Additionally, during this period total molar quantities of ketones and alcohols formed were significantly less than the quantity of AIBN initiator used. Similarly, the low temperature oxidation of *n*-decane ($C_{10}H_{22}$) using O_2 was investigated by Hutchings *et al.* using an oxygen-free radical initiator, selecting the azo -initiator AIBN.[74] Producing a range of C_{10} products under mild reaction conditions (70 °C, air), the addition of Au/nano-CeO_2 produced no improvements to the conversion of $C_{10}H_{22}$ above the auto-oxidation with AIBN and O_2.

AIBN was therefore selected as a potential initiator for the oxidation of CH_4. Initial screening was carried out at 80 °C in a mixture of AIBN and HFB using an autoclave reactor. Investigations began using an excess of AIBN (250 μmoles), with total volume of HFB maintained at 10 mL. This was selected due to the reported low yield of initiating radicals produced by AIBN, instead undergoing recombination of primary radicals to produce tetramethyl -succinonitrile (tMeSN).

Reported by Okhubo *et al.*[19], the addition of an aqueous phase was utilised in the oxidation of CH_4 to CH_3OH using perfluoro-hexane. The presence of a second H_2O phase provided an oxygenate -soluble phase to stabilise CH_3OH and HCOOH products. Furthermore, removed from active perfluoro-hexane phase, further oxidation of aqueous soluble products minimised over-oxidation to CO or CO_2. Therefore, reactions in HFB were carried out with addition of D_2O (5 mL). Catalyst mass was fixed at 27 mg, and the reactor pressurised using CH_4 (27.5 bar) and O_2 (3.0 bar). During testing, stirring speed was maintained at 1500 pm, beginning at the start of heating and stopped at the end of the reaction period.

Liquid phase products such as methyl hydroperoxide (CH_3OOH), methanol (CH_3OH) or formic acid (HCOOH) were analysed via ^1H NMR of aqueous D_2O phase and quantified against an internal standard consisting 1% trimethylsilane in $CDCl_3$. Gaseous products, such as CO_2, were analysed by gas chromatography fitted with FID detector and methaniser. Products were quantified using a CO_2 calibration curve.

Table 4.3: Attempts at AIBN initiated methane oxidation catalysed by 5 wt.% AuPd/ TiO_2 using hexafluorobenzene.

Entry	Temperature [°C]	Gaseous Mix	Time [h]	Products [µmoles]			
				CH_3OH	HCOOH	CH_3OOH	CO_2
1	80	CH_4/O_2	1	0	0	0	1.40
2		N_2/O_2	3	0	0	0	0.24
3		CH_4/O_2	3	0	0	0	1.35
4		CH_4/O_2	5	0	0	0	1.22
5	100	CH_4/O_2	1	0	0	0	1.28
6		N_2/O_2	3	0	0	0	0.36
7		CH_4/O_2	3	0	0	0	1.42

Standard reaction conditions: time: 24 hours, temperature: 80 °C, P(CH_4): 27.5, P(O_2): 3.0 bar, stirring rate: 1500 rpm, all catalysts (5 wt. % total): 9.77×10^{-6} mol of metals equal to 27 mg of solid catalysts, 250 µmoles of radical initiator (2,2'-azobis(2-methylpropionitrile, AIBN), total volume: 15 mL of D_2O (5 mL).HFB (10 mL)

Typically utilised at temperatures of 60 °C, AIBN shows a slow rate of decomposition with a half-life ($t_{1/2}$) in the order of tens of hours (10h $t_{1/2}$ at 65 °C).[75] Initial investigations carried out at 80 °C for 1 hour, but showed no selective oxygenate formation, with CO_2 detected in comparable quantities to previous investigations (Table 4.3, Entry 1). To determine the source of CO_2, experiment design was modified by degassing HFB solution with N_2 bubbling for 3 hours prior to testing. In addition, the gaseous mixture of CH_4/O_2 was substituted for a mixture of N_2/O_2. The resulting experiment was carried out for 3 hours and showed a significant decrease in CO_2 detected post reaction, suggesting an adventitious origin (Entry 2). The reaction time was extended to 3 and 5 hours to determine if longer reaction time was required (Entries 4 and 5). However, similar results were observed with no selective oxygenate detected post reaction and comparable yields of CO_2 found.

Further investigation examined the effect of increased reaction temperature, raising the temperature to 100 °C. The increase in temperature would expectedly yield an increase in thermally initiated decomposition of AIBN. Even so, an increase in reaction temperature may assist in facilitating CH_4 oxidation. Shown in Table 4.3, the increase in reaction temperature was investigated for similar reaction lengths (Entries 4-7). However, the reaction temperature yielded no change in activity or the synthesis of selective

oxygenates. The analysis for the source of CO_2, by substitution of CH_4 to N_2, yielded a similar decrease in CO_2 detected, suggesting no overoxidation of CH_4 during initial reactions.

Previously discussed, the thermal decomposition of AIBN results in low amount of radical species capable of initiating the desired chain reaction. Alternatively, the generated radical species preferentially undergo recombination to produce the inactive tMeSN dimer. Furthermore, consideration of the activity demonstrated by AIBN for the oxygen free oxidation of n-decane by Hutchings *et al.* also illustrates an important factor. [74] Under reaction temperatures of 70 °C, the conversion of $C_{10}H_{22}$ achieved was *ca.* 0.5 %. Further investigations at 90 °C improved upon this activity marginally, achieving the conversion of 1.2% of $C_{10}H_{22}$. In both experiments, AIBN was utilised in similar quantities (305 µmoles) yielding low activity. Therefore, AIBNs activity may be insufficient for application in the oxidation of the least reactive hydrocarbon, CH_4.[18]

4.4.2 Peroxy- based Initiators

Industrially, benzoyl peroxide is an important diacyl peroxide compound, finding applications for bulk polymerisation of plastics such as styrene. [76] Furthermore, BPO finds application in medicine due to bactericidal properties as treatment of acne.[77,78]

Recently, various peroxide-based initiators have been applied to polymerisation-based self-healing systems, including BPO.[79] In contrast to azo-based initiators, the complex radical pathways resulting from homolytic cleavage of O-O bond is strongly dependent upon solvent employed.[80] For BPO, solvent polarity may influence the rate of radical decomposition with ethanol producing rapid decomposition. Alternatively, the use of aromatic solvents such as benzene produces a stabilising influence.[80]

The benzoyl peroxide promoted phenanthridinylation of simple alkanes using isonitrile was reported by Sha *et al.*[81]. Subsequent C-C bond formation was promoted by C-H bond cleavage, with Fe -catalysed reactions displaying yields of *ca.* 67% at 100 °C. Alternatively, removal of transition metal catalysts for BPO only catalysed reactions displayed higher yields of *ca.* 76%. For the oxidation of benzyl alcohol, the application of BPO as radical initiator was shown to increase the rate of auto-oxidation for benzaldehyde to benzoic acid.[82]

Utilising oxo-vanadium(IV) catalyst complexes the oxidation of cyclohexane was investigated using mild reaction conditions using homogenous and immobilised forms.[83] For reactions with an homogenous oxo-vanadium (IV) complex, the application of BPO showed TON 1030 h^{-1} for conversion of cyclohexane to cyclohexanol and cyclohexone.

This activity was comparable with alternative peroxy-compounds such as *m*-chloroperoxybenzoic acid (mCPBA) where a TON 1110 h^{-1} were achieved.

Subsequently, BPO was selected as an organic peroxy initiator for the oxidation of CH_4. Initial screening was carried out at 80 °C in a mixture of BPO and HFB using an autoclave reactor. Investigations began using an excess of BPO (250 μmoles), with total volume of HFB maintained at 10 mL. For consistency with AIBN, the investigation of HFB was carried out by addition of D_2O (5 mL). Catalyst mass was fixed at 27 mg, and the reactor pressurised using CH_4 (27.5 bar) and O_2 (3.0 bar). During testing, stirring speed was maintained at 1500 pm, beginning at the start of heating and stopped at the end of the reaction period. The following conditions were utilised unless specified.

Liquid phase products such as methyl hydroperoxide (CH_3OOH), methanol (CH_3OH) or formic acid (HCOOH) were analysed via ^1H NMR with the D_2O phase and quantified against an internal standard consisting 1% trimethylsilane in $CDCl_3$. Gaseous products, such as CO_2, were analysed by gas chromatography fitted with FID detector. Products were quantified using a CO_2 calibration curve.

Table 4.4: Preliminary investigation of BPO -initiated methane oxidation using 5 wt.% AuPd/ TiO_2 carried out at 80 °C for 3 hours.

Radical Intiator	Temperature / °C	Products [μmol]			
		CH_3OH	HCOOH	CH_3OOH	CO_2
BPO	80	0.30	0	0.04	22.5

Standard reaction conditions: time: 24 hours, temperature: 80 °C, P(CH_4): 27.5, P(O_2): 3.0 bar, stirring rate: 1500 rpm, all catalysts (5 wt. % total): 9.77×10^{-6} mol of metals equal to 27 mg of solid catalysts, 250 μmoles of radical initiator (benzoyl peroxide, BPO), total volume: 15 mL of D_2O (5 mL).HFB (10 mL)

Possessing a 10h $t_{1/2}$ at 70 °C, thermal decomposition of BPO is similar to that of AIBN at 65 °C.[68] Utilising identical reaction conditions to previous experiments with AIBN, a notable difference is observed in the activity for CH_4 oxidation after 3 hours. Post reaction analysis of aqueous D_2O phase detected the formation of small quantities of methanol (0.3 μmoles) in addition to trace amounts of CH_3OOH intermediate.

The high yield of CO_2 detected post reaction, although concerning, is believed to be the result of BPO decomposition. After initial homolytic cleave of peroxy- bond to produce the alkoxy radical intermediate, additional carboxylation can occur to produce a phenyl radical species (Figure 4.11). The resulting decarboxylation of alkoxy species liberates CO_2, which would suggest the high CO_2 detected.

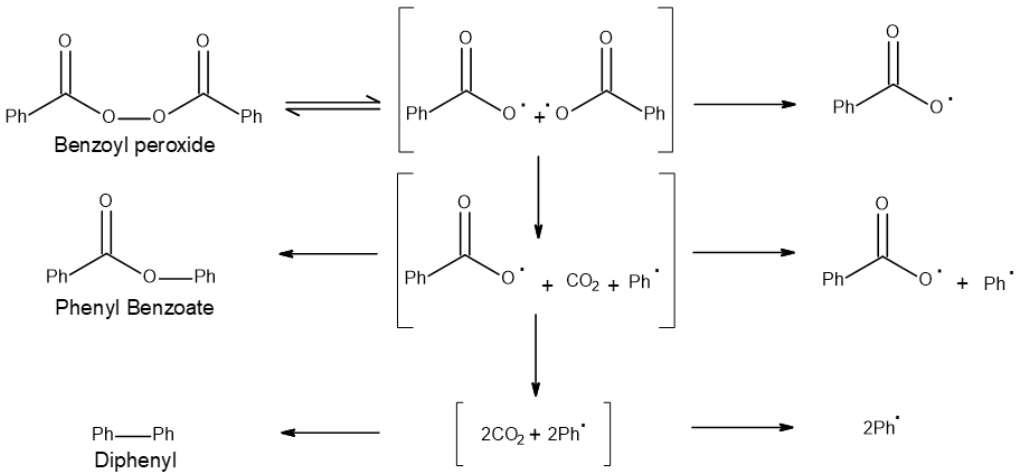

Figure 4.11: Decomposition pathway of benzoyl peroxide resulting in the formation of initiating radicals. Adapted from reference [84].

4.6 Further Investigation of Benzoyl Peroxide Initiated Methane Oxidation

During previous investigations, the screening of radical initiators was applied for the direct oxidation of CH_4 using O_2. Initial application of the commonly used azo-compound, AIBN, yielded no activity for the synthesis of selective oxygenates. Alternatively, the application of peroxy- based BPO showed marked differences in activity for CH_4 oxidation. Producing small amounts of selective oxygenates, the oxidation of CH_4 was carried out at 80 °C using hexafluorobenzene. The following section will further investigate the variables to improve previous results.

4.6.1 The Effect of catalyst Mass

Directly influencing the number of active sites present within a reaction, the variation of catalyst mass is an important variable for consideration. In previous experiments, the application of 5wt.% AuPd/TiO_2 (Iw) was carried out under fixed catalyst mass (27 mg), equating to 9.77 x10^{-6} moles of metal present within the catalyst. During which a small quantity of selective oxygenates, namely CH_3OH was detected. To determine the relationship of catalyst mass for BPO initiated CH_4 oxidation, the effect of catalyst mass was varied.

Previously defined, testing was carried out using a mixture of BPO and HFB (250 μmoles, 10 mL) with further addition of deuterium oxide (5 mL). The reaction was carried out using

an autoclave reactor at 80 °C. The reactor was pressurised using CH_4 (27.5 bar) and O_2 (3.0 bar). During testing, stirring speed was maintained at 1500 pm, beginning at the start of heating and stopped at the end of the reaction period. The following conditions were utilised unless specified.

Liquid phase products such as methyl hydroperoxide (CH_3OOH), methanol (CH_3OH) or formic acid (HCOOH) were analysed via ^1H NMR of aqueous D_2O phase and quantified against an internal standard consisting 1% trimethylsilane in $CDCl_3$. Remaining BPO was determined via analysis of HFB phase by HPLC fitted with a diode array detector and products quantified using a BPO calibration curve. Gaseous products, such as CO_2, were analysed by gas chromatography fitted with FID detector. Products were quantified using a CO_2 calibration curve.

Dependency of CO_2 generation

The resulting decomposition of BPO via homolytic cleavage of O-O leads to the formation of alkoxy radical species. Suggested in Figure 4.11, the continued decomposition via decarboxylation can lead to the liberation of CO_2, which was proposed as the origin of high quantities of CO_2 detected post reaction (Table 4.4). To confirm the source of CO_2 evolution, preliminary testing was carried out by substitution of CH_4/O_2 gaseous mixture with N_2 only.

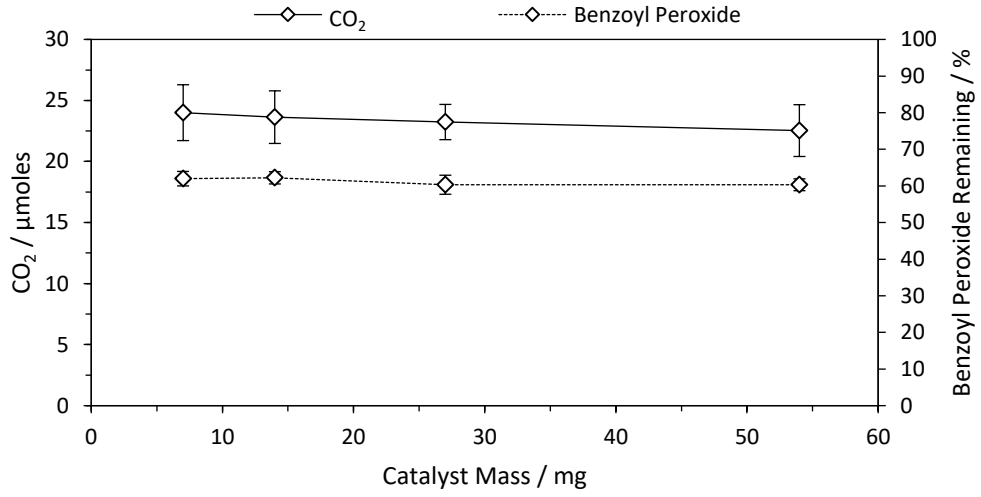

Figure 4.12: Relationship of evolved CO_2 and the BPO remaining for reactions at 80 °C under N_2 atmosphere in the presence of varying mass of 5 wt.% AuPd/ TiO_2 (I_w) catalyst.

Standard reaction conditions: time: 3 hours, temperature: 80 °C, P(N_2): 30 bar, stirring rate: 1500 rpm, all catalysts (5 wt. % total): catalyst mass varied (7 mg, 14mg, 27mg, 54 mg), 250 µmoles of radical initiator (benzoyl peroxide, BPO), total volume: 10 mL of D_2O (5 mL).HFB (10 mL)

Substitution to N_2 atmosphere sees no variation in the quantity of CO_2 observed when catalyst mass was changed. Instead, *ca.* 23.5 μmoles CO_2 was detected post reaction for all masses examined. Furthermore, consistent amounts of BPO are detected post reaction (*ca.*61%), correlating with the CO_2 evolved during reaction.

Catalysed BPO -initiated Methane Oxidation

Table 4.5: The effect of 5 wt.% AuPd/ TiO_2 catalyst mass on BPO -initiated methane oxidation using HFB.

Entry	Catalyst Mass [mg]	Products [μmoles]				Methanol Sel.[a] [%]	BPO Remaining[b] [%]
		CH_3OH	HCOOH	CH_3OOH	CO_2		
1	54	0.28	0	0.08	21.7	1.3	60.9
2	27	0.29	0	0	22.0	1.3	59.7
3	14	0.30	0	0.04	22.5	1.3	59.5
4	7	0.29	0	0	22.6	1.3	58.7

Standard reaction conditions: time: 3 hours, temperature: 80 °C, P(CH_4): 27.5, P(O_2): 3.0 bar, stirring rate: 1500 rpm, all catalysts (5 wt. % total): catalyst mass varied, 250 μmoles of radical initiator (benzoyl peroxide, BPO), total volume: 15 mL of D_2O (5 mL).HFB (10 mL) [a] methanol selectivity calculated as $(moles_{oxygenates}/moles_{total\ products})x100$. [b] Calculated as $(moles\ BPO_{final}/moles\ BPO_{initial})x100$.

Shown in Table 4.5 (Entry 2), the initial investigation into catalyst mass was carried out using 27 mg catalyst. Producing similar results to preliminary investigations, at 80 °C *ca.* 60 % of BPO remaining after 3 hours. Despite variations in catalyst mass, no relationship is observed in selective oxygenates with changes to mass of 5 wt.% AuPd/ TiO_2 catalyst. Instead, a consistent CH_3OH yield is observed (*ca.* 0.30 μmoles) and evolution of CO_2 (*ca.* 22.0 μmoles) detected. Similarly, the concentration of BPO detected post reaction is unaffected by variation in catalyst mass, with *ca.* 60% remaining post reaction. The data shown suggests no requirement for the presence of catalyst for BPO-initiated CH_4 oxidation.

Uncatalysed BPO -initiated Methane Oxidation

Table 4.6: Comparison of BPO -initiated methane oxidation with and without catalyst.

Entry	Catalyst Mass [mg]	Products [µmoles]				Methanol Sel. [%]	BPO Remaining [%]
		CH_3OH	HCOOH	CH_3OOH	CO_2		
1	27	0.27	0	0	22.3	1.2	59.9
2	0	0.30	0	0.04	22.5	1.3	59.5

Standard reaction conditions: time: 3 hours, temperature: 80 °C, P(CH_4): 27.5, P(O_2): 3.0 bar, stirring rate: 1500 rpm, all catalysts (5 wt. % total): catalyst mass varied, 250 µmoles of radical initiator (benzoyl peroxide, BPO), total volume: 15 mL of D_2O (5 mL).HFB (10 mL) [a] methanol selectivity calculated as $(moles_{oxygenates}/moles_{total\ products})x100$. [b] Calculated as $(moles\ BPO_{final}/moles\ BPO_{initial})x100$.

To determine whether the catalyst possesses an influence for BPO -initiated CH_4 oxidation, reactions were repeated with and without 5 wt.% AuPd/TiO_2 catalyst. Maintaining BPO concentration at 250 µmoles, experimentation with catalyst present produced 0.27 µmoles of CH_3OH with *ca.* 60 % BPO remaining (Table 4.6, Entry 1). This result is consistent with previous experiments conducted under identical reaction conditions. In the absence of catalyst, a similar yield of selective oxygenates is observed after 3 hours. Analysis of aqueous D_2O phase via ^1H NMR detected 0.3 moles of CH_3OH, with post reaction BPO determined to be *ca.* 60% of initial concentration. Therefore, strong evidence is presented demonstrating that catalyst is not essential for the oxidation of CH_4 by BPO.

4.6.2 The effect of BPO concentration

In previous investigations, the variation in catalyst mass was found to produce no changes in the overall formation of selective oxygenates. Subsequently, BPO -initiated CH_4 oxidation is independent of catalyst mass, and dependent only upon BPO concentration. Here, the relationship between BPO concentration and selective oxygenate formation was investigated by examining reactions using 50, 125, 250 and 500 µmoles of BPO. In addition, reactions were repeated without the presence of catalyst to further investigate if any influence can be discerned.

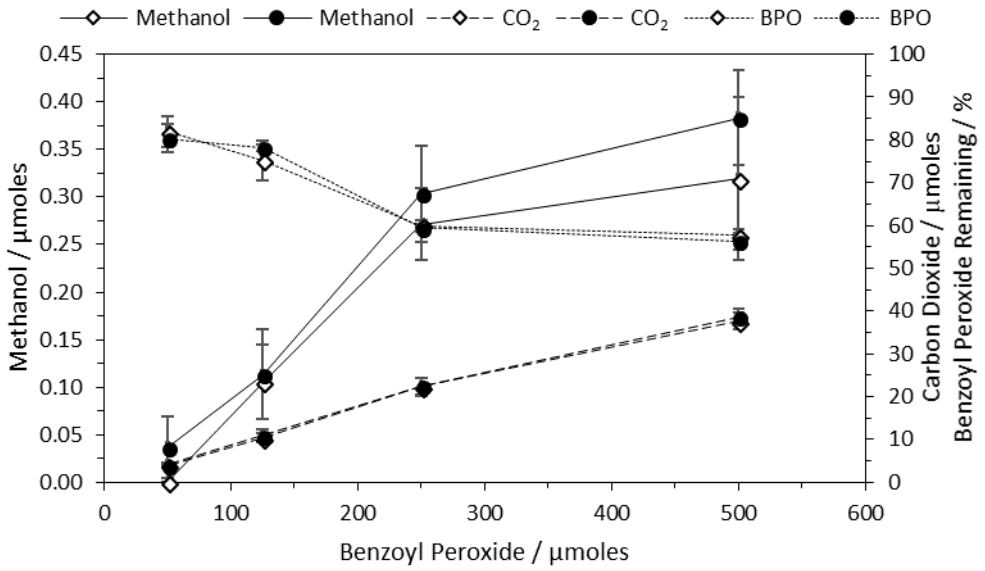

Figure 4.13: Dependence of methanol formation on BPO concentration in the presence (●: Catalysed) or absence (◇: Uncatalysed) of 5wt.% AuPd/ TiO_2 (P25) (I_w) catalyst.

Standard reaction conditions: time: 3 hours, temperature: 80 °C, P(CH_4): 27.5, P(O_2): 3.0 bar, stirring rate: 1500 rpm, all catalysts (5 wt. % total): 9.77×10^{-6} mol of metals equal to 27 mg of solid catalysts, µmoles of radical initiator varied (BPO)(50, 125, 250 and 500 , total volume: 15 mL of D_2O (5 mL).HFB (10 mL)

Examination of the influence of BPO concentration began with 50 µmoles BPO, detecting only trace amounts of CH_3OH (Figure 4.13). The reduction in initial BPO concentration, sees a significant decrease in detected CO_2 (ca. 4.0 µmoles) post reaction. Increasing to higher concentrations of BPO sees a correlation with production of selective oxygenates. That is, increases in BPO concentration from 50 µmoles to 125 moles sees 0.11 µmoles CH_3OH produced. This increase continues for all concentrations examined, observing 0.38 µmoles of CH_3OH at 500 µmoles BPO. Additionally, a relationship is observed in BPO concentration and post reaction CO_2 detected, beginning at *ca.* 4.0 µmoles at lowest concentration and a maximum of *ca*. 38 µmoles at highest examined concentration.

Continuing to investigate the influence of catalyst, reactions were repeated without 5wt.% AuPd/ TiO_2. Illustrated in Figure 4.13, only marginal differences are observed between reaction with and without catalyst.

4.7 Methane Oxidation using *in situ* H_2O_2

Industrially, the generation of H_2O_2 from H_2 and O_2 *in situ* as terminal oxidant provides a more desirable approach to preformed H_2O_2. Instead, the pre-formed H_2O_2 used is exclusively produced by the anthraquinone oxidation process on large scales to produce economic viability.[85] Alternatively, the economically and environmentally cleaner direct synthesis of H_2O_2 from H_2 and O_2 using catalysis offers an attractive alternative to oxidation catalysis. Importantly, the direct synthesis of H_2O_2 onsite provides a small-scale route to dilute concentrations of H_2O_2.[85] This is a major advantage over current large-scale processes, removing the hazards associated with high H_2O_2 concentrations.[85]

Demonstrating high activity for catalytic oxidation[86,87] and the direct synthesis of H_2O_2[88–90], AuPd catalyst are of great interest for the synthesise H_2O_2 *in situ* for catalytic oxidation. Reported by Hutchings *et al.*[91,92] the oxidation of benzyl alcohol to benzaldehyde was demonstrated using bimetallic AuPd catalysts. Carried out at 50 °C, generation of H_2O_2 in-situ was demonstrated *ca.* 6% conversion at *ca.* 85% selectivity. This contrasts with routes typically employing elevated temperatures (>100 °C) for oxidation using molecular oxygen.

Ab Rahim *et al.* similarly applied *in situ* generation H_2O_2 for the selective oxidation of CH_4 in aqueous solution using 5wt.% AuPd/TiO_2.[21,22] Although resulting in a lower catalyst productivity for oxygenates, CH_3OH selectivity improved (68% vs 49%). Importantly, H_2O_2 reactivity yielded a 3 -fold improvement when compared with similar quantities of preformed H_2O_2.

Therefore, given higher gas solubility, the *in situ* generation of H_2O_2 was investigated for CH_4 oxidation using HFB. The *in situ* oxidation was carried out at 50 °C in a mixture of HFB (10 mL) and D_2O (5 mL) using an autoclave reactor. For *in situ* synthesis of H_2O_2 a gas composition of CH_4 (75.86%), H_2 (0.86%), O_2 (1.72 %) with N_2 (21.55%) as a diluent was used with a total pressure of 30.5 bar. Testing was carried out using 5 wt.% AuPd/TiO_2 with the mass of catalyst was fixed at 27 mg. During testing, stirring speed was maintained at 1500 rpm from the initiation of heating to the end of reaction period (30 mins). These conditions were used, unless specified otherwise.

Liquid phase products such as methyl hydroperoxide (CH_3OOH), methanol (CH_3OH) or formic acid (HCOOH) were analysed via ^1H NMR of aqueous D_2O phase and quantified against an internal standard consisting 1% trimethylsilane in $CDCl_3$. Gaseous products, such as CO_2, were analysed by gas chromatography fitted with FID detector. Products were quantified using a CO_2 calibration curve.

Preliminary Investigation

Table 4.7: Comparison of catalytic activity of 2.5wt.% Au- 2.5wt.% Pd/TiO_2 (P25) (I_w) for methane oxidation using *in-situ* generated H_2O_2 from H_2 and O_2.

Entry	Support	Solvent	Products [µmol]				Oxy. Sel.[a] [%]	Meth. Sel.[b] [%]	H_2O_2 Remain.[c] [µmol]
			CH_3OH	HCOOH	CH_3OOH	CO_2			
1	TiO_2	H_2O	0.95	0	0.7	0.65	71.6	41.3	<30
2	TiO_2	HFB/H_2O	0.33	0	0.12	1.34	25.2	18.3	<30
3	Carbon	HFB/H_2O	0.28	0	0.19	1.44	24.6	14.7	<30

Standard reaction conditions: time: 3 hours, temperature: 80 °C, total pressure: 30.5 bar, Gas composition: CH_4(75.86%), N_2(21.55%), H_2(0.86%), O_2(1.72%):, stirring rate: 1500 rpm, all catalysts (5 wt. % total): $9.77x10^{-6}$ mol of metals equal to 27 mg of solid catalysts, 250 µmoles of radical initiator (benzoyl peroxide, BPO), total volume: 15 mL of D_2O (5 mL).HFB (10 mL) [a] Oxygenate selectivity calculated as $(moles_{oxygenates}/moles_{total\ products})x100$. [b] Methanol selectivity calculated as $(moles_{methanol}/moles_{total\ products})x100$. [c] Calculated as $(moles_{final}/moles_{initial})x100$. Oxy. Sel.: Oxygenate selectivity, Meth. Sel.: Methanol Selectivity, H_2O_2 Remain.: H_2O_2 remaining.

For comparison against HFB, the in-situ oxidation was carried out using aqueous reaction media (H_2O, 15 mL). Shown in Table 4.7, under aqueous conditions 1.65 µmoles of selective oxygenates is produced with *ca.* 71 % oxygenate selectivity (Entry 1). The observed activity is comparable with reported work by Ab Rahim *et al.*[21] producing 1.6 µmoles of selective oxygenates. The achieved oxygenate selectivity, however, is lower than reported work (*ca.* 71 % vs *ca.* 83%), resulting from greater CO_2 detected post reaction. Similarly, primary oxygenate selectivity lies towards CH_3OH (*ca.* 41%).

Evaluation of the effect of HFB in the in-situ generated H_2O_2 for CH_4 oxidation began with 5 wt.% AuPd/TiO_2 (Entry 2). Notably, lower activity is observed for selective oxygenate formation, producing *ca.* 0.45 µmoles primary oxygenates. As observed with previous reactions using HFB, selectivity of primary oxygenates lies with CH_3OH (*ca.* 18%) and adventitious CO_2 results in high values detected post reaction.

To improve the interaction between active solvent phase and catalyst and promote catalyst activity, hydrophilic TiO_2 support was substituted for the hydrophobic carbon (Darco G60) support.[93,94] Even so, no variation in activity is observed for 5 wt.% AuPd/carbon with comparable selective oxygenates produced after 30 minutes (*ca.* 0.47 µmoles) with similar oxygenate selectivity *ca.* 25%.

The Effect of Solvent ratio

Initial investigation into the applicability of HFB for CH_4 oxidation using in-situ generated H_2O_2 compared catalyst activity against reaction carried out in H_2O_2. Illustrated in Table

4.7 are reactions that were carried out under aqueous conditions and which demonstrated significantly higher activity for the production of primary oxygenates.

Reported by Flaherty *et al.*[95], the formation of H_2O_2 is proposed to occur via a two-electron oxygen reduction reaction, requiring a protic solvent for facilitation of H_2O_2 formation. Experiments compared H_2O_2 formation for protic (H_2O and CH_3OH) and aprotic solvents (acetonitrile or dimethyl sulfoxide), concluding a 10^3 -times greater turnover rate for H_2O_2 synthesis in protic solvents.

Therefore, to further elucidate this dependence for in-situ generation of H_2O_2 for CH_4 oxidation, the effect of solvent ratio was investigated. Utilising previously defined reaction conditions, total solvent was maintained, whilst ratio of HFB and D_2O solvent mixture was varied.

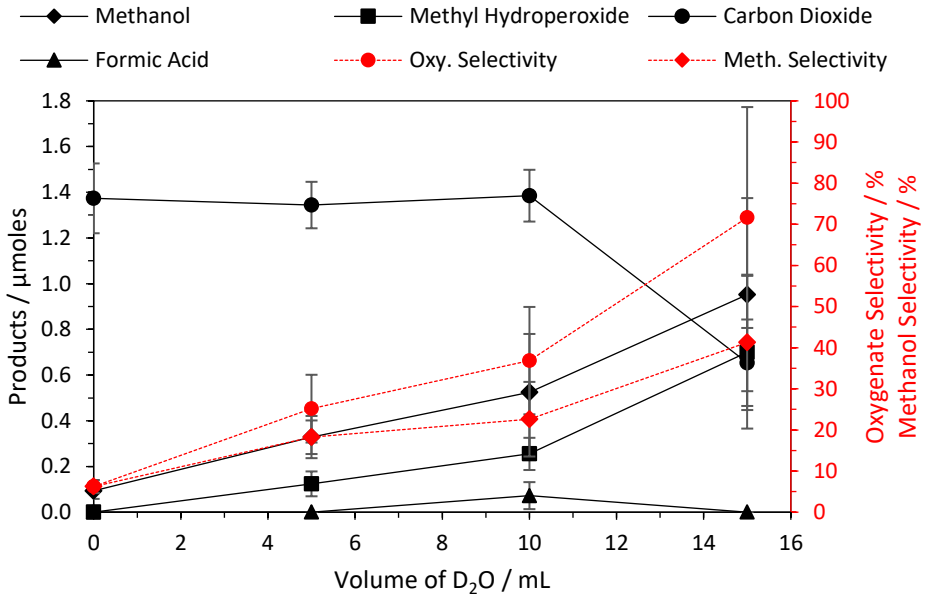

Figure 4.14: The influence of HFB and D_2O solvent ratio upon the oxidation of methane by in-situ generated H_2O_2 using 5wt.%AuP/TiO_2.

Standard reaction conditions: time: 3 hours, temperature: 80 °C, total pressure: 30.5 bar, Gas composition: CH_4(75.86%), N_2(21.55%), H_2(0.86%), O_2(1.72%):, stirring rate: 1500 rpm, all catalysts (5 wt. % total): 9.77×10^{-6} mol of metals equal to 27 mg of solid catalysts, 250 µmoles of radical initiator (benzoyl peroxide, BPO), total volume: 15 mL of D_2O (5 mL).HFB (10 mL)

Initial investigation considered a single HFB phase as reaction media, removing D_2O as the second solvent phase. Illustrated by Figure 4.14, the absence of an aqueous phase results in only small amounts of primary oxygenates detected post reaction, resulting in low primary oxygenate selectivity (*ca.* 6%).

The introduction of H_2O (5mL) sees a small increase in formation of CH_3OH (*ca.* 0.3 μmoles) and CH_3OOH (*ca.* 0.12 μmoles), raising primary oxygenate selectivity to *ca.* 25%. Further increase of D_2O to produce a 2-to-1 mixture of H_2O-to-HFB sees further improvements to selective oxygenates from lower volumes of D_2O. The resulting formation of CH_3OH (*ca.* 0.5 μmoles) and CH_3OOH (*ca.* 0.25 μmoles) produces an oxygenate selectivity of *ca.* 37% with *ca.* 23% CH_3OH selectivity. Even so, the highest activity was found in an aqueous -only phase, producing CH_3OH (*ca.* 0.95 μmoles) and CH_3OOH (*ca.* 0.7 μmoles). Similarly, the decrease in gas solubility resulting from HFB sees a decrease in adventitious CO_2 detected post reaction. Subsequently, oxygenate and CH_3OH selectivities of *ca.* 71 and *ca.* 41 % are achieved, respectively. Evidenced by this, the requirement of H_2O or protic solvent is necessary for higher activity for in-situ CH_4 oxidation. Proposed by Ohkubo *et al.*[19], the presence of H_2O may also produce a soluble media to stabilise primary oxygenates formed, prevent overoxidation to CO_2.

4.8 Conclusion

The perfluorinated solvent, hexafluorobenzene, was used as a method to significantly enhance the solubility of gaseous reactants such as CH_4 and O_2. This increase was then investigated for its effect upon the oxidation of alkane C-H bonds, namely CH_4 and toluene.

Preliminary investigations were carried out using the model substrate toluene and was demonstrated using direct oxidation via O_2. Carried out at 160 °C, a near linear improvement with increasing volume of HFB was discerned. The addition of HFB improved toluene conversion by *ca*. 8% over 48 hours when 1:1 volume mixture was used. This improvement in conversion also maintained selectivity to the desired product, benzaldehyde (*ca.* 95%).

Considered a holy grail of catalytic chemistry, the direct and selective oxidation of CH_4 to CH_3OH presents an incredible challenge for industry and academia.[96] Furthermore, the oxidation using molecular O_2 presents the ultimate goal for an environmentally benign oxidation process.[61] Therefore, providing a reaction media with significantly higher concentrations in solution, hexafluorobenzene was applied for the oxidation of CH_4 using O_2.

The promotion of C-H bond activation was trialled using common radical initiators under mild reaction conditions (80 °C). The application of azo -initiators displayed no influence and subsequent experiments yielded no primary oxygenates. Alternatively, the peroxy -based initiator benzoyl peroxide produced marked improvement with *ca.* 0.3 μmoles of CH_3OH produced. Although promising, further examination of the influence of catalyst by

variation of catalyst mass revealed the oxidation of CH_4 to be independent of catalyst presence. Instead, activity for the oxidation was only dependent upon BPO concentration for the synthesis of primary oxygenates.

In lieu of this, activation of O_2 was investigated by synthesis of H_2O_2 from O_2 and H_2. Extensively reported, bimetallic AuPd catalysts have been demonstrated as efficient catalysts for the direct synthesis of H_2O_2 from O_2 and H_2.[89,90,97,98] Also proficient as oxidation catalysts[99,100], the synthesis of H_2O_2 *in situ* has been studied as a method of producing a green oxidation process.[91,92,101] Applied to the selective oxidation of CH_4, Ab Rahim *et al.* reported a three-fold improvement in H_2O_2 reactivity compared to pre-formed H_2O_2 using an AuPd for an aqueous system.[20]

Under aqueous-free solvent conditions, the formation of selective oxygenates was unfavourable despite higher gas solubility, detecting only trace formation of CH_3OH. The introduction of D_2O saw marked improvement which continued to improve with increased ratio of D_2O, yielding increases in primary oxygenate formation. Subsequently, the highest productivity for selective oxygenate formation was observed when an aqueous system was employed.

Overall, the application of perfluorinated solvent has provided no improvement to the selective oxidation of CH_4. Crucially, further investigation into improving the interaction of solvent and support are required, believed to limit the activity of AuPd catalysts for systems.

4.9 References

1 P. J. Dyson and P. G. Jessop, *Catal. Sci. Technol.*, 2016, **6**, 3302–3316.

2 S. Moret, P. J. Dyson and G. Laurenczy, *Nat. Commun.*, 2014 , **5**, 1-7.

3 B. Cornils, *Angew. Chemie Int. Ed. English*, 1995, **34**, 1575–1577.

4 W. Keim, in *Green Chemistry*, 2003, **5**, 105–111.

5 M. Scott, B. Blas Molinos, C. Westhues, G. Franciò and W. Leitner, *ChemSusChem*, 2017, **10**, 1085–1093.

6 Y. Wang, J. Jiang and Z. Jin, *Catal. Surv. from Asia*, 2004, **8**, 119–126.

7 M. P. Krafft, *Adv. Drug Deliv. Rev.*, 2001, 47, 209–228.

8 P. Srinivasan, C. Corti, L. Montagna and P. Savelli, *J. Synth. Lubr.*, 1993, **10**, 143–164.

9 S. Banerjee and D. E. Curtin, *J. Fluor. Chem.*, 2004, **125**, 1211–1216.

10 Y. Q. Shi, C. Wu, L. Li and J. Yang, *J. Electrochem. Soc.*, 2017, **164**, A2031–A2037.

11 V. M. Sadtler, M. P. Krafft and J. G. Riess, *Angew. Chemie (International Ed. English)*, 1996, **35**, 1976–1978.

12 E. P. Wesseler, R. Iltis and L. C. Clark, *J. Fluor. Chem.*, 1977, **9**, 137–146.

13 C. M. Sharts, H. R. Reese, K. A. Ginsberg, F. K. Multer, M. D. Nielson, A. G. Greenburg, G. W. Peskin and D. M. Long, *J. Fluor. Chem.*, 1978, **11**, 637–641.

14 C. Samojłowicz, M. Bieniek, A. Zarecki, R. Kadyrov and K. Grela, *Chem. Commun.*, 2008, 6282–4.

15 D. Rost, M. Porta, S. Gessler and S. Blechert, *Tetrahedron Lett.*, 2008, **49**, 5968–5971.

16 K. Neimann and R. Neumann, *Org. Lett.*, 2000, **2**, 2861–2863.

17 J.-M. Vincent, A. Rabion, V. K. Yachandra and R. H. Fish, *Angew. Chemie Int. Ed. English*, **36**, 2346–2349.

18 M. Lin, T. E. Hogan and A. Sen, *J. Am. Chem. Soc.*, 1996, **118**, 4574–4580.

19 K. Ohkubo and K. Hirose, *Angew. Chemie - Int. Ed.*, 2018, **57**, 2126–2129.

20 M. H. Ab Rahim, M. M. Forde, C. Hammond, R. L. Jenkins, N. Dimitratos, J. A. Lopez-Sanchez, A. F. Carley, S. H. Taylor, D. J. Willock, G. J. Hutchings, M. Hasbi, A. Rahim, M. M. Forde, C. Hammond, R. L. Jenkins, N. Dimitratos, J. A. Lopez-Sanchez, A. F. Carley, S. H. Taylor, D. J. Willock and G. J. Hutchings, *Top. Catal.*,

2013, **56**, 1843–1857.

21 M. H. Ab Rahim, M. M. Forde, R. L. Jenkins, C. Hammond, Q. He, N. Dimitratos, J. A. Lopez-Sanchez, A. F. Carley, S. H. Taylor, D. J. Willock, D. M. Murphy, C. J. Kiely and G. J. Hutchings, *Angew. Chemie - Int. Ed.*, 2013, **52**, 1280–1284.

22 M. H. Ab Rahim, R. D. Armstrong, C. Hammond, N. Dimitratos, S. J. Freakley, M. M. Forde, D. J. Morgan, G. Lalev, R. L. Jenkins, J. A. Lopez-Sanchez, S. H. Taylor, G. J. Hutchings, M. Hasbi, A. Rahim, R. D. Armstrong, C. Hammond, N. Dimitratos, S. J. Freakley, M. M. Forde, D. J. Morgan, G. Lalev, R. L. Jenkins, J. A. Lopez-Sanchez, S. H. Taylor and G. J. Hutchings, *Catal. Sci. Technol.*, 2016, **6**, 3410–3418.

23 L. Kesavan, R. Tiruvalam, M. H. A. Rahim, M. I. bin Saiman, D. I. Enache, R. L. Jenkins, N. Dimitratos, J. A. Lopez-Sanchez, S. H. Taylor, D. W. Knight, C. J. Kiely and G. J. Hutchings, *Science*, 2011, **331**, 195–199.

24 J. A. J. A. Moulijn, P. W. N. M. van Leeuwen, R. A. van Santen, I. Chorkendorff, J. W. Niemantsverdriet, J. A. J. A. Moulijn, P. W. N. M. van Leeuwen and R. A. van Santen, in *Catalysis*, 1993, **79**, 401–417.

25 F. David Evans and R. Battino, *J. Chem. Thermodyn.*, 1971, **3**, 753–760.

26 C. Williams, J. H. Carter, N. F. Dummer, Y. K. Chow, D. J. Morgan, S. Yacob, P. Serna, D. J. Willock, R. J. Meyer, S. H. Taylor and G. J. Hutchings, *ACS Catal.*, 2018, 2567–2576.

27 C. Hammond, N. Dimitratos, J. A. Lopez-Sanchez, R. L. Jenkins, G. Whiting, S. A. Kondrat, M. H. Ab Rahim, M. M. Forde, A. Thetford, H. Hagen, E. E. Stangland, J. M. Moulijn, S. H. Taylor, D. J. Willock and G. J. Hutchings, *ACS Catal.*, 2013, **3**, 1835–1844.

28 C. Hammond, N. Dimitratos, R. L. Jenkins, J. A. Lopez-sanchez, S. A. Kondrat, M. Hasbi Ab Rahim, M. M. Forde, A. Thetford, S. H. Taylor, H. Hagen, E. E. Stangland, J. H. Kang, J. M. Moulijn, D. J. Willock, G. J. Hutchings, M. Hasbi, M. M. Forde, A. Thetford, S. H. Taylor, H. Hagen, E. E. Stangland, J. H. Kang, J. M. Moulijn, D. J. Willock and G. J. Hutchings, *ACS Catal.*, 2013, **3**, 689–699.

29 A. N. Campbell and S. S. Stahl, *Acc. Chem. Res.*, 2012, **45**, 851–863.

30 R. A. Periana, D. J. Taube, E. R. Evitt, D. G. Löffler, P. R. Wentrcek, G. Voss, T. Masuda and D. G. L6ffler, *Science*, 1993, **259**, 340–343.

31 R. A. Periana, D. J. Taube, S. Gamble, H. Taube, T. Satoh and H. Fujii, *Science*, 1998, **280**, 560–564.

32 Q. Yuan, W. Deng, Q. Zhang and Y. Wang, *Adv. Synth. Catal.*, 2007, **349**, 1199–1209.

33 E. Roduner, W. Kaim, B. Sarkar, V. B. Urlacher, J. Pleiss, R. Gläser, W. D. Einicke, G. A. Sprenger, U. Beifuß, E. Klemm, C. Liebner, H. Hieronymus, S. F. Hsu, B. Plietker and S. Laschat, *ChemCatChem*, 2013, **5**, 82–112.

34 C. E. Tinberg and S. J. Lippard, *Acc. Chem. Res.*, 2011, **44**, 280–288.

35 A. I. Olivos-Suarez, À. Szécsényi, E. J. M. Hensen, J. Ruiz-Martinez, E. A. Pidko and J. Gascon, *ACS Catal.*, 2016, **6**, 2965–2981.

36 D. Munz and T. Strassner, *Inorg. Chem.*, 2015, 54, 5043–5052.

37 L. Que, in *Accounts of Chemical Research*, 2007, **40**, 493–500.

38 J. Hohenberger, K. Ray and K. Meyer, *Nat. Commun.*, 2012, **3**, 1-13.

39 C. Krebs, D. G. Fujimori, C. T. Walsh and J. M. Bollinger, *Accounts of Chemical Research*, 2007, **40**, 484–492.

40 H. Fujii, *Coordination Chemistry Reviews*, 2002, **226**, 51–60.

41 A. B. Sorokin, E. V Kudrik and D. Bouchu, *Chem. Commun.*, 2008, 2562–2564.

42 M. M. Forde, B. C. Grazia, R. Armstrong, R. L. Jenkins, M. H. A. Rahim, A. F. Carley, N. Dimitratos, J. A. Lopez-Sanchez, S. H. Taylor, N. B. McKeown and G. J. Hutchings, *J. Catal.*, 2012, **290**, 177–185.

43 W. Chen, J. A. Kocal, T. A. Brandvold, M. L. Bricker, S. R. Bare, R. W. Broach, N. Greenlay, K. Popp, J. T. Walenga, S. S. Yang and J. J. Low, *Catal. Today*, 2009, **140**, 157–161.

44 H. Tang, C. Shen, M. Lin and A. Sen, *Inorganica Chim. Acta*, 2000, **300**–**302**, 1109–1111.

45 T. Strassner, S. Ahrens, M. Muehlhofer, D. Munz and A. Zeller, *Eur. J. Inorg. Chem.*, 2013, 3659–3663.

46 Z. An, X. Pan, X. Liu, X. Han and X. Bao, *J. Am. Chem. Soc.*, 2006, **128**, 16028–16029.

47 N. J. Gunsalus, A. Koppaka, S. H. Park, S. M. Bischof, B. G. Hashiguchi and R. A. Periana, *Chem. Rev.*, 2017, **117**, 8521–8573.

48 F. Lefebvre, E. Grinenval and P. Putaj, *J. Catal.*, 2013, **2013**, 1–9.

49 J. Yuan, L. Wang and Y. Wang, *Ind. Eng. Chem. Res.*, 2011, **50**, 6513–6516.

50 J. Yuan, L. Liu, L. Wang and C. Hao, *Catal. Letters*, 2013, **143**, 126–129.

51 J. Yuan, Y. Wang and C. Hao, *Catal. Letters*, 2013, **143**, 610–615.

52 J. J. Bravo-Suárez, K. K. Bando, J. Lu, T. Fujitani and S. T. Oyama, *J. Catal.*, 2008, **255**, 114–126.

53 M. Conte, X. Liu, D. M. Murphy, K. Whiston and G. J. Hutchings, *Phys. Chem. Chem. Phys.*, 2012, **14**, 16279–16285.

54 X. Liu, M. Conte, M. Sankar, Q. He, D. M. Murphy, D. Morgan, R. L. Jenkins, D.

Knight, K. Whiston, C. J. Kiely and G. J. Hutchings, *Appl. Catal. A Gen.*, 2015, **504**, 373–380.

55 L.-X. Xu, C.-H. He, M.-Q. Zhu and S. Fang, *Catal. Letters*, 2007, **114**, 202–205.

56 G. Lü, D. Ji, G. Qian, Y. Qi, X. Wang and J. Suo, *Appl. Catal. A Gen.*, 2005, **280**, 175–180.

57 Y. Liu, H. Tsunoyama, T. Akita, S. Xie and T. Tsukuda, *ACS Catal.*, 2011, **1**, 2–6.

58 G. Walther, G. Jones, S. Jensen, U. J. Quaade and S. Horch, *Catal. Today*, 2009, **142**, 24–29.

59 C. Li and Y. Liu, *Bridging Heterogeneous and Homogeneous Catalysis: Concepts, Strategies, and Applications*, 2014.

60 C. J. C. J. Jones, D. Taube, V. R. Ziatdinov, R. A. Periana, R. J. Nielsen, J. Oxgaard and W. A. Goddard, *Angew. Chemie - Int. Ed.*, 2004, **43**, 4626–4629.

61 N. Agarwal, S. J. Freakley, R. U. McVicker, S. M. Althahban, N. Dimitratos, Q. He, D. J. Morgan, R. L. Jenkins, D. J. Willock, S. H. Taylor, C. J. Kiely and G. J. Hutchings, *Science*, 2017, **358**, 223–227.

62 R. Battino, *Solubility Data Series: Volume 7 Oxygen and Ozone*, International Union of Pure and Applied Chemistry, https://srdata.nist.gov/solubility/IUPAC/iupac.aspx#vol1.htm, (accessed 30 July 2017).

63 A. Li, S. Tang, P. Tan, C. Liu and B. Liang, *J. Chem. Eng. Data*, 2007, **52**, 2339–2344.

64 J. Pritchard, L. Kesavan, M. Piccinini, Q. He, R. Tiruvalam, N. Dimitratos, J. A. Lopez-Sanchez, A. F. Carley, J. K. Edwards, C. J. Kiely and G. J. Hutchings, *Langmuir*, 2010, **26**, 16568–16577.

65 A. A. Fokin and P. R. Schreiner, *Chem. Rev.*, 2002, **102**, 1551–1593.

66 K. Matyjaszewski and S. G. Gaynor, *Appl. Polym. Sci.*, 2000, 929–977.

67 M. I. Binsaiman, G. L. Brett, R. Tiruvalam, M. M. Forde, K. Sharples, A. Thetford, R. L. Jenkins, N. Dimitratos, J. A. Lopez-Sanchez, D. M. Murphy, D. Bethell, D. J. Willock, S. H. Taylor, D. W. Knight, C. J. Kiely and G. J. Hutchings, *Angew. Chemie - Int. Ed.*, 2012, **51**, 5981–5985.

68 D. Braun, H. Cherdron, M. Rehahn, H. Ritter and B. Voit, *Polymer Synthesis : Theory and Practice*, 2005.

69 H. H. Abdel-Razik and E. R. Kenawy, *J. Appl. Polym. Sci.*, 2012, **125**, 1136–1145.

70 L. Z. Guo, X. J. Wang, Y. F. Zhang and X. Y. Wang, *J. Appl. Polym. Sci.*, 2014, **131**, 40238.

71 M. N. Siddiqui, *J. Hazard. Mater.*, 2009, **167**, 728–735.

72 H. Xu, P. T. Liu, Y. H. Li and F. S. Han, *Org. Lett.*, 2013, **15**, 3354–3357.

73 A. Goosen, C. W. McCleland, D. H. Morgan, J. S. O'Connell and A. Ramplin, *J. Chem. Soc. Perkin Trans. 1*, 1993, 401–402.

74 R. Lloyd, R. L. Jenkins, M. Piccinini, Q. He, C. J. Kiely, A. F. Carley, S. E. Golunski, D. Bethell, J. K. Bartley and G. J. Hutchings, *J. Catal.*, 2011, **283**, 161–167.

75 J. Meijer and A. Hogt, *Acros Org. Rev.*, 2006, 1–11.

76 C. H. Han, S. Butz and G. Schmidt-Naake, *Angew. Makromol. Chemie*, 1999, **265**, 69–74.

77 Ghosh and K. Das, *J. Pharmacol. Pharmacother.*, 2018, **9**, 27.

78 K. McKeage and G. M. Keating, *Am. J. Clin. Dermatol.*, 2008, 9, 193–204.

79 G. O. Wilson, J. W. Henderson, M. M. Caruso, B. J. Blaiszik, P. J. McIntire, N. R. Sottos, S. R. White and J. S. Moore, *J. Polym. Sci. Part A Polym. Chem.*, 2010, **48**, 2698–2708.

80 A. Uhl, M. Bitzer, H. Wolf, D. Hermann, S. Gutewort, M. Völkl and I. Nagl, in *Ullmann's Encyclopedia of Industrial Chemistry*, American Cancer Society, 2018, pp. 1–45.

81 W. Sha, J. T. Yu, Y. Jiang, H. Yang and J. Cheng, *Chem. Commun.*, 2014, **50**, 9179–9181.

82 M. Sankar, E. Nowicka, E. Carter, D. M. Murphy, D. W. Knight, D. Bethell and G. J. Hutchings, *Nat. Commun.*, 2014, **5**, 1-6.

83 T. F. S. Silva, T. C. O. M. Leod, L. M. D. R. S. Martins, M. F. C. Guedes Da Silva, M. A. Schiavon and A. J. L. Pombeiro, *J. Mol. Catal. A Chem.*, 2013, **367**, 52–60.

84 G. Moad and D. H. Solomon, *The Chemistry of Radical Polymerization*, 2005.

85 C. Samanta and V. R. Choudhary, *Appl. Catal. A Gen.*, 2007, **326**, 28–36.

86 D. I. Enache, J. K. Edwards, P. Landon, B. Solsona-Espriu, A. F. Carley, A. A. Herzing, M. Watanabe, C. J. Kiely, D. W. Knight and G. J. Hutchings, *Science* , 2006, **311**, 362-365.

87 E. Rucinska, P. J. Miedziak, S. Pattisson, G. L. Brett, S. Iqbal, D. J. Morgan, M. Sankar and G. J. Hutchings, *Catal. Sci. Technol.*, 2018, **8**, 2987–2997.

88 J. K. Edwards, S. J. Freakley, A. F. Carley, C. J. Kiely and G. J. Hutchings, *Acc. Chem. Res.*, 2013, **47**, 845–854.

89 J. K. Edwards, B. Solsona, E. N. N, A. F. Carley, A. A. Herzing, C. J. Kiely and G. J. Hutchings, *Science*, 2009, **323**, 1037-1041.

90 J. K. Edwards, B. E. Solsona, P. Landon, A. F. Carley, A. Herzing, C. J. Kiely and G. J.

Hutchings, *J. Catal.*, 2005, **236**, 69–79.

91 M. Santonastaso, S. J. Freakley, P. J. Miedziak, G. L. Brett, J. K. Edwards and G. J. Hutchings, *Org. Process Res. Dev.*, 2014, **18**, 1455–1460.

92 I. Moreno, N. F. Dummer, J. K. Edwards, M. Alhumaimess, M. Sankar, R. Sanz, P. Pizarro, D. P. Serrano and G. J. Hutchings, *Catal. Sci. Technol.*, 2013, **3**, 2425.

93 B. Erdem, R. A. Hunsicker, G. W. Simmons, E. D. Sudol, V. L. Dimonie and M. S. El-Aasser, *Langmuir*, 2001, **17**, 2664–2669.

94 C.-C. Leng and N. G. Pinto, *Carbon N. Y.*, 1997, **35**, 1375–1385.

95 N. M. Wilson and D. W. Flaherty, *J. Am. Chem. Soc.*, 2016, **138**, 574–586.

96 C. Hammond, S. Conrad and I. Hermans, *ChemSusChem*, 2012, **5**, 1668–1686.

97 V. Paunovic, V. V. Ordomsky, V. L. Sushkevich, J. C. Schouten and T. A. Nijhuis, *ChemCatChem*, 2015, **7**, 1161–1176.

98 J. K. Edwards, S. J. Freakley, R. J. Lewis, J. C. Pritchard and G. J. Hutchings, *Catal. Today*, 2015, **248**, 3–9.

99 A. Villa, N. Janjic, P. Spontoni, D. Wang, D. S. Su and L. Prati, *Appl. Catal. a-General*, 2009, **364**, 221–228.

100 C. M. Olmos, L. E. Chinchilla, E. G. Rodrigues, J. J. Delgado, A. B. Hungría, G. Blanco, M. F. R. Pereira, J. J. M. Órfão, J. J. Calvino and X. Chen, *Appl. Catal. B Environ.*, 2016, **197**, 222–235.

101 L. Torrente-Murciano, T. Villager and D. Chadwick, *ChemCatChem*, 2015, **7**, 925–927.

Chapter 5: Conclusion and Future Work

5.1 General Conclusion

Representing one of the greatest challenges for catalytic chemistry, the direct oxidation of methane (CH_4) to methanol (CH_3OH) would provide an alternative route to valuable petrochemicals.[1] The application would allow currently underutilised natural gas to supplement dwindling reserves of crude oil as avenue to valuable petrochemicals, avoiding the current practice of flaring. [2]

This primary focus of the following thesis was to investigate the low temperature oxidation of CH_4 to CH_3OH. Subsequently, the two sections of work were studied as approaches to address the primary aims of the thesis.

5.1.1 Selective oxidation of methane to methanol using supported Au-Pd catalysts prepared by Stabiliser-free Sol-Immobilisation

Previously reported as effective catalysts for the selective oxidation of CH_4 to CH_3OH), $AuPd/TiO_2$ catalysts prepared by impregnation possess a broad particle size distribution with varying composition of metal nanoparticles.[3,4] The resulting poor control of catalyst material yields poor use of preformed H_2O_2 which is required in excess to produce moderate yields of primary oxygenates. Instead the use of H_2O_2, whilst an environmentally benign oxidant, requires efficient utilisation to overcome the economic costs associated with its production, via the anthraquinone oxidation process[5,6]

The initial aims of this body of work aimed to understand the influence of AuPd particle size for the oxidation of CH_4 to CH_3OH and demonstrated a structure-activity relationship to oxygenate formation. In additions to nanoparticle size, however, further influences from support phase were discerned to contribute to the enhancements in activity observed.

Continued investigations into the influences demonstrated that a beneficial strong metal-support interaction was produced when utilising rutile phase TiO_2, instead of conventionally used P25 TiO_2 comprised of predominantly anatase phase TiO_2. Inducing marked activity for the production of primary oxygenates, the influence of support also

extended to stabilisation of deleterious metallic state Pd^0, which produced high rates of H_2O_2 decomposition alongside moderate productivity of primary oxygenates.

The reduction of metal concentration was rationalised to limit deleterious activity towards H_2O_2 decomposition and to compare the influence of significantly decreased surface area of rutile support (6 m^2 g^{-1} vs 45 m^2 g^{-1}). Therefore, 0.13 wt.% AuPd loading was used instead of 1 wt.% to produce a similar ratio of metal loading to surface area (0.022 wt.% m^{-2}). The resulting reduction in AuPd concentration significantly decreased undesired H_2O_2 decomposition and produced catalysts displayed significant productivity to primary oxygenates with reduced metal concentration.

Consequently, the catalyst produced displayed the controlled decomposition of H_2O_2, which facilitated efficient use of H_2O_2 for selective oxidation. The resulting catalysts exhibited the highest oxygenate productivity of 0.90 mol $kg_{(cat)}^{-1}$ h^{-1} and TOF was calculated at 137 h^{-1}, significantly higher than previously reported AuPd supported catalysts.[3,4]

5.1.2 Methane oxidation using hexafluorobenzene solvent

Exhibiting significantly larger gas solubilities for gases such as CH_4, O_2 and H_2 than most commonly used solvents, such as H_2O, perfluorinated solvents represent highly attractive and inert reaction media for a wide array of processes.[7–9]

In this section, the application of hexafluorobenzene was trialled as an alternative solvent to previously established aqueous systems using H_2O_2, improving solubility of reactants considerably.[3,10] In addition, the utilisation of molecular O_2 was investigated as a green, abundantly available and cheap oxidant. The use of O_2 represents a considerable challenge for industry and academia.[11]

Avenues investigated for incorporation of molecular O_2 trialled C-H bond activation by radically initiated H-abstraction or by O_2 activation via the in-situ generation of H_2O_2. However, several key issues were found during the investigations. For C-H activation, the examination of azo-initiators were shown to be inactive for CH_4 oxidation. More reactive, benzoyl peroxide demonstrated low activity for CH_4 oxidation, but displayed activity independent of catalyst presence.

Alternatively, activation of O_2 via *in-situ* generation of H_2O_2 was trialled. Producing low activity for HFB only, however, the presence of a second aqueous phase was required to improve productivity for CH_4 oxidation. Even so, maximum activity was achieved with an aqueous only system. The low activity observed with HFB solvent is proposed to originate from poor interaction of the catalyst with the solvent.

5.2 Future work

5.2.1 Selective oxidation of methane to methanol using supported Au-Pd catalysts prepared by Stabiliser-free Sol-Immobilisation

1) Strong Metal-Support Interactions:

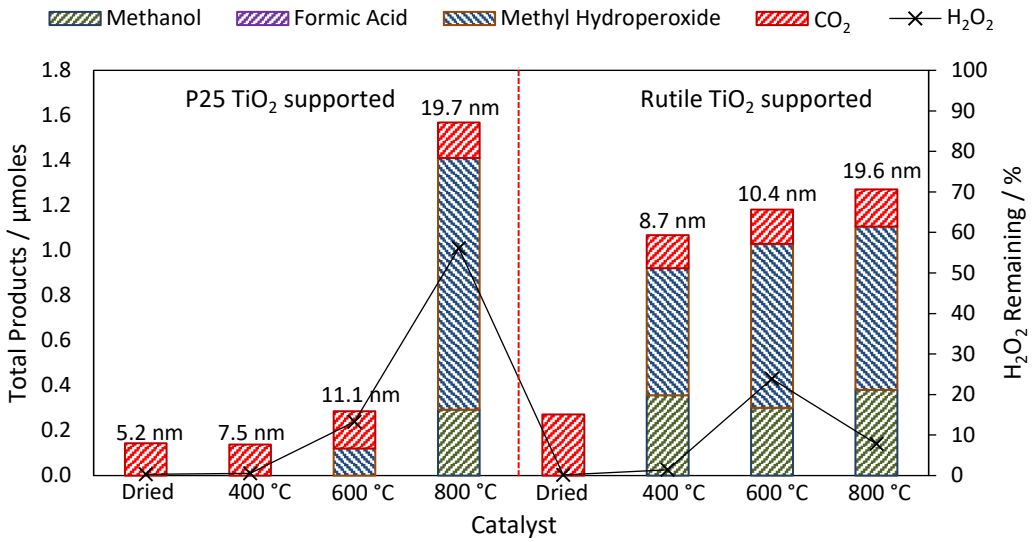

Figure 5.1: Comparison of the influence of P25- and rutile- TiO_2 support upon the catalytic activity of 1 wt.% AuPd catalysts prepared by SF-S_i at 70 °C for methane oxidation.

Throughout investigations for TiO_2-supported AuPd catalysts the effect of heat treatment upon catalyst performance was evaluated through influences to nanoparticle size. Although relationships were observed, additional influences from the support were identified during the testing of rutile- and P25- TiO_2 (Figure 5.1). Importantly, for P25-supported AuPd, the improvement in use of H_2O_2 is accompanied by a shift in binding energy for Pd^{2+} peak of Pd(3d) band. Contrastingly, this phenomenon was not observed for rutile TiO_2 -supported AuPd, with no improvement to reducing the H_2O_2 decomposition observed. The observed shift in binding energy, determined by XPS, was proposed to originate from strong metal support interactions (SMSI). This is suggested despite predominantly being observed in reducible oxide supports after high temperature reducing processes.[12] Similarly, the improvement observed for 1wt.%AuPd/ rutile TiO_2 with heat treatment showed no correlation with increasing nanoparticle size for both H_2O_2 decomposition and CH_4 oxidation. This relationship was observed for P25 TiO_2. Subsequently, a change in support interaction was concluded to be the cause. Further observation of geometric influences, via the partial or complete encapsulation of nanoparticles was not observed during TEM analysis. Therefore, further work is required to elucidate the origin of the observed increase in binding energy, which may originate

from (i) oxidative strong metal support interactions (OSMI) or (ii) Phase transition of predominantly anatase P25- to rutile TiO_2.

Alternatively, the quantification of metal leaching post reaction may indicate that catalytic activity stem from homogenous reactions of AuPd nanoparticle in solution. The resulting activities could then be independent of support.

2) Time-On-Line Analysis and confirmation of CO_2

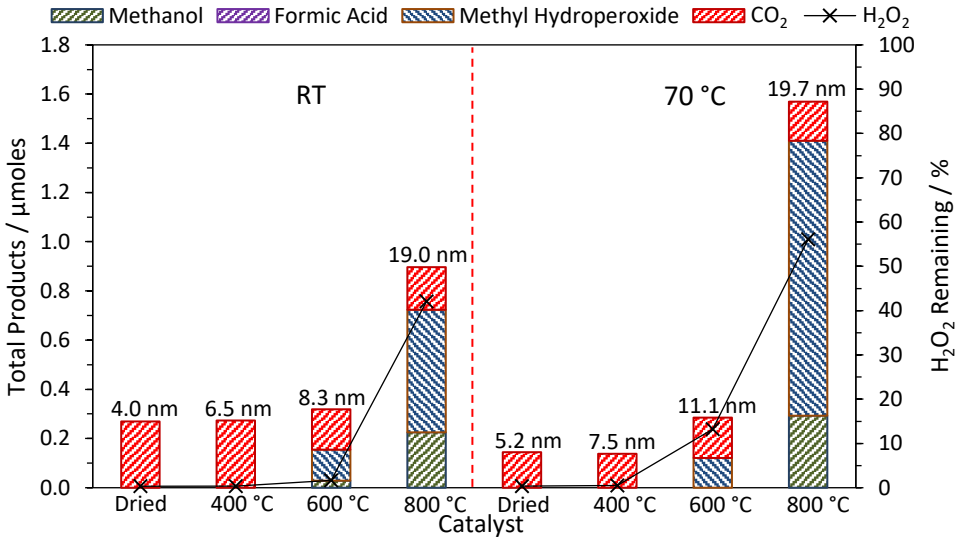

Figure 5.2: Comparison of the influence preparation temperature upon the catalytic activity of 1 wt.% $AuPd/TiO_2$ (P25) catalysts prepared by SF-S_i at 70 °C for methane oxidation.

During the preliminary testing of blank and bare P25 TiO_2 testing (Table 3.2), initial work identified the presence of CO_2 which was attributed to adventitious origins. Consequently, the resulting inaccuracy limits the assignment of CO_2 detected during catalyst testing for CH_4 oxidation. Further work is proposed to implement an improved technique for more accurate determination of CO_2 in gaseous samples taken after CH_4 testing.

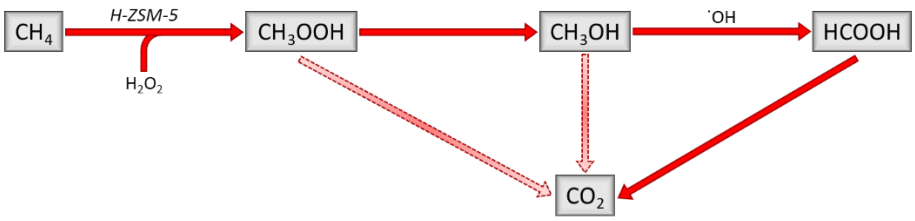

Figure 5.3: Proposed reaction scheme for H-ZSM-5 (30) catalysed oxidation of CH_4 using H_2O_2.[13]

Furthermore, additional investigation to accurately determine the activity of catalysts, such as dried only and 400 °C heat treated catalysts (Figure 5.2). The use of time-on-line

(TOL) analysis can be used to determine the formation of selective oxygenates at shorter reaction intervals. This may conclude the source of detected CO_2 after testing to result from the over-oxidation of selective oxygenates produces at earlier periods.

3) Influence of Catalyst preparation temperature

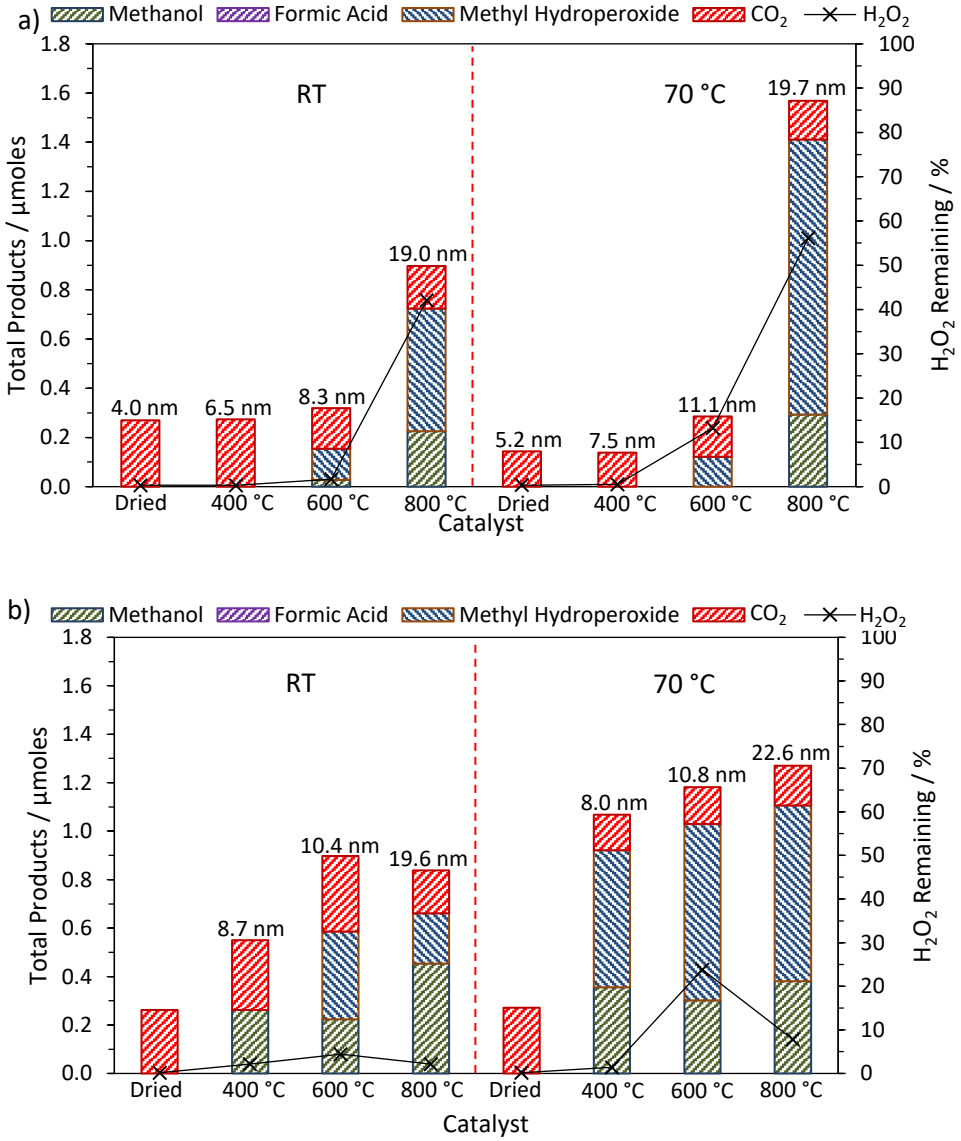

Figure 5.4: Comparison of the influence of preparation temperature on the catalytic activity of 1 wt.% AuPd catalysts supported on (a) P25 TiO_2 and (b) rutile TiO_2 for methane oxidation using preformed H_2O_2. RT: prepared at room temperature

Discussed in Chapter 3, the structure-activity relationship between AuPd particle size was shown to increase primary oxygenate productivity with increasing nanoparticle size. To further discern the influence, minor changes in nanoparticle sizes were produced by raising the temperature of catalyst preparation. Importantly, the elevation of temperature produced catalysts which exhibited improved activity (*ca.* 2-fold) to room temperature counterparts (Figure 5.4), with marginally larger mean particle size. Despite this, the large difference in catalyst activity which displayed similar AuPd size distribution profiles cannot be explained by small differences in particle size.

Reported by Rogers *et al.*, a similar observation was observed when examining the influence of solvent for the preparation of Au nanoparticles. Despite producing similar Au nanoparticle profiles, the variation of solvent decreased achieved TOF for the oxidation of glycerol. This work highlighted the relationship of nanoparticle structure to catalyst activity. Therefore, further work may be able to discern the additional influence of preparation temperature.

4) The Influence of AuPd composition

Reported by Wong *et al.*[14–16] the room temperature hydrochlorination of trichloroethene was shown for Pd-on-Au catalysts. Proposing that smaller Pd-on-Au nanoparticle diameters would allow improved activity for hydrochlorination, Wong *et al.* produced Au nanoparticles of *ca.* 4 nm diameter and studied the effect of different Pd loadings. The study demonstrated a volcano-like activity with increasing Pd metal loading, however, maximum activity was observed at 70 % surface coverage of Pd-on-Au. A similar study was repeated for Au nanoparticles of 10 and 20 nm diameter.

Previously examined by Hutchings *et al.* for AuPd catalysts prepared by sol immobilisation, the influence of Pd/Au molar ratio was also shown to increase activity for the synthesis of H_2O_2.[17,18] Unfavourably, however, a similar trend was observed for the deleterious hydrogenation of H_2O_2 to H_2O. For CH_4 oxidation using preformed H_2O_2, varying the composition of Au:Pd in 5 wt.% AuPd/TiO_2 produced a volcano-like variation in activity.[4] Au only catalysts exhibited the lowest TOF (0.39 h^{-1}) with low CH_3OH selectivity (37.8 %) and *ca.* 60% H_2O_2 remaining post reaction.[4] Contrastingly, Pd only catalyst displayed highest CH_3OH selectivity (*ca.* 72%) however, near -complete H_2O_2 decomposition was observed (*ca.* 2% remaining.). maximum activity for oxidation was achieved with 4Au:1Pd ratio, producing 3.46 moles of primary oxygenates with *ca*. 16 % H_2O_2 remaining.

Preliminary work was, therefore, carried out to understand the influence of Pd surface coverage for AuPd catalysts produced via sol immobilisation. Inspired by Wong *et al.*[15], the preparation of colloidal Au nanoparticles (*ca.* 20 nm) were further modified with

varying coverages of Pd layers, before immobilisation to TiO_2 (P25). However, as seen in Figure 6.3, the preparation of core-shell Pd-on-Au does not yield marked improvement in selective oxygenates and activity is not comparable to homogenous nanoparticles of larger sizes, as evidenced by Chapter 3.

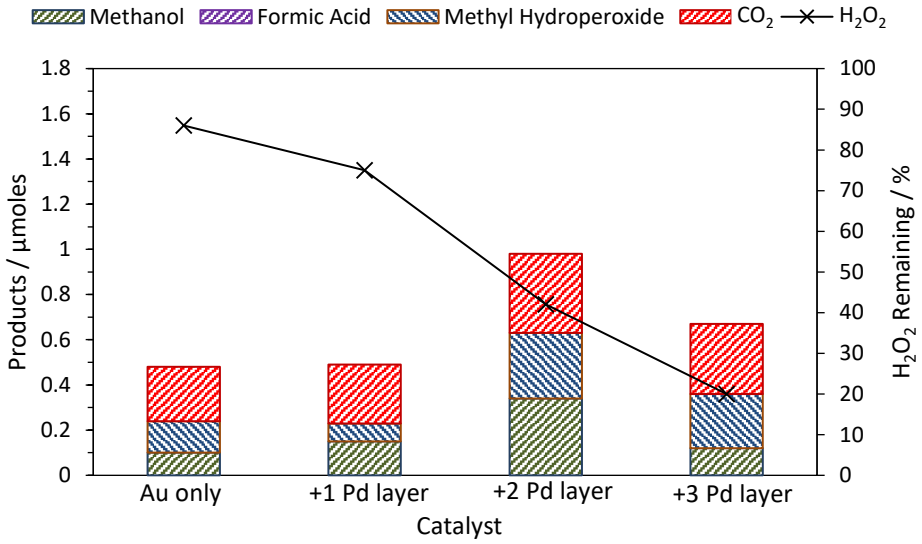

Figure 5.4: The effect of Pd layer coverage upon Au nanoparticles (*ca.* 20 nm) for selective oxidation of methane using preformed H_2O_2.

Therefore, further work may consider the influence of nanoparticle composition utilising a homogeneous morphology. As previously shown, the variation of Pd metal provides a mode of tuning catalyst activity towards H_2O_2 decomposition which was identified as key to selective production of primary oxygenates.

5.2.1 Methane Oxidation using Hexafluorobenzene

Describing a green method for the oxidation of alcohols, olefins and sulfides, Sato *et al.*[19] reported substrate oxidation using H_2O_2. Carried out in organic media, the application of quaternary ammonium hydrogensulfate as phase transfer catalyst (PTC) facilitated the oxidation of substrate using H_2O_2 and tungstate polyacid. Similarly, the use of PTC, H_2O_2 and H_2WO_4 was reported for the large-scale oxidation of cyclohexene to adipic acid using a continuous flow process, achieving a yield of *ca.* 95% at 99% purity.[20]

The ion exchange of caesium and rubidium within heteropolyacids have been reported as excellent supports for AuPd catalyst applied to the direct synthesis of H_2O_2.[21] The

resulting catalyst saw improved activity due to stabilisation of synthesised H_2O_2 and decreased hydrogenation activity resulting from the support acidity.

Therefore, the use of heteropolyacids and phase transfer catalyst is suggested as a route to effectively use H_2O_2, additionally addressing the proposed poor interaction of catalyst and solvent.

5.3 References

1 R. Horn and R. Schlögl, *Catal. Letters*, 2015, **145**, 23–39.

2 E. V. Kondratenko, T. Peppel, D. Seeburg, V. Kondratenko, N. Kalevaru, A. Martin and S. Wohlrab, *Catal. Sci. Technol.*, 2017, **7**, 366–381.

3 M. H. Ab Rahim, M. M. Forde, R. L. Jenkins, C. Hammond, Q. He, N. Dimitratos, J. A. Lopez-Sanchez, A. F. Carley, S. H. Taylor, D. J. Willock, D. M. Murphy, C. J. Kiely and G. J. Hutchings, *Angew. Chemie - Int. Ed.*, 2013, **52**, 1280–1284.

4 M. H. Ab Rahim, M. M. Forde, C. Hammond, R. L. Jenkins, N. Dimitratos, J. A. Lopez-Sanchez, A. F. Carley, S. H. Taylor, D. J. Willock, G. J. Hutchings, M. Hasbi, A. Rahim, M. M. Forde, C. Hammond, R. L. Jenkins, N. Dimitratos, J. A. Lopez-Sanchez, A. F. Carley, S. H. Taylor, D. J. Willock and G. J. Hutchings, *Top. Catal.*, 2013, **56**, 1843–1857.

5 C. Samanta, *Appl. Catal. A Gen.*, 2008, **350**, 133–149.

6 J. K. Edwards, S. J. Freakley, R. J. Lewis, J. C. Pritchard and G. J. Hutchings, *Catal. Today*, 2015, **248**, 3–9.

7 C. M. Sharts, H. R. Reese, K. A. Ginsberg, F. K. Multer, M. D. Nielson, A. G. Greenburg, G. W. Peskin and D. M. Long, *J. Fluor. Chem.*, 1978, **11**, 637–641.

8 E. P. Wesseler, R. Iltis and L. C. Clark, *J. Fluor. Chem.*, 1977, **9**, 137–146.

9 V. M. Sadtler, M. P. Krafft and J. G. Riess, *Angew. Chemie (International Ed. English)*, 1996, **35**, 1976–1978.

10 C. Hammond, N. Dimitratos, R. L. Jenkins, J. A. Lopez-sanchez, S. A. Kondrat, M. Hasbi Ab Rahim, M. M. Forde, A. Thetford, S. H. Taylor, H. Hagen, E. E. Stangland, J. H. Kang, J. M. Moulijn, D. J. Willock, G. J. Hutchings, M. Hasbi, M. M. Forde, A. Thetford, S. H. Taylor, H. Hagen, E. E. Stangland, J. H. Kang, J. M. Moulijn, D. J. Willock and G. J. Hutchings, *ACS Catal.*, 2013, **3**, 689–699.

11 C. Hammond, S. Conrad and I. Hermans, *ChemSusChem*, 2012, **5**, 1668–1686.

12 C. J. Pan, M. C. Tsai, W. N. Su, J. Rick, N. G. Akalework, A. K. Agegnehu, S. Y. Cheng and B. J. Hwang, *J. Taiwan Inst. Chem. Eng.*, 2017, **74**, 154–186.

13 C. Hammond, R. L. Jenkins, N. Dimitratos, J. A. Lopez-Sanchez, M. H. Ab Rahim, M. M. Forde, A. Thetford, D. M. Murphy, H. Hagen, E. E. Stangland, J. M. Moulijn, S. H. Taylor, D. J. Willock and G. J. Hutchings, *Chem. - A Eur. J.*, 2012, **18**, 15735–15745.

14 M. O. Nutt, K. N. Heck, P. Alvarez and M. S. Wong, *Appl. Catal. B Environ.*, 2006, **69**, 115–125.

15 M. O. Nutt, J. B. Hughes and M. S. Wong, *Environ. Sci. Technol.*, 2005, **39**, 1346–1353.

16 M. S. Wong, P. J. J. Alvarez, Y. L. Fang, N. Ak??in, M. O. Nutt, J. T. Miller and K. N. Heck, *J. Chem. Technol. Biotechnol.*, 2009, 84, 158–166.

17 G. J. Hutchings and C. J. Kiely, *Acc. Chem. Res.*, 2013, **46**, 1759–1772.

18 J. Pritchard, L. Kesavan, M. Piccinini, Q. He, R. Tiruvalam, N. Dimitratos, J. A. Lopez-Sanchez, A. F. Carley, J. K. Edwards, C. J. Kiely and G. J. Hutchings, *Langmuir*, 2010, **26**, 16568–16577.

19 R. Noyori, M. Aoki and K. Sato, *Chem. Commun.*, 2003, **3**, 1977–1986.

20 Y. Wen, X. Wang, H. Wei, B. Li, P. Jin and L. Li, *Green Chem.*, 2012, **14**, 2868–2875.

21 S. J. Freakley, R. J. Lewis, D. J. Morgan, J. K. Edwards and G. J. Hutchings, *Catal. Today*, 2015, **248**, 10–17.

Chapter 6:
Appendix

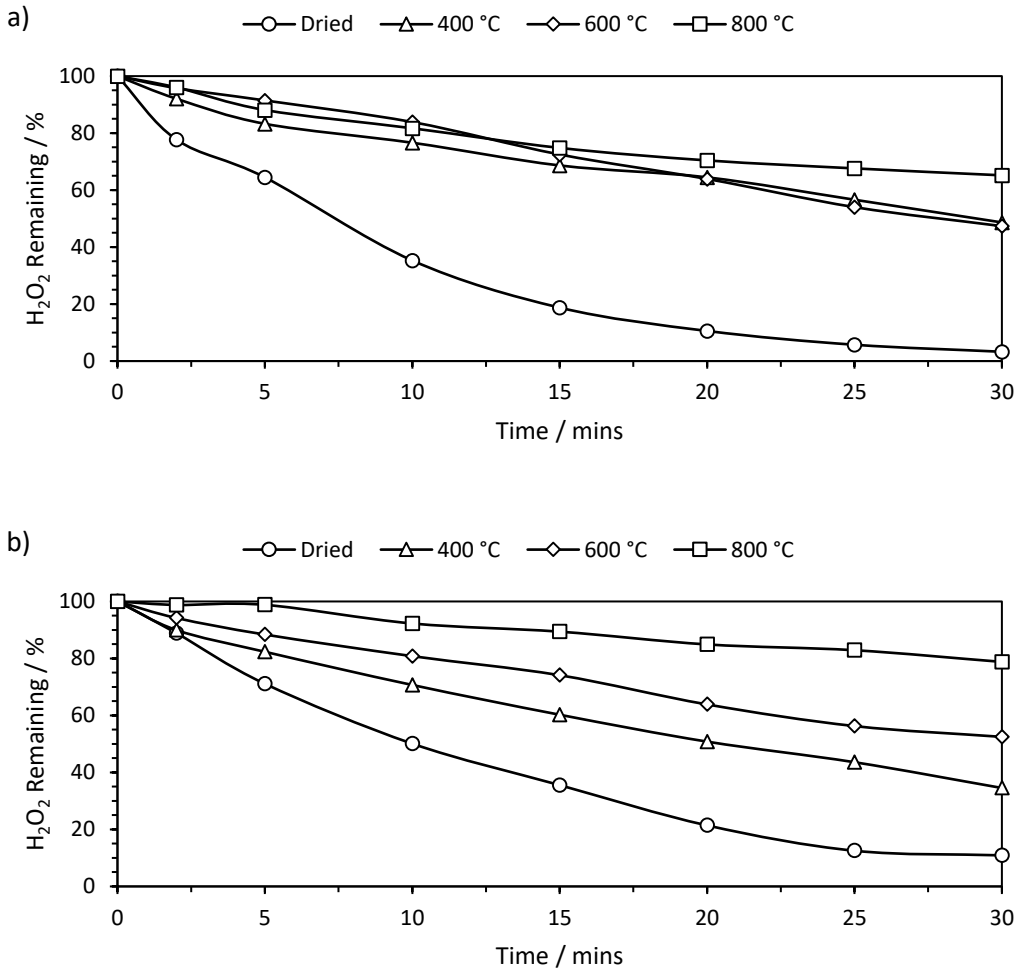

Figure A7.1: Time-on-line analysis for H_2O_2 decomposition for 1 wt. % AuPd/TiO_2 prepared at (a) room temperature and (b) elevated temperature (70 °C).

Standard reaction conditions: time: 30 minutes, temperature: 24 °C, stirring rate: 1000 rpm, all catalysts (1 wt. % total): 7.24×10^{-7} mol of metals equal to 10 mg of solid catalysts, volume: 10 mL of H_2O.[H_2O_2]: 0.5 M

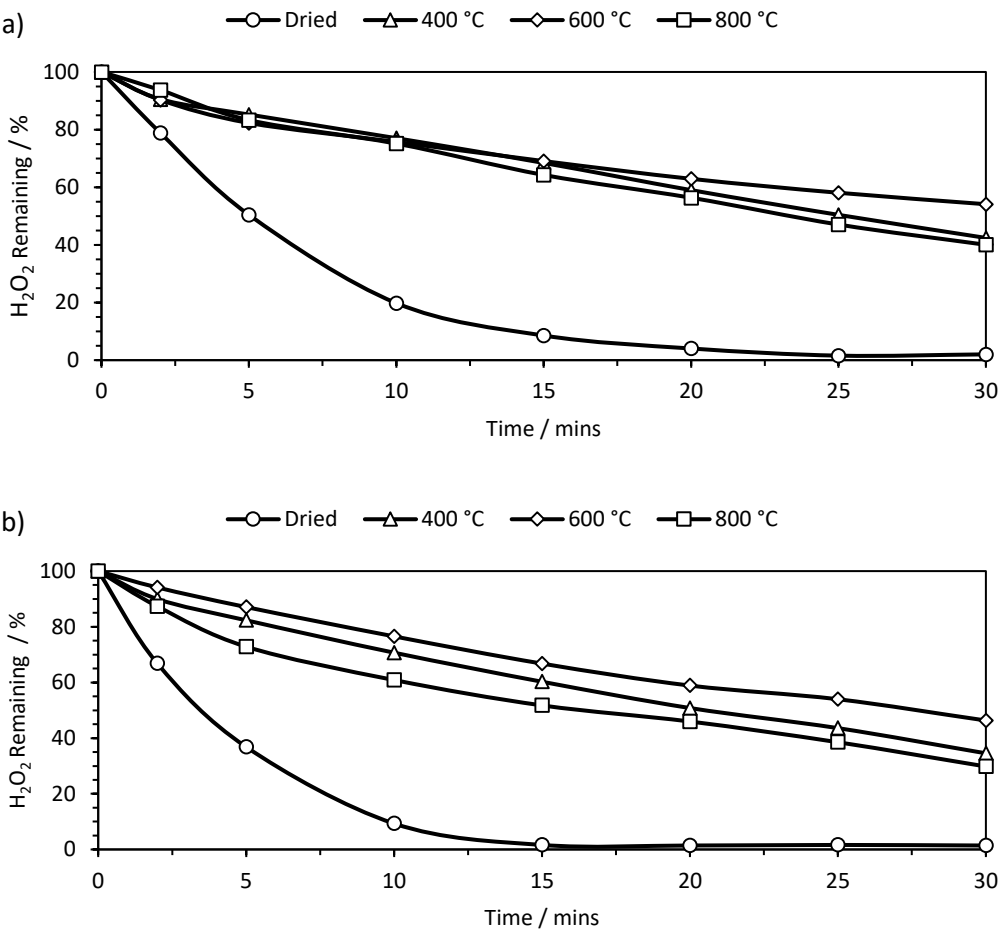

Figure A7.2: Time-on-line analysis of H_2O_2 decomposition for 1 wt. % AuPd/TiO_2 (rutile) catalyst prepared at (a) room temperature and (b) elevated temperature (70 ˚C).

Standard reaction conditions: time: 30 minutes, temperature: 24 °C, stirring rate: 1000 rpm, all catalysts (1 wt. % total): 7.24×10^{-7} mol of metals equal to 10 mg of solid catalysts, volume: 10 mL of H_2O.[H_2O_2]: 0.5 M

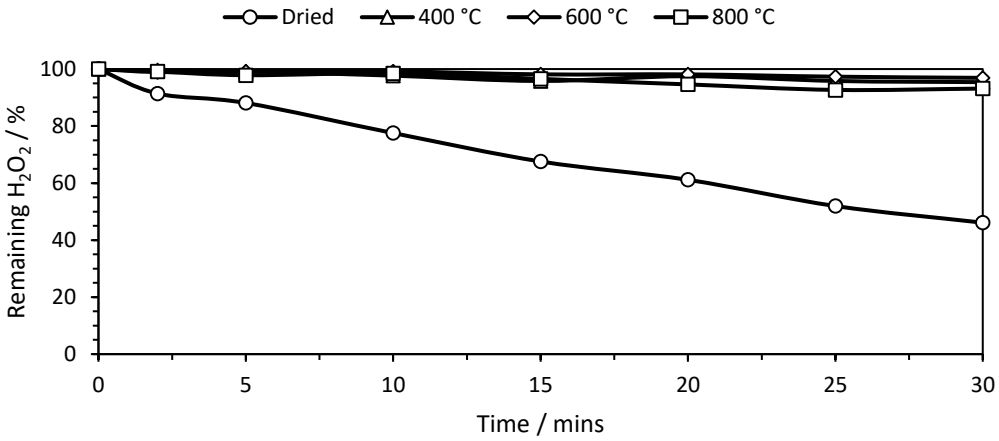

Figure A7.3: Time-on-line analysis for H_2O_2 decomposition for 0.13 wt. % AuPd/ rutile TiO_2 (S_i) prepared at room temperature.

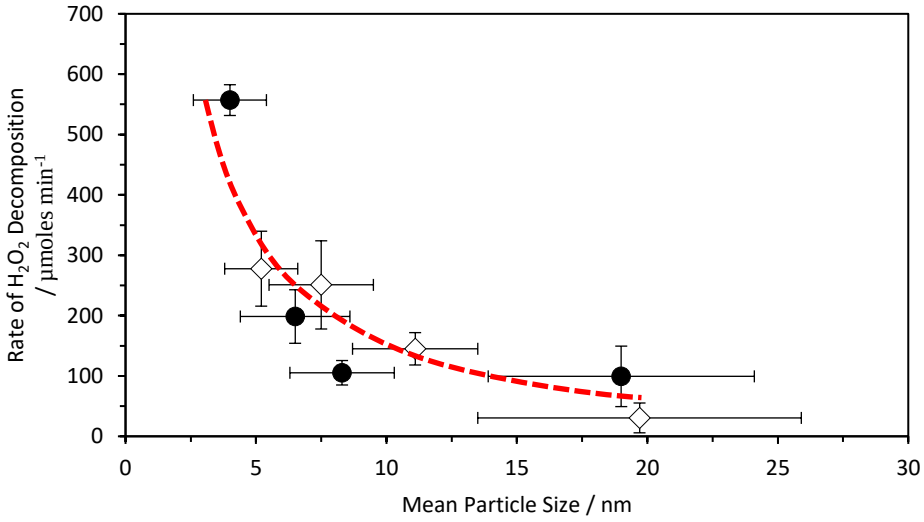

Figure A7.4: Structure-activity relationship of 1 wt.% AuPd/TiO_2 (P25) for methane oxidation illustrating the increase in mean particle size results the decrease of H_2O_2 decomposition rates. ● = RT and ◊ = 70 °C.

Standard reaction conditions: time: 30 minutes, temperature: 24 °C, stirring rate: 1000 rpm, all catalysts (1 wt. % total): 7.24×10^{-7} mol of metals equal to 10 mg of solid catalysts, volume: 10 mL of H_2O.[H_2O_2]: 0.5 M

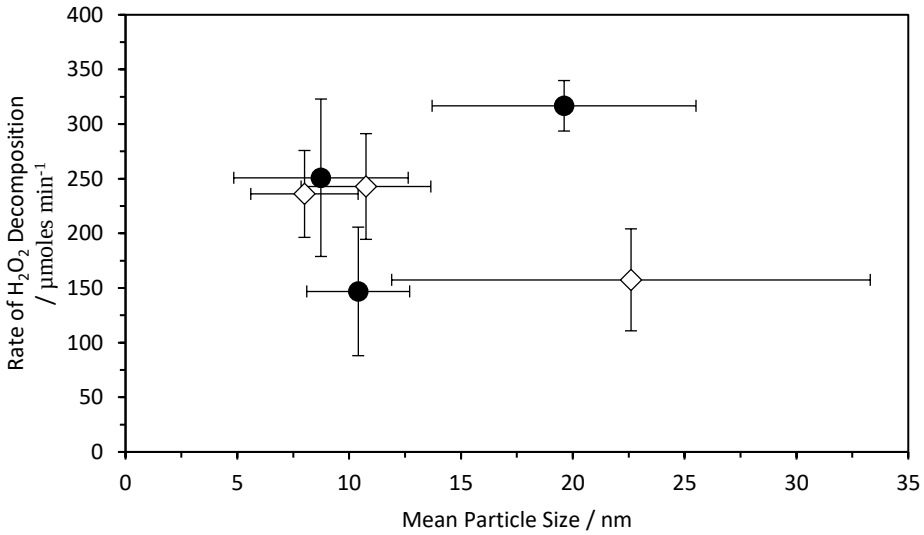

Figure A7.5: Structure-activity relationship for 1 wt.% AuPd/TiO_2 (rutile) catalyst series for methane oxidation. Contrasting the P25 series, no link between particle size and H_2O_2 decomposition rate is found. ● = RT and ◊ = 70 °C.

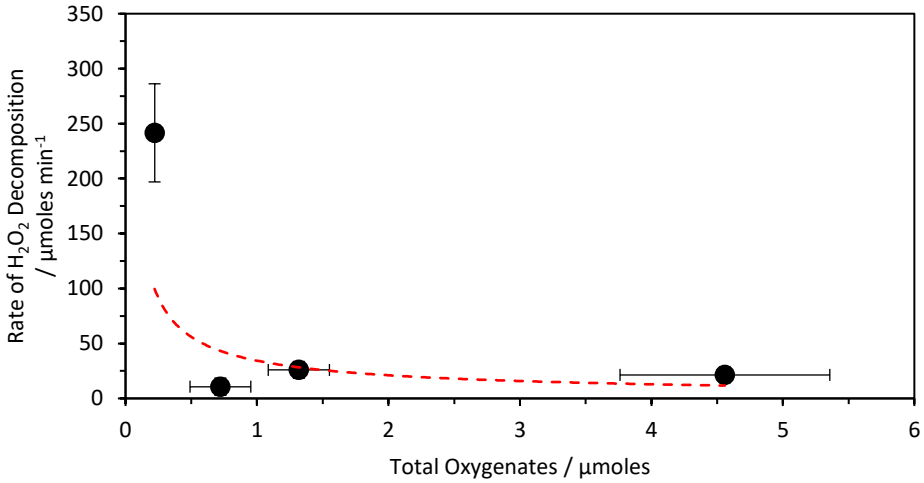

Figure A7.5: Structure-activity relationship for 0.13 wt.% AuPd/TiO_2 (rutile) catalyst series for methane oxidation correlating H_2O_2 decomposition rate with total oxygenates produced after 0.5 h, ● = RT

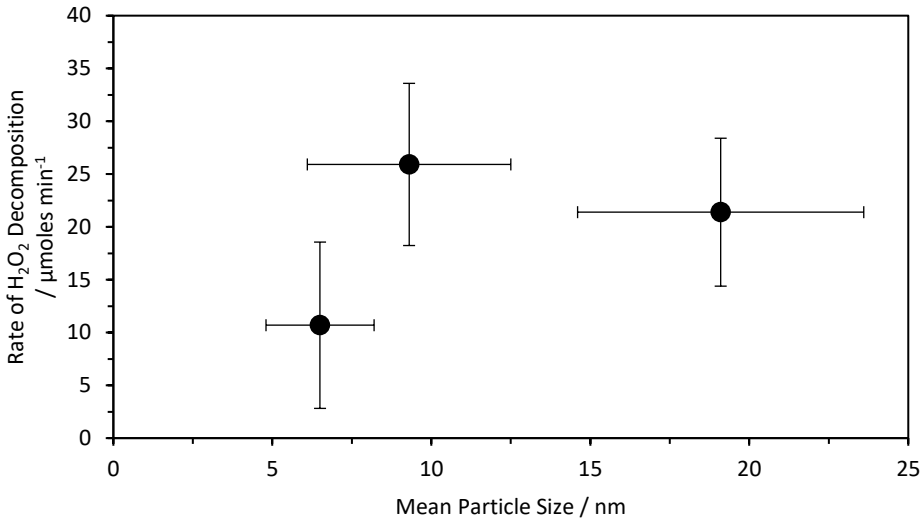

Figure A7.6 Structure-activity relationship for 0.13 wt.% AuPd/TiO_2 (rutile) catalyst series for methane oxidation showing no correlation between particle size and exhibited rated of H_2O_2 decomposition. ● = RT

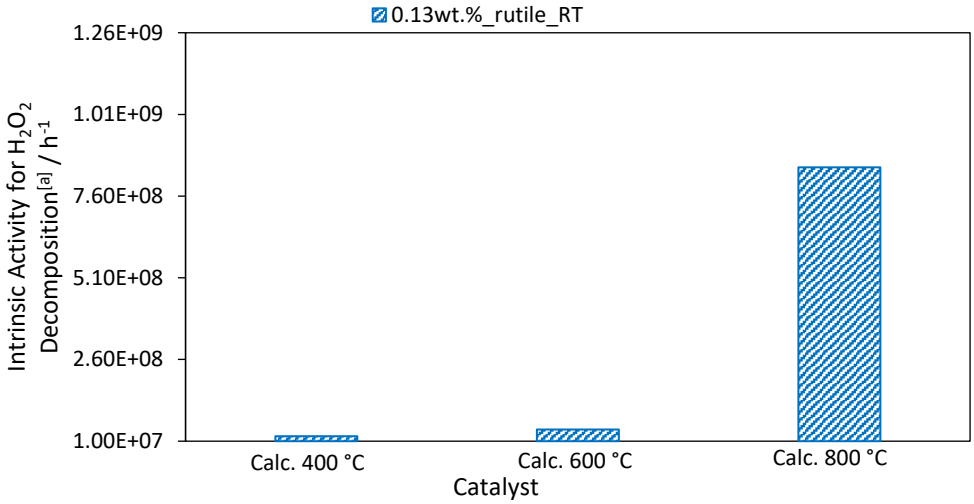

Figure A7.7: The intrinsic activity of 0.13wt.% AuPd/ rutile TiO_2 catalysts prepared by stabiliser-free sol immobilisation at room temperature for the decomposition of H_2O_2, showing that larger mean particles size possess higher activity for H_2O_2 decomposition. ● = RT.

Standard reaction conditions: time: 30 minutes, temperature: 24 °C, stirring rate: 1000 rpm, all catalysts (0.13 wt. % total): 9.41x10^{-8} mol of metals equal to 10 mg of solid catalysts, volume: 10 mL of H_2O.[H_2O_2]: 0.5 M [a] calculated as $Moles_{(H2O2\ decomposed)}/Moles_{(metal\ surface\ atoms)}/time\ (h)$

Table 3A: The effect of post-synthesis heat treatment on the catalytic activity of 1wt.% AuPd/ TiO_2 (P25) for the oxidation of methane.[a] (Entries 3-6; prepared at room temperature, Entries 7-10; prepared at 70°C)

Entry	Heat Treatment	Products [μmoles]				Oxygenate selectivity [d]	Total Productivity[e]	TOF[f]	H_2O_2 Remaining[g]	Mean Particle Size[h]	H_2O_2 Decomposition Rate[g][i]
		CH_3OH [b]	HCOOH [b]	CH_3OH [b]	CO_2[c]	[%]	[mol $kg_{(cat)}^{-1}$ h^{-1}]	[h^{-1}]	[%]	[nm]	[μmol min^{-1}]
1	Blank	0	0	0	0.14	0	0	0	97.6	n/a	n/a
2	TiO_2	0	0	0	0.20	0	0.039	0	97.4	n/a	n/a
3	RT, Dried	0	0	0	0.27	0	0.054	0.75	0.3	4.0 ± 1.4	557
4	RT, 400 °C	0	0	0	0.27	0	0.054	0.74	0.3	6.5 ± 2.1	199
5	RT, 600 °C	0.03	0	0.13	0.16	46.6	0.063	0.88	1.7	8.3 ± 2.0	105
6	RT, 800 °C	0.23	0	0.50	0.17	80.8	0.172	2.38	42.1	19.0 ± 5.1	99.0
7	70 °C, Dried	0	0	0	0.16	0	0.032	0.44	0.3	5.2 ± 1.4	278
8	70 °C, 400 °C	0	0	0	0.14	0	0.018	0.25	0.5	7.5 ± 2.0	251
9	70 °C, 600 °C	0	0	0.12	0.16	42.5	0.057	0.79	13.3	11.1 ± 2.4	145
10	70 °C, 800 °C	0.29	0	1.12	0.16	90.0	0.312	4.31	56.1	19.7 ± 6.2	31

[a]Standard reaction conditions: time: 30 minutes, temperature: 50 °C, P_{CH_4}: 30.5 bar, stirring rate: 1500 rpm, all catalysts (1 wt. % total): 7.24 x10^{-7} mol of metals equal to 10 mg for solid catalysts, volume: 10 mL of H_2O.[H_2O_2]: 0.5 M. Catalysts were prepared by SF-S_i at room temperature (Entries 3-6) or at 70 °C (Entries 7-10). Catalyst is dried at 110 °C, 10 °C min^{-1}, 16 h, static air. Calcined at various temperatures (20 °C min^{-1}, 3 h, static air). [b] Analysed by ^{1}H NMR spectroscopy with 1 % TMS in $CDCl_3$ internal standard. [c] Analysed by gas chromatography using a flame ionization detector. Values obtained using CO_2 calibration curve. [d] Oxygenate selectivity calculated as (moles oxygenates/total moles of products) x 100. [e] Total productivity calculated as (moles(products)/ weight(catalyst))/ time). [f] TOF: Turn-over frequency, calculated as (moles(products)/ total moles(metal))/ time (h). [g] Remaining H_2O_2 assayed by Ce^{4+} (aq.) titration. Calculated as (moles(initial)/ moles(final) x100. [h] Determined by transmission electron microscopy. [i] H_2O_2 decomposition reaction conditions: time: 30mins, temperature: 24 °C, atmospheric pressure, stirring rate: 1000rpm, all catalysts (1 wt. % total): 7.24 x10^{-7} mol of metals equal to 10 mg for solid catalysts, volume: 10 mL of H_2O.[H_2O_2]: 0.5 M.

Table A7.2: The effect of support pre-calcination for 1wt.% AuPd/ rutile TiO_2 prepared at room temperature (Entries 2-5) and at 70 °C (Entries 6-9) [a]

Entry	Heat Treatment	Products [µmoles]				Oxygenate selectivity [d][%]	Total Productivity [e] [mol $kg_{(cat)}^{-1}$ h^{-1}]	TOF[f] [h^{-1}]	H_2O_2 Remaining[f] [%]	Mean Particle Size[h] [nm]	H_2O_2 Decomposition Rate [µmol min^{-1}]
		CH_3OH [b]	HCOOH [b]	CH_3OOH [b]	CO_2[c]						
1	rutile	0	0	0	0.33	0	0.040	0	97.5	n/a	n/a
2	RT, Dried	0	0	0	0.26	0	0.052	0.72	0.2	n/a	830
3	RT, 400 °C	0.26	0	0	0.29	47.9	0.109	1.50	2.2	8.7 ± 3.9	251
4	RT, 600 °C	0.22	0	0.36	0.31	65.4	0.176	2.43	4.5	10.4 ± 2.3	147
5	RT, 800 °C	0.45	0	0.21	0.18	83.4	0.163	2.25	2.1	19.6 ± 5.9	317
6	70 ˚C, Dried	0	0	0	0.27	0	0.053	0.74	0.2	n/a	530
7	70 °C, 400 °C	0.36	0	0.56	0.15	86.2	0.214	2.95	1.4	8.0 ± 2.4	236
8	70 °C, 600 °C	0.30	0	0.73	0.15	87.1	0.228	3.15	23.8	10.8 ± 2.9	243
9	70 °C, 800 °C	0.38	0	0.73	0.16	86.5	0.243	3.35	7.8	22.6 ± 10.7	158

[a]Standard reaction conditions: time: 30 minutes, temperature: 50 °C, P_{CH_4}: 30.5 bar, stirring rate: 1500 rpm, all catalysts (1 wt. % total): 7.24 x10^{-7} mol of metals equal to 10 mg for solid catalysts, volume: 10 mL of H_2O.[H_2O_2]: 0.5 M. TiO_2 support pre-treated by calcination at 800 °C prior to use in catalyst preparation (denoted rutile). Catalysts were prepared by SF-S_i at room temperature (Entries 2-5) or at 70 °C (Entries 6-9). Catalyst is dried at 110 °C, 10 °C min^{-1}, 16 h, static air. Calcined at various temperatures (20 °C min^{-1}, 3 h, static air). [b] Analysed by ^{1}H NMR spectroscopy with 1 % TMS in $CDCl_3$ internal standard. [c] Analysed by gas chromatography using a flame ionization detector. Values obtained using CO_2 calibration curve. [d] Oxygenate selectivity calculated as (moles oxygenates/ total moles of products) x 100. [e] Total productivity calculated as (moles(products)/ weight(catalyst))/ time). [f] TOF: Turn-over frequency, calculated as (moles(products)/ total moles(metal))/ time (h). [g] Remaining H_2O_2 assayed by Ce^{4+}(aq.) titration. Calculated as (moles(initial)/ moles(final) x100. [h] Determined by transmission electron microscopy. [i] H_2O_2 decomposition reaction conditions: time: 30mins, temperature: 24 °C, atmospheric pressure, stirring rate: 1000 rpm, all catalysts (1 wt. % total): 7.24 x10^{-7} mol of metals equal to 10 mg for solid catalysts, volume: 10 mL of H_2O.[H_2O_2]: 0.5 M.

Table A7.3: The effect of reduced metal loading on pre-calcined support for the oxidation of methane (0.13 wt.% AuPd/rutile TiO_2)[a]

Entry	Heat Treatment	Products [µmol]				Oxygenate selectivity[d] [%]	Total Productivity[e] [mol $kg_{(cat)}^{-1}$ h^{-1}]	TOF[f] [h^{-1}]	H_2O_2 Remaining[g] [%]	Mean Particle Size[h] [nm]	H_2O_2 Decomposition Rate[g][i] [µmol min^{-1}]
		CH_3OH [b]	HCOOH [b]	CH_3OOH [b]	CO_2[c]						
1	Dried	0	0	0	0.22	0	0.046	7.00	0.23	n/a	215
2	400 °C	0.06	0.00	0.41	0.25	64.8	0.142	21.7	55.1	6.5 ± 1.7	10.7
3	600 °C	0.13	0.00	0.86	0.33	75.0	0.252	38.3	75.5	9.3 ± 3.2	25.9
4	800 °C	0.43	0.32	3.51	0.30	93.2	0.902	137	64.3	19.1 ± 4.5	21.4

[a]Standard reaction conditions: time: 30 min, temperature: 50 °C, PCH4: 30.5 bar, stirring rate: 1500 rpm, all catalysts (0.13 wt. % total): 9.41 $x10^{-8}$ mol of metals equal to 10 mg for solid catalysts, volume: 10 mL of H_2O.[H_2O_2]: 0.5 M. TiO_2 support pre-treated by calcination at 800 °C prior to use for catalyst preparation (denoted rutile TiO_2). Catalyst prepared by SF-S_i at RT. Catalyst is dried at 110 °C, 10 °C min^{-1}, 16 h, static air. Calcined at various temperatures (20 °C min^{-1}, 3 h, static air). [b] Analysed by ^{1}H NMR NMR spectroscopy with 1% TMS in $CDCl_2$ internal standard. [c] Analysed by gas chromatography using a FID methaniser. Values obtained using CO_2 calibration curve. [d] Oxygenate selectivity calculated as (moles oxygenates/total moles of products) x 100. [e] Total productivity calculated as (moles(oxygenates) /weight(catalyst))/time). [f] TOF: Turn-over frequency, calculated as (moles(products) / total moles(metal)) / time (h). [g]Remaining H_2O_2 assayed by Ce^{4+}(aq.) titration. Calculated as (moles(initial)/moles(final) x100. [g] Determined by transmission electron microscopy. [h] [i] H_2O_2 decomposition reaction conditions: time: 30mins, temperature: 24 °C, atmospheric pressure, stirring rate: 1000rpm, all catalysts (0.13 wt. % total): 9.41 $x10^{-8}$ mol of metals equal to 10 mg for solid catalysts, volume: 10 mL of H_2O.[H_2O_2]: 0.5 M.